

Dissertation

submitted to the
Combined Faculty of Natural Sciences and Mathematics
of Heidelberg University, Germany
for the degree of
Doctor of Natural Sciences

Put forward by
M.Sc. Dennis Wörthmüller
born in Mannheim, Germany
Oral examination: 27.07.2022

Finite Element Modeling of Optogenetic Control of Cell Contractility

Referees: Prof. Dr. Ulrich Schwarz
Prof. Dr. Heinz Horner

Finite Element Modeling of Optogenetic Control of Cell Contractility

Biological cells use physical force to interact with their environment, with dramatic consequences for survival, proliferation, differentiation and migration. Force is generated mainly by the contractile actomyosin cytoskeleton and propagated through cell-matrix and cell-cell adhesions. In this thesis, I use finite element methods to model adherent cells as thin active viscoelastic solids to study the dynamics of active force-generation in single cells and force propagation in small cell clusters. The theoretical models are complemented by experiments in which optogenetic activation of the Rho-pathway is combined with traction force microscopy and adhesive micropatterning. For single cells on circular micropatterns, we find perfect homeostasis with a setpoint that strongly depends on cell size and cytoskeletal organization. For epithelial cells, we find that the responder cells actively respond to generate a similar contractile stress as the sender cells, and that force generation and propagation again strongly depends on cytoskeletal organization. Finally, a discontinuous Galerkin method is used to couple the biochemistry of signaling pathways to cell contractility. Overall, our work shows that the active mechanics of adherent cells is strongly modulated by their internal organization, which in turn depends on the adhesive geometry of their environment, thus generating a tightly integrated mechanochemical feedback loop that allows for high-level control structures.

Finite-Elemente-Modellierung der optogenetischen Steuerung von Zellkontraktilität

Biologische Zellen nutzen physikalische Kräfte, um mit ihrer Umgebung zu interagieren, was dramatische Folgen für das Überleben, Proliferation, Differenzierung und Migration hat. Die Kraft wird hauptsächlich durch das kontraktile Aktomyosin-Zytoskelett erzeugt und durch Zell-Matrix- und Zell-Zell-Adhäsionen weitergeleitet. In dieser Arbeit verwende ich Finite-Elemente-Methoden, um adhärente Zellen als dünne aktive viskoelastische Festkörper zu modellieren und die Dynamik der aktiven Krafterzeugung in einzelnen Zellen und die Kraftausbreitung in kleinen Zellverbänden zu untersuchen. Die theoretischen Modelle werden durch Experimente ergänzt, in denen die optogenetische Aktivierung des Rho-Reaktionswegs mit Zellkraftmikroskopie und adhäsiver Mikromusterung kombiniert wird. Für einzelne Zellen auf kreisförmigen Mikromustern finden wir eine perfekte Homöostase mit einem Sollwert, der stark von der Zellgröße und der Organisation des Zytoskeletts abhängt. Bei Epithelzellen stellen wir fest, dass die Antwortzellen aktiv reagieren, um eine ähnliche kontraktile Spannung zu erzeugen wie die Senderzellen, und dass die Krafterzeugung und -ausbreitung wiederum stark von der Organisation des Zytoskeletts abhängt. Schließlich wird eine diskontinuierliche Galerkin-Methode verwendet, um die Biochemie der Signalwege mit der Zellkontraktilität zu verbinden. Insgesamt zeigt unsere Arbeit, dass die aktive Mechanik adhärenter Zellen stark durch ihre interne Organisation moduliert wird, die wiederum von der adhäsiven Geometrie ihrer Umgebung abhängt, wodurch eine eng integrierte mechanisch-chemische Rückkopplungsschleife entsteht, die Kontrollstrukturen auf hoher Ebene ermöglicht.

Contents

1	Introduction	1
1.1	The cytoskeleton	2
1.1.1	Cytoskeletal substructures	2
1.1.2	Cell adhesion	9
1.2	Measuring cell contractility	12
1.2.1	Traction force microscopy	12
1.2.2	Micropatterning	15
1.2.3	Non-neuronal optogenetics	15
1.3	Modelling cell contractility	18
1.3.1	Bulk-based models	18
1.3.2	Contour models	22
1.3.3	Interface-based models	23
1.4	Summary	25
1.5	Outline	26
2	Theory	27
2.1	Continuum model	27
2.1.1	Continuum mechanics in a nutshell	27
2.1.2	Isotropically contracting disc	34
2.2	Contour model	38
2.2.1	Derivation of the equilibrium equation	39
2.2.2	The tension elasticity model revisited	41
2.3	Summary	43
3	Implementation	45
3.1	The finite element method - divide and conquer	45
3.1.1	Weak form and function spaces	46
3.1.2	Discretization	47
3.1.3	Error estimate and convergence rates	50
3.2	Simulating the isotropically contraction disc	50
3.3	Contour simulations with FEM	53
3.4	Concluding remarks	54
4	Optogenetic control of single cells	57
4.1	Introduction	57
4.2	Experimental setup	58
4.3	Modelling	59
4.3.1	Active Kelvin-Voigt model	59
4.3.2	Substrate strain energy	60

4.3.3	Time course of the photoactivation stress	63
4.3.4	Adhesion geometry of the hazard pattern	66
4.3.5	Anisotropic contractile stress	67
4.3.6	Parametrization and scaling considerations from analytical solution	68
4.3.7	Finite element implementation and time discretization	69
4.4	Results.	70
4.4.1	Influence of pattern size on actin ordering and strain energy . .	71
4.4.2	Influence of actin architecture on strain energy and force generation dynamics	74
4.4.3	Influence of varying pulse duration on force generation	79
4.5	Conclusion	79
5	Optogenetic control of cell pairs	83
5.1	Introduction	83
5.2	Experimental setup	84
5.3	Characterization of the homeostatic state of doublets and singlets . . .	86
5.3.1	Contour model based cell shape analysis	86
5.3.2	Results	92
5.4	Photoactivation- doublets vs. singlets	95
5.4.1	Modeling	95
5.4.2	Results	101
5.5	Stress propagation in small tissues	109
5.6	Summary and discussion	111
6	Coupling Biochemistry to Cell Mechanics	113
6.1	Introduction	113
6.2	Blueprint for a cell pair model.	115
6.2.1	Reaction diffusion on deformable domain	115
6.2.2	Diffusion with hindrance - membrane	117
6.2.3	Weak form for discontinuous Galerkin approach	118
6.2.4	Coupling to mechanics	120
6.3	RhoA-pathway	121
6.3.1	Linear RhoA - pathway	123
6.3.2	Parametrization	125
6.4	Photoactivation with feedback.	127
6.4.1	Baseline contractility	127
6.4.2	Photoactivation	128
6.5	Conclusion	130
7	Summary and outlook	133
A	Appendix	137
A.1	Supplementary Information for Chapter 4	137
A.2	Supplementary Information for Chapter 5	141
A.3	Supplementary Information for Chapter 6	153

A.4 Actin polarization analysis (Structure Tensor)	158
A.5 Analytical Calculations	160
List of Abbreviations	163
List of Figures	165
References	167
Danksagung	187

Chapter 1

Introduction

Complex multicellular organisms, such as the human body, consist of billions of cells. The function and fate of these organisms are highly dependent on the correct interplay of various intra- and intercellular processes, and even the smallest deviations from expected cell behavior can lead to drastic consequences such as disease and finally death. Throughout their lives, cells must perform a variety of tasks, including growth, division, and movement, that are directly related to other tasks such as interpreting external and internal stimuli and deciding how to respond to them. Although research has yielded many new insights in recent years, not least through interdisciplinary collaboration in fields such as molecular biology, cell biology, biophysics, biochemistry and others, many questions remain unanswered. In particular, it is still puzzling how cells integrate information from their environment into their decision-making process. However, over the course of the last two decades, it became progressively clear that physical, i.e. mechanical forces play a major role in cellular decision making and aid in regulating important physiological processes like tissue growth and morphogenesis. This insight has led to the new field of mechanobiology. In addition to the forces they are exposed to externally, they also use a highly complex and self-organized contractile structure called the actin cytoskeleton to actively generate forces and explore the mechanical and geometric properties of their environment. These informations are then fed back to the cell, and evaluated by means of chemical signals, a process which is known as mechanotransduction. Therefore, it is important to study how cells generate forces, how the internal molecular machinery regulates them, and how these forces transmit information in multicellular systems to understand processes such as development, organogenesis, homeostasis or diseases like cancer.

In this thesis we focus on the modeling of active force generation in adherent single cells and few cell systems. We use a combination of analytical and computational models accompanied by a series of experiments that were carried out by the group of Martial Balland at the Université Grenoble Alpes, to study the dynamics of force generation and force propagation. In particular, we focus on the influences adhesion geometry and the organization of the actin cytoskeleton have on force generation. A central part of this work is the numerical implementation of two-dimensional viscoelastic continuum models which account for the elastic and viscous properties of the cytoskeleton. We apply these models to single cells, cell pairs and small cell clusters, and show that these models are capable to adequately capture the contractile behavior of cells. In addition to the two-dimensional models, we establish a computational framework to describe the cell shape by means of elastic contour models.

This approach is validated by analytical calculations and image-based cell shape measurements obtained from experiments. Furthermore, we use a discontinuous Galerkin method to constrain a model for an interacting pair of cells and use reaction-diffusion systems to couple cell mechanics and biochemistry to design a blueprint of a model which allows to study actively sustained force propagation across cells. In the remainder of this chapter, we first provide an overview of the biology of the cytoskeleton and associated regulating mechanisms. Next, we summarize the most important aspects of the experimental methods mentioned throughout this work and finally conclude with a comparison of well established models for cell contractility and cell shape.

1.1. THE CYTOSKELETON

To function and thrive in a complex environment, biological cells must be able to sense their surroundings and interact with other cells. This important ability is provided by the complex and highly dynamic cytoskeleton (CSK). The CSK is a dense filamentous network that primarily provides the cell with structure and mechanical stability. Moreover, it also aids in intracellular transport processes, can rapidly rearrange itself to better suit cellular needs, and is key to cell movement in many cell types.

1.1.1. CYTOSKELETAL SUBSTRUCTURES

The cytoskeletal substructure consists of three different filaments: actin filaments, microtubules and intermediate filaments. Each of these filaments is composed of small protein subunits that are held together by weak non-covalent bonds. In addition, the filaments interact with various other proteins such as passive crosslinkers, molecular motors or proteins that, for example, initiate the assembly or disassembly of filaments (*Howard et al.*, 2002). Fig. 1.1A depicts the three different filaments and their characteristic organization within the cell. Fig. 1.1B and C show their molecular structure together with experimental images. In the following, we will take a closer look at each of the three filament types and discuss their mechanical properties in the context of the mechanics of the whole cell.

ACTIN

Actin filaments form the so called actin CSK which, together with the molecular motor protein myosin II, forms the main contractile structure in all eucaryotic cells. The filamentous F-actin is formed by assembly of the monomeric globular protein G-actin into a right-handed double-stranded helix (Fig. 1.1A) with a typical cross-sectional diameter of ~ 7 nm and a persistence length¹ of ~ 15 μm (*Phillips et al.*, 2012). The asymmetry of G-actin makes the composite F-actin a polar filament, with one end

¹The persistence length defines the length scale on which semi-flexible polymers in a thermal environment are approximately straight. It can be calculated from a comparison of the bending rigidity of the polymer and the thermal energy as $l_{\text{pers}} = EI/(k_B T)$, where E denotes the Young's modulus, I the geometric moment and $k_B T$ the thermal energy.

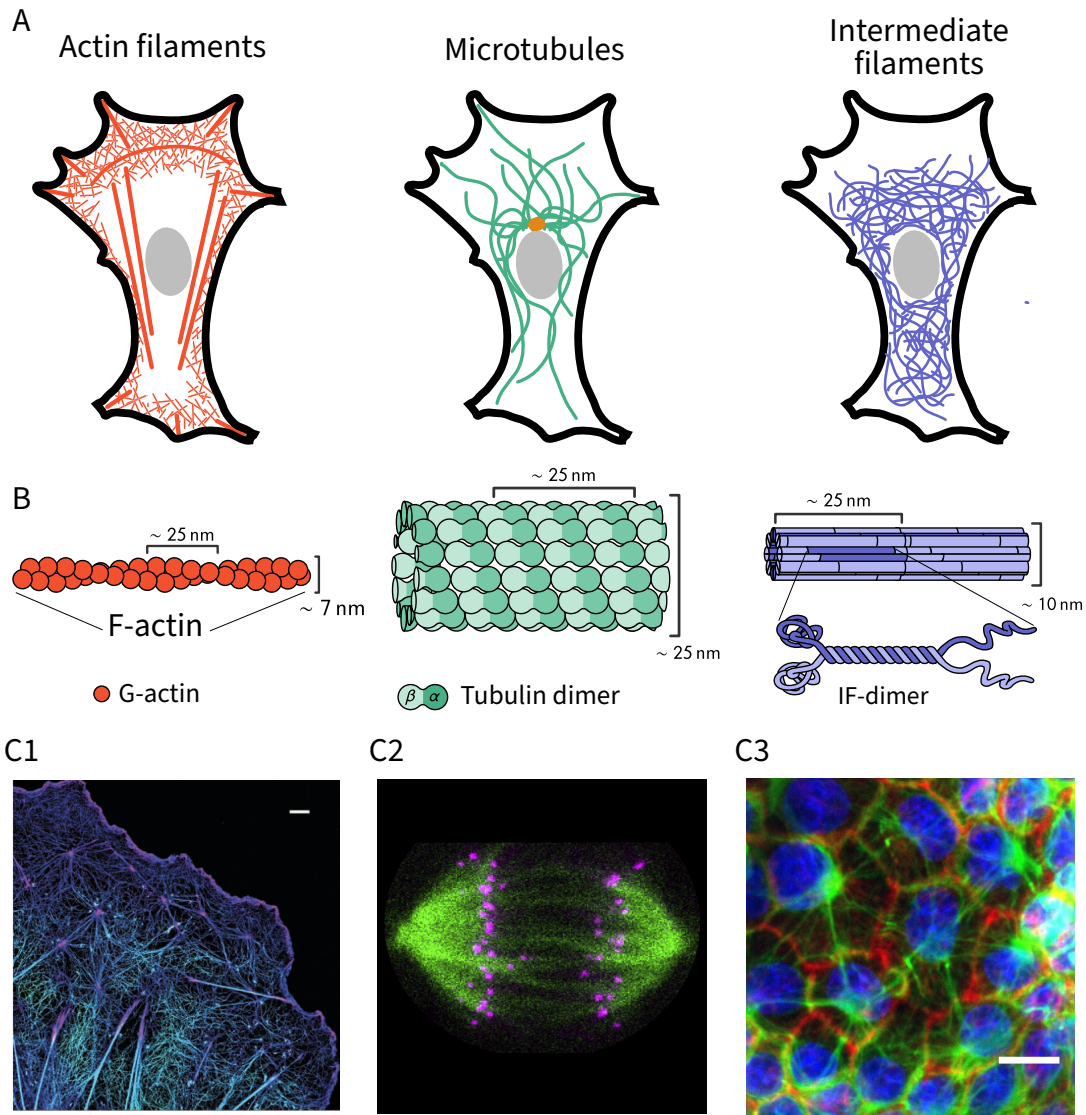


Figure 1.1: Overview of the three filament systems which make up the cytoskeleton alongside their molecular structure. Panel **A** schematically depicts the organization and localization of actin filaments (left), microtubules (middle) and intermediate filaments (right). The actin CSK occurs both as polymer mesh and highly organized into stress fibers. Microtubules originate from the centrosome (orange) as rod-like stiff filaments spanning the whole cell. Intermediate filaments are very flexible and not directly involved in cell movement but provide mechanical strength to the cell. Panel **B** shows the molecular structure of the three filament types and the involved spatial dimensions. Both actin and microtubules are comprised of globular proteins which make them polar filaments. Intermediate filaments consist of fibrous protein dimers and are nonpolar. Panel **C1** shows a dual-objective STORM microscopy image of the ventral actin layer of a cell with clearly visible ventral stress fibers. Panel **C2** depicts a spindle apparatus (green) pulling apart kinetochores (pink) during mitosis. Panel **C3** shows strained intermediate filaments interconnecting epithelial cells. Figures: A adapted from (Huber et al., 2015); B adapted from (Purves et al., 2003); C1 taken from (Xu et al., 2012); C2 taken from (Vukušić et al., 2017); C3 taken from (Latorre et al., 2018).

being the barbed end (plus) and the other the pointed end (minus) (Fig. 1.1B).

Single actin filaments organized into larger structures have in principle two crucial functions. First, they provide mechanical stability to the cell and second, they enable quick rearrangements of the actin CSK in order to react to external or internal stimuli or as a part of cell motility. The former is achieved by their flexible yet stable structure, which allows them to withstand tensile forces of the order of ~ 100 pN (*Rajagopal et al.*, 2018) while the latter is possible due to the myosin-driven contraction and the fast actin assembly rates on time scales of milliseconds (*Pollard*, 1986). Fig. 1.2 depicts the various supramolecular actin structures, which result from the interaction of actin and a variety of other proteins like crosslinkers, nucleation factors or adaptor and capping proteins. These structures are broadly classified into network-like and bundle-like (*Blanchoin et al.*, 2014). For the network-like structures, one further distinguishes branched networks, for example the lamellipodium, and cross-linked networks like the actin cortex (Fig. 1.2B). The lamellipodium is located at the leading edge of the cell and exhibits a branched structure. This structure is initiated by the Arp2/3-complex and regulated by capping proteins which terminate the growth of the network (Fig. 1.2B). During cell migration this network polymerizes against the plasma membrane, thereby pushing it forward. The actin cortex is attached to the inner cell membrane via membrane-anchoring proteins. Passive and active cross-linking proteins, such as α -actinin and myosin II, provide the network with stability and the ability to actively deform. In this sense, it allows the cells to change shape during cell migration and cell division while simultaneously stabilizing the plasma membrane against mechanical disturbance from outside (*Alberts et al.*, 2003).

Bundle-like structures can also be divided into parallel bundles and anti-parallel bundles. A prominent example for non-contractile parallel actin bundles are the so-called filopodia (Fig. 1.2A). These finger-like protrusions typically form at the leading edge of the cell and play a role in sensing, cell-cell interactions and cell migration (*Mattila*, 2008). The bundle-like shape is achieved by crosslinkers like α -actinin, fascin and fimbrin, whereas growth is mainly regulated by proteins like formins or Ena/VASP (*Blanchoin et al.*, 2014) (Fig. 1.2B).

In contrast to parallel bundles, anti-parallel bundles are predominantly contractile structures. Typical examples for anti-parallel bundles are stress fibers which make up the main contractile structures in animal cells like fibroblast, smooth muscle and endothelial cells (*Pellegrin et al.*, 2007). They consist of 10 to 30 actin filaments which are cross-linked by α -actinin and categorized into dorsal stress fibers, ventral stress fibers, transverse arcs and the perinuclear actin cap as illustrated in (Fig. 1.2A and B (*Heath*, 1983; *Khatau et al.*, 2009; *Tojkander et al.*, 2012)). The distinction is made on the basis of characteristics such as location of the stress fiber, coupling to the extracellular matrix and its specific morphology.

Dorsal stress fibers are anchored to the extracellular matrix only at one end, typically near the leading edge of the cell. In contrast to the other three types, dorsal stress fibers are not contractile as they do not contain myosin II (*Tojkander et al.*, 2011). Although they lack the ability to contract, they are important when it comes to the assembly of new stress fibers as dorsal stress fibers and transverse arcs may be con-

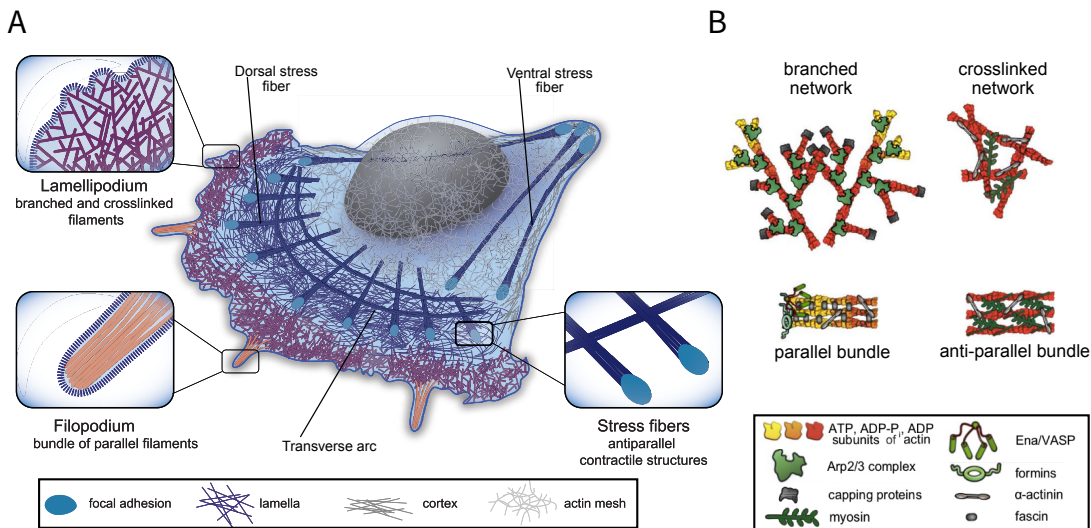


Figure 1.2: The actin cytoskeleton. Panel **A** depicts the versatile organization of the actin cytoskeleton which include the lamellipodium, the filopodium, the actin cortex and different kinds of stress fibers. Panel **B** schematically illustrates the structure of the two occurring network and bundle-like structures together with the involved proteins regulating growth and function. Figures: A adapted from (Letort *et al.*, 2015); B adapted from (Blanchoin *et al.*, 2014).

verted to ventral stress fibers (Hotulainen *et al.*, 2006; Letort *et al.*, 2015; Tojkander *et al.*, 2011).

Transverse arcs exhibit a sarcomeric structure with a periodically arranged α -actinin-myosin pattern and are therefore contractile, in contrast to the dorsal stress fibers. However, transverse arcs do not attach to the extracellular matrix and their contractile nature only contributes indirectly through their connections to dorsal stress fibers. In combination with dorsal stress fibers, the contractility of the transverse arcs flattens the lamellum. Thereby, the focal adhesions of the dorsal stress fibers act as a hinge, while their the strut-like composition presses on the lamellum (Burnette *et al.*, 2014). (Fig. 1.2A).

Ventral stress fibers have a similar sarcomeric morphology as the transverse arcs but are connected to focal adhesions at both ends (Burridge *et al.*, 2013). From all of the above discussed linear bundles, ventral stress fibers are the strongest as they are able to build up forces around 10 nN (Livne *et al.*, 2016). In addition, they are important for signal transduction and mechanical sensing and provide contraction of the posterior end of the cell during cell migration. Fig. 1.1C1 shows a super resolution microscopy image of ventral stress fibers of an adherent cell.

As already mentioned, the motor protein myosin II is responsible for contractility in non-muscle cells. Briefly said, molecular motors convert chemical energy, that is stored in molecular bonds, into motion or mechanical work. A prominent example for this metabolic process is the hydrolysis of adenosine triphosphate (ATP). During this dephosphorylation reaction, a certain class of enzymes, so-called ATPases, catalyze the decomposition of ATP into adenosine diphosphate (ADP) and inorganic phosphate, thereby releasing energy. This reaction plays a crucial role in the contraction of actin filaments by myosin motors. The structure of non-muscle myosin II (NM II) is illustrated in Fig. 1.3A and B. NMII is a polar hexamer comprised of two

identical sub-units which in turn consist of a heavy chain, two light chains and a globular domain (Fig. 1.3). In its inactive state, referred to as 10s assembly-incompetent, NM II is folded onto itself and thereby inhibiting its ATPase activity and preventing binding to actin (*Yang et al.*, 2019). The conformational change into the unfolded 6s assembly-competent NM II is achieved by phosphorylation² of the regulatory light chain (RLC) (Fig. 1.3A). For simplicity one often refers to this conformation as the NM II monomer. Subsequent phosphorylation of the heavy chain then allows the assembly into minifilaments as depicted in Fig. 1.3B (*Levayer et al.*, 2012). These bipolar filaments consist of approximately 30 myosin monomers and are typically around 300 nm long (Fig. 1.3B). The NM II minifilaments then bind to actin filaments through their head domain. Bound to actin, NM II may contract actin filaments by “walking” along them (Fig. 1.3A). The contraction of actin by NM II is known as the crossbridge cycle (*Huxley*, 1957) and schematically illustrated in Fig. 1.3C. The crossbridge cycle starts with binding of ATP to the myosin head and thereby dissociating it from the actin filament. Next, hydrolysis of ATP to ADP and phosphate at the free myosin head enforces a conformational change with subsequent actin rebinding of the head. Due to the conformational change the association takes place at about 11 nm closer to the barbed end of the actin filament (*Finer et al.*, 1994). After that, dissociation of the phosphate from the ATP-binding pocket causes a second conformational change of the myosin head which is known as the power stroke. It brings the myosin head back to its original conformation. Since myosin and actin are tightly bound, this motion results in a force that causes the actin filament to move. The release of ADP then completes the crossbridge cycle as the initial configuration is reached again (*Alberts et al.*, 2003; *Lodish et al.*, 2008).

Myosin II activity is regulated by complex and diverse signaling pathways. The main regulators of the actin cytoskeleton are the small GTPases (enzymes) Rac1, Cdc42 and RhoA. These enzymes can bind guanosine triphosphate (GTP) and mediate signal transduction by acting as molecular “switches” through controlled GTP-loading and hydrolysis of GTP to guanosine diphosphate (GDP) (*Lundquist*, 2006). Rac1 is principally contributing to the formation of large protrusive structures such as the lamellipodium and therefore important in cell spreading processes and migration while Cdc42 contributes to the formation of filopodia (Fig. 1.4A). RhoA promotes the assembly of actin-myosin bundles and additionally regulates actomyosin contraction. A very basic version of the RhoA signaling transduction pathway is depicted in Fig. 1.4A and B. The membrane bound GTPase RhoA exists in inactive (GDP-bound) or active (GTP-bound) state. The transition from GTP- to GDP-bound is mediated by so called GTPase-activating proteins (GAP) which inactivate the GTPase by hydrolysis of GTP to GDP. Conversely, Guanine Exchange Factors (GEF) may phosphorylate GDP to GTP and hence activating the GTPase. In its active state, RhoA then activates its downstream effectors Rho-associated protein kinase (ROCK) and Diaphanous-related formin (Dia). ROCK activity then effectively leads

²In biochemistry, phosphorylation is the chemical attachment of a phosphoryl group to an organic molecule.

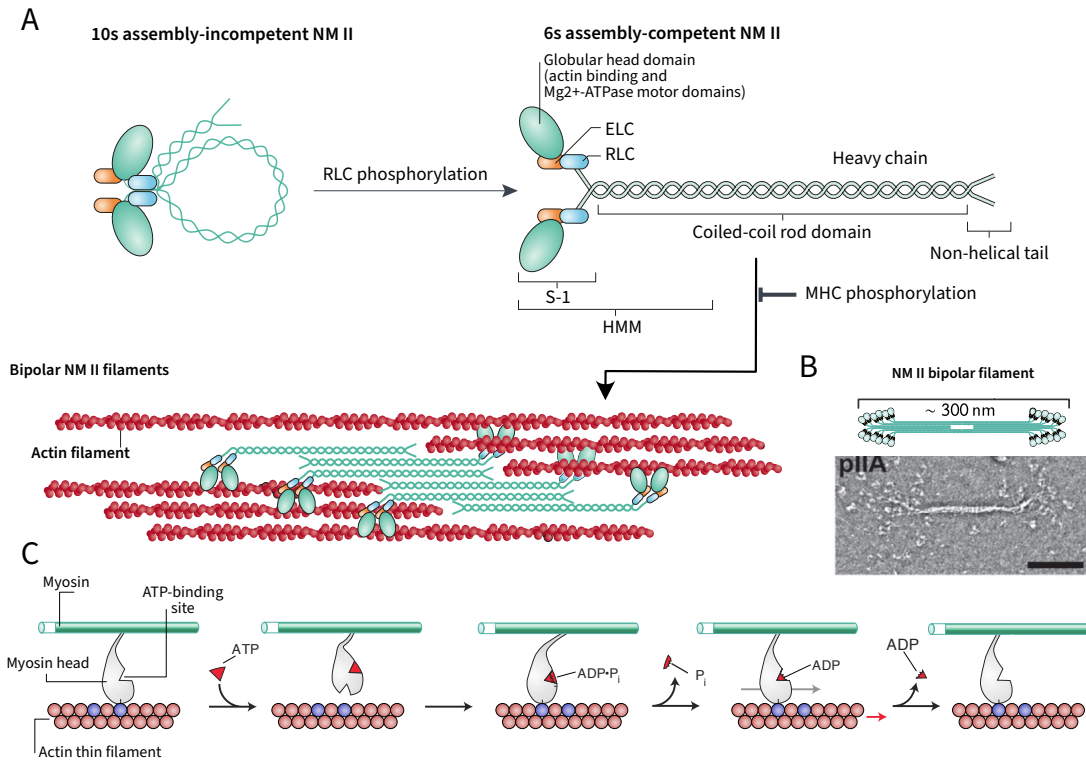


Figure 1.3: Structure and regulation of non-muscle myosin II. Panel **A**: Two identical protein subunits consisting of a globular head domain, two light-chains and a heavy chain form a polar hexamer. In its assembly-incompetent form, the protein is folded due to head to tail interactions which prevents further interaction with other NMII dimers. Phosphorylation of the regulatory light chains, for example mediated by ROCK or MLCK, unfolds the protein into an assembly-competent form. In this configuration NMII can self-assemble into NMII minifilaments through interactions of the coiled-coil rod domain which can further bind to actin filaments through the head-domains. Panel **B** depicts the structure and typical dimensions of a NMII minifilament in comparison to an electron microscopy image of NMII A. The scalebar corresponds to 100 nm. Panel **C** shows the crossbridge cycle. ATPase activity of the head domain translates into mechanical forces which slides the actin filaments in an anti-parallel fashion. Figures: A adapted from (Vicente-Manzanares *et al.*, 2009); B (top) adapted from (Lodish *et al.*, 2008) and (bottom) taken from (Billington *et al.*, 2013); C adapted from (Lodish *et al.*, 2008).

to myosin light chain (MLC) activity through two pathways (Fig. 1.4B). On one hand, it effectively elevates the phosphorylation level of myosin light chain by phosphorylating the myosin binding subunit (MBS) of myosin light chain phosphatase (MLCP). This inhibits the phosphatase activity of MLCP and therefore reduces dephosphorylation of MLC and hence increases contractility by NMII motors. On the other hand, ROCK may directly phosphorylate MLC. Parallel to ROCK activity, activation of Dia promotes actin polymerization by Arp2/3. A fundamental understanding of these signaling pathways is crucial for developing techniques to affect cellular contractility. Optogenetic techniques, as recently developed by Valon *et al.* (2015) and Wagner *et al.* (2016), use this knowledge to trigger myosin activity through the RhoA signaling cascade by targeting GEFs to the cell membrane. This method is further discussed in Section 1.2.3.

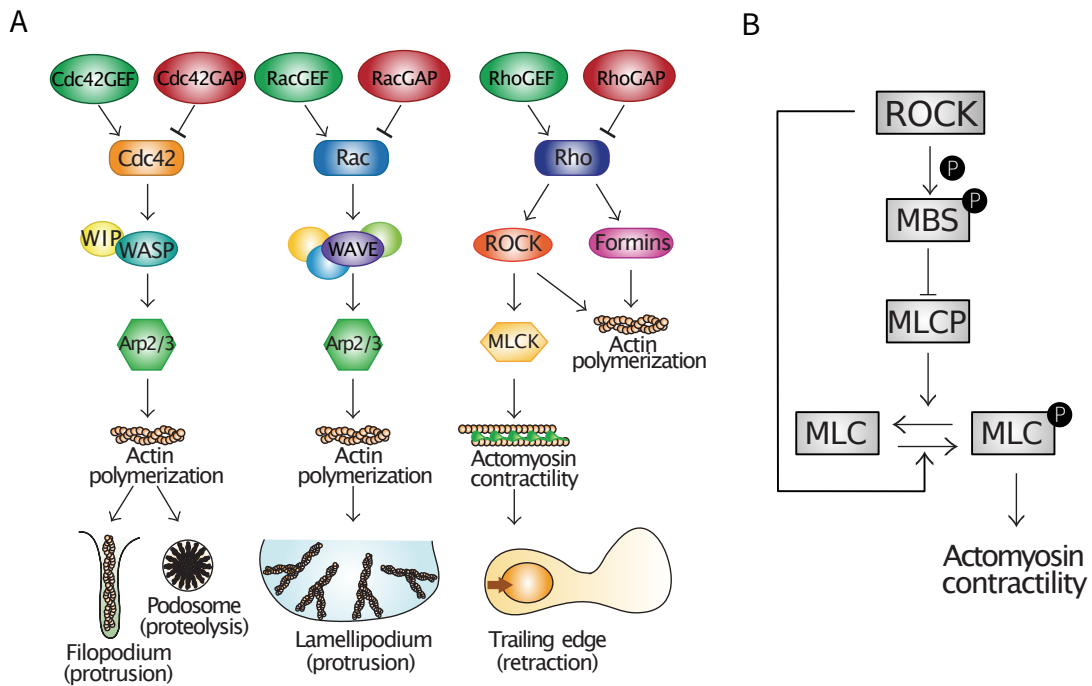


Figure 1.4: Main signaling pathways for the regulation of the actin cytoskeleton (here shown for a macrophage). Panel **A** shows the GTPase activity of Cdc42, Rac and Rho which is controlled by the upstream regulators here generically denoted as GEFs and GAPs. Cdc42 and Rac are mainly involved in the formation of protrusive structures while RhoA, in addition to actin-myosin assembly, also regulates myosin contractility. Panel **B** shows the RhoA pathway and its downstream signaling processes in more detail. By activating ROCK, RhoA effectively increases MLC-P activity through two distinct pathways. Figures: A adapted from (*Pixley, 2012*).

MICROTUBULES

Microtubules are rod-like, stiff filaments which can be found in all animal cells. A cross-sectional diameter of ~ 25 nm and a persistence length of around 1–3 μ m makes them the least flexible of the three filaments (*Alberts et al., 2003; Phillips et al., 2012*). As Fig. 1.1B illustrates, microtubules are polar filaments made of tubulin-dimers, which in turn are polymerized from α - and β -tubulin, arranged in a helical fashion to form a hollow cylinder. Microtubules often originate from so-called microtubule-organizing centers (MTOCs) and grow with their plus end towards the cell membrane. In animal cells, the two most prominent MTOCs are the basal bodies and the centrosome which is located near the nucleus (Fig. 1.1A). The former are associated with formation of cilia and flagella while the latter are associated with formation of the mitotic spindle during mitosis (Fig. 1.1C2). Further, microtubules not only organize the cell interior by positioning of organelles through pushing and pulling forces (*Tolić-Nørrelykke, 2008*) but also guide and direct intracellular transport processes (*Welte, 2004*). For example the two motor proteins dynein and kinesin are responsible for vesicle transport towards and away from the nucleus (*Howard et al., 2002*).

INTERMEDIATE FILAMENTS

In contrast to actin filaments and microtubules, intermediate filaments are not present in all eucaryotic cells. Structurally, with a cross-sectional diameter of 8–12 nm, they

are in between microtubules and actin filaments (*Alberts et al.*, 2003; *Phillips et al.*, 2012). They are comprised of fibrous protein dimers (Fig. 1.1B) that form a rope-like structure which is very resistant to tension despite the very short persistence length of $< 1 \mu\text{m}$ (*Huber et al.*, 2015). In marked contrast to the other two filament types, intermediate filaments are non-polar such that they neither actively participate in cell contraction nor in transport processes by motor proteins (*Block et al.*, 2015). However, they permeate the whole cell, thereby providing it with mechanical stability. They also assist in forming connections between cells in epithelial cell sheets as can be seen in Fig. 1.1C3 which shows an epithelial sheet of Madin- Darby Canine Kidney cells (MDCK). Here, the intermediate filaments become very stressed and straight when the cell is stretched to many times its typical area, demonstrating their enormous resistance to tension (*Latorre et al.*, 2018).

1.1.2. CELL ADHESION

Under physiological conditions, cells are either surrounded by the so called extracellular matrix (ECM) or by neighboring cells. The ECM is a large three-dimensional network consisting of various fibrous proteins such as collagen, fibronectin, vitronectin or also proteoglycans which are large polysaccharide-protein complexes (*Alberts et al.*, 2003). Besides providing structural support for surrounding cells by acting as a substrate, it further plays a central role in cellular processes like cell growth, cell migration, intercellular communication and differentiation (*Abedin et al.*, 2010). The interaction with the ECM is established by cell-ECM adhesion through structures like podosomes, fibrillar adhesions and focal adhesions. Fig. 1.5A, for example, shows a fibroblast in interaction with a three-dimensional collagen matrix.

In addition to cell-ECM connections, cells interact directly via intercellular connections (Fig. 1.5C). These are referred to as cell-cell junctions and can be divided into desmosomes, tight junctions, gap junctions, and adherens junctions. They play an important role in collective cell migration by maintaining the integrity of the cell ensemble and regulating coordinated movement (*Etienne-Manneville*, 2011; *Peglion et al.*, 2014), which in turn controls many physiological and pathophysiological processes such as wound healing, tissue renewal, or even embryonic development and metastasis. In the following, we briefly discuss the structure and composition of focal adhesions and adherens junctions, since they occur in a large number of systems and play a crucial role in mechanosensing.

FOCAL ADHESIONS

Fig. 1.5B depicts a stress fiber connected to the ECM via a focal adhesion. Adaptor proteins like talin and vinculin connect the actin CSK to trans-membrane proteins like integrins. The extracellular domain of the integrins then binds to the proteins of the ECM like, for example, fibronectin. The stresses focal adhesions exert onto the ECM are typically around 5 kPa (*Balaban et al.*, 2001) although studies suggest that this strongly depends on the stiffness of the ECM (*Trichet et al.*, 2012). Focal adhesions are rather stable in non-motile, sessile cells but can be quickly disassembled

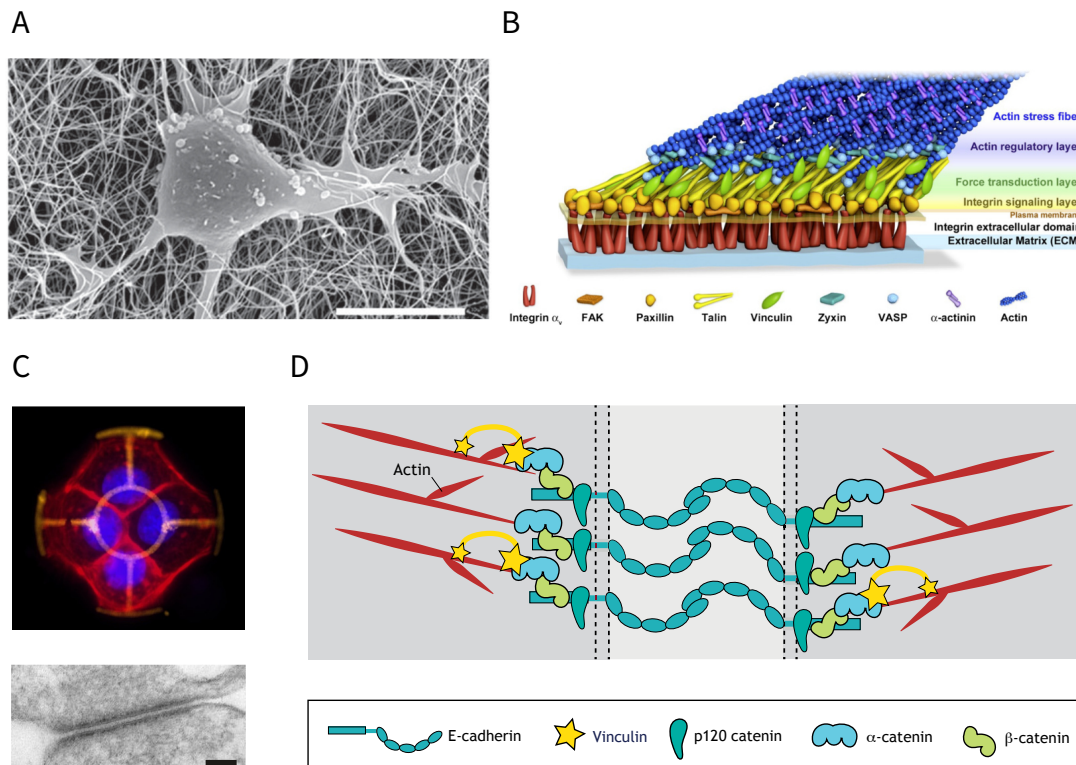


Figure 1.5: Cell-extracellular matrix and cell-cell adhesions. Panel **A** depicts an electron-microscopy image of a fibroblast in interaction with a three-dimensional collagen matrix. The fibroblast forms dendritic extensions which are hard to distinguish from the matrix. Scale bar corresponds to 10 μm . Panel **B** schematically illustrates the hierarchical structure of a focal adhesion connected to the extracellular matrix. Panel **C** shows opto-MDCK cells forming a quadruplet on a specifically designed micropattern (top) and an electron micrograph of an adherens junction (bottom). Scale bar corresponds to 100 nm. Panel **D** shows the molecular decomposition of an adherens junction. Figures: A taken from (*Jiang et al.*, 2005); B adapted from (*Kanchanawong et al.*, 2010); C (top) by courtesy of Artur Ruppel, (bottom) adapted from (*T. J. Harris et al.*, 2010); D adapted from (*Broussard et al.*, 2020).

and assembled in moving cells in order to break old contacts at the trailing edge and build new focal adhesions at the leading edge of the cell. In addition, focal adhesions serve as signal interfaces through which the cell can perceive the physical properties of the ECM and thus adapt to external influences (*Riveline et al.*, 2001).

ADHERENS JUNCTIONS

The principle structure of adherens junctions is similar to cell-ECM adhesions as they are also established by trans-membrane adhesion proteins. In adhesion junctions, these proteins are called cadherins, which are almost entirely outside the cell membrane and form homodimers with cadherins of neighboring cells, as depicted in Fig. 1.5C (for epithelial cells). Cadherins are connected to the actin CSK via the adaptor proteins α - and β -catenin as well as vinculin and, beyond their stabilizing function in cell-cell adhesion, they are important for the regulation of the actin CSK as well as signaling processes (*Hartsock et al.*, 2008).

MECHANOTRANSDUCTION

As mentioned above, signaling processes start at the mechanosensitive interfaces. The intracellular processes that convert external stimuli into biochemical signals are commonly referred to as mechanotransduction. Experimental evidence for mechanotransduction may be difficult to obtain, since the involved processes may happen on several distinct time scales, ranging from fractions of seconds to seconds for the force sensing, hours for adaptation of gene expression, days for behavioral changes, and weeks for tissue growth and morphogenesis (*Iskratsch et al.*, 2014). However, for focal adhesions and adherens junctions, mechanotransduction was directly demonstrated by experiments in which externally applied forces led to the growth of both structures (*Balaban et al.*, 2001; *Z. Liu et al.*, 2010). Additionally, several important studies shine light on the role of mechanotransduction in processes such as differentiation, migration and fate (*C. S. Chen et al.*, 1997; *Engler et al.*, 2006; *Kilian et al.*, 2010; *Luciano et al.*, 2021; *McBeath et al.*, 2004; *Pathak et al.*, 2012; *Shellard et al.*, 2021; *Sunyer et al.*, 2020; *Wen et al.*, 2014).

In the context of this work, it is important to take a closer look at mechanotransduction at focal adhesions and adherens junctions. Although the details of many signal transduction pathways have not been fully elucidated, the starting point of some of them could be traced back to the mechanosensory properties of integrins (*Kong et al.*, 2009), vinculin (*Yao et al.*, 2014) and talin (*Del Rio et al.*, 2009). Fig. 1.6 exemplarily shows cell-cell and cell-ECM signaling pathways reduced to the most important elements. At adherens junctions, triggered by force, E-cadherins activate Tyrosine-protein kinase ABL1 (ABL1) which in turn phosphorylates vinculin. Vinculin then sets off the typical RhoA-pathway which eventually results in the activation of myosin light chain and hence the reinforcement of cell-cell-adhesion. In focal adhesions, the reinforcement of the cell-ECM adhesion is ultimately also due to the typical RhoA signaling pathway (Fig. 1.6). However here, the RhoA-cascade is triggered by integrins. Subject to force loads, the integrins activate two distinct signaling branches involving the two RhoA guanine nucleotide exchange factors GEF-H1 and leukemia-associated RhoGEF (LARG) (*Salvi et al.*, 2018).

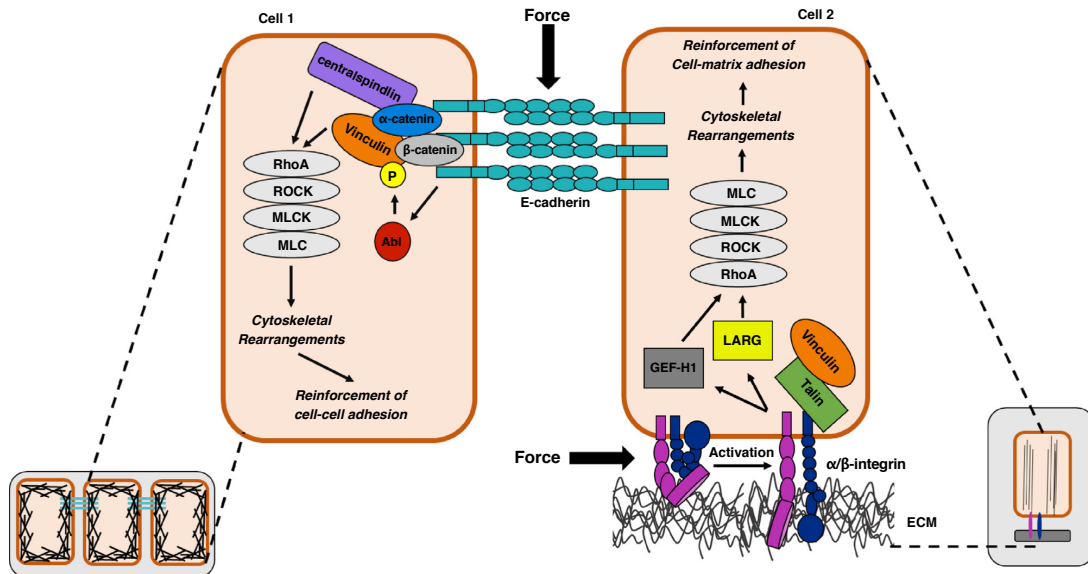


Figure 1.6: Typical mechanotransduction pathways triggered at cell-cell junctions and focal adhesions. At cell-cell junctions E-cadherins of neighboring cells bind. Forces acting at cell-cell junctions can trigger the RhoA pathway which in turn leads to a reinforcement of the cell-cell adhesion. Similarly, forces acting at the cell-matrix interface trigger RhoA signaling events which lead to a reinforcement of the cell-matrix adhesion. Taken from (Salvi *et al.*, 2018)

1.2. MEASURING CELL CONTRACTILITY

After introducing the main force-generating structures as well as the most prominent involved signal transduction pathways of adherent cells we will now provide an overview of the main experimental tools used by our collaboration partners from the Université Grenoble Alpes. These tools include Traction force microscopy, micropatterning, and non-neuronal optogenetics and have been used in Chapter 4 and Chapter 5.

1.2.1. TRACTION FORCE MICROSCOPY

Traction force microscopy (TFM) is a multi-scale force quantification method which allows to measure cell contractility on more than one spatial scale. In particular, two-dimensional traction force microscopy is one of the most prominent techniques in the field of mechanobiology. The first visualization of cell traction forces goes back to the study by A. K. Harris *et al.* (1980). Seeded onto a thin soft silicone rubber substrate, cell tractions buckled the silicon substrate and visible wrinkles appeared. Since then, several methods have been developed that take the basic principles of this qualitative observation and exploit them in quantitative methods. One of these methods is depicted in Fig. 1.7A where the cell is plated on a so called micropillar array (Tan *et al.*, 2003). It consists of elastomeric posts with known properties such as width, height and Young's modulus. Subject to cellular forces, the microposts get deflected from which the cell forces can be deduced (Fig. 1.7B,C). Although the discrete nature of the substrate allows a direct computation of the traction forces, the cell stresses are only obtained at discrete positions. This, the limited variability of the substrate rigidity and the fact, that it is not a natural environment for cells are clear

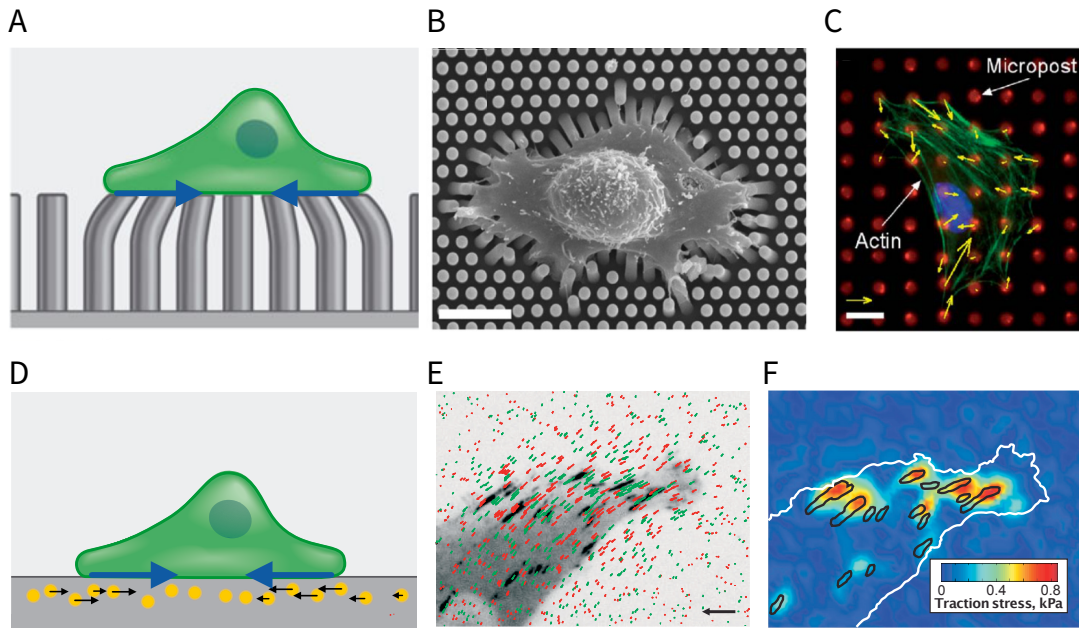


Figure 1.7: Force quantification based on micropillar arrays and traction force microscopy. Panel **A** depicts the principle of micropillar based force measurements. Traction forces can be deduced from the elastic and geometric properties of the pillars and their deflection. Panel **B** shows an electron micrograph image of a fibroblast adhered to a micropillar substrate. Scale bar corresponds to $15\ \mu\text{m}$. Panel **C** depicts the forces calculated from pillar deflections (yellow arrows) due to forces exerted by the cell. (Actin is shown in green, nucleus is shown in blue). Scale bar corresponds to $10\ \mu\text{m}$ and the scale arrow corresponds to $20\ \text{nN}$. Panel **D** shows the basic setup of traction force microscopy. Sub-micron sized fluorescent beads are embedded in a thick elastic gel. Traction forces can then be calculated from the displacement of the beads. Panel **E** shows a vector plot of laterally displaced beads overlaid on an inverted paxilin image of the cell. The scale vector corresponds to $1\ \mu\text{m}$. Panel **F** shows the traction stresses reconstructed from bead images. The white line highlights the cell periphery while the black line outlines the focal adhesions. Figures: A,D adapted from (Muthinja *et al.*, 2018); B taken from (Trichet *et al.*, 2012); C taken from (Sniadecki *et al.*, 2007); E,F taken from (Plotnikov *et al.*, 2014)

disadvantages of this method (Roca-Cusachs *et al.*, 2017).

The classical TFM approach which goes back to the work by Dembo *et al.* (1999) is schematically illustrated in Fig. 1.7D. In this approach, cells are plated on top of a flat, thick elastic hydrogel. These gels are usually made of polyacrylamide (PAA) or polydimethylsiloxane (PDMS), and the elastic properties (substrate stiffness) can be controlled by the mesh size of these polymer networks during fabrication. Further, these substrates are coated with ECM proteins such as fibronectin and collagen. This enables the cells to spread on the substrate and to establish cell-ECM connections via focal adhesions. Deformation of the elastic substrate is then visualized by small fluorescent microbeads with a diameter of $0.2\ \mu\text{m} - 1\ \mu\text{m}$ which are embedded in the gel close to the surface. In principle, knowing the elastic properties of the gel and the displacement field of the beads allows to calculate the traction forces (Fig. 1.7E,F). Although fabrication of the involved elements in the TFM setup is straightforward and gives rise to independent control of topography and rigidity of the substrate, the measurement of the substrate deformation and calculation of traction forces is more complicated than for pillar arrays.

The first difficulty is the tracking of the bead displacement. For this, one typically

uses sophisticated algorithms which combine two well-established approaches known as particle tracking velocimetry (PTV) and particle image velocimetry (PIV). The former approach tracks the movement of individual beads while the latter uses cross-correlation to statistically derive local displacements (*Sabass et al.*, 2008). Once the displacement field is obtained, traction forces can be calculated by making use of the known elastic properties of the substrate. The starting point for traction force computation on flat elastic substrates is given by the integral equation

$$\mathbf{u}(\mathbf{x}) = \int \mathbf{G}(\mathbf{x}, \mathbf{x}') \mathbf{t}(\mathbf{x}') d\mathbf{x}' , \quad (1.1)$$

where \mathbf{u} is the displacement vector field, \mathbf{t} is the unknown traction field and \mathbf{G} is the Green's function (Boussinesq solution) for the point loading of a flat isotropic elastic half-space. This assumption is justified by the fact that dimensions of the substrate are usually much larger than the lateral extent of the cell. Additionally, one typically neglects out-of-plane substrate displacements since the, in good approximation, flat cells exert traction forces mainly parallel to the surface. Hence, the Green's function is given by a 2×2 matrix. Since the analytical Green's function \mathbf{G} is known (*Landau et al.*, 1986), the traction forces can be finally obtained by inversion of Eq. (1.1).

In their pioneering study, *Dembo et al.* (1999) solved Eq. (1.1) by means of the boundary element method (BEM). However, this method involves triangulation of the cell area and therefore one has to measure the cell periphery. In addition, due to the long-ranged nature of elastic forces, the matrix \mathbf{G} is dense and calculating the inverse of it is computationally expensive especially if a high-resolution of the estimated traction forces is desired.

A computationally more efficient approach was introduced by *Butler et al.* (2002). The idea of this approach, which goes with the name of Fourier transform traction cytometry (FTTC), relies on solving the problem in Fourier space where Eq. (1.1) reads

$$\tilde{\mathbf{t}}(\mathbf{k}) = \tilde{\mathbf{G}}^{-1}(\mathbf{k}) \tilde{\mathbf{u}}(\mathbf{k}) . \quad (1.2)$$

Here, the tilde denotes the Fourier transform and \mathbf{k} its wave vector. Solving the inverse problem is simpler in the sense that the convolution factorizes into a product in Fourier space. This, in practice, reduces the problem to the calculation of the fast Fourier transform of the bead displacement field from which the Fourier transform of the traction field follows by multiplication with the inverse matrix $\tilde{\mathbf{G}}^{-1}$. The traction force field in real space is then obtained by the inverse Fourier transform of $\tilde{\mathbf{t}}$. Similar to the problem in real space, to overcome the omnipresent noise in the displacement field data, one typically regularizes the FTTC procedure (Reg-TFM) by introduction of a regularization kernel. The regularized inverse problem reads

$$\tilde{\mathbf{t}} = \left(\tilde{\mathbf{G}}^T \tilde{\mathbf{G}} + \lambda^2 \mathbf{L} \right)^{-1} \tilde{\mathbf{G}}^T \tilde{\mathbf{u}} , \quad (1.3)$$

for which it has been demonstrated that $\mathbf{L} = \mathbf{I}$, with \mathbf{I} the identity matrix, yields the best results (*Plotnikov et al.*, 2014; *Sabass et al.*, 2008). Here, the regularization parameter λ should be as small as possible such that the reconstructed \mathbf{t} is as close

as possible to the real solution. The larger the parameter λ , the more smoothed out the traction field becomes. For $\lambda = 0$ one recovers the un-regularized inverse problem Eq. (1.2).

1.2.2. MICROPATTERNING

As discussed in Section 1.1 cells are very sensitive to the mechanical and geometrical properties of its surrounding. To study the interplay between the ECM geometry, cell shape and cell generated forces, micro-engineering techniques have been developed which allow to impose geometrical restrictions on the cell. One of these techniques is referred to as micropatterning. It separates the substrate into regions to which the cell can adhere (micropatterns) and regions which are designed to prevent the formation of cell-ECM contacts (passivation layer). A possible procedure to produce such micropatterned substrates is illustrated in Fig. 1.8A where a photomask is used to impose the shape of the micropattern. A detailed description of the fabrication process can be found in the work by *Ruppel (2022)* and *Vignaud et al. (2014)*.

A selection of different adhesion geometries and their influence on the actin organization of the cells is shown in Fig. 1.8B. On small disc-shaped patterns (i) cells predominantly assemble a branched actin network. In contrast, when spreading on larger disc patterns (ii) cells additionally form directional internal stress fibers, actin bundles and are more contractile and flatter than on small patterns (*Théry, 2010*). Patterns with straight edges and corners (iii) promote the formation of small protrusions and focal adhesions in the corner of the pattern as well as the formation of stress fibers between them (*Brock et al., 2003*). If the cell is confronted with larger non-adhesive gaps (iv), it manages to spread over it by forming large and pronounced stress fibers which are highly contractile and therefore span over the non-adhesive area (*Théry et al., 2006*). An experimental image of this particular situation is depicted on the right-hand side of Fig. 1.8B (right) with the thick stress fibers stained in green.

We investigate cellular dynamics on disc pattern in more detail in Chapter 4. In Chapter 5, we further use an H-shaped micropattern (Fig. 1.8A) as it allows the formation of a stable cell doublet with a clear intercellular junction (*Tseng et al., 2012*).

1.2.3. NON-NEURONAL OPTOGENETICS

The term optogenetics refers to a light-based approach which, in combination with genetic engineering, allows to intervene and control biological processes. Among others, it has been applied in several studies for example to control neural activity (*Boyden et al., 2005*), the regulation of gene expression (*Konermann et al., 2013; Wang et al., 2012*) or even to regulate engineered metabolic pathways in cells (*Zhao et al., 2018*).

In the context of the here presented work, we use non-neuronal optogenetics to induce signaling cascades that lead to cellular contractility. In combination with TFM and micropatterning, this allows to study the dynamics of the cytoskeleton and force generation in distinct adhesive environments provided by the ECM or other cells. A huge advantage of this technique is its minimal invasive and reversible nature which

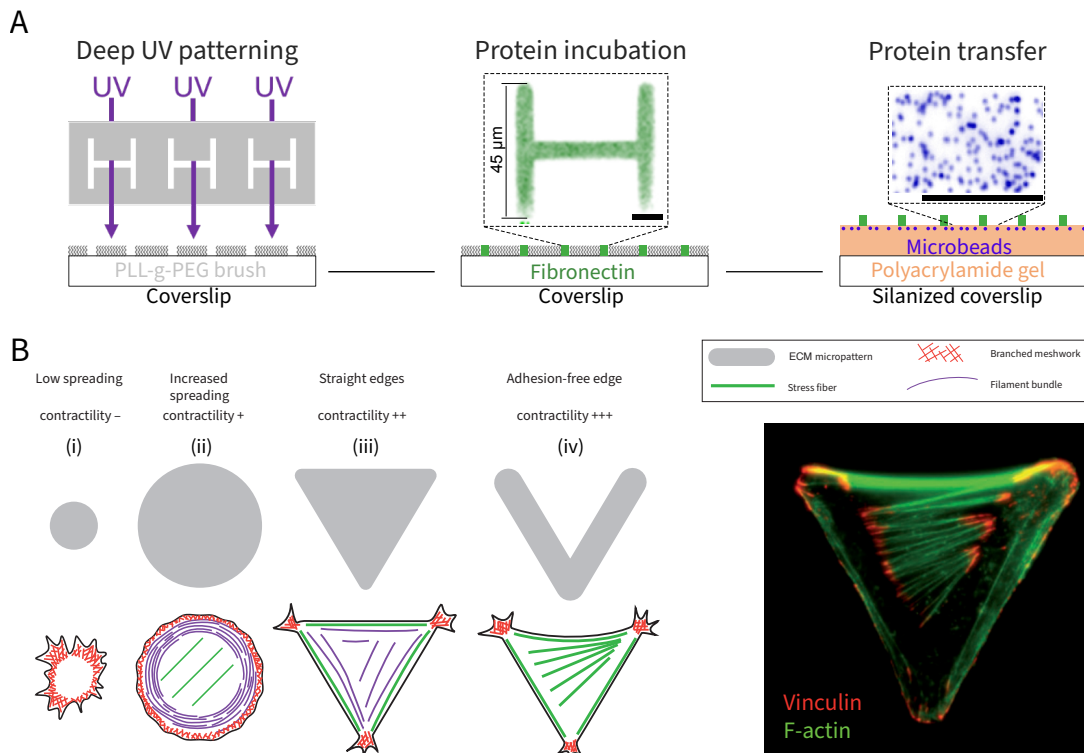


Figure 1.8: Micropatterning and its applications in mechanobiology. Panel **A** schematically depicts the fabrication process of the micropatterns used to impose geometric constraints on the adherent cell. With this technique our collaborators from the Université Grenoble Alpes created the micropatterns used in Chapter 4 and Chapter 5. Panel **B** depicts the influence of pattern size and shape on the internal actin organization and spreading process of the cells. Figures: A by courtesy of Artur Ruppel; B taken and adapted from (Théry, 2010).

additionally allows a precise spatiotemporal control of the cytoskeletal dynamics and hence makes it superior over other techniques such as chemical treatments using drugs like blebbistatin (myosin II inhibitor) or Y27632 (ROCK inhibitor).

The central element of optogenetic techniques are photosensitive proteins (Farahani *et al.*, 2021; Tischer *et al.*, 2014). Subjected to light, typically of a certain wave length, some photosensitive proteins may undergo a conformational change and uncage a certain protein domain which enables their signaling activity. For others, a conformational change might increase their affinity towards another protein which then leads to heterodimerization. Although both components might not have intrinsic signaling capabilities, this light-induced binding affinity can be used to localize a certain target signaling protein to a specific part of the cell by fusing it to the light sensitive component.

As already discussed at the beginning of this chapter, the membrane bound GTPase RhoA is a major regulator of cellular contractility. We further know that RhoA activity is controlled by GEFs and GAPs such that RhoA activity can be increased by targeting GEF to the cell membrane. An optogenetic construct which provides this sort of control is the CRY/CIBN dimerization system as illustrated in Fig. 1.9A. As depicted, one part of the construct, CIBN, is fused to the plasma membrane via a CAAX linker and additionally carries a green fluorescent marker (GFP). The catalytic domain of GEF (DHPH) is fused to CRY2, which is the photosensitive part of

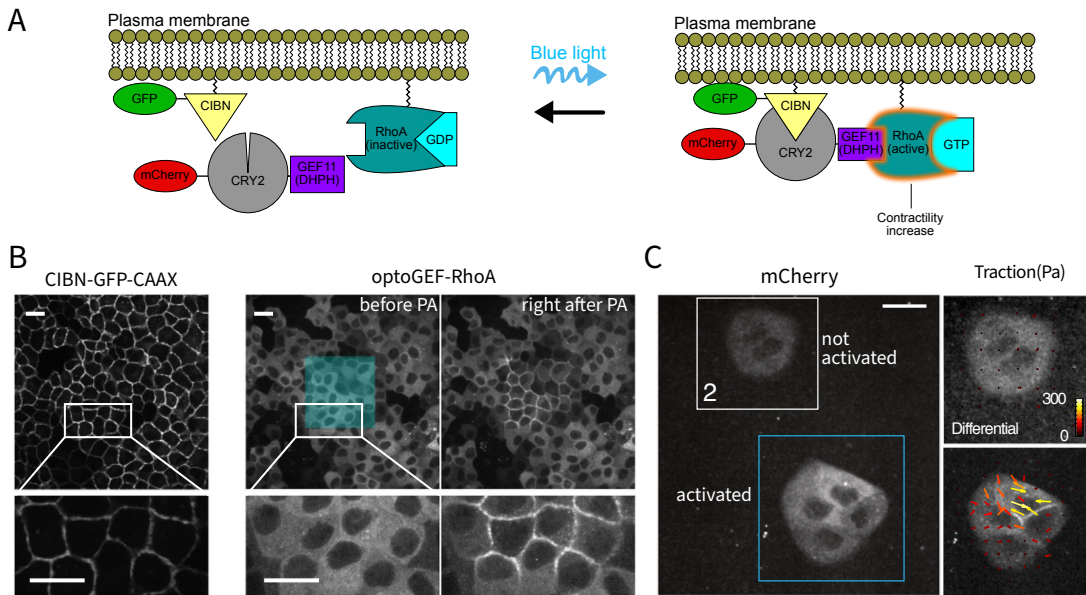


Figure 1.9: Optogenetic control of RhoA with the CRY2/CIBN dimerization system. Panel **A** depicts the functionality of the CRY2/CIBN system. CIBN, is anchored to the plasma membrane via a CAAX linker. The GEF DHPH-domain is fused to the photosensitive CRY2 which changes conformation upon illumination with blue light. Due to this conformation change it can now bind to CIBN and hence effectively recruit the catalytic domain of GEF to the plasma membrane. Here, GEF can activate the membrane-bound RhoA which ultimately triggers cell contractility by activation of MLC. Panel **B** shows MDCK cells stably expressing CIBN (left) and the activity of ARHGEF11(DHPH)-CRY2-mCherry at the cell membrane before and after illumination (right). Panel **C** shows the differential traction of a non-activated cell cluster (white square) in comparison to an activated cell cluster (blue square). The activated cell cluster showed a significant increase in traction forces. Figures: A by courtesy of Artur Ruppel from the Université Grenoble Alpes; B,C taken and adapted from (Valon *et al.*, 2017).

the opto-construct and further carries a red fluorescent tag (mCherry). The fluorescent proteins are used to visualize the recruitment and verify that the system works as expected (Fig. 1.9B). For example, the left panel of Fig. 1.9B shows the fluorescent tag of the membrane anchored CIBN. Upon illumination with blue light (wavelength of ~ 460 nm), CRY2 changes its conformation and can bind to its optogenetic counterpart CIBN and effectively recruits GEF to the plasma membrane where it can trigger the RhoA signaling cascade (Fig. 1.9A). The right panel of Fig. 1.9B visualizes the GEF increase at the membrane as the fluorescence signal increases in the illuminated region. The membrane recruitment of target proteins using this system has been demonstrated by Kennedy *et al.* (2010) while Valon *et al.* (2015) studied this system in great detail with respect to varying light intensity and duration of photoactivation. In a follow up work, Valon *et al.* (2017) demonstrated that this system can be used to control cell contractility in epithelial sheets (Fig. 1.9C).

Some of the main advantages of this approach are its fast reversibility and low toxicity such that repeated activation cycles can be carried out on the same cell without influencing its viability. The response of the cell is further entirely due to the endogenous level of RhoA, since the cell is only transfected with the RhoA activator.

Moreover, the activation level of RhoA can be controlled by controlling the duration of photoactivation and in addition, the specificity of this approach prevents other

pathways and proteins from being affected by the perturbations. Additionally, the light induced perturbation can be assumed to be instantaneous as the CRY2 membrane recruitment happens on a much faster time scale than most of the intracellular signaling cascades (Valon *et al.*, 2015). For completeness, we should mention other optogenetic constructs which provide a similar level of control. For example, the Light-Oxygen-Voltage (LOV) construct which has been used by Oakes *et al.* (2017) to probe the viscoelastic properties of stress fibers and by Cavanaugh *et al.* (2020) to investigate viscoelastic properties of cell-cell junctions.

1.3. MODELLING CELL CONTRACTILITY

Each of the existing mathematical models of cellular contractility has its own advantages and disadvantages and therefore in many cases it is necessary to weigh up which of the models is most suitable for the description of certain aspects of the cellular dynamics as they are in many cases dictated by the experimental setup. In the following, we discuss the main ideas of the various available models and highlight their respective strengths and weaknesses. We distinguish three model classes, referred to as bulk-based, contour and interface-based models, and will decide on a main modeling approach by considering the experimental restrictions and objectives discussed in this thesis.

1.3.1. BULK-BASED MODELS

Bulk-based models can be broadly classified into discrete models, typically spring and cable networks and continuum models. Both of the models focus on the internal mechanical properties of the cell like, for example, the actin cytoskeleton which, together with myosin II activity, is the main contractile structure in the cell (Svitkina, 2018). Besides that, these models can also account for other important building blocks like directed internal stresses and localized adhesive islands. Both models naturally allow to include coupling of the cell to its surrounding such as adhesion on elastic substrates or cell-cell adhesion in tissues and under certain conditions the continuum models can be deduced from the discrete models through homogenization techniques.

SPRING AND CABLE NETWORKS

Within this approach the actin cytoskeleton is modeled as a network of elastic links as illustrated in Fig. 1.10A (inset) and B. Thereby, the links can be either spring-like or cable-like. In the framework of traditional spring-networks and the limit of small deformations the links are approximated by a Hookean force-extension curve (Fig. 1.10A) (Boal, 2002). In the limit of a very fine network, homogenization techniques (Caillerie *et al.*, 2010) can be used to derive the continuum limit of these networks which for Hookean spring networks lead to a linear elastic constitutive relation. However, a contractile spring-network cannot properly represent the mechanical attributes of the cytoskeleton which motivates the invention of cable networks. The cable-like description incorporates the experimental findings that actin filaments ex-

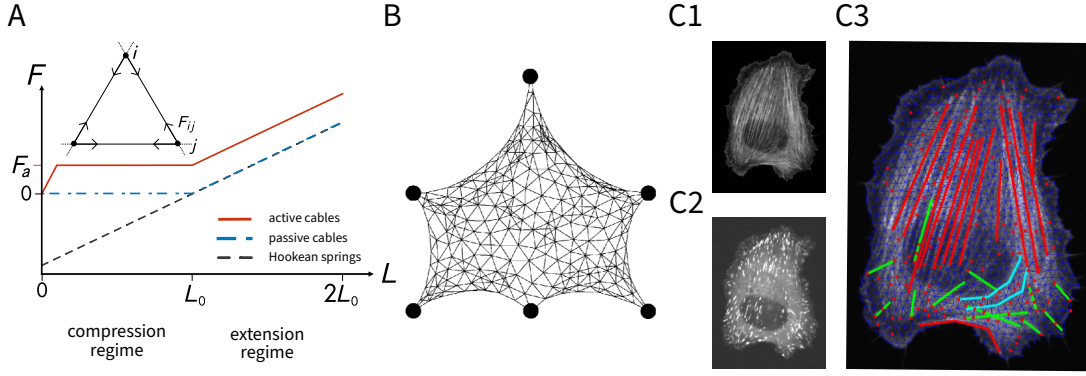


Figure 1.10: Cellular contractility modeled with discrete cable networks. Panel **A** shows the force-extension behavior for the single network links of the three common network models. Panel **B** depicts the equilibrium shape of an active cable network with a certain adhesion geometry. Panel **C** displays the network representation of a real cell's actin cytoskeleton with embedded stress fibers (red, blue and green lines) and segmented focal adhesions (red dots) constructed from a raw actin fluorescence (C1) and paxillin (C2) images. Figures: B taken from (*Bischofs et al.*, 2008); C created with the SOFAST ImageJ plugin which contained the images.

hibit a spring-like behavior upon extension but start to buckle, slide or depolymerize if compressed (*Broedersz et al.*, 2014; *Gittes et al.*, 1993; *Kojima et al.*, 1994). In case of passive cable networks, contractility is modeled by reducing the rest length of the links and hence pre-tensing the network, while for active cable networks each link actively contracts with constant force resembling contraction by molecular motors. Mathematically speaking, the equilibrium shape of the cell is obtained by solving

$$F_{ij} = \begin{cases} F_a L_0 + EA \frac{L_{ij} - L_0}{L_0} & , L_0 < L_{ij} \\ F_a L_0 & , L_c \leq L_{ij} \leq L_0 \\ F_a L_0 \frac{L_{ij}}{L_c} & , L_{ij} < L_c \end{cases} \quad (1.4)$$

where F_{ij} denotes the total force that the nodes i and j exert onto each other, EA is the one-dimensional elastic stiffness of the links, F_a is the active link tension and L_0 the rest length. Further, L_c describes a critical length below which the active link force approaches zero (Fig. 1.10A red curve). Equilibrium is reached if

$$\sum_j F_{ij} = 0, \quad \forall \text{ non-adherent nodes } i. \quad (1.5)$$

It has been shown by *Bischofs et al.* (2008), and further confirmed by *Brand et al.* (2017) (for cells in three-dimensional scaffolds) that active cable network simulations can explain experimentally observed cell shapes and furthermore, that they predict circular shaped contours between adhesion points (Fig. 1.10)B. In addition, *Guthardt Torres et al.* (2012) showed that the global adhesion geometry of passive networks is sensitive to local changes in adhesion geometry, which is not the case for active networks, where only the boundary is affected, since changing the spanning distance between adhesion sites greatly alters the stress in the contour. Moreover, *Kassianidou et al.* (2017) made use of the above mentioned possibility to include internal stress fibers in order to study the influence they have on the force loads of peripheral stress fibers. An example of embedded stress fibers and segmented focal adhesions

based on actin fluorescence and paxillin images is shown in Fig. 1.10C3. By changing the connectivity properties of the network from elastic to viscoelastic, *Oakes et al.* (2017) showed that the contractility of stress fibers upon optogenetic activation is dominant over the contractility of the background actin network in which they are embedded. Moreover, that stress fibers are completely embedded in a contractile network of cortical actin filaments has been recently demonstrated by *Vignaud et al.* (2021) by comparing the energy release during laser photoablation of “shaved”³ and “unshaved” peripheral stress fibers. Although network models have been proven to be very versatile when it comes to studying different mechanical aspects of the actin cytoskeleton a huge drawback are their computationally expensive nature since for N non-adherent nodes one has to solve $2N$ coupled nonlinear equations (Eqs. 1.4, 1.5).

CONTINUUM MODEL

The continuum approach aims at modeling the cell as a continuous elastic material. Thereby, an appropriate constitutive relation of the form

$$\sigma_{ij} = C_{ijkl}\varepsilon_{kl} + \sigma_{ij}^a \quad (1.6)$$

relates internal stress σ_{ij} and strain ε_{ij} through a stiffness tensor C_{ijkl} while the contractility of the actin cortex is introduced as an active contractile stress σ_{ij}^a . The equation for mechanical equilibrium is given by

$$\partial_j \sigma_{ij} = b_i, \quad (1.7)$$

where b_i is the so called external body-force i.e. the sum of all forces acting on the elastic bulk. For strongly spreaded (flattened) cells on elastic substrates, for which a two-dimensional representation is in most cases sufficient, one typically chooses

$$b_i = Y u_i \quad (1.8)$$

relating the body forces to the restoring forces (traction forces), arising due to cellular deformation u_i and adhesion to the elastic foundation with spring stiffness density Y (Fig. 1.11A). The quantity Y turns out to be the key parameter used to enforce certain adhesion geometries on the cell as, e.g. shown in Fig. 1.11C.

In the past, this model has been used to show analytically that the strong localization of traction forces at the periphery of cell layers naturally follows from the above stated elastic problem and not necessarily as a result of local activity in the cell (*Edwards et al.*, 2011). In addition, more focused on dynamic processes, similar continuum models have been used, for example by *Kruse et al.* (2005), to model the actin CSK as a viscoelastic material comprised of polar filaments and motors, nowadays widely known as active gels. However, in many situations it is not possible to calculate an analytical solution such that finite element simulations are used to obtain numerical

³“Shaving” is the process of disconnecting the peripheral stress fiber from the actin mesh.

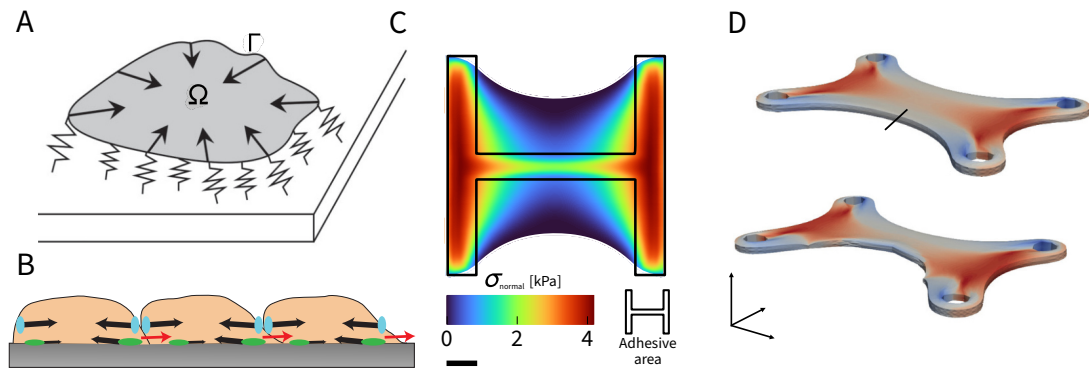


Figure 1.11: Continuum model for cellular contractility on elastic substrates.

Panel **A** schematically illustrates a cell layer adhered at discrete positions which e.g. represent a pillar array. Panel **B** shows the main idea of monolayer stress microscopy. Stress gradients in the cell layer have to be balanced in the substrate for non-migrating cells. Panel **C** depicts the case of continuous adhesion on a micropatterned substrate together with the associated internal stress distribution obtained by means of a finite element simulation. Scale bar corresponds to $5\ \mu\text{m}$. Panel **D** depicts a three dimensional continuum model of a contractile tissue. The model was used to predict the internal stress distribution before and after surgical intervention with a cut as indicated by the black line in the upper panel. Scale bar corresponds to $\approx 200\ \mu\text{m}$. Figures: A taken from (*Edwards et al.*, 2011); B taken from (*Gov*, 2011); C own simulation according to Chapter 5; D taken from (*Kim et al.*, 2021).

solutions of Eq. 1.7 (see e.g. Fig. 1.11C,D). Before we discuss continuum models in the context of computational modeling, we should mention one of the most famous applications of the above introduced equations, the so-called monolayer stress microscopy (MSM) which is schematically illustrated in Fig. 1.11B. MSM uses Eq. (1.7) together with a linear elastic material law to deduce internal cell stresses in a monolayer based on the forces it exerts on the substrate. A detailed explanation and review of this method can be found in the publications by *Gov* (2011) and D. T. *Tambe et al.* (2011; 2013).

Especially in computational modeling of the actin cytoskeleton, the versatility and adaptability of continuum models has often been demonstrated: For example, *Mertz et al.*, 2012 used a similar model to the one proposed by *Edwards et al.* (2011) to quantify the influence of cell colony size on the scaling and spatial distribution of traction forces. Almost concurrent, *Banerjee et al.* (2013) exploited a very similar continuum model to theoretically investigate the effect of the adhesion geometry on the internal distribution of cell stresses and traction forces. Further, *Hanke et al.* (2018) applied this model to spreading blood platelets in order to study the force generation dynamics on substrates of variable stiffness, while *Vishwakarma et al.* (2018) utilized it to investigate the formation of leader cells at epithelial wound margins. In very recent advances, *Kim et al.* (2021) developed a three-dimensional continuum-based approach to model the shape and internal stress changes of microtissues in response of surgical intervention (Fig. 1.11D). Here, the authors make use of a nonlinear material law together with active surface and bulk contractility.

In summary, continuum models are applicable on a variety of scales, ranging from single cells ($5\ \mu\text{m} - 50\ \mu\text{m}$) to microtissues ($\approx 800\ \mu\text{m}$). They allow to couple cells to their environment in a mathematically natural way through force balance equations

and boundary conditions and give the opportunity to consider anisotropy and inhomogeneity in the cell properties. A further advance is that the parameters describing these cell properties, like e.g. Young’s modulus, viscous modulus and Poisson’s ratio, are accessible through experiments, which makes it easier to parametrize such models. However, the purely “meso/macrosopic” parameterization makes it more complicated to account for microscopic features of the actin cytoskeleton. Among others, those include density changes of actin and myosin filaments across the cell or, for example, the discrete nature of focal adhesions. In addition, the repelling forces upon compression of the elastic cell layer prevent the formation of the experimentally observed circular shaped peripheral arcs. Instead, the cell periphery is comparable to the shape obtained by Hookean spring networks with flattening of the arc for long spanning distances. Further, we note that discrete structures such as stress fibers can be incorporated by asymptotic homogenization techniques by relating global and local material parameters (*Probst, 2018*).

1.3.2. CONTOUR MODELS

Contour models of cellular adhesion are motivated by the experimental observation that in flat adherent cells, the cell edge between two adhesion points has a characteristic invaginated arc. *Zand et al. (1989)* found that those cell edges are mainly supported by a dominant cytoskeletal structure which they called the actin edge-bundle. A schematic illustration of the cell edge of a flat adherent cell is depicted in Fig. 1.12A. The plasma membrane of the cell is wrapped around the actin edge-bundle that is pulled towards the interior of the cell. The inward pull is associated with an isotropic constant surface tension σ stemming from actomyosin contractility of the cell and is balanced by a constant tension λ within the edge fiber. The counterplay of those two quantities defines a circular shaped edge (see Fig. 1.12B) with radius of curvature given by

$$R = \frac{\lambda}{\sigma}, \quad (1.9)$$

known as the simple tension model (STM) (*Bar-Ziv et al., 1999; Bischofs et al., 2008*). However, the radius of curvature of the free spanning arcs is not independent of the spanning distance d between two adhesion sites as can be seen in Fig. 1.12B for the case of a cell plated on a dot-like micropattern. The measured increasing R - d -dependency can be explained by postulating an elastic origin of the line tension, leading to the so-called tension elasticity model (TEM) (*Bischofs et al., 2008; Bischofs et al., 2009*). Very recently, *Weißbruch et al. (2021)* introduced an extension of the classical STM and TEM to study how knockout of non muscle myosin II isoforms influences the cell shape. Here, in the so-called dynamic tension elasticity model (dTEM) a dynamical equation for the length of the circular arc is derived based on a linear force velocity relationship.

However, in the presence of strong internal stress fibers, the assumption of an isotropic surface tension certainly does not hold anymore as the directed forces stemming from these internal stress fibers lead to a clearly non-circular shaped contour, especially for long arcs (see Fig. 1.12C). The varying curvature along the contour can

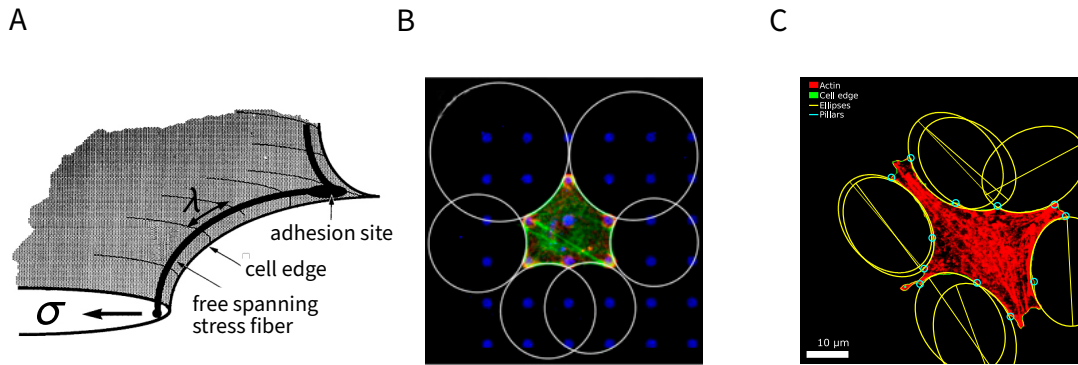


Figure 1.12: Contour model of cellular adhesion. Panel **A** highlights the main ideas of a contour-based description of cellular contractility. Panel **B** illustrates the circular shaped peripheral actin bundles as predicted by contour models for cells on dot-like micropatterned fibronectin substrates. Panel **C** shows the predicted elliptical arcs for contour models which include local anisotropy of the actin cytoskeleton near the peripheral actin due to internal stress fibers. Figures: A adapted from (Zand *et al.*, 1989); B taken from (Bischofs *et al.*, 2008); C taken from (Pomp *et al.*, 2018).

be explained by the anisotropic tension model (ATM) in which the anisotropy of the actin cortex is incorporated by extending the isotropic surface tension by a directed component (Giomi, 2019; Pomp *et al.*, 2018). This extension predicts elliptical contours, where the orientation of the resulting ellipse determines the direction of the internal stress fibers (Fig. 1.12).

Beyond being successful in predicting cell shapes, the contour model also allows to calculate traction forces purely based on the equilibrium cell shape, for both, continuous and discrete adhesion of the peripheral fiber (Bischofs *et al.*, 2009). The simplicity and versatility of the contour model and its rather small parameter space make it a great tool to estimate basic cellular properties such as surface and line tension of the cell. It can be used as an analysis tool or in the context of predictive numerical simulations.

1.3.3. INTERFACE-BASED MODELS

Interface based models focus on the dynamics of the cell's interface while connecting the cell shape to generated traction stresses. The three most important approaches are the cellular Potts model, the phase-field model and the vertex model.

CELLULAR POTTS MODEL

The cellular Potts model (CPM), also known as the Glazier-Graner-Hogeweg model (Graner *et al.*, 1992), is essentially based on the Ising-model and designed to model cell and tissue dynamics. As illustrated in Fig. 1.13A1, the cell is represented by discrete lattice sites which are either occupied or unoccupied, corresponding to values 1 and 0, respectively. Occupied lattice sites correspond to the cell and unoccupied lattice sites represent the surrounding medium. Cellular dynamics is then driven by a Hamiltonian which is usually comprised of terms involving cellular tension and cell-ECM adhesions. In multi-cellular Potts models, one extends the Hamiltonian by energy contributions stemming from cell-cell adhesions. Once the Hamiltonian is defined, the cell shape/cell

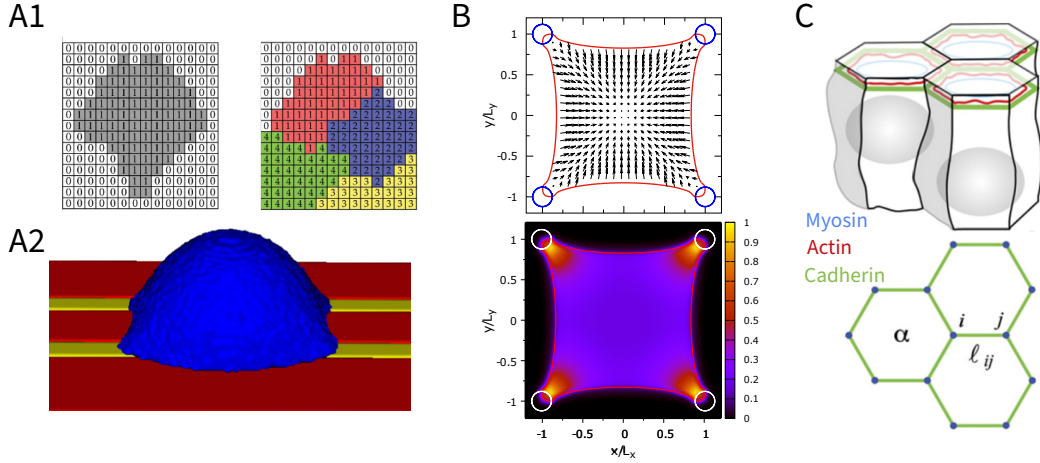


Figure 1.13: Cellular Potts model, phase field model and vertex model. Panel **A** shows the shapes of adherent cells modeled with the cellular Potts model. Sub-panel A1 illustrates the two-dimensional cellular and multicellular Potts model. The extracellular environment is represented by zeros while cells are labeled positive numbers. Sub-panel A2 shows a three-dimensional cell attached to a two-dimensional substrate calculated with a three-dimensional version of the cellular Potts model. Panel **B** depicts the shape of an adherent cell simulated with an elastic phase field model. The cell is pinned at four corners representing focal adhesions. The upper panel shows the displacement field represented by arrows while the lower panel shows the normalized von Mises stress, a scalar quantity to visualize the stress level (Chojowski *et al.*, 2020). The cell contour is shown in red and takes on the typical invaginated shape. Panel **C** shows the central element of vertex models. Here, cells are represented by hexagons which are stacked together to build a whole cell layer. Figures: A1 taken from (Albert *et al.*, 2014; Albert *et al.*, 2016b), A2 by courtesy of Rabea Link, B adapted from (Chojowski *et al.*, 2020), C adapted from (Farhadifar *et al.*, 2007).

cluster dynamics are computed by means of probabilistic algorithms which minimize the total energy and hence propagate the system by randomly inverting lattice sites until the counteracting contributions in the Hamiltonian are balanced.

The CPM has been successfully applied to various problems in the context of cell mechanics. For example Marée *et al.* (2006) used a CPM approach to model the dynamics of epidermal fish keratocytes by combining the CPM and regulatory biochemical processes of Rho, Rac and Cdc42. Käfer *et al.* (2007) exploited the CPM to study the packing of cells in a drosophila retina by introducing adhesion-dependent surface increase, which is balanced by cell contraction. Further, Albert *et al.* (2014; 2016) demonstrated that the CPM reproduces experimentally observed cell shapes in strongly adherent cells on micropatterns. Moreover, by combining the cell shape of the CPM with analytical results of the TEM, they were able to successfully predict traction force patterns for different adhesion geometries. Very recently Hino *et al.* (2020) combined the CPM with a mechano-chemical feedback mediated by extracellular signal-regulated kinases (ERKs) to describe the sustained propagation of contraction waves in epithelial cell layers. Beyond the original two-dimensional CPM, generalizations to three dimensions can be used to describe cell sorting (Iber *et al.*, 2015) or to study three-dimensional cells adhered to two dimensional substrates (Fig. 1.13A2). Although being very effective in describing dynamical processes such as cell migration, division and signalling a huge drawback of the CPM is the difficulty to account for a detailed structure of the actin CSK which, however, plays a central role in cell spreading and mechanosensing.

PHASE FIELD MODEL

The phase field model (PFM) is a model particularly developed to describe interfacial dynamics typically based on a free energy functional in terms of the so-called phase field. The phase field $\rho(x, t)$ assigns a constant value to each of two distinct phases, which for example in the context of cell mechanics are the cell interior ($\rho = 1$) and exterior ($\rho = 0$). The interface is then represented by a smooth transition between the two phases where its equation of motion is obtained by the functional derivative of the free energy. Although originally developed for problems like solidification (*Langer et al.*, 1975), it nowadays finds application in the mathematical description of fractures (*Aranson et al.*, 2000), the dynamics of vesicles in shear flow (*Biben et al.*, 2003) or cell motility (*Ziebert et al.*, 2012). Very recently, *Chojowski et al.* (2020) proposed an approach to couple the phase field method to linear elasticity by accounting for reversibility. This method allowed them to model the mechanics of adherent cells (Fig. 1.13B) although the diffusive nature of the cellular interface makes it complicated to directly connect it to contour models or other discrete cell-ECM interactions.

VERTEX MODEL

The spirit of vertex models is to model larger cell ensembles like epithelial sheets in a coarse grained fashion. Instead of a detailed three-dimensional model for each cell, only the relevant horizontal packing topology is considered. The whole epithelial layer is therefore approximated by a collection of vertices and edges building a polygonal network (Fig. 1.13C). Force- and motion-driving cell features such as actomyosin contractility, cell adhesion but also elastic properties are usually collected in an energy function which is minimized to obtain the equilibrium state of the tissue by which force balance at each vertex is satisfied. Typical areas of application include cell packing in epithelial sheets (*Farhadifar et al.*, 2007), tissue growth and other morphogenetic processes (*Hufnagel et al.*, 2007). Just recently *Cavanaugh et al.* (2020) used a vertex model approach to explain rheological properties of epithelial cell junctions subject to optogenetic activation. However, vertex models are not designed to model adherent single cells and additionally, based on their mathematical structure, suffer from the same computational difficulties as the network models.

1.4. SUMMARY

In this chapter we provided an overview over the fundamental working principle of the cytoskeleton of the cell. We additionally introduced traction force microscopy, micropatterning and non-neuronal optogenetics as the main experimental techniques in the context of the here presented work. Finally, we discussed models of cellular contractility and compared their weaknesses and strengths. Being aware of all recent theoretical and computational approaches to modeling the mechanical properties of adherent cells, we have chosen continuum models and contour models. Continuum models allow adherent cells to be simulated with results closely resembling experiments. They are versatile, allow the introduction of optogenetic activation, and are

computationally efficient. However, as mentioned earlier, they do not explicitly include the mechanical properties of the cell contour which, however, is a concise structure in certain adhesion geometries. Therefore, in situations where cell shape is an essential element of the analysis, we will rely on contour models as an analysis tool and further use it in the context of predictive numerical simulations.

1.5. OUTLINE

Chapter 2 lays down the theoretical concepts providing the basis for continuum and contour models. The central elements of continuum mechanics are introduced and used to review the important model of an isotropically contracting cell connected to an elastic foundation. Following a similar strategy, a mathematically rigorous notion of contour models for adhering cells is introduced, followed by a recapitulation of the tension elasticity model.

Chapter 3 focuses on the numerical treatment of the two used model classes by means of finite element simulations. At first, the general work flow of finite element methods is briefly introduced. After deriving the weak formulation for the equations of mechanical equilibrium for both, continuum models and contour models, the implementation is validated by a detailed comparison to the analytical counterparts discussed in Chapter 2.

Chapter 4 presents the results that were obtained in a first collaborative work with experimentalists. There, we investigate how cell size and actin architecture influence the dynamics of force generation in adherent fibroblasts. By combining finite element simulations and experimental techniques, we are able to study how the internal structure of the actin cytoskeleton, which, to some extent can be controlled by the adhesive geometry, influences the cellular contractile energy.

Chapter 5 is structured similarly to Chapter 4 and describes the results of another collaboration with experimentalists, which focuses on the quantification of force propagation and active coupling in epithelial cells. By extending the models used in Chapter 4 by incorporating local photo-activation we are able to show that cells are actively coupled and further, that the coupling strength is influenced by the mechanical and structural polarization of the cytoskeleton. In addition, we introduce the contour model as a tool to analyze the cell shape and exploit it to demonstrate that cortices of cells are stronger coupled than stress fibers.

Finally, Chapter 6 deals with the numerical treatment of a cell doublet and pays particular attention to its most important features. These include, for example, that the cells are characterized by an intercellular connection which keeps the cytosols of the two cells isolated from each other. This property is accounted for by a discontinuous Galerkin method. By introducing a minimal model for a typical signaling pathway leading to cell contraction, this approach allows us to show that strain-dependent feedback can explain the active coupling in cell doublets which in turn leads to a symmetric response of an asymmetrically stimulated cell doublet.

Chapter 2

Theory

Following the general introduction provided in the previous chapter, we will now examine continuum models and contour models in more detail. We will present the central mathematical foundations of both models and, building on this, discuss the main analytical results for each model class. For the continuum model we recapitulate the example problem of the isotropic contractile disk connected to an elastic foundation and for the contour models we recapitulate the tension-elasticity model using a mathematically rigorous formalism.

2.1. CONTINUUM MODEL

2.1.1. CONTINUUM MECHANICS IN A NUTSHELL

It is well known that matter, irrespective of the phase, consists of discrete particles. Physical properties of matter can therefore be traced back to the molecular structure, the intermolecular distance and intermolecular forces. However, on sufficiently large length scales (≥ 100 nm) these microscopic structures can be disregarded for many applications. In such cases, the effective properties of the matter can be represented well by a continuous density distribution. This branch of physics is known as continuum mechanics and deals with the movement and deformation of matter under the action of forces. Within this framework, physical properties are described by continuous fields such as, e.g.

$$\begin{aligned} \rho(\mathbf{x}, t) & \text{ mass density ,} & \mathbf{u}(\mathbf{x}, t) & \text{ deformation field ,} \\ \mathbf{v}(\mathbf{x}, t) & \text{ velocity field ,} & T(\mathbf{x}, t) & \text{ temperature field ,} \end{aligned}$$

which, from a mathematically standpoint, makes continuum mechanics a classical field theory. In real life applications and interdisciplinary science like engineering, astrophysics, material sciences, biophysics and more, it is often combined with other important branches of physics like electrodynamics or thermodynamics. The two main branches of continuum mechanics are fluid dynamics and solid mechanics which again split up into various sub-disciplines ranging from gas dynamics to imperfections. The substructure of continuum mechanics is depicted in Fig. 2.1 where the models used in this work are located at the interface between fluid mechanics and solid mechanics known as rheology (blue shading). Our mathematical formulation of the most important aspects of continuum mechanics is based on the work by *Abeyaratne* (1988),

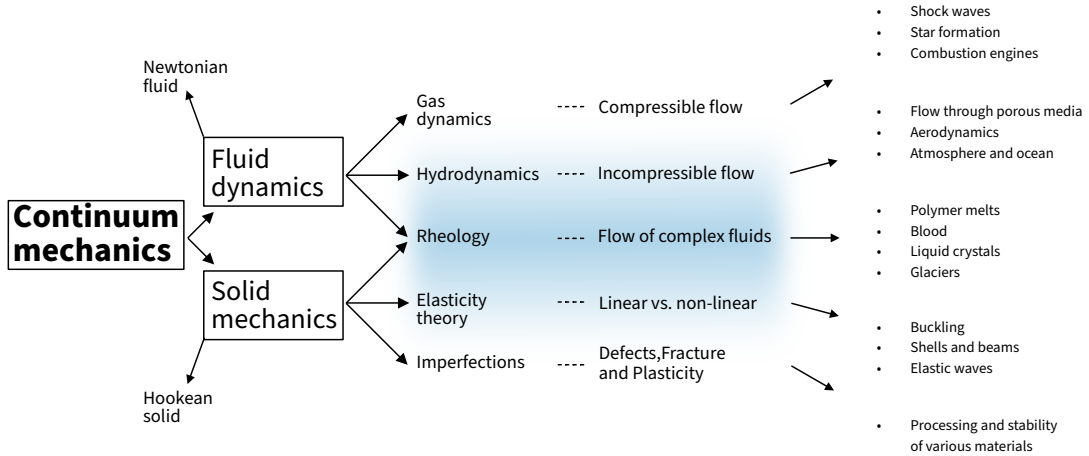


Figure 2.1: Different branches of continuum mechanics. The blue region highlights the sub-disciplines which will be important in this thesis. Based on (Schwarz, 2018)

Holzapfel (2000), Howell et al. (2009), and T. Richter (2017).

COORDINATE SYSTEMS

Closely following the literature and textbooks cited above, we distinguish between three different representations of a continuum body as depicted in Fig. 2.2A. \mathcal{B} denotes the abstract representation of a continuum body which is a collection of material particles labeled by m . In contrast, the remaining two representations correspond to specific configurations of the body where each particle m has a position in three-(two-) dimensional space. One of these representations is denoted by \mathcal{R} and describes the reference (initial) configuration of the body at time $t_0 \in \mathbb{R}$. In the absence of external macroscopic forces, \mathcal{R} refers to the undeformed state or stress free state. The volume of the undeformed configuration is denoted by $\Omega_0 \subset \mathbb{R}^d$, with $d = 2, 3$, and the spatial positions are represented by $\hat{\mathbf{x}} \in \Omega_0$. At some later time $t > t_0$ and under the influence of external forces and moments, the body will be displaced and deformed i.e. arrive in its current (deformed) configuration \mathcal{C} . The volume of the deformed configuration is denoted by $\Omega_t \subset \mathbb{R}^d$ with position vectors $\mathbf{x} \in \Omega_t$. Although it is possible to construct mappings between each of the three representations we want to focus on the so called motion function $\mathcal{X}(t) : \Omega_0 \rightarrow \Omega_t$ which maps the undeformed to the deformed configuration by relating the position vectors at any given time through

$$\mathbf{x} = \mathcal{X}(t)(\hat{\mathbf{x}}) := \mathcal{X}(\hat{\mathbf{x}}, t) . \quad (2.1)$$

Further, we assume the motion function to be invertible $\mathcal{X}^{-1}(\mathbf{x}, t) = \hat{\mathbf{x}}$ and continuously differentiable in space and time. Following the trajectories of material particles over time is known as the Lagrangian description and is the most common choice for problems in solid mechanics. Within this view point all quantities are expressed in terms of the Lagrangian coordinates $\hat{\mathbf{x}}$ which are fixed in the material. An alternative view point is the so called Eulerian description which is common to use for problems in fluid dynamics since it is more natural to formulate mass and momentum conservation. Here, all quantities are described with respect to the spatially fixed coordinates

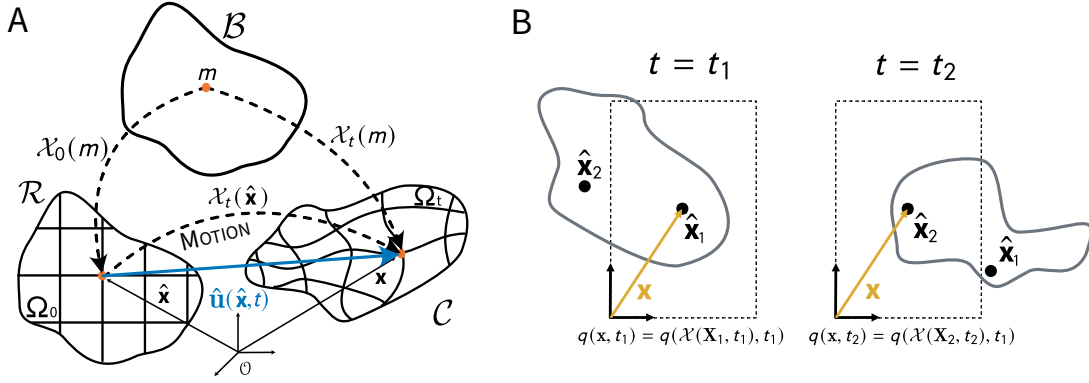


Figure 2.2: Lagrangian and Eulerian description of continuum mechanics. Panel **A** depicts the Lagrangian view point in which the paths of material particles are traced over time. A deformable object is mathematically represented by a so called body \mathcal{B} which is a set of material points m without any particular geometrical shape. The reference configuration (initial configuration) \mathcal{R} is obtained by choosing a frame of reference and assigning a specific position $\mathbf{X} = \mathcal{X}_0(m) \in \mathbb{R}^d$ to each particle label m at a given initial time t_0 . The region in space which the body \mathcal{B} occupies at any given time $t > t_0$ is called current configuration \mathcal{C} which is obtained by the motion function \mathcal{X}_t . The resulting displacement vector $\hat{\mathbf{u}}(\hat{\mathbf{x}}, t)$ for a material particle is drawn in blue. Panel **B** schematically illustrates the equivalent Eulerian approach in which an arbitrary quantity $q(\mathbf{x}, t)$ is evaluated at a fixed position in space at a given time t . As the body moves the value of $q(\mathbf{x}, t)$ changes as different material particles are passing through position \mathbf{x} .

\mathbf{x} as illustrated in Fig. 2.2B. For example, the value of an arbitrary quantity $q(\mathbf{x}, t)$ is given by the properties of a particle $\hat{\mathbf{x}}$ that happens to be at position \mathbf{x} at time t . If not stated otherwise, we will use the symbol “ \wedge ” to denote quantities defined in a Lagrangian frame of reference.

DISPLACEMENT AND DEFORMATION GRADIENT

Next, we introduce the displacement field $\hat{\mathbf{u}} : \Omega_0 \rightarrow \mathbb{R}^d$ which connects the initial position $\hat{\mathbf{x}}$ and the current position \mathbf{x} of a particle by

$$\hat{\mathbf{u}}(\hat{\mathbf{x}}, t) = \mathbf{x}(\hat{\mathbf{x}}, t) - \hat{\mathbf{x}}. \quad (2.2)$$

The Eulerian equivalent of Eq. (2.2) is given by $\mathbf{u}(\mathbf{x}, t) = \mathbf{x} - \hat{\mathbf{x}}(\mathbf{x}, t)$ highlighting the equivalence of the two descriptions, since $\hat{\mathbf{u}}(\hat{\mathbf{x}}, t) = \hat{\mathbf{u}}(\mathcal{X}^{-1}(\mathbf{x}, t), t) = \mathbf{u}(\mathbf{x}, t)$.

Another fundamental quantity in structure dynamics is the so called deformation gradient tensor which is defined as the Jacobian matrix of the motion function. Thus, for a differentiable displacement field $\hat{\mathbf{u}}(\hat{\mathbf{x}}, t)$ we have

$$\hat{\mathbf{F}}(\hat{\mathbf{x}}, t) = \frac{\partial}{\partial \hat{\mathbf{x}}} \mathcal{X}(\hat{\mathbf{x}}, t) = \frac{\partial \mathbf{x}}{\partial \hat{\mathbf{x}}} = \mathbf{I} + \hat{\nabla} \hat{\mathbf{u}}(\hat{\mathbf{x}}, t), \quad (2.3)$$

or in index notation

$$\hat{F}_{ij}(\hat{\mathbf{x}}, t) = \frac{\partial x_i}{\partial \hat{x}_j}, \quad (2.4)$$

where \mathbf{I} denotes the unit tensor, $i, j = 1, \dots, d$ with $d = 2, 3$ as usual, and $\nabla \mathbf{v} = \partial_i (v_j \mathbf{e}_j) \otimes \mathbf{e}_i$ defines the vector gradient of a vector field \mathbf{v} . The tensor $\hat{\mathbf{F}}$ measures the local change of relative position of two points at the transition from undeformed

to deformed configuration and plays a central role in mappings between the two configurations. In addition, the local change of volume under deformation is given by the determinant $\hat{J} := \det(\hat{\mathbf{F}})$ of the deformation gradient tensor which can be easily seen from

$$|\Omega(t)| = \int_{\Omega(t)} 1 \, d\mathbf{x} = \int_{\Omega_0} \det(\mathbf{I} + \hat{\nabla}\hat{\mathbf{u}}) \, d\hat{\mathbf{x}} = \int_{\Omega_0} \hat{J} \, d\hat{\mathbf{x}}, \quad (2.5)$$

where $\Omega(t)$ and Ω_0 are the current and initial volume, respectively.

STRAIN

Strain is a dimensionless quantity measuring the change of relative distances between material elements under deformation. The most prominent example is Hooke's law for a simple spring which can be formulated as

$$K = \tilde{k} \frac{L - L_0}{L_0}, \quad (2.6)$$

where K describes the tensile force resulting from stretching a spring with rest length L_0 to new length L . \tilde{k} is the elastic modulus and $(L - L_0)/L$ the strain. The generalization to higher dimensions can be achieved by exploiting the relationship

$$\delta\mathbf{x} = \hat{\mathbf{F}} \delta\hat{\mathbf{x}} + \mathcal{O}(\delta\hat{l}^2), \quad (2.7)$$

i.e. relating the vectors of two infinitesimal line segments $\delta\mathbf{x} = \mathbf{e}\delta l$ and $\delta\hat{\mathbf{x}} = \hat{\mathbf{e}}\delta\hat{l}$ in deformed and undeformed configurations, respectively. The length of the line segment in the deformed configuration is given by

$$\delta l = \sqrt{(\hat{\mathbf{F}} \delta\hat{\mathbf{x}}) \cdot (\hat{\mathbf{F}} \delta\hat{\mathbf{x}})} + \mathcal{O}(\delta\hat{l}^2) = \delta\hat{l} \sqrt{\hat{\mathbf{e}}^\top (\hat{\mathbf{F}}^\top \hat{\mathbf{F}}) \hat{\mathbf{e}}} + \mathcal{O}(\delta\hat{l}^2), \quad (2.8)$$

with $\hat{\mathbf{C}} := \hat{\mathbf{F}}^\top \hat{\mathbf{F}}$ being the symmetric and positive definite right Cauchy-Green deformation tensor. A convenient choice for a strain measure is the Green-Lagrange strain tensor

$$\hat{\mathbf{E}} := \frac{1}{2}(\hat{\mathbf{C}} - \mathbf{I}), \quad (2.9)$$

measuring the squared length change of a line-element under deformation. It holds that $\hat{\mathbf{E}} = \mathbf{0}$ in case of vanishing deformation, which is consistent with the idea, that in the absence of strain no stress is induced within the material. Further, it can be shown that $\hat{\mathbf{E}}$ is invariant under rigid body transformations (*Howell et al.*, 2009).

STRESS

In simple terms, (internal) stress quantifies the resisting force across material cross-sections that arise when a material body is subjected to external surface and body forces. Additionally, in active materials internal stresses can arise due to active force producing mechanisms leading to deformations. Stress is measured in units of force per area. According to Cauchy's stress theorem, the stress state of a body can be uniquely described by a second order tensor field $\boldsymbol{\sigma}(\mathbf{x}, t)$ such that the traction vector

\mathbf{t} on an arbitrary surface element dA with surface normal \mathbf{n} is given by

$$\mathbf{t}(\mathbf{x}, t, \mathbf{n}) = \boldsymbol{\sigma}(\mathbf{x}, t)\mathbf{n} . \quad (2.10)$$

Since the symmetric Cauchy stress tensor $\boldsymbol{\sigma}(\mathbf{x}, t)$ gives the stress state in the current configuration, it is useful to introduce another important stress measure, which relates the stress in the current configuration to surface elements in the reference configuration. Therefore, one introduces the first Piola-Kirchhoff stress tensor $\hat{\mathbf{P}}(\hat{\mathbf{x}}, t)$, for which, in analogy to Eq. (2.10), the first Piola-Kirchhoff traction vector is defined as

$$\hat{\mathbf{t}}(\hat{\mathbf{x}}, t, \hat{\mathbf{n}}) = \hat{\mathbf{P}}(\hat{\mathbf{x}}, t)\hat{\mathbf{n}} , \quad (2.11)$$

where $\hat{\mathbf{n}}$ denotes the surface normal to the surface element dA_0 in the reference configuration. The two stress tensors are related by

$$\hat{\mathbf{P}} = \hat{J}\boldsymbol{\sigma}(\hat{\mathbf{F}}^\top)^{-1} , \quad (2.12)$$

which immediately follows from $\mathbf{t}dA = \hat{\mathbf{t}}dA_0$ and Nanson's formula, relating the surface elements in the current and reference configuration by $dA\mathbf{n} = \hat{J}dA_0(\hat{\mathbf{F}}^\top)^{-1}\hat{\mathbf{n}}$.

MOMENTUM CONSERVATION

Following Newton's second law for an arbitrary small volume element that moves with the deforming solid, momentum conservation can be formulated as¹

$$\frac{d}{dt} \int_{\Omega_t} \frac{\partial \mathbf{u}}{\partial t} \rho(\mathbf{x}, t) d\mathbf{x} = \int_{\Omega_t} \mathbf{g}\rho(\mathbf{x}, t) d\mathbf{x} + \int_{\Gamma_t} \boldsymbol{\sigma}(\mathbf{x}, t)\mathbf{n} dA , \quad (2.13)$$

where the first term gives the change in momentum of the mass density $\rho(\mathbf{x}, t)$, the second term describes the action of an external body force like gravity and the third term accounts for the traction forces acting on the boundary $\partial\Omega_t = \Gamma_t$ of the volume element Ω_t . Further, exploiting that $\rho(\mathbf{x}, t) d\mathbf{x} = \rho(\hat{\mathbf{x}}, 0)\hat{J}d\hat{\mathbf{x}} = \hat{\rho}(\hat{\mathbf{x}})d\hat{\mathbf{x}}$ is time independent, we can interchange time derivative and integration in the first term of Eq. (2.13). By additionally applying the divergence theorem to the last term of Eq. (2.13) we obtain Cauchy's momentum equation

$$\rho \frac{\partial^2 \mathbf{u}}{\partial t^2} = \rho \mathbf{g} + \nabla \cdot \boldsymbol{\sigma} . \quad (2.14)$$

For biological tissue the inertial term can be usually neglected such that Eq. (2.14) can be simplified to

$$\nabla \cdot \boldsymbol{\sigma}(\mathbf{x}, t) = \mathbf{b} , \quad (2.15)$$

with an arbitrary body force \mathbf{b} .

¹Momentum conservation is naturally formulated in the current configuration.

LINEAR ELASTICITY

Linear elasticity theory is the limit of infinitesimal deformations and strains. In a regime of infinitesimal displacements we have $\mathbf{x} \approx \hat{\mathbf{x}}$ and hence, the mass density in the current configuration can be approximated by the mass density in the reference state since $\hat{\mathbf{F}} = \partial \mathbf{x} / \partial \hat{\mathbf{x}} \approx \mathbf{I}$ and therefore $\hat{J} \approx 1$. Moreover, for $|\hat{\nabla} \hat{\mathbf{u}}| \ll 1$ we can neglect the second order term in $\hat{\mathbf{C}} = \mathbf{I} + \hat{\nabla} \hat{\mathbf{u}} + \hat{\nabla} \hat{\mathbf{u}}^\top + \hat{\nabla} \hat{\mathbf{u}}^\top \hat{\nabla} \hat{\mathbf{u}}$ which, consequently, leads to the linearized version of the Green-Lagrange strain tensor given by

$$\hat{\boldsymbol{\varepsilon}} = \frac{1}{2}(\hat{\mathbf{F}} + \hat{\mathbf{F}}^\top - 2\mathbf{I}) . \quad (2.16)$$

As a conclusion from the above assumptions, we do not have to distinguish between the Lagrangian and Eulerian description and can simply substitute $\hat{\mathbf{x}}$ by \mathbf{x} and $\partial/\partial \hat{\mathbf{x}}_i$ by $\partial/\partial \mathbf{x}_i$ i.e. omitting the “ \wedge ”-symbol whenever we are dealing with linear elasticity. Finally, the linear strain tensor can be written as

$$\boldsymbol{\varepsilon} = \frac{1}{2}(\nabla \mathbf{u} + \nabla \mathbf{u}^\top) . \quad (2.17)$$

The constitutive relation is formulated as a multidimensional generalization of Hooke’s law

$$\boldsymbol{\sigma}(\mathbf{x}, t) = \mathbf{C}(\mathbf{x}) : \boldsymbol{\varepsilon}(\mathbf{x}, t) . \quad (2.18)$$

Here, \mathbf{C} denotes the stiffness tensor, “ $:$ ” denotes the double contraction of two indices $C_{ijkl}\varepsilon_{kl}$ and, if not stated otherwise, we use the Einstein summation convention which implies summation over equal indices. In case of an isotropic material, \mathbf{C} must be an isotropic tensor and thus its components can be expressed as

$$C_{ijkl} = \lambda \delta_{ij} \delta_{kl} + \mu (\delta_{ik} \delta_{jl} + \delta_{il} \delta_{jk}) , \quad (2.19)$$

in which λ and μ are the two Lamé coefficients. Together with Eq. (2.18) the constitutive relation of an isotropic linear elastic material yields

$$\boldsymbol{\sigma} = \lambda \operatorname{tr}(\boldsymbol{\varepsilon}) \mathbf{I} + 2\mu \boldsymbol{\varepsilon} , \quad (2.20)$$

and the Lamé parameters in terms of Young’s modulus E and Poisson’s ratio ν are given by

$$\lambda = \frac{\nu E}{(1 + \nu)(1 - 2\nu)} , \quad \mu = \frac{E}{2(1 + \nu)} . \quad (2.21)$$

2D SYSTEMS- THIN LAYER AND PLANE STRESS APPROXIMATION

In a regime where one spatial dimension (without loss of generality the z -direction) is much smaller compared to the others, as is the case for adherent cells where the cell height $h_c \approx 1 \mu\text{m} - 5 \mu\text{m}$ is much smaller than the lateral extent $L_c \approx 30 \mu\text{m} - 50 \mu\text{m}$, the stress tensor components associated with this small spatial dimension are set to zero. Further, variations of the remaining stress tensor components along the z -direction are assumed to be small and thus, it is sufficient to look at the thickness-averaged

quantities. Conclusively, the plane-stress approximation translates to $\sigma_{zz} = \sigma_{xz} = \sigma_{zx} = \sigma_{yz} = \sigma_{zy} = 0$ yielding the stress-strain relationship in Voigt notation

$$\begin{bmatrix} \sigma_{xx} \\ \sigma_{yy} \\ \sigma_{xy} \end{bmatrix} = \frac{E_c}{1 - \nu_c^2} \begin{bmatrix} 1 & \nu_c & 0 \\ \nu_c & 1 & 0 \\ 0 & 0 & \frac{1-\nu_c}{2} \end{bmatrix} \begin{bmatrix} \varepsilon_{xx} \\ \varepsilon_{yy} \\ \varepsilon_{xy} \end{bmatrix}, \quad (2.22)$$

where we neglect out of plane strains ε_{zz} . Integrating Eq. (2.15) along the z-direction gives

$$\frac{1}{h_c} \int_0^{h_c} dz \partial_j \sigma_{ij} = \frac{1}{h_c} \int_0^{h_c} dz b_i \quad (2.23)$$

$$\iff h_c \partial_j \tilde{\sigma}_{ij} = \int_0^{h_c} dz b_i \quad (2.24)$$

$$\iff \partial_j \sigma_{ij}^{2D} = t_i(x, y), \quad (2.25)$$

where $\tilde{\sigma}_{ij}(x, y)$ is the thickness averaged stress tensor, $\sigma_{ij}^{2D} = h_c \tilde{\sigma}_{ij}$ denotes the two dimensional stress tensor with physical units of surface tension $[\sigma_{ij}^{2D}] = \text{N m}^{-1}$ and $t_i(x, y)$ is the two-dimensional equivalent of a body force and has physical units of a traction $[t_i] = \text{N m}^{-2}$. Hence, in a two-dimensional system surface tractions enter the equations of mechanical equilibrium as a body force. Moreover, comparing the thickness-averaged version of Eq. (2.22) with the general version of Hooke's law

$$\sigma_{ij} = \lambda \varepsilon_{kk} \delta_{ij} + 2\mu \varepsilon_{ij}, \quad (2.26)$$

allows to determine the two dimensional Lamé parameters as

$$\lambda^{2D} = \frac{\nu_c h_c E_c}{1 - \nu_c^2}, \quad \mu^{2D} = \frac{h_c E_c}{2(1 + \nu_c)}. \quad (2.27)$$

LINEAR VISCOELASTICITY

In order to account for the viscoelastic nature of the actin cytoskeleton (*Clément et al.*, 2017; *Saha et al.*, 2016) we briefly introduce two fundamental rheological models, the Kelvin-Voigt model and the Maxwell model. As depicted in Fig. 2.3A, the Kelvin-Voigt model consists of a dashpot and spring connected in parallel, while for the Maxwell model, shown in Fig. 2.3B, these elements are connected in series. The one-dimensional constitutive relations for the two elements are given by

$$\sigma(t) = E\varepsilon(t) \quad \text{spring}, \quad (2.28)$$

$$\sigma(t) = \eta \frac{\partial \varepsilon}{\partial t}(t) \quad \text{dashpot}. \quad (2.29)$$

Eq. (2.29) is the constitutive relation for a linear viscous fluid, where the stress σ is proportional to the strain rate $\frac{\partial \varepsilon}{\partial t}$. Thereby, the constant of proportionality is the viscosity (viscous modulus) η . In case of the Kelvin-Voigt model, an externally applied stress is distributed onto the two subelements and hence, can be written as $\sigma = \sigma_E + \sigma_\eta$.

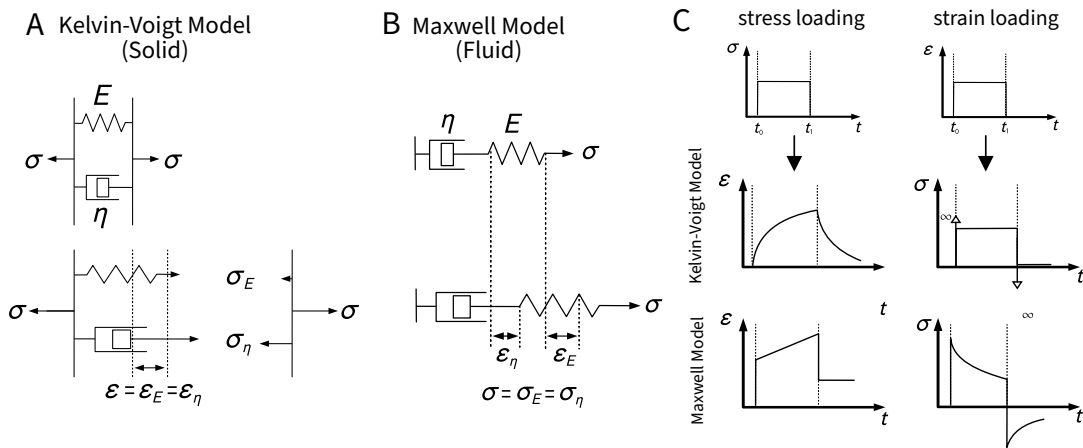


Figure 2.3: Basic viscoelastic models. Panel **A** depicts a Kelvin-Voigt element which consists of a parallel connection of a linear elastic spring E and a dashpot η . Applied stress σ is distributed onto both elements. Panel **B** shows a Maxwell element which consists of a spring E and a dashpot η connected in series. Upon loading, both elements experience equal stresses but different strain. Panel **C** shows the time course of both models under sudden stress and strain load, respectively. Image idea adapted from (*Gutierrez-Lemini, 2014*)

The strain, however, is the same for both subelements and thus $\varepsilon = \varepsilon_E = \varepsilon_\eta$. Together with Eqs. (2.28) and (2.29), this yields the constitutive relation for the Kelvin-Voigt model

$$\sigma = E\varepsilon + \eta \frac{\partial \varepsilon}{\partial t}. \quad (2.30)$$

In contrast, for the Maxwell model strains are additive $\varepsilon = \varepsilon_E + \varepsilon_\eta$ and stresses are equal $\sigma = \sigma_E = \sigma_\eta$ such that here, the constitutive relation reads

$$\eta \frac{\partial \sigma}{\partial t} + E\sigma = E\eta \frac{\partial \varepsilon}{\partial t}. \quad (2.31)$$

The solutions of the above ordinary differential equations in the special case of a sudden stress or strain loading are illustrated in Fig. 2.3C, highlighting the solid- and fluid-like Kelvin-Voigt and Maxwell model, respectively. In most cases, experimental data will indicate which of the two models is a better fit for describing certain aspects of the dynamics of the actin cytoskeleton. And further, these two models can easily be extended to describe more complicated rheological behavior.

2.1.2. ISOTROPICALLY CONTRACTING DISC

Using the basic concepts of continuum mechanics as introduced above, we solve the important system of a disc-shaped active contractile cell layer coupled to an elastic foundation² analytically. Those models have served as the basis of various more complicated models used to study mechanotransduction of cells on pillar arrays or gel substrates (*Edwards et al., 2011; Solowiej-Wedderburn et al., 2022*) and provide an important theoretical counterpart to experiments.

²The terms “elastic foundation”, “substrate” and “(micro)pattern” are used interchangeably.

Fig. 2.4A depicts the basic system setup in which the disc shaped cell layer (black) is attached to the substrate (blue). The key parameters to describe the elastic layer are Young's modulus E_c , Poisson's ratio ν_c , disc radius r_0 and active contractile stress σ_a . The effective cell-substrate coupling is here represented by the spring stiffness density Y , i.e. a layer of equally distributed springs, which describe the combined elastic properties of focal adhesions and substrate.

For a radially symmetric system with isotropic contraction, we can conclude that the resulting displacement field \mathbf{u} is pointing along the radial direction and therefore only the radial component

$$\mathbf{u} = u_r \mathbf{e}_r, \quad (2.32)$$

is non-zero. The stress - strain relationship for a plane stress setup in polar coordinates reads (*Slaughter*, 2012)

$$\sigma_{rr} = (2\mu + \lambda)\varepsilon_{rr} + \lambda\varepsilon_{\theta\theta} + \sigma_a, \quad (2.33)$$

$$\sigma_{\theta\theta} = (2\mu + \lambda)\varepsilon_{\theta\theta} + \lambda\varepsilon_{rr} + \sigma_a, \quad (2.34)$$

with the strain displacement relations $\varepsilon_{rr} = \partial_r u_r$ and $\varepsilon_{\theta\theta} = u_r/r$ and the two-dimensional Lamé parameters μ and λ . The force balance equation is given by

$$\nabla \cdot \boldsymbol{\sigma} = Y(\mathbf{x})\mathbf{u}, \quad (2.35)$$

in which the term $\mathbf{T} = Y\mathbf{u}$ describes the traction force which takes on the role of a body force in case of a purely two-dimensional system. Transforming the force balance equation into polar coordinates yields

$$\frac{\partial}{\partial r}\sigma_{rr} + \frac{1}{r}(\sigma_{rr} - \sigma_{\theta\theta}) = Y(\mathbf{x})u_r. \quad (2.36)$$

Inserting Eqs. 2.33 and 2.34 together with

$$\frac{\partial}{\partial r}\sigma_{rr} = (2\mu + \lambda)\frac{\partial^2}{\partial r^2}u_r + \frac{\lambda}{r}\frac{\partial}{\partial r}u_r - \frac{\lambda}{r^2}u_r + \frac{\partial}{\partial r}\sigma_a, \quad (2.37)$$

into the force balance Eq. 2.36 leads to the second order ordinary differential equation for the displacement field $u_r(r)$ of the isotropically contracting disc with elastic foundation

$$r^2 \frac{\partial^2}{\partial r^2}u_r + r \frac{\partial}{\partial r}u_r - \left(\frac{r^2}{l_p^2} + 1\right)u_r = -\frac{r^2}{2\mu + \lambda} \frac{\partial}{\partial r}\sigma_a. \quad (2.38)$$

Thereby, l_p denotes the so-called localization length

$$l_p = \sqrt{\frac{2\mu + \lambda}{Y}} = \sqrt{\frac{h_c E_c}{Y(1 - \nu_c^2)}}, \quad (2.39)$$

which can be interpreted as the typical length scale on which the substrate deformations decay.

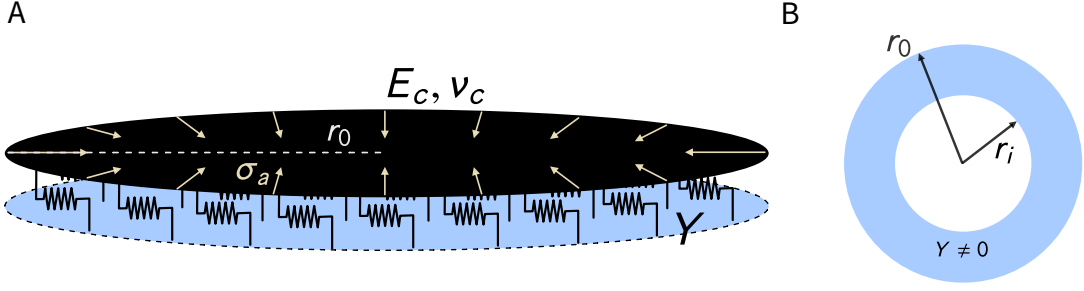


Figure 2.4: Illustration of an isotropically contracting disc of radius r_0 , Young's modulus E_c , Poisson's ratio ν_c and active contractile stress σ_a . The parameter Y is the effective spring stiffness density which defines the rigidity of the elastic foundation. Panel **A** depicts the case of a full disc-shaped adhesion pattern. Panel **B** shows a ring-shaped adhesion pattern. In this, case the cell can only adhere to the area between r_i and r_0 , i.e where $Y \neq 0$.

ADHESION ON DISC PATTERN

In case of a constant active stress σ_a and a circular shaped adhesion pattern the equilibrium solution fulfills the following boundary value problem: For a given interval $[0, r_0] \subset \mathbb{R}$ find the function $u_r : [0, r_0] \rightarrow \mathbb{R}$, $u_r \in C^2((0, r_0)) \cap C^0([0, r_0])$ such that

$$r^2 \frac{\partial^2}{\partial r^2} u_r + r \frac{\partial}{\partial r} u_r - \left(\frac{r^2}{l_p^2} + 1 \right) u_r = 0, \quad (2.40)$$

together with the boundary conditions

$$u_r(0) = 0 \quad \text{Dirichlet BC (i)}, \quad \sigma_{rr}(r_0) = 0 \quad \text{zero-stress BC (ii)}. \quad (2.41)$$

Rewriting Eq. 2.40 by introducing the non dimensional parameter $\xi = r/l_p$ leads to

$$\xi^2 \frac{\partial^2}{\partial \xi^2} u_r + \xi \frac{\partial}{\partial \xi} u_r - (\xi^2 + 1) u_r = 0, \quad (2.42)$$

whose solution can be written in terms of the modified Bessel functions of the first and second kind³

$$u_r(\xi) = c_1 I_1(\xi) + c_2 K_1(\xi), \quad (2.43)$$

with two constants c_1 and c_2 . In order to fulfill boundary condition 2.41(i) it follows that $c_2 = 0$ since $\lim_{\xi \rightarrow 0} K_1(\xi) = \infty$. Writing out the zero-stress boundary condition 2.41(ii) yields

$$\frac{\partial}{\partial \xi} u_r \Big|_{\xi=\xi_0} + \frac{\lambda}{2\mu + \lambda} \frac{u_r}{\xi_0} = -\frac{l_p}{2\mu + \lambda} \sigma_a, \quad (2.44)$$

where we set $\xi_0 = l_p r_0$. Inserting Eq. 2.43 into Eq. 2.44 and solving for c_1 leads to

$$c_1 = -l_p \frac{\sigma_a}{2\mu + \lambda} \frac{1}{I_0(\xi_0) - \frac{2\mu}{2\mu + \lambda} \frac{I_1(\xi_0)}{\xi_0}}, \quad (2.45)$$

³The general form of Eq. 2.42 is given by $\xi^2 \frac{\partial^2}{\partial \xi^2} f + \xi \frac{\partial}{\partial \xi} f - (\xi^2 + n) f = 0$. The solutions are a linear combination of Bessel functions of the first and second kinds $f = \alpha I_n(\xi) + \beta K_n(\xi)$.

from which we obtain the full solution to Eq. (2.40)

$$u_r(r) = -l_p \frac{\sigma_a}{2\mu + \lambda} \frac{I_1\left(\frac{r}{l_p}\right)}{I_0\left(\frac{r_0}{l_p}\right) - \frac{2\mu - l_p}{2\mu + \lambda} \frac{l_p}{r_0} I_1\left(\frac{r_0}{l_p}\right)}. \quad (2.46)$$

ADHESION ON RING PATTERN

In case of a ring shaped adhesion pattern as depicted in Fig. 2.4B we can obtain the ODE for the non-adhesive inner circle by exploiting the fact that the spring stiffness density is zero and thus $\lim_{Y \rightarrow 0} l_p(Y) = \infty$ such that $r^2/l_p^2 = 0$. Hence, Eq. 2.40 turns into the well known Euler-Cauchy equation. The problem of solving the isotropically contracting disc on the ring pattern can be stated as: For a given interval $[0, r_0] \subset \mathbb{R}$ with $r_i \in [0, r_0]$ find the function $u_r : [0, r_0] \rightarrow \mathbb{R}$, $u_r \in C^2((0, r_0)) \cap C^0([0, r_0])$ such that

$$r^2 \frac{\partial^2}{\partial r^2} u_r + r \frac{\partial}{\partial r} u_r - u_r = 0, \quad \text{for } r \in [0, r_i] \quad (2.47)$$

$$r^2 \frac{\partial^2}{\partial r^2} u_r + r \frac{\partial}{\partial r} u_r - \left(\frac{r^2}{l_p^2} + 1 \right) u_r = 0, \quad \text{for } r \in [r_i, r_0] \quad (2.48)$$

together with the boundary conditions

$$\begin{aligned} \text{(i)} \quad u_r^{\text{in}}(0) &= 0, & \text{(ii)} \quad u_r^{\text{in}}(r_i) &= u_r^{\text{out}}(r_i), \\ \text{(iii)} \quad \sigma_{rr}^{\text{in}}(r_i) &= \sigma_{rr}^{\text{out}}(r_i), & \text{(iv)} \quad \sigma_{rr}^{\text{out}}(r_0) &= 0, \end{aligned} \quad (2.49)$$

where the superscripts $(\cdot)^{\text{in}}$ and $(\cdot)^{\text{out}}$ highlight the solutions on the intervals given in Eqs 2.47 and 2.48. The general solution of the Euler-Cauchy Eq. 2.47, i.e. the inner part of the ring pattern, is given by

$$u^{\text{in}}(\xi) = \frac{c_1}{\xi} + c_2 \xi, \quad (2.50)$$

where we again introduce the non-dimensional variable $\xi = r/l_p$. The solution of Eq. 2.48, i.e the adhesive outer part of the pattern, is as before

$$u^{\text{out}}(\xi) = c_3 I_1(\xi) + c_4 K_1(\xi). \quad (2.51)$$

We omit the details of the lengthy calculation for determining the constants $c_1 - c_4$ which can be directly obtained through the boundary conditions of the problem. Our calculation yields

$$c_1 = 0, \quad c_3 = -\sigma_a \frac{l_p}{2\mu + \lambda} \frac{M(\xi_i)}{Q(\xi_0)M(\xi_i) - S(\xi_0)N(\xi_i)}, \quad (2.52)$$

$$c_2 = c_3 \frac{I_1(\xi_i)}{\xi_i} + c_4 \frac{K_1(\xi_i)}{\xi_i}, \quad c_4 = -\sigma_a \frac{l_p}{2\mu + \lambda} \frac{N(\xi_i)}{Q(\xi_0)M(\xi_i) - S(\xi_0)N(\xi_i)}, \quad (2.53)$$

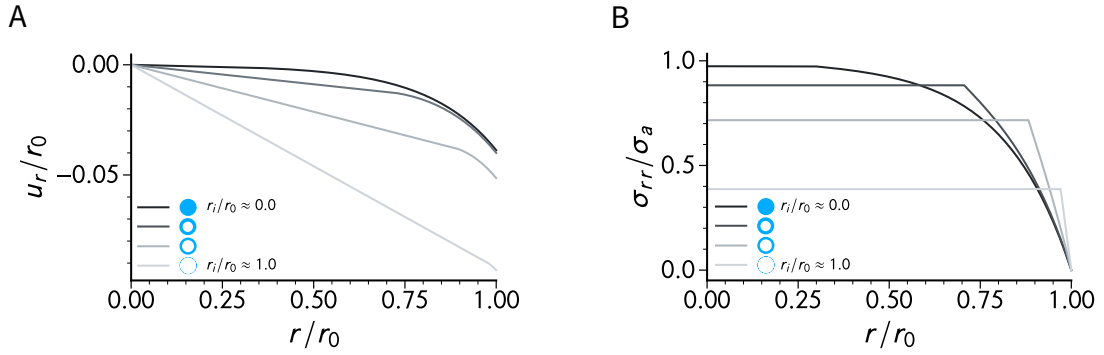


Figure 2.5: Radial displacement and stress field for contractile disc. Panel **A** shows the radial profile of displacement field $u_r(r)$ for different adhesive ring areas. Panel **B** depicts the radial component of the stress tensor $\sigma_{rr}(r)$ for different adhesive ring areas. Darker line colors correspond to larger ring areas with the limiting case of a fully adhesive disc-pattern.

where $\xi_i = r_i/l_p$ and

$$M(\xi_i) = 2 \frac{K_1(\xi_i)}{\xi_i} + K_0(\xi_i), \quad N(\xi_i) = I_0(\xi_i) - 2 \frac{I_1(\xi_i)}{\xi_i}, \quad (2.54)$$

$$Q(\xi_0) = I_0(\xi_0) - \frac{2\mu}{2\mu + \lambda} \frac{I_1(\xi_0)}{\xi_0}, \quad S(\xi_0) = K_0(\xi_0) + \frac{2\mu}{2\mu + \lambda} \frac{K_1(\xi_0)}{\xi_0}. \quad (2.55)$$

The solution is illustrated in Fig. 2.5A together with the radial component of the total stress tensor σ_{rr} for four different adhesion areas ranging from a fully adherent disc ($r_i/r_0 \approx 0$) to an almost non-adherent freely contracting disc ($r_i/r_0 \approx 1$). Fig.2.5A shows that the absolute displacement $|u_r(r)|$ at the cell edge increases with decreasing adhesion area. The cross over from linear to non-linear scaling is more pronounced for smaller adhesion areas as well. Fig.2.5B depicts that the total stress stays constant in the non-adhesive domain $r < r_i$ and exhibits a steep decrease for $r \geq r_i$ with $\sigma_{rr}(r_0) = 0$ at the cell edge in order to fulfill the zero-stress boundary condition. The results of this section serve as important minimal examples which we will use throughout the thesis as a reference in order to understand and interpret more complicated situations, especially situations with changes in the adhesive area, for which no analytical solutions exist.

2.2. CONTOUR MODEL

In this section we will focus on the mathematical foundation of contour models. Although the equations for mechanical equilibrium can be derived by geometric considerations (*Schwarz et al.*, 2013), we follow the concept of the book on nonlinear structural mechanics by *Lacarbonara* (2013) and discuss the derivation in a more rigorous way. This is especially useful when it comes to calculating the equilibrium configuration of fibers under specified loading conditions and in more complicated situations which go beyond the already mentioned TEM, dTEM or ATM. Further, a stringent formalism facilitates a numerical treatment of such problems.

2.2.1. DERIVATION OF THE EQUILIBRIUM EQUATION

Motivated by the introductory discussion on cable networks and the characteristic feature of actin filaments and stress fibers we define an elastic fiber to be resisting to tension only and in this sense, we neglect torsion, shear and bending of the fiber. The fiber is supposed to start and end at localized adhesion sites such that both ends of the fiber are constrained and cannot move. Since adherent cells are very flat, we restrict ourselves to a two-dimensional description, but generalizations to three dimensions are possible using the same formalism.

In analogy to the coordinate systems introduced in Section 2.1.1 we distinguish between an undeformed (stress free) reference state \mathcal{R} and a deformed current state \mathcal{C} . Quantities referring to the reference state carry a “ \wedge ”-symbol. The length of the fiber in the reference configuration is denoted by \hat{L} with arc length parameter $\hat{s} \in [0, \hat{L}] \subset \mathbb{R}$ while for the current configuration the respective quantities are given by L with $s \in [0, L] \subset \mathbb{R}$. Without loss of generality, we fix a coordinate system in one of the adhesion sites as shown in Fig. 2.6A in which the position vectors describing the shape of \mathcal{R} and \mathcal{C} are denoted by $\hat{\mathbf{x}}(\hat{s}), \mathbf{x}(\hat{s}) \in \mathbb{R}^2$, respectively. We note that the natural parameter for the shape in the current configuration is s .

The position vector $\mathbf{x}(\hat{s})$ is assumed to be sufficiently often continuously differentiable with respect to \hat{s} and the derivatives are assumed to be non-zero on $[0, \hat{L}]$. Using the differentiability of $\mathbf{x}(\hat{s})$ we can relate the length element in the current state to its undeformed reference length by

$$ds = |\mathbf{x}(\hat{s} + d\hat{s}) - \mathbf{x}(\hat{s})| = |\partial_{\hat{s}}\mathbf{x}(\hat{s})| d\hat{s}, \quad (2.56)$$

and hence, the arc length along the curve in the current configuration follows as

$$s(\hat{s}) = \int_0^{\hat{s}} \left| \frac{\partial \mathbf{x}}{\partial q} \right| dq. \quad (2.57)$$

The stretch of the curve at position \hat{s} is then defined by the non-linear strain-displacement relationship

$$\nu(\hat{s}) := \left| \frac{\partial \mathbf{x}}{\partial \hat{s}} \right| = \frac{ds}{d\hat{s}} = \sqrt{(\partial_{\hat{s}}x)^2 + (\partial_{\hat{s}}y)^2}. \quad (2.58)$$

For a profound geometrical description of the equilibrium shape we introduce a co-moving set of basis vectors given by the two-dimensional Frenet-Serret formulas as depicted in Fig. 2.6B

$$\frac{d\mathbf{x}}{ds} = \mathbf{T} = \frac{1}{\nu} \frac{d\mathbf{x}}{d\hat{s}}, \quad (2.59)$$

$$\frac{d\mathbf{T}}{ds} = \kappa \mathbf{N}, \quad (2.60)$$

where \mathbf{T} denotes the local unit tangent vector to the curve, \mathbf{N} the local unit normal vector (outward directed as shown in Fig. 2.6A) and $\kappa = \left| \frac{d\mathbf{T}}{ds} \right|$ the local curvature. The fiber attains its equilibrium shape if the contact forces $\mathbf{F}(\hat{s})$ within the material balance the externally applied force load $\mathbf{f}(\hat{s})$ per unit reference length \hat{s} . For an arbitrary line element $[\hat{s}_0, \hat{s}] \subset (0, \hat{L})$ as depicted in Fig. 2.6C the balance of linear

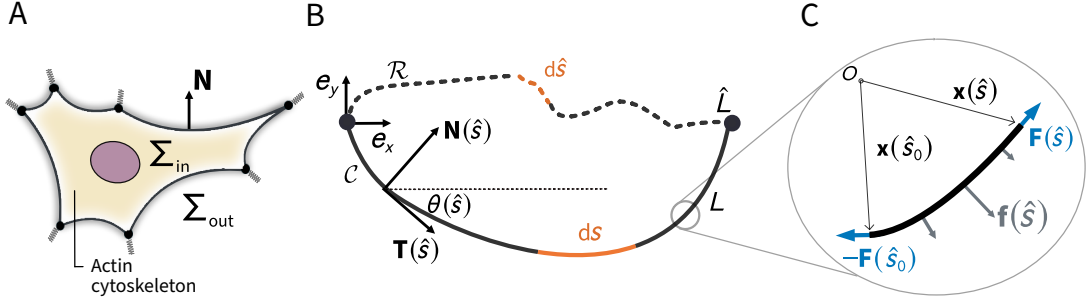


Figure 2.6: Basic notions for the description of a slender fiber. Panel **A** schematically illustrates an adherent cell as a two-dimensional continuum separated by a one-dimensional interface from its environment with stress tensors Σ_{in} for the interior and Σ_{out} for the exterior of the cell. For closed curves an always outward pointing normal is defined. Panel **B** shows the reference (unstretched) and current (stretched) configuration of a suspended fiber. Panel **C** depicts the force balance between internal forces \mathbf{F} and external force loads \mathbf{f} for an infinitesimal line element in the current configuration.

momentum is therefore given by

$$-\mathbf{F}(\hat{s}_0) + \mathbf{F}(\hat{s}) + \int_{\hat{s}_0}^{\hat{s}} \mathbf{f}(\zeta) d\zeta = 0, \quad \forall [\hat{s}_0, \hat{s}] \subset (0, \hat{L}). \quad (2.61)$$

Moreover, assuming that the contact force is differentiable along the entire line element leads to $\mathbf{F}(\hat{s}) = \mathbf{F}(\hat{s}_0) - \int_{\hat{s}_0}^{\hat{s}} \partial_{\zeta} \mathbf{F}(\zeta) d\zeta$. By comparison of the two integrands we arrive at the local force balance statement given by

$$\partial_{\hat{s}} \mathbf{F} + \mathbf{f} = 0. \quad (2.62)$$

Demanding local torque balance with respect to the origin of the coordinate system yields

$$\mathbf{x}(\hat{s}) \times \mathbf{F}(\hat{s}) - \mathbf{x}(\hat{s}_0) \times \mathbf{F}(\hat{s}_0) + \int_{\hat{s}_0}^{\hat{s}} \mathbf{x}(\zeta) \times \mathbf{f}(\zeta) d\zeta = \int_{\hat{s}_0}^{\hat{s}} \partial_{\zeta} [\mathbf{x}(\zeta) \times \mathbf{F}(\zeta)] + \mathbf{x}(\zeta) \times \mathbf{f}(\zeta) d\zeta = 0, \quad (2.63)$$

which together with Eq. 2.62 simplifies to

$$\partial_{\hat{s}} \mathbf{x}(\hat{s}) \times \mathbf{F}(\hat{s}) = 0. \quad (2.64)$$

Using the fact that $\partial_{\hat{s}} \mathbf{x} \sim \mathbf{T}$ (Eq. (2.59)) we can conclude that the internal tensile forces always point in tangential direction $\mathbf{F} \sim \mathbf{T}$ in order to fulfill Eq. 2.64. Therefore we generally express the internal forces as

$$\mathbf{F} = \lambda(\hat{s}) \mathbf{T}(\hat{s}) \quad (2.65)$$

and refer to the parameter λ as the line tension of the fiber.

The formalism for the planar problem as introduced above can be applied to a huge variety of different problems. Moreover, stating the equations of motion as a function of the material coordinate \hat{s} allows to easily exploit numerical solution techniques as we will briefly discuss in Chapter 3.

2.2.2. THE TENSION ELASTICITY MODEL REVISITED

In case of adherent cells, as depicted in Fig. 2.6A, the force load acting on the fiber is very generally determined by the stress difference $\Sigma_{\text{in}} - \Sigma_{\text{out}}$ across the cell contour (Giomì, 2019). Therefore, the force load can be expressed as the product of a stress tensor and the outward pointing normal to the cell periphery

$$\mathbf{f} = (\Sigma_{\text{in}} - \Sigma_{\text{out}}) \mathbf{N}. \quad (2.66)$$

Under the assumption that the cell interior contracts isotropically it is reasonable to describe the force load by means of an isotropic tensor given by

$$(\Sigma_{\text{in}} - \Sigma_{\text{out}}) = -\sigma(s(\hat{s}))\nu(\hat{s})\mathbf{I}, \quad (2.67)$$

where σ is an isotropic surface tension, which denotes the force per actual reference length s , and \mathbf{I} is the two dimensional unit tensor. Hence, together with Eq. (2.65) the force balance equation is given by

$$\frac{d\lambda}{ds}\mathbf{T} + (\lambda\kappa - \sigma)\mathbf{N} = 0. \quad (2.68)$$

Since \mathbf{T} and \mathbf{N} are orthogonal vectors both terms in Eq. (2.68) must equate to zero. Consequently, the equilibrium shape is characterized by a constant line tension λ and a Laplace law, which in this context is better known as the simple tension model

$$R = \frac{\lambda}{\sigma}, \quad (2.69)$$

which relates line and surface tension to the radius of curvature $R = 1/\kappa$ of the fiber for a given constant surface tension σ (Fig. 2.7). In consequence, a constant isotropic surface tension leads to circular peripheral arcs independently of the specific adhesion geometry. However, as already discussed in Section 1.3.2, experiments on cells on pillar arrays revealed a dependency of the arc radius on the adhesion geometry, i.e. the distance of the two adhesion sites (Bischofs *et al.*, 2009). In order to account for this dependency, one assumes an elastic origin of the line tension λ_{el} which, in its simplest form, can be described by a linear constitutive relation

$$\lambda_{\text{el}} = EA \left(\frac{ds - d\hat{s}}{d\hat{s}} \right) = EA(\nu - 1), \quad (2.70)$$

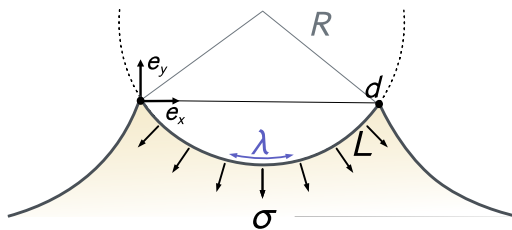


Figure 2.7: Interplay between surface and line tension for a free spanning fiber between two adhesion points. The surface tension σ pulls the fiber inwards. The tangentially acting line tension λ counteracts the inward pull until equilibrium is reached. For an isotropic surface tension the contour is described by a Laplace law relating the radius of curvature directly to surface and line tension.

where EA is the product of the cross-sectional area A and Young's modulus E of the fiber. Very generally, expressing the tangent vector in terms of the turning angle $\mathbf{T} = (\partial_s x)\mathbf{e}_x + (\partial_s y)\mathbf{e}_y = \cos\theta\mathbf{e}_x + \sin\theta\mathbf{e}_y$ (Fig. 2.6B) the shape of the curve is determined by

$$\mathbf{x}(s) = \mathbf{x}(0) + \int_0^s [\cos\theta(\zeta)\mathbf{e}_x + \sin\theta(\zeta)\mathbf{e}_y] d\zeta. \quad (2.71)$$

Considering Eq. (2.60), curvature $\kappa(s)$ and turning angle $\theta(s)$ are related by $\partial_s\theta(s) = \kappa(s)$ such that $\theta(s) = \theta(0) + \frac{\sigma}{\lambda}s$ for constant λ and σ and thus, the second term in Eq. (2.71) yields

$$x(s) = \frac{\lambda}{\sigma} \sin\left(\theta(0) + \frac{\sigma}{\lambda}s\right) + C_x, \quad (2.72)$$

$$y(s) = -\frac{\lambda}{\sigma} \cos\left(\theta(0) + \frac{\sigma}{\lambda}s\right) + C_y. \quad (2.73)$$

The four unknowns $C_x, C_y, \theta(0), \lambda$ are yet to be determined by the boundary conditions which are dictated by the adhesion geometry. According to our specific choice of the coordinate system as shown in Fig. 2.7 these boundary conditions can be expressed as

$$x(0) = 0, \quad y(0) = 0, \quad y(L) = 0, \quad x(L) = d, \quad (2.74)$$

where the reference shape corresponds to a straight fiber of length $\hat{L} = d$ connecting the two adhesion sites. The first three boundary conditions yield

$$C_x = -\frac{\lambda}{\sigma} \sin\theta(0), \quad (2.75)$$

$$C_y = \frac{\lambda}{\sigma} \cos\theta(0), \quad (2.76)$$

$$C_y = \frac{\lambda}{\sigma} \cos\left(\theta(0) + \frac{\sigma}{\lambda}L\right), \quad (2.77)$$

and by demanding equality of Eqs. (2.76) and (2.77), while only considering solutions with $\theta \in [0, 2\pi)$, it follows for the turning angle at the origin

$$\theta(0) = -\frac{\sigma}{2\lambda}L. \quad (2.78)$$

Hence, the equilibrium shape of a cable under isotropic surface tension is given by

$$x(s) = \frac{\lambda}{\sigma} \sin\left(\frac{\sigma}{\lambda}\left(s - \frac{L}{2}\right)\right) + \frac{\lambda}{\sigma} \sin\left(\frac{\sigma L}{2\lambda}\right), \quad (2.79)$$

$$y(s) = -\frac{\lambda}{\sigma} \cos\left(\frac{\sigma}{\lambda}\left(s - \frac{L}{2}\right)\right) + \frac{\lambda}{\sigma} \cos\left(\frac{\sigma L}{2\lambda}\right), \quad (2.80)$$

$$\theta(s) = \frac{\sigma}{\lambda}\left(s - \frac{L}{2}\right). \quad (2.81)$$

The line tension λ , as the remaining unknown, follows from the last boundary condition in Eq. (2.74) and leads to the transcendental equation

$$\frac{1}{2} \frac{\sigma}{\lambda} d = \sin\left(\frac{1}{2} \frac{\sigma}{\lambda} \int_0^d \nu(\lambda, \hat{s}) d\hat{s}\right), \quad (2.82)$$

where we used Eq. (2.57) to write $L = \int_0^d \nu(\lambda, \hat{s}) \, d\hat{s}$. Solving the constitutive relation Eq. (2.70) for the stretch ν leads to $\int_0^d \nu(\lambda, \hat{s}) \, d\hat{s} = \left(1 + \frac{\lambda}{EA}\right) d$ which in turn yields a closed solution for the line tension

$$\lambda(d) = \frac{EA}{d} \left(2R \arcsin\left(\frac{d}{2R}\right) - d \right). \quad (2.83)$$

Eq. (2.83) is the result obtained by *Bischofs et al.* (2009) and implies a dependency of the radius of curvature on the distance between the adhesion points and is known as the tension elasticity model.

2.3. SUMMARY

In this chapter, we have provided the mathematical basis for the continuum-based description of contractile elastic sheets. We have also analytically calculated the radial displacement field of an isotropic contractile disc adhering to a disc and a ring pattern. In this scenario, the absolute displacement field is largest at the cell edge. For a ring-shaped adhesion pattern, the cell stresses remain constant on the non-adhesive parts of the pattern and decrease steeply to zero over the adhesive parts toward the cell periphery. In addition, we introduced the mathematical foundation of contour models and applied it to elastic fibers under isotropic loading conditions to recapitulate the tension elasticity model.

Chapter 3

Implementation

After having introduced the theoretical concepts of continuum and contour models, we dedicate this chapter to the numerical implementation. Section 3.1 introduces the finite element method as a numerical treatment of PDEs. Next, in Section 3.2 we derive the weak form of the equation of mechanical equilibrium for a contractile sheet with elastic foundation and solve it numerically in case of isotropic contraction. This allows us to validate the implementation by comparing it to the analytical solution from Chapter 2. Subsequently, we derive the weak form of the boundary value problem of a freely spanning elastic fiber subject to an external load. Here, we compare the numerical results to two analytical cases, namely the TEM and the elastic catenary.

3.1. THE FINITE ELEMENT METHOD - DIVIDE AND CONQUER

Almost all physical processes are formulated in terms of partial differential equations (PDEs) which, dependent on the complexity of the system, cannot be solved analytically. Therefore, numerical methods in combination with computer software are necessary to obtain numerical solutions. One of these methods is the finite element method (FEM), which has its origin mainly in structural analysis where it is often applied as a tool to solve problems in the car and aerospace industry. Nowadays, it is applied to a whole range of different problems, ranging from electromagnetism to fluid mechanics to bio-mechanics and much more. In addition to very advanced commercial software, many useful open source software packages have been developed to help solve complicated partial differential equations efficiently. Although these software packages are very user-friendly and in most cases do much of the work in the background, a basic understanding of the FEM is still required to efficiently implement complex mathematical systems.

In particular, FEM-simulations follow a typical workflow independent of the specific problem, which is illustrated schematically in Fig. 3.1. At first one has to setup the geometry of the underlying physical problem and specify the boundary conditions (Fig. 3.1A). Next, the simulation domain is divided into smaller finite elements mostly of triangular or quadrilateral shape for which one typically exploits mesh generating algorithms (Fig. 3.1B). Once the weak form of the PDE has been derived it can be discretized on these finite elements such that the initial PDE is converted into an algebraic equation that can be solved by standard numerical methods (Fig. 3.1C1,2). After finding the solution of the algebraic equation, post-processing routines may be utilized to convert the discrete solution into a continuous solution by interpolation

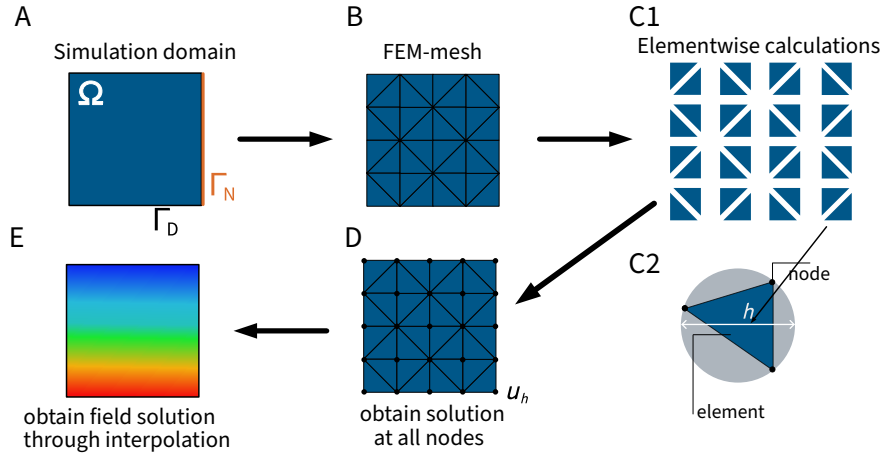


Figure 3.1: Basic FEM workflow. From **A** to **D**: The FEM workflow starts with the definition of the simulation domain and the respective boundary conditions (**A**). Subsequently, the simulation domain is discretized, usually by triangulation (in 2D) (**B**). Once suitable basis functions (polynomials of certain degree) are specified, the weak form can be converted to a linear system of equations for each element (**C1,C2**). These systems are then assembled into a global system of equations which can be solved to obtain the solution at all nodes of the FEM mesh (**D**). Panel **E** shows the post-processing step in which a field solution can be obtained by interpolation in between the nodes using the finite element basis functions.

(Fig. 3.1D,E).

In this section we follow more or less the standard literature (*Langtangen et al.*, 2017; *J. Reddy*, 1993; *Seshu*, 2003; *Zienkiewicz et al.*, 2005) to briefly discuss and summarize the main mathematical concepts of FEM with focus on the construction of the weak form and the discretization.

3.1.1. WEAK FORM AND FUNCTION SPACES

For the sake of simplicity we will use the Poisson equation to demonstrate the FEM-workflow. In our example we are interested in solving

$$-\nabla^2 \varphi = f, \quad \text{in } \Omega \quad (3.1)$$

$$\varphi = 0, \quad \text{on } \Gamma_D \quad (3.2)$$

$$\nabla \varphi \cdot \mathbf{N} = g, \quad \text{on } \Gamma_N, \quad (3.3)$$

where $\Omega \subset \mathbb{R}^2$ is the simulation domain, $\partial\Omega$ denotes the boundary of the domain with outward pointing unit normal vector \mathbf{N} . Further, Γ_D and Γ_N denote the portions of the boundary on which Dirichlet and Neumann boundary conditions are imposed. The solution φ , source term f and boundary data g are scalar valued functions with $\varphi, f : \Omega \rightarrow \mathbb{R}$ and $g : \Omega \rightarrow \mathbb{R}$. Based on the formulation of the PDE we search for a strong solution $\varphi \in C^2(\Omega) \cap C^0(\bar{\Omega})$ which is twice continuously differentiable and continuous on the boundary. The source term further fulfills $f \in C^0(\Omega)$.

In order to solve Eq. (3.1) by means of a finite element simulation one has to re-formulate the PDE as an integral equation, which is also known as the weak formulation of the PDE. This is obtained by multiplication of the PDE by a test function

$w \in \mathcal{V}$ and subsequent integration over the whole simulation domain Ω . Application of appropriate integral theorems further reduces the order of the involved derivatives to a minimum.

Before we derive the weak form, we introduce the so called Hilbert-Sobolev space

$$\mathcal{H}^p := \left\{ \varphi \in L^2(\Omega) \mid \frac{\partial^{|\alpha|} \varphi}{\partial x_1^{\alpha_1} \dots \partial x_p^{\alpha_p}} \in L^2(\Omega) \quad \forall |\alpha| \leq p \right\}, \quad (3.4)$$

which contains all functions whose partial derivatives up to order p are square-integrable. This is the natural choice for test and trial functions such that the existence of the integrals in the weak form is ensured. The space of test functions is defined as

$$\mathcal{V} := \{w \in \mathcal{H}^1(\Omega) \mid w = 0 \text{ on } \Gamma_D\} \equiv \mathcal{H}_0^1, \quad (3.5)$$

and functions $w \in \mathcal{V}$ vanish on the Dirichlet part Γ_D of $\partial\Omega$. The trial function space \mathcal{S} is a translation of the test function space \mathcal{V} in the sense, that it contains functions in \mathcal{H}^1 which fulfill the Dirichlet boundary condition $\varphi = \varphi_D$ on Γ_D

$$\mathcal{S} := \{\varphi \in \mathcal{H}^1(\Omega) \mid \varphi = \varphi_D \text{ on } \Gamma_D\}. \quad (3.6)$$

Following the recipe discussed above, the integral form of Eq. (3.1) is given by

$$-\int_{\Omega} w \nabla^2 \varphi \, dx = \int_{\Omega} w f \, dx. \quad (3.7)$$

At this stage, it is clear that the integral form of Eq. (3.1) "weakens" the regularity requirements of the solution φ and second derivatives do not have to be in $C^2(\Omega)$ anymore since square-integrability is sufficient. Integration by parts further yields

$$-\int_{\Gamma} w (\nabla \varphi \cdot \mathbf{N}) \, ds + \int_{\Omega} \nabla w \cdot \nabla \varphi \, dx = \int_{\Omega} w f \, dx, \quad (3.8)$$

such that the solution only has to fulfill $\varphi \in \mathcal{H}^1(\Omega)$. Because $w = 0$ on Γ_D we can write the final weak form of Eq. (3.1) as

$$\int_{\Omega} \nabla w \cdot \nabla \varphi \, dx = \int_{\Omega} w f \, dx + \int_{\Gamma_N} w g \, ds. \quad (3.9)$$

A solution φ of the strong form is by construction a solution of the weak form. The existence and uniqueness of a solution to the weak form can be shown by utilizing the *Lax-Milgram lemma* (Donea et al., 2003).

3.1.2. DISCRETIZATION

The weak form as stated in Eq. (3.9) can now be discretized. The main idea is to find an approximate solution in finite-dimensional subspaces of \mathcal{V} and \mathcal{S} . In these

subspaces one may define approximate solution and test functions as

$$\varphi_h = \sum_{i=0}^N \alpha_i \psi_i, \quad (3.10)$$

$$w_h = \sum_{i=0}^N \beta_i \psi_i, \quad (3.11)$$

with coefficients α_i, β_i , basis functions ψ_i and dimension of the subspace N . Note that choosing the same basis functions for the solution and the test functions is referred to as the Galerkin method (Bubnov-Galerkin) and is the most prominent approach (Ahmed *et al.*, 2020). In many cases this choice leads to symmetric matrices. Inserting the approximate functions into Eq. (3.9) and setting $g = 0$ for simplicity, we find

$$\sum_{i=0}^N \beta_i \left(\sum_{j=0}^N \int_{\Omega} \nabla \psi_i \cdot \nabla \psi_j \alpha_j dx - \int_{\Omega} \psi_i f dx \right) = \sum_{i=0}^N \beta_i \left(\sum_{j=0}^N K_{ij} \alpha_j - F_i \right) = 0, \quad (3.12)$$

in which $K_{ij} = \int_{\Omega} \nabla \psi_i \cdot \nabla \psi_j dx$ is the so called stiffness matrix and $F_i = \int_{\Omega} \psi_i f dx$ the load vector. Since the coefficients β_i are arbitrary, finding a solution to the weak form is now reduced to solving

$$\sum_{j=0}^N K_{ij} \alpha_j - F_i = 0. \quad (3.13)$$

In practice, the partition of the original domain into finite elements Ω_e is typically achieved by a triangulation $\mathcal{T}(\Omega)$ i.e. by creating a finite element mesh which is a set of elements and nodal points (vertices) and a characteristic mesh size defined as $h = \text{diam}(\Omega_e)$. The (discrete) finite-dimensional function spaces (interpolation spaces) are defined through

$$\mathcal{V}_h := \left\{ w \in \mathcal{H}^1(\Omega) \mid w|_{\Omega_e} \in \mathcal{P}_m(\Omega_e) \forall e \text{ and } w = 0 \text{ on } \Gamma_D \right\}, \quad (3.14)$$

$$\mathcal{S}_h := \left\{ \varphi \in \mathcal{H}^1(\Omega) \mid \varphi|_{\Omega_e} \in \mathcal{P}_m(\Omega_e) \forall e \text{ and } \varphi = \varphi_D \text{ on } \Gamma_D \right\}, \quad (3.15)$$

where \mathcal{P}_m defines the finite element interpolation space which denotes a set of polynomials of total degree $\leq m$. Any function belonging to \mathcal{V}_h or \mathcal{S}_h is a piecewise-polynomial function defined on the domain Ω . The notation $\varphi|_{\Omega_e}$ highlights the piecewise nature of the solution and emphasizes that the function is interpolated over each element Ω_e by a polynomial of degree m . Although, FEM is not limited to piecewise-linear basis functions, one often chooses Lagrange polynomials as finite element basis functions in the context of the continuous Galerkin method. In one dimension they are defined by

$$\psi_i = \begin{cases} 0, & \text{if } x < x_{i-1} \\ \frac{x-x_{i-1}}{x_i-x_{i-1}}, & \text{if } x_{i-1} \leq x \leq x_i \\ \frac{x_{i+1}-x}{x_{i+1}-x_i}, & \text{if } x_i < x \leq x_{i+1} \\ 0, & \text{if } x > x_{i+1}, \end{cases} \quad (3.16)$$

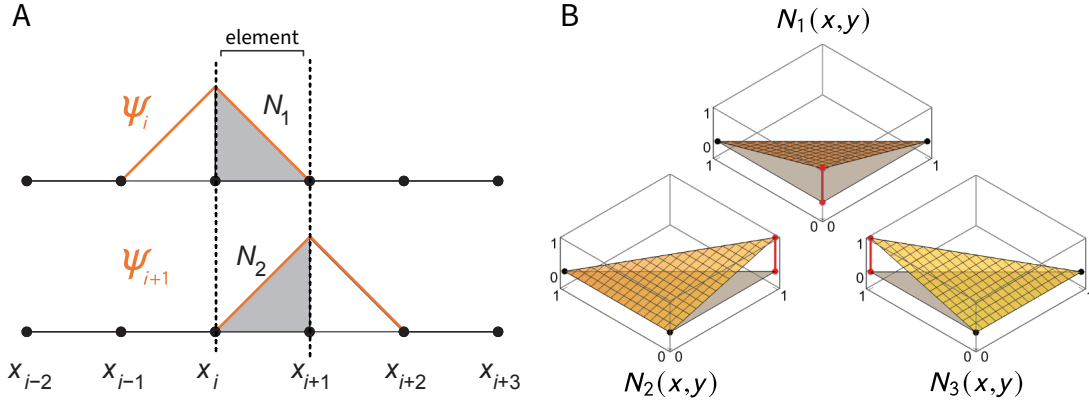


Figure 3.2: Linear Lagrange polynomials as FEM basis functions in one and two dimensions. Panel **A** depicts the Lagrange polynomials on a one dimensional discretized space. Two consecutive hat-functions form the shape functions N_1, N_2 which are the same for each element. Panel **B** shows the two dimensional version of the Lagrange polynomials. Each shape function attains the value 1 at a specific node and is 0 at all other nodes of the element. In between the nodes the linear combination of the shape functions linearly interpolates the FEM solution. Figures: A inspired by (Zienkiewicz et al., 2005); B adapted from (Theisen, 2019).

and illustrated in Fig. 3.2A. For completeness, Fig. 3.2B shows a generalization to two dimensions.

As the basis functions are only defined for each element, the integrals appearing in the stiffness matrix K_{ij} and the load vector F_i can now be evaluated individually over each element

$$\int_{\Omega} (\cdot) dx \equiv \sum_e \int_{\Omega_e} (\cdot) dx . \quad (3.17)$$

Hence, this choice of basis functions finally allows to express the solution and test function for each element in terms of known shape functions $N_n(x)$ which purely depend on the shape of the element

$$\varphi_e = \sum_n N_n(x) \varphi_{e,n} , \quad (3.18)$$

$$w_e = \sum_n N_n(x) w_{e,n} , \quad (3.19)$$

where n denotes the number of nodes of a single element and $\varphi_{e,n}$ the value of φ_e at node n . Since the shape functions are known, the integrals in K_{ij} and F_i can be carried out and the result is a system of linear equations in the unknown nodal values $\varphi_{e,n}$. The contribution from all the elements can be assembled into a global linear system of equations

$$[\mathbf{K}] \{\varphi\} = \{\mathbf{F}\} , \quad (3.20)$$

with global stiffness matrix \mathbf{K} and global load vector \mathbf{F} . Here, $[\cdot]$ and $\{\cdot\}$ indicate that this vector-matrix product is the fully assembled system consisting of the contributions of all finite elements. At this point, we want to note that over the course of this thesis all finite element simulations were carried out using the open source FE software FEniCS (Alnæs et al., 2015) together with the programming languages Python 2 (Van Rossum et al., 1995) and Python 3 (Van Rossum et al., 2009). For solving a PDE in FEniCS, it is sufficient to provide the continuous version of the weak form and

the boundary conditions together with a suitable choice for the interpolation space. The discretization is then performed in the backend of the solver. In the following chapters, whenever we derive the weak form of our PDE, we omit the specification of the function spaces. For all PDEs considered in this thesis well-posedness of the problems can be found in the respective literature.

3.1.3. ERROR ESTIMATE AND CONVERGENCE RATES

Under the assumptions of the Lax-Milgram lemma, Cea's lemma (*Quarteroni et al., 2008*) can be used to prove that the error of an FEM approximation is bounded and thus the approximation converges to the exact solution of the weak form as the mesh size h decreases. From a practical point of view, error estimates and convergence rates can be used to verify the finite element implementation, if an exact solution to the problem is known. It can be shown, that the L^2 -error

$$e_{L^2} := \|\varphi - \varphi_h\|_{L^2} \leq ch^r \quad (3.21)$$

is bounded by the mesh size to the power r . The convergence rate r of the method for the L^2 -norm is typically expected to be $r = m + 1$ for a polynomial degree m of the finite element basis functions. By varying the mesh size h and polynomial degree m the convergence rate can be empirically verified.

3.2. SIMULATING THE ISOTROPICALLY CONTRACTION DISC

All two-dimensional finite element simulations presented in this thesis are based on the force balance equation for an adhesive cell layer. The problem we want to solve numerically reads: Find the displacement vector $\mathbf{u}(\mathbf{x})$ such that

$$\nabla \cdot \boldsymbol{\sigma} = Y \mathbf{u}, \quad \text{in } \Omega \quad (3.22)$$

$$\boldsymbol{\sigma} = 0, \quad \text{on } \Gamma = \partial\Omega, \quad (3.23)$$

where the stress-strain relationship follows that of a linear elastic material in the plane stress approximation

$$\boldsymbol{\sigma}(\mathbf{x}) = \lambda \operatorname{tr}(\boldsymbol{\varepsilon}) \mathbf{I} + 2\mu \boldsymbol{\varepsilon} + \boldsymbol{\sigma}_a(\mathbf{x}), \quad (3.24)$$

with two-dimensional Lamé parameters (Eq. (2.27)) and linearized strain tensor $\boldsymbol{\varepsilon}(\mathbf{x})$. The deformation of the cell layer is achieved by introduction of an active contractile stress $\boldsymbol{\sigma}_a$ which in general can depend on space and time and resembles the forces generated by myosin II motors. A first simulation is carried out on a circular shaped pattern with an isotropic active stress tensor $\boldsymbol{\sigma}_a = \sigma_a \mathbf{I}$. In this way, the simulation results can be directly compared to the analytical solution of an isotropic contractile disc of initial radius r_0 which we derived in the previous chapter, given by

$$u_r(r) = -l_p \frac{\sigma_a}{2\mu + \lambda} \frac{I_1\left(\frac{r}{l_p}\right)}{I_0\left(\frac{r_0}{l_p}\right) - \frac{2\mu}{2\mu + \lambda} \frac{l_p}{r_0} I_1\left(\frac{r_0}{l_p}\right)}, \quad (3.25)$$

together with the force-localization length

$$l_p = \sqrt{\frac{2\mu + \lambda}{Y}} = \sqrt{\frac{h_c E_c}{Y(1 - \nu_c^2)}}. \quad (3.26)$$

To derive the weak formulation of Eq. (3.22) we multiply with a vector valued test function $\mathbf{v} \in \mathcal{V}(\Omega)$ and integrate over the domain Ω of the un-contracted disc

$$\int_{\Omega} (\nabla \cdot \boldsymbol{\sigma}) \cdot \mathbf{v} \, dx = \int_{\Omega} Y(\mathbf{x}) \mathbf{u}(\mathbf{x}) \cdot \mathbf{v} \, dx. \quad (3.27)$$

The left hand side can be integrated using integration by parts i.e. using the following identity

$$\nabla \cdot (\boldsymbol{\sigma}^T \cdot \mathbf{v}) = (\nabla \cdot \boldsymbol{\sigma}) \cdot \mathbf{v} + \boldsymbol{\sigma} : \nabla \mathbf{v}. \quad (3.28)$$

This allows to simplify Eq. (3.27) to

$$\int_{\Omega} \boldsymbol{\sigma} : \nabla \mathbf{v} \, dx - \int_{\Gamma} (\boldsymbol{\sigma} \cdot \mathbf{N}) \cdot \mathbf{v} \, ds + \int_{\Omega} Y \mathbf{u} \cdot \mathbf{v} \, dx = 0. \quad (3.29)$$

Here, $\boldsymbol{\sigma} \cdot \mathbf{N}$ is the traction vector at the boundary $\Gamma = \partial\Omega$ which is set to zero in case of stress free boundaries. We further use that $\boldsymbol{\sigma}$ is symmetric and thus, the double contraction with the antisymmetric part $\mathbf{a}(\mathbf{v}) = \frac{1}{2}(\nabla \mathbf{v} - \nabla \mathbf{v}^T)$ of $\nabla \mathbf{v}$ is zero i.e. $\boldsymbol{\sigma} : \mathbf{a}(\mathbf{v}) = 0$. This allows us to replace $\nabla \mathbf{v}$ by its symmetric part $\mathbf{s}(\mathbf{v}) = \frac{1}{2}(\nabla \mathbf{v} + \nabla \mathbf{v}^T)$ and leads to the final weak form statement

$$\int_{\Omega} \boldsymbol{\sigma} : \mathbf{s}(\mathbf{v}) \, dx + \int_{\Omega} Y \mathbf{u} \cdot \mathbf{v} \, dx = 0. \quad (3.30)$$

The trial simulations were carried out with a disc radius $r_0 = 17.8 \mu\text{m}$ which corresponds to a cell area of $1000 \mu\text{m}^2$. The mesh size was varied from a minimal value of $h = 0.5 \mu\text{m}$ to a maximum mesh size of $h = 20 \mu\text{m}$ which was the upper limit for the triangulation of our cell domain. Further, we simulated each mesh size for different Lagrangian finite elements $\mathcal{P}_1, \mathcal{P}_2$ and \mathcal{P}_3 , ranging from linear to cubic polynomials. To calculate the error between the analytical solution \mathbf{u}_a and the approximated solution \mathbf{u}_h one has to interpolate the analytical solution into a finite element function space. In detail, we followed the procedure explained in (*Langtangen et al., 2017*) and interpolated both the analytical solution and the numerical solution into a higher order function space, typically of polynomial order $m' = m + 3$ in order to obtain a reliable error estimate. The final error is then calculated by

$$e_{L^2} = \|u'_a - u'_h\|_{L^2} = \sqrt{\int_{\Omega} |u'_a - u'_h|^2 \, dx}. \quad (3.31)$$

The convergence rate r can be obtained by exploiting Eq. (3.21) and assuming $e_{L^2,i} = ch_i^r$ such that for consecutive mesh sizes $h_i > h_{i+1}$, r is given by

$$r = \frac{\log(e_{L^2,i+1}/e_{L^2,i})}{\log(h_{i+1}/h_i)}. \quad (3.32)$$

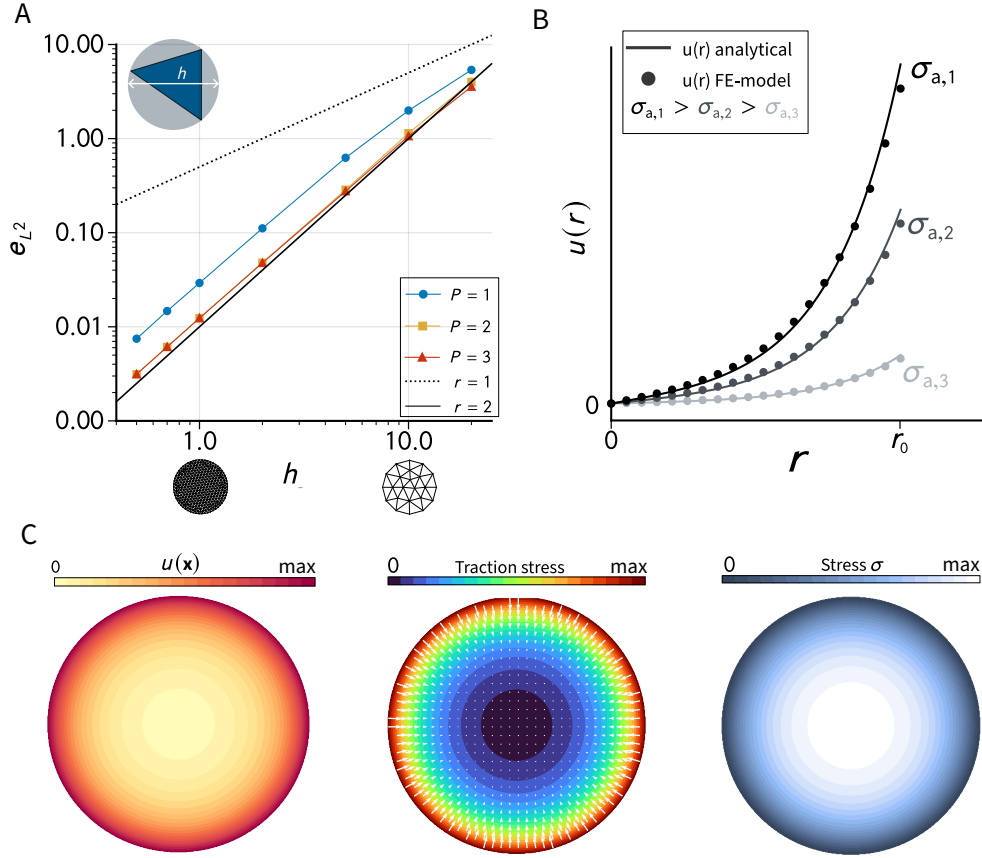


Figure 3.3: Simulation results for the isotropic contractile disc with elastic foundation. Panel **A** shows a log-log-plot of the L^2 -error as a function of the mesh size for linear (\mathcal{P}_1), quadratic (\mathcal{P}_2) and cubic (\mathcal{P}_3) polynomials. The dashed lines indicate the convergence rates $r = 1$ and $r = 2$. For all polynomial degrees the error converges to zero for decreasing mesh size. However, the optimal convergence rate for the respective polynomial is not obtained due to the fact that the circular domain cannot be fully represented by a polygonal mesh. Panel **B** shows the radial displacement field for three different active contractile stresses. Dots represent simulation results and solid lines depict the analytical counterpart. Simulation parameters are $\sigma_{a,1} = 7$ kPa, $\sigma_{a,2} = 4$ kPa and $\sigma_{a,3} = 1$ kPa. Panel **C** shows the numerically obtained displacement field, traction stresses and internal cell stresses (Frobenius norm). Maximal color bar values correspond to $u_{\max} = 1.2 \mu\text{m}$ (displacement), $t_{\max} = 1.0$ kPa (traction) and $\sigma_{\max} = 5.4$ kPa (Frobenius norm of the stress tensor). Active stress is set to $\sigma_a = 4$ kPa. All other cell parameters are fixed according to Table A.1.

The result of our error analysis is shown in Fig. 3.3A. For all simulated polynomial degrees the numerical solution improves with decreasing mesh size. However, the convergence rate does not improve with increasing polynomial degree as one would expect. The reason for this is that our exact simulation domain Ω is a circle and hence not polyhedral. In other words, since Ω has a curved boundary, a piece-wise linear mesh cannot exactly represent the underlying geometry of Ω and thus Cea’s lemma fails. In FEM theory this problem is known as “committing a variational crime” and for further information on this topic we refer the reader to the work of *Brenner et al.* (2008), *Holst et al.* (2012), and *Strang* (1973)¹. Fig. 3.3B shows the radial component of the displacement field as a function of the radial position for different

¹In case of a circular domain, this problem can be solved by introduction of curved elements which exactly represent the boundary of Ω .

active stresses. Our finite element simulation approximates the analytical solution well. Additionally, together with our FEM implementation we established a post-processing routine for the typical output data of our interest. The typical simulation output is the deformation field from which the traction field and the total internal cell stresses can be deduced (Fig. 3.3C).

3.3. CONTOUR SIMULATIONS WITH FEM

FEM contour simulations follow the same procedure as described in Section 3.1. However, the elastic fiber is a one dimensional object embedded in a two-dimensional space. Therefore, we exploit a mixed variational approach that allows us to approximate two variables simultaneously².

The starting point of the finite element implementation of the contour model is the static force balance equation as a function of the reference arc length

$$\partial_{\hat{s}} \mathbf{F} + \mathbf{f} = 0, \quad (3.33)$$

where, analog to Section 2.2, \mathbf{F} denotes the contact forces within the material (line tension) and \mathbf{f} is the load acting on the fiber (surface tension). The simulation domain is defined by the arc length parameter of the undeformed fiber configuration $\hat{s} \in [0, \hat{L}] \subset \mathbb{R}$. Using $\mathbf{F}(\hat{s}) = \lambda(\hat{s})\mathbf{T}(\hat{s})$ and assuming a very general load in terms a surface tension tensor $\boldsymbol{\Sigma}$ and normal vector \mathbf{N} as $\mathbf{f} = \boldsymbol{\Sigma}(\hat{s})\nu(\hat{s})\mathbf{N}(\hat{s})$ yields

$$\frac{d}{d\hat{s}} \left(\lambda(\hat{s}) \frac{1}{\nu(\hat{s})} \frac{d\mathbf{x}}{d\hat{s}} \right) + \boldsymbol{\Sigma}(\hat{s}) \left(\frac{d\mathbf{x}}{d\hat{s}} \right)_{\perp} = 0, \quad (3.34)$$

where we used that $\mathbf{T}(\hat{s}) = \nu(\hat{s})^{-1} (d\mathbf{x}/d\hat{s})$ and $\mathbf{N}(\hat{s}) = \nu(\hat{s})^{-1} (d\mathbf{x}/d\hat{s})_{\perp}$. The normal vector is constructed by multiplication with a matrix \mathbf{M} for a counter-clockwise rotation by 90° such that $(d\mathbf{x}/d\hat{s})_{\perp} = \mathbf{M}(d\mathbf{x}/d\hat{s})$. Let $\mathbf{w} = (w_1, w_2) \in \mathcal{W}^h([0, \hat{L}]) = \mathcal{V}^h \times \mathcal{V}^h$ be the test function vector in the mixed function space \mathcal{W}^h defined over the interval $[0, \hat{L}]$. Multiplying Eq. (3.34) with the test function \mathbf{w} and integration over the simulation domain yields

$$- \int_0^{\hat{L}} \frac{\lambda(\hat{s})}{\nu(\hat{s})} \frac{dx_i}{d\hat{s}} \frac{dw_i}{d\hat{s}} d\hat{s} + \int_0^{\hat{L}} \frac{1}{\nu(\hat{s})} \Sigma_{ij} M_{jl} \frac{dx_l}{d\hat{s}} w_i d\hat{s} = 0, \quad (3.35)$$

for indices $i = 1, 2$ and where we used integration by parts to reduce the order of appearing derivatives

$$\int_0^{\hat{L}} \frac{d}{d\hat{s}} (\cdot) w_i d\hat{s} = (\cdot) w_i \Big|_0^{\hat{L}} - \int_0^{\hat{L}} (\cdot) \frac{dw_i}{d\hat{s}} d\hat{s}. \quad (3.36)$$

The boundary terms vanish, since by construction, the test functions equate to zero

²A standard example for this approach is the stokes problem to obtain velocity and pressure field simultaneously.

on the boundary. The finite element solution can be validated by a direct comparison to analytical solutions. We decided to test the case of isotropic surface tension and a directed load as in the case of the TEM and the elastic catenary, respectively. For the latter case, the load acting on the contour is always perpendicular to the unstretched configuration which is realized in simulations by setting the load vector \mathbf{f} in Eq. (3.33) to

$$\mathbf{f} = -f_y \mathbf{e}_y = \text{const.}, \quad (3.37)$$

where f_y is a constant force per unit reference length. The analytically obtained shape of the elastic catenary is shifted to Appendix A.5. Further, at the endpoints of the fiber we imposed Dirichlet boundary conditions to fix the position of the focal adhesions.

Fig. 3.4 shows the comparison of the numerical (circles and squares) and the analytical solution (solid lines) for increasing loading strength. For both simulated scenarios we find perfect agreement between the simulated and analytical solutions. The solution for the TEM is, according to Eqs. (2.79) to (2.80), described by a circular shape while the elastic catenary takes on a shape in between the ordinary catenary and a parabola (Fig. 3.4A,B and Eqs. (A.47) and (A.48)). The tangent angle $\theta(\hat{s}) = \arctan(\partial_{\hat{s}}y/\partial_{\hat{s}}x)$ additionally illustrates the difference of the two computed shapes with a linear and non-linear variation along the unstretched fiber (Fig. 3.4C). Further, we numerically obtained the line tension by computing $\lambda(\hat{s}) = EA \left(\sqrt{(\partial_{\hat{s}}x)^2 + (\partial_{\hat{s}}y)^2} - 1 \right)$. Fig. 3.4D shows the numerical solution for TEM and elastic catenary represented by circles and squares, respectively. The analytical counterpart was obtained by evaluating Eq. (2.83) for the TEM and Eqs. (A.49) and (A.50) for the elastic catenary. Again, the numerical and analytical solutions perfectly agree (Fig. 3.4D).

3.4. CONCLUDING REMARKS

In this chapter we discussed the most important aspects of finite element simulations. We further demonstrated that our FEM implementation for the two-dimensional contractile cell layer with elastic foundation and the contour model reproduce the analytical solutions.

While FEM approaches are widely used to model adherent cells as thin elastic sheets, contour models have been regarded as a tool to predict and analyze cell shapes and traction forces based on very few assumptions. However, the numerical treatment of contour models is a very promising approach which enables to increase the level of complexity and may aid in predicting cell shapes also beyond the very restrictive assumptions of an isotropic surface tension and a linear elastic fiber. For example in Chapter 5 we exploit this numerical framework to compute cell shapes under spatially dependent loading profiles for which analytical solutions do either not exist or are very difficult to obtain. Besides the position dependent loading profiles, it is also possible to account for defects in the fiber. This could be incorporated by a position dependent elastic modulus of the fiber for example representing fluctuations in actin or myosin

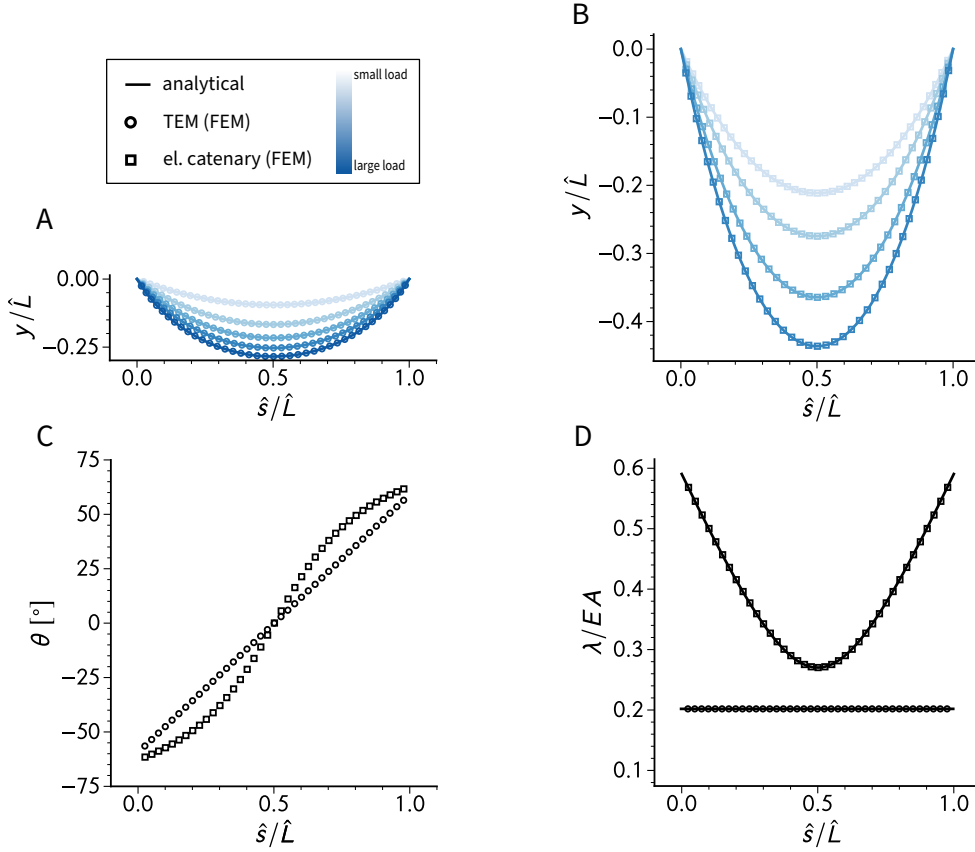
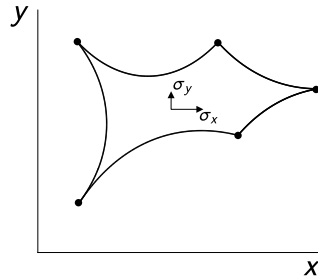


Figure 3.4: Sanity check for contour simulations with FEM. In all simulations the spanning distance between the adhesion points corresponds to $\hat{L} = 35 \mu\text{m}$. The one-dimensional mesh contains 401 nodes, of which only every tenth is shown. Further, the one-dimensional elastic modulus was set to $EA = 200 \text{ nN}$. Those parameters correspond to the typical order of magnitude measured for adherent cells. Circles and squares correspond to simulation data and solid lines depict the corresponding analytical solution. Darker blues correspond to larger loading forces. Panel **A** shows the contour shape of a linear elastic fiber subject to an isotropic load. The strength of the isotropic loads corresponds to $0.1 \text{ nN } \mu\text{m}^{-1}$, $0.5 \text{ nN } \mu\text{m}^{-1}$, $1 \text{ nN } \mu\text{m}^{-1}$, $1.5 \text{ nN } \mu\text{m}^{-1}$ and $2 \text{ nN } \mu\text{m}^{-1}$ (from light blue to dark blue). Panel **B** shows the contour shape of the elastic catenary. The strength of the isotropic loads corresponds to $1 \text{ nN } \mu\text{m}^{-1}$, $2 \text{ nN } \mu\text{m}^{-1}$, $4 \text{ nN } \mu\text{m}^{-1}$ and $6 \text{ nN } \mu\text{m}^{-1}$ (from light blue to dark blue). Panel **C** illustrates that the turning angle of the tangent vector θ varies linearly along the arc in the case of an isotropic load showing that the contour attains a circular shape. This does not hold true for a directional load in the case of the elastic catenary. Panel **D** compares the line tension along the fiber as a function of the reference arc length parameter \hat{s} . As expected, the line tension is constant in the case of an isotropic load and varies along the contour in the elastic catenary.

density along the fiber³. Moreover, in future works, one may step away from a purely static description of the cells contour and turn to dynamic simulations by making the force balance equation time dependent. Then, the dynamic version of Eq. (2.62) would read $\partial_{\hat{s}}\mathbf{F} + \mathbf{f} = \mathbf{f}_{\text{ext}}$. The standard choice would be $\mathbf{f}_{\text{ext}}(\hat{s}, t) = \rho A \partial_{tt}\mathbf{x}(\hat{s}, t)$ where ρA is the mass per unit reference length. For biological applications inertia is usually negligible and thus in the over-damped limit one would choose an external force $\mathbf{f}_{\text{ext}}(\hat{s}, t) \propto \partial_t\mathbf{x}(\hat{s}, t)$ which resembles a velocity dependent friction force. An example for this dynamic approach can be found in the publication by *Schakenraad et al.* (2020) where the authors couple the contour model to the nematic order parameter of a liquid crystal to simulate the interaction of the actin cytoskeleton and the peripheral stress fiber.

As a tool, the numerical approach to contour models can be exploited to directly fit cell shapes to actin images by simply segmenting the position of the focal adhesions. Fig. 3.5 exemplarily shows a full cell contour simulated with the FEM contour model approach. Here each arc experiences a different surface tension depending on its orientation. With this method one could gain insight into the local anisotropy of the actin cortex in the vicinity of the cell periphery. In conclusion, a finite element treatment of contour models opens up a variety of new applications that go beyond the examples presented in this thesis. The CPU time for FEM contour simulations is in the order of seconds while for example network models, dependent on the mesh size, have a CPU time in the order of minutes to several hours. Therefore, the simplicity of the force balance equation and the one dimensional FEM setup render it a numerically cheap alternative to network models.

Figure 3.5: A whole cell contour simulated with the numerical contour model FEM. An anisotropic surface tension tensor acts differently on each arc, depending on its specific orientation. Here the cell adheres to a rigid substrate but elastic substrates can be treated as well by balancing the combined pull of the arcs in the deformed substrate.



³An example can be found in the work by *Lepidi et al.* (2007) where the authors exploit this idea to study the influence of damages in cable-stayed structures.

Chapter 4

Optogenetic control of single cells

The two main factors influencing cellular contractility are the underlying biochemistry of actomyosin contractility and the organization of the highly dynamic actin cytoskeleton. Their interplay enables the cell to change its shape and mechanically sense the physical properties of its environment. In this study, we especially focus on the main output of the contractile actin cytoskeleton, which is the force cells apply to the physical environment. The results presented in this chapter were obtained in collaboration with Tomas Andersen and Martial Balland from the Université Grenoble Alpes, who performed the optogenetic experiments and the traction force analysis and Dimitri Probst from the Group of Ulrich Schwarz, who contributed to the design of the finite element simulations. The results are documented in detail in the preprint “*Cell size and actin architecture determine force generation in optogenetically activated adherent cells*” (Andersen *et al.*, 2022).

4.1. INTRODUCTION

As already known from the work of Balaban *et al.* (2001), Butler *et al.* (2002), and Dembo *et al.* (1999), the traction forces generated by the cells are of the order of \sim kPa and thus, correspond to the elastic stiffness of the ECM (Discher *et al.*, 2017; Schwarz *et al.*, 2013). However, in a physiological context, cells are permanently subject to external mechanical perturbations. For instance, on a tissue-level, cells respond to external mechanical perturbations by effectively working towards a setpoint stress, a concept which is known as tensional homeostasis (Boudou *et al.*, 2019; Brown *et al.*, 1998). In recent years, several studies showed that this concept even translates to the level of single cells which suggests that cells use regulatory mechanisms to control their tensional state (Hippler *et al.*, 2020; Webster *et al.*, 2014; Weng *et al.*, 2016). Homeostatic processes are essential for the morphology and function of organs and tissues, and an imbalance of these processes is closely related to various types of diseases. For example, recent studies have linked the dysregulation of RhoA activity, an important element of the force generating actomyosin contractility, to the progression of cancer (Gulhati *et al.*, 2011; Paszek *et al.*, 2005). In this context, it is still unclear to what extent the RhoA system itself produces homeostasis, on which time scales this response operates and how this is related to physical processes such as force generation.

To address these relevant questions, we used non-neuronal optogenetics in combination with traction force microscopy on soft elastic substrates which allows us to directly quantify the input-output relation between activation of the small GTPase RhoA and force generation in the context of varying cell size and differing acting organization. The experimental measurements are complemented by a mathematical model based on the results of Chapters 2 and 3. This model enables us to decouple biochemistry and mechanics and gain insight to the dynamic evolution of the internal cellular stresses and the strain energy invested by the cells during and after optogenetic perturbation.

In Section 4.2 we briefly explain the experimental setup. Further, in Section 4.3 we make use of the basic experimental observation to constrain a mechanical model in the spirit of the work by *Banerjee et al.* (2013) and *Edwards et al.* (2011). However, we extend this modeling approach by considering viscoelastic material properties and by incorporating the anisotropy of the actin CSK. Additionally, we introduce optogenetic stimulation by a time-dependent active stress. By this, in Section 4.4, we are able to apply our versatile model to different experimental data. Our results reveal tensional homeostasis of the RhoA-system with a varying setpoint dependent on cell size and actin architecture, both of which are determined by the adhesive environment. Further, we test the limits of the CRY2/CIBN-system by increasing the duration of photoactivation pulses, which revealed saturation of the cellular stress response above a certain activation duration.

4.2. EXPERIMENTAL SETUP

All experiments in this chapter have been performed on stable cell line NIH 3T3 fibroblasts with a CIBN-GFP-CAAX and optoGEF-RhoA construct. Cell shape and internal actin organization was controlled by the shape and size of the micropatterns deposited over polyacrylamide hydrogels with a Young's modulus of $E_s = 4.47$ kPa. Prior to photoactivation, the cells were allowed to completely spread on the micropattern and adopt a stable contractile baseline level. Fig. 4.1 depicts the cells in a state of mature adhesion. Cells on the disc pattern (Fig. 4.1A) spontaneously polarized and developed approximately parallel neighboring stress fibers. In marked contrast, the hazard pattern with its three T-shaped branches induces three domains with each containing a family of parallel stress fibers (Fig. 4.1B).

Next, the cells were globally illuminated with light pulses of 460 nm wavelength and duration of 10 ms – 200 ms, depending on the experiment. This light pulse recruits ArhGEF11 to the cell membrane, where it phosphorylates RhoA-GDP, thereby activating it. The increase in active RhoA concentration subsequently leads to enhanced myosin activity through the typical RhoA signaling pathways (Section 1.1.1 and Fig. 1.4). After photoactivation cells return to baseline. Given enough time between light pulses, several activation episodes could be carried out on the same cell without altering the baseline level. Additional experimental details can be found in the thesis of Tomas Andersen (*Tomas Andersen*, 2018) and the preprint (*Andersen et al.*, 2022).

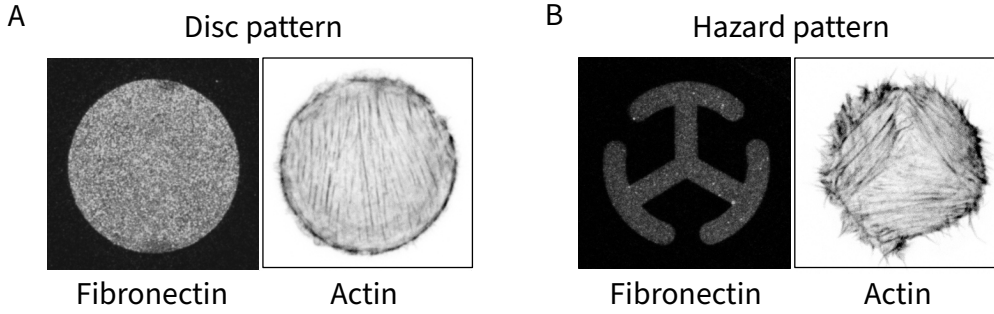


Figure 4.1: Stress fiber architecture of cells plated on a fibronectin disc and hazard pattern. Cells on the disc pattern show a polarized actin architecture while cells on the hazard pattern develop three families of stress fibers arranged in a triangular shape.

4.3. MODELLING

Based on the experimental setup, our model has to fulfill certain basic requirements in order to be applicable. It has to represent the geometry and stiffness of the adhesive environment of the cell, the internal actin organization as well as the active mechanical properties of the cytoskeleton, including the effect of photoactivation. To tune our model parameters, we also need a quantity that we have access to in both the model and the experiment. The most suitable quantity is the substrate strain energy which shows a characteristic time course after photoactivation. We made use of the results of the previous chapter, in which we demonstrated the basic finite element implementation of the isotropically contracting disc and validated our implementation by comparing it to the analytically obtained result. Here, we used this analytical solution to calculate the strain energy of a fully adherent isotropic contractile disc and subsequently exploited this result to parametrize our model. Overall, we followed a mixed strategy by fixing a subset of the free parameters from general considerations and literature values while the remaining parameters were determined by fitting the FEM model to the experimental data.

4.3.1. ACTIVE KELVIN-VOIGT MODEL

Instead of a purely elastic model as used in the previous chapter, we decided to use a viscoelastic constitutive relation of the Kelvin-Voigt type to account for the viscous nature of the actin cytoskeleton. A purely viscous and fluid-like viscoelastic model such as the Maxwell model was disregarded, since it cannot maintain a stable stress baseline without a constant rate of deformation as can be seen from the constitutive relation (Eq. (2.31), Fig. 2.3C). However, fluid-like viscoelastic models are typically used in active gel theory (*Prost et al.*, 2015). The constitutive relation of the two-dimensional active Kelvin-Voigt model reads

$$\sigma_{ij}(\mathbf{x}, t) = \left(1 + \tau_c \frac{\partial}{\partial t}\right) (\lambda \varepsilon_{kk}(\mathbf{x}, t) \delta_{ij} + 2\mu \varepsilon_{ij}(\mathbf{x}, t)) + \sigma_{ij}^a(\mathbf{x}, t), \quad (4.1)$$

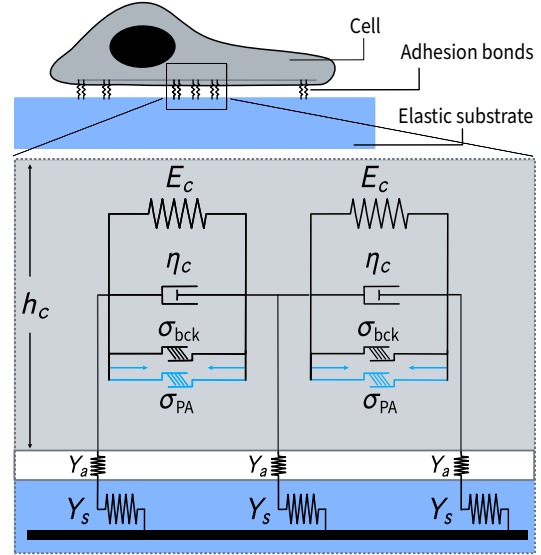


Figure 4.2: Viscoelastic continuum model of an adherent cell. The actin cytoskeleton described by a Kelvin-Voigt model i.e. an active serial connection of spring E_c and dashpot η_c . Active contraction is introduced through a constant background stress σ_{bck} and a time dependent photoactivation stress σ_{PA} . Cellular adhesion is modeled as a serial connection of adhesion bonds and gel elasticity represented by Y_a and Y_s , respectively.

where $\varepsilon_{ij} = (\partial_i u_j + \partial_j u_i)/2$ is the linearized strain tensor and σ_a describes an active contractile stress. σ_a is split into background stress $\sigma_{\text{bck}}(\mathbf{x})$ describing the homeostatic baseline contractility and a time dependent photoactivation stress tensor $\sigma_{\text{PA}}(\mathbf{x}, t)$ accounting for the additional stress generated during and after photoactivation. The information of the elastic properties of the cell, Young's modulus and Poisson's ratio, E_c and ν_s respectively, are contained in the two-dimensional Lamé parameters

$$\lambda = \frac{\nu_c h_c E_c}{1 - \nu_c^2}, \quad \mu = \frac{h_c E_c}{2(1 + \nu_c)}, \quad (4.2)$$

where h_c is the effective thickness of the contractile unit (effective cell height), which is similar to but smaller than the actual cell height. The quantity $\tau_c = \eta_c/E_c$ is the relaxation time scale defined by the ratio of the effective cell viscosity η_c and the Young's modulus of the cell. In case of vanishing viscosity we have $\tau_c = 0$ which corresponds to the purely elastic model.

4.3.2. SUBSTRATE STRAIN ENERGY

The force balance between the contractile cell and the elastic foundation is given by

$$\partial_j \sigma_{ij}(\mathbf{x}, t) = Y(\mathbf{x}, t) u_i(\mathbf{x}, t), \quad (4.3)$$

and allows to predict the substrate strain energy by relating the cellular deformation to the deformation of the substrate. In particular, we split the elastic properties of the foundation into the rigidity of the elastic gel Y_s and the stiffness Y_a of the layer of adhesion molecules which connect the cell to the substrate. This serial connection of elastic elements leads to an overall effective stiffness given by $1/Y = 1/Y_a + 1/Y_s$. The substrate stiffness can be estimated by (*Banerjee et al.*, 2012)

$$Y_s = \frac{\pi E_s}{h_{\text{eff}}}, \quad (4.4)$$

where the effective substrate thickness h_{eff} is a function of substrate thickness h_s , the Poisson's ratio of the substrate and the lateral extent of the cell layer L_c

$$h_{\text{eff}}^{-1} = \frac{1}{2\pi h_s(1 + \nu_s)} + \frac{1}{L_c}. \quad (4.5)$$

The equation for the effective height can be understood as an interpolation between the limits of infinitely thick and thin substrates. In the case of thin substrates $h_s \ll L_c$ the second term in Eq. (4.5) can be neglected and the substrate stiffness is given by the ratio of the shear modulus $\mu_s = E_s/(2(1 + \nu_s))$ and the substrate thickness. In contrast, if $h_s \gg L_c$, as it is the case for infinitely thick substrates, the first term is negligible. As a consequence, the cell experiences an elastic foundation only up to the thickness comparable to its size. The stiffness of the adhesion layer is approximated by

$$Y_a = \frac{k_a}{d^2}, \quad (4.6)$$

where k_a describes the molecular stiffness of the adhesion bonds and d the distance between them. Demanding force balance at the cell-substrate interface $\mathbf{T} = Y\mathbf{u} = Y_s\mathbf{u}_s$, where \mathbf{u}_s denotes the substrate deformation field, the total exerted force F_{tot} and the substrate strain energy E_s may be expressed directly in terms of the cellular deformation field \mathbf{u}

$$F_{\text{tot}} = \int_{\Omega} |\mathbf{T}| \, d\Omega = \int_{\Omega} Y |u_r(r)| \, d\Omega, \quad (4.7)$$

$$E_s = \frac{1}{2} \int_{\Omega} \mathbf{T}\mathbf{u}_s \, d\Omega = \frac{1}{2} \int_{\Omega} \frac{Y^2}{Y_s} \mathbf{u}^2 \, d\Omega. \quad (4.8)$$

In the limiting case of $Y_a \gg Y_s$ the cell effectively only ‘‘feels’’ the softer component and we simply have $dE_s = Y_s\mathbf{u}_s/2 \, d\Omega$. For our academic example, the isotropic contractile disc, analytical solutions of Eqs. (4.7) and (4.8) exist, which is helpful when it comes to estimating force and energy values for given parameter estimates. Since the analytical solution Eq. (2.46) for the displacement field is radially symmetric, we express the integral measure $d\Omega = r \, dr \, d\phi$ in polar coordinates

$$E_s = \frac{Y^2}{2Y_s} \int_0^{2\pi} d\phi \int_0^{r_0} r u_r(r)^2 \, dr, \quad (4.9)$$

where r_0 is the initial disc radius. By simply inserting the solution $u_r(r)$

$$u_r(r) = -l_p \frac{\sigma_a}{2\mu + \lambda} \frac{I_1\left(\frac{r}{l_p}\right)}{I_0\left(\frac{r_0}{l_p}\right) - \frac{2\mu}{2\mu + \lambda} \frac{l_p}{r_0} I_1\left(\frac{r_0}{l_p}\right)}, \quad (4.10)$$

into Eqs. (4.7) and (4.8) we obtain for the force

$$F_{\text{tot}} = \frac{2\pi Y l_p \sigma_a}{\lambda + 2\mu} \frac{\int_0^{r_0} r I_1\left(\frac{r}{l_p}\right) \, dr}{I_0\left(\frac{r_0}{l_p}\right) - (1 - \nu_c) \frac{l_p}{r_0} I_1\left(\frac{r_0}{l_p}\right)} = \frac{2\pi \sigma_a}{l_p} \beta \left(\frac{r_0}{l_p}\right), \quad (4.11)$$

in which we introduced the function

$$\beta(x) = \frac{\pi}{2} x \frac{L_0(x)I_1(x) - L_1(x)I_0(x)}{I_0(x) - (1 - \nu_c)\frac{1}{x}I_1(x)}, \quad (4.12)$$

where L_0 and L_1 denote the modified Struve functions. For more details see Appendix A.5. Similarly we find for the substrate strain energy

$$E_s = \frac{\pi}{Y_s} \cdot \left(\frac{Y l_p \sigma_a (1 - \nu_c^2)}{E_c h_c} \right)^2 \cdot \frac{\int_0^{r_0} dr r I_1\left(\frac{r}{l_p}\right)^2}{\left(I_0\left(\frac{r_0}{l_p}\right) - (1 - \nu_c)\frac{l_p}{r_0} I_1\left(\frac{r_0}{l_p}\right) \right)^2} = \frac{\pi \sigma_a^2}{2Y_s} \zeta\left(\frac{r_0}{l_p}\right), \quad (4.13)$$

where we introduced the function

$$\zeta(x) = x^2 \frac{I_1(x)^2 + \frac{2}{x} I_0(x) I_1(x) - I_0(x)^2}{\left(I_0(x) - (1 - \nu_c)\frac{1}{x} I_1(x) \right)^2}. \quad (4.14)$$

We can determine the two asymptotic limits $r_0 \ll l_p$ and $r_0 \gg l_p$ by investigating the scaling behavior of β and ζ in the limits $x \ll 1$ and $x \gg 1$, respectively. In the limit $x \ll 1$, the nominator of Eq. (4.12) can be approximated as

$$\int_0^x \tilde{x} I_1(\tilde{x}) d\tilde{x} \approx \frac{x^3}{6} + \frac{x^5}{80} + \frac{x^7}{2688} + \mathcal{O}(x^9), \quad (4.15)$$

and generally it holds for the modified Bessel functions of the first kind

$$I_n(x) \xrightarrow{x \ll 1} \frac{1}{n!} \left(\frac{x}{2} \right)^n, \quad (4.16)$$

such that

$$\beta(x) \xrightarrow{x \ll 1} \frac{x^3}{3(1 + \nu_c)} + \mathcal{O}(x^4), \quad (4.17)$$

$$\zeta(x) \xrightarrow{x \ll 1} \frac{x^4}{2(1 + \nu_c)^2} + \mathcal{O}(x^5), \quad (4.18)$$

and finally

$$F_{\text{tot}} \xrightarrow{r_0 \ll l_p} \frac{2\pi l_p \sigma_a}{3(1 + \nu_c)} \left(\frac{r_0}{l_p} \right)^3, \quad (4.19)$$

$$E_s \xrightarrow{r_0 \ll l_p} \frac{\pi (\sigma_a)^2}{4Y_s (1 + \nu_c)^2} \left(\frac{r_0}{l_p} \right)^4. \quad (4.20)$$

For the limit $x \gg 1$ we use the approximations

$$\int_0^x \tilde{x} I_1(\tilde{x}) d\tilde{x} \approx \frac{e^x}{\sqrt{2\pi x}} \left(x - \frac{7}{8} \right), \quad (4.21)$$

and further, that any modified Bessel function of the first kind can be approximated as

$$I_n \approx \frac{\exp x}{\sqrt{2\pi x}} \left[1 - \frac{4n^2 - 1^2}{1(8x)} \left(1 - \frac{4n^2 - 3^2}{2(8x)} \left(1 - \frac{4n^2 - 5^2}{3(8x)} (1 - \dots) \right) \right) \right], \quad (4.22)$$

in the case of $x \gg 1$ such that the approximations yield

$$I_0 \approx \frac{\exp x}{\sqrt{2\pi x}} \left[1 + \frac{1}{8x} \right], \quad (4.23)$$

$$I_1 \approx \frac{\exp x}{\sqrt{2\pi x}} \left[1 - \frac{3}{8x} \right]. \quad (4.24)$$

Given these approximations, the scaling of β and ζ follows from

$$\beta(x) \approx x \frac{1 - \frac{7}{8x}}{1 + \frac{1}{8x} - (1 - \nu_c) \frac{1}{x} - \frac{3}{8x^2}} \xrightarrow{x \gg 1} x + \mathcal{O}(x^2), \quad (4.25)$$

$$\zeta(x) \approx x \frac{64 - \frac{24}{x} - \frac{6}{x^2}}{64 - \frac{48}{x} + \frac{3}{x^2} - \frac{9}{x^3} + \frac{9}{4x^4}} \xrightarrow{x \gg 1} x + \mathcal{O}(x^2), \quad (4.26)$$

and consequently

$$F_{\text{tot}} \xrightarrow{r_0 \gg l_p} 2\pi\sigma_a r_0, \quad (4.27)$$

$$E_s \xrightarrow{r_0 \gg l_p} \frac{\pi\sigma_a^2}{2Y_s} \cdot \frac{r_0}{l_p}. \quad (4.28)$$

The result of this detailed asymptotic analysis is summarized in Fig. 4.3. This figure shows the scaling behavior for the total force and substrate strain energy, together with the limiting cases of large and small disc radii. For large disc radii $r_0 \gg l_p$, both the total force and the substrate strain energy scale linearly with r_0 , corresponding to a tension-dominated regime. However, for the elastic-dominated regime $r_0 \ll l_p$ total force and substrate strain energy have distinct scaling behavior $F_{\text{tot}} \sim r_0^3$ and $E_s \sim r_0^4$. In our experiments, the system size is always much larger than l_p so we are always operating in the tension-dominated regime. Therefore, we conclude that the relevant scaling of the total force and the substrate strain energy is best captured by the linear regime.

4.3.3. TIME COURSE OF THE PHOTOACTIVATION STRESS

The exact time behavior of the photoactivation stress cannot be measured directly and is therefore a degree of freedom in our modeling. Based on the overall time evolution of the substrate strain energy, we considered multiple functions which could qualitatively represent the active stress as a function of time. The simplest form of an activation profile, usually exploited to describe the creep behavior of viscoelastic models, is a rectangular profile as depicted in Fig. 4.4A and mathematically realized as

$$\sigma_{\text{PA}}^{\text{rec}}(t) = \begin{cases} \sigma_0 & \text{for } t_0 \leq t \leq t_1 \\ 0 & \text{else} \end{cases}, \quad (4.29)$$

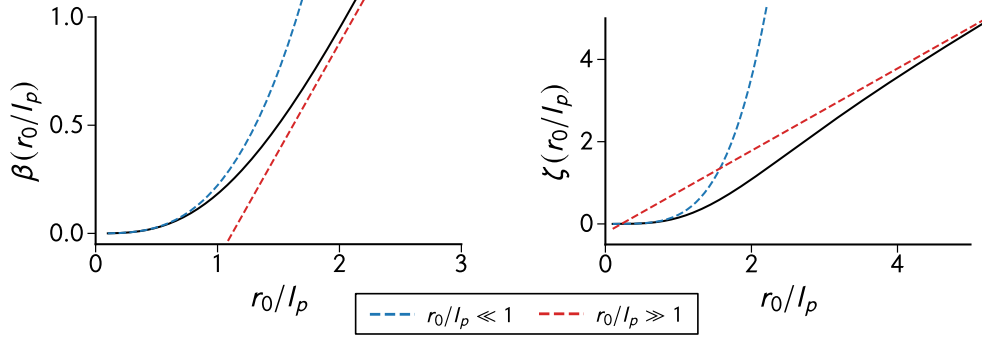


Figure 4.3: Analytical solution for the scaling of the total force β and the substrate strain energy ζ . The dashed lines indicate the scaling for $r_0 \ll l_p$ (blue) and $r_0 \gg l_p$ (red). For large disc radii, both total force and substrate strain energy scale linearly with r_0 .

with activation time t_0 , pulse duration $\Delta t = t_1 - t_0$ and peak activation stress σ_0 . However, the infinitely steep stress increase/release upon activation/relaxation are unphysical and lead to a kink in the strain energy profile at $t = t_1$ (Fig. 2.3C and Fig. 4.4A). A delayed response upon activation and during relaxation can be achieved by an exponential profile of the form

$$\sigma_{\text{PA}}^{\text{exp}}(t) = \begin{cases} \sigma_0 \left(1 - \exp\left(-\frac{t-t_0}{\tau_{\text{act}}}\right)\right) & \text{for } t_0 \leq t \leq t_1 \\ \sigma_0 \left(1 - \exp\left(-\frac{t_{\text{act}}-t_0}{\tau_{\text{act}}}\right)\right) \exp\left(-\frac{t-(t_0+t_1)}{\tau_{\text{rel}}}\right) & \text{else} \end{cases}, \quad (4.30)$$

which is depicted in Fig. 4.4B. It produces much better fits to the strain energy data but still leads to an asymmetric strain energy curve. We choose a double sigmoidal as activation profile, given by

$$\sigma_{\text{PA}}^{\text{sig}}(t) = \frac{\sigma_0}{1 + \exp\left(-\frac{t-t_{\text{act}}}{\tau_{\text{act}}}\right)} \cdot \left(1 - \frac{1}{1 + \exp\left(-\frac{t-t_{\text{rel}}}{\tau_{\text{rel}}}\right)}\right), \quad (4.31)$$

an depicted in Fig. 4.4C. It is realized by the product of two sigmoids, an ascending and a descending sigmoid, both of which saturate at a stress level σ_0 . Their centers t_{act} and t_{rel} describe the respective onsets of stress activation and relaxation, while the two time constants τ_{act} and τ_{rel} define the time scales on which stress is generated and relaxed. The physically relevant peak stress is given by σ_{max} which in principle may be lower than σ_0 . This activation profile leads to excellent fits of the time course of the substrate strain energy (Fig. 4.4C). Nonetheless, the quality of the fits is not the only justification for this specific choice of stress profile. The stress generation upon photoactivation can be regarded as the end of a long signaling cascade that starts with membrane recruitment of CRY2 (Valon *et al.*, 2015; Valon *et al.*, 2017) and terminates with phosphorylation of myosin light chain (MLC), which in turn leads to actomyosin contraction. The underlying reaction kinetics is complicated but simplified coarse grained models for the GEF-RhoA-MLC cascade describe the activation and inactivation of the involved species by means of Michaelis-Menten kinetics (Besser *et al.*, 2007; Kamps *et al.*, 2020; Michaelis *et al.*, 1913; Staddon *et al.*, 2022). In those studies, the observed increase in active RhoA and myosin concentration during single

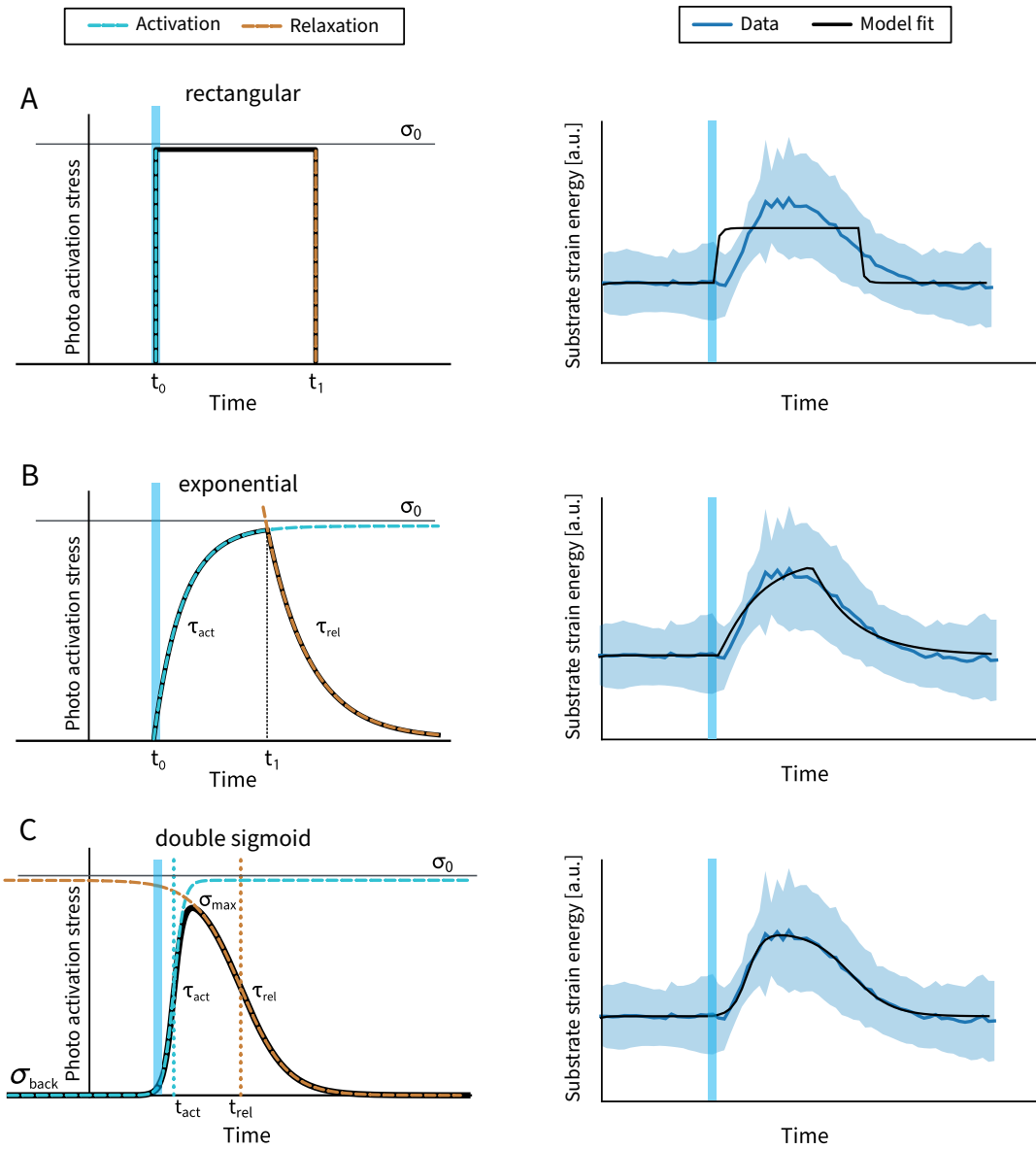


Figure 4.4: Time course of the substrate strain energy response for different profiles for the photo activation stress $\sigma_{PA}(t)$ combined with the active Kelvin-Voigt model. The activation profiles in the left column are generic illustrations while the black lines in the right column correspond to actual model fits where the free parameters of each activation profile were optimized. For illustrational purposes we used the mean strain energy data for the cell plated on $1500\ \mu\text{m}^2$ pattern. The shaded regions correspond to the standard deviation. Cell parameters are the same as used throughout all simulations in this chapter and which are gathered in Table A.1. The double-sigmoidal shape of the photoactivation stress fits best to the experimental data.

contraction pulses exhibits the same smooth ascending and descending time course as provided by the double sigmoid. In addition, it has also been shown theoretically, that weakly activated linear signaling cascades lead to signal-outputs that are comparable to a double sigmoid (*Beguerisse-Díaz et al.*, 2016). It is even possible to obtain analytical solutions for the time evolution of all signaling molecules for certain input signals. A typical example would be the signal of the CRY2 membrane recruitment with its very steep increase of only a few seconds upon photoactivation that is followed by an exponential decrease (*Valon et al.*, 2015).

4.3.4. ADHESION GEOMETRY OF THE HAZARD PATTERN

An important aspect of this experiment is the geometry of the fibronectin pattern as it allows to influence the organization of the actin cortex and the embedded stress fibers. As can be seen in Fig. 4.1B, the hazard pattern covers the same projected area as the disc pattern but the spreading area amounts to only $570 \mu\text{m}^2$ which is approximately half of the adhesive area of the disc pattern ($1000 \mu\text{m}^2$). Within the FEM-simulations, the adhesive geometry can be accounted for by specifying the region in space in which the spring stiffness density is non-zero. On the disc pattern, the cell could in principle form connections throughout the whole area. Consequently, the spring stiffness density Y is constant, non-zero and independent of position and no geometric constraint has to be specified. However for the hazard pattern $Y = Y(x, y)$ is position dependent and we have to geometrically define the set of points $(x, y)_{Y \neq 0}$ with non-zero spring stiffness density corresponding to the fibronectin-coated area on which the cell can adhere to the substrate. For a better understanding, Fig. 4.5 illustrates the hazard pattern geometry along with all relevant parameters. The arm width of the T-shaped branches is set to $w = 5 \mu\text{m}$, the inner radius to $R_{\text{in}} = R - w$, where $R = \sqrt{1000 \mu\text{m}^2 / \pi} \approx 17.8 \mu\text{m}$ is the radius of the convex hull of the hazard pattern, and $\alpha_{\text{out}} = \pi/2$ is the angular range of each of the branches. Given those parameters we define the hazard-pattern as (*Probst*, 2018)

$$(x, y)_{Y \neq 0} = \left\{ x, y \mid \begin{aligned} & \left[R_{\text{in}} \leq \sqrt{x^2 + y^2} \leq R \wedge \left(\frac{\pi}{2} - \frac{\alpha_{\text{out}}}{2} \leq \arctan2(x, y) \leq \frac{\pi}{2} + \frac{\alpha_{\text{out}}}{2} \right. \right. \\ & \quad \vee -\frac{\pi}{6} - \frac{\alpha_{\text{out}}}{2} \leq \arctan2(x, y) \leq -\frac{\pi}{6} + \frac{\alpha_{\text{out}}}{2} \\ & \quad \vee -\frac{5\pi}{6} - \frac{\alpha_{\text{out}}}{2} \leq \arctan2(x, y) \leq -\frac{5\pi}{6} + \frac{\alpha_{\text{out}}}{2} \\ & \quad \left. \left. \vee \pi - \alpha_{\text{overhang}} \leq \arctan2(x, y) \leq \pi \right) \right] \vee \\ & \left[\sqrt{x^2 + y^2} \leq R_{\text{in}} \wedge \left(\left(-\frac{w}{2} \leq x_1 \leq \frac{w}{2} \wedge y_1 \geq 0 \right) \right. \right. \\ & \quad \vee \left(-\frac{w}{2} \leq x_2 \leq \frac{w}{2} \wedge y_2 \geq 0 \right) \\ & \quad \left. \left. \vee \left(-\frac{w}{2} \leq x_3 \leq \frac{w}{2} \wedge y_3 \geq 0 \right) \right) \right] \right\}, \end{aligned}$$

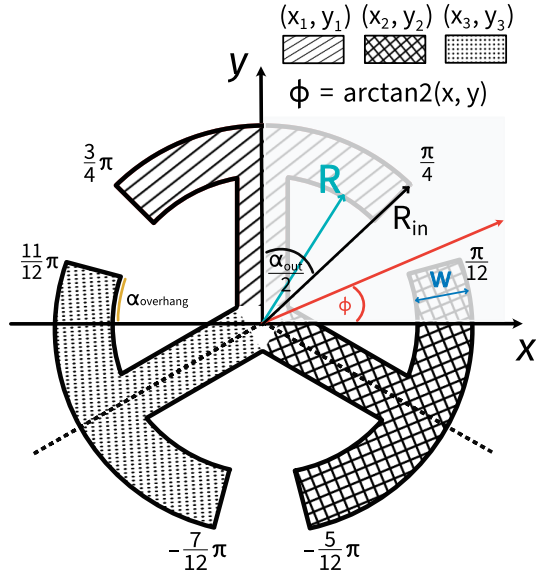


Figure 4.5: Illustration of the adhesive geometry of the hazard pattern. The parameters are chosen such that the dimensions of the pattern and the adhesive area match the experiment. The T-shaped branches span a pre-defined angular range of $\alpha_{\text{out}} = \frac{\pi}{2}$. The radius is set to $R \approx 17.8 \mu\text{m}$ and the width of the branches is set to $w = 5 \mu\text{m}$. The three hashed regions are mathematically defined in the main text.

where the remaining parameters, that define the orientation of the branches relative to the x -axis, are given by

$$\begin{aligned} (x_1, y_1) &= (x, y) \\ (x_2, y_2) &= \left(x \cdot \cos\left(\frac{2\pi}{3}\right) - y \cdot \sin\left(\frac{2\pi}{3}\right), x \cdot \sin\left(\frac{2\pi}{3}\right) + y \cdot \cos\left(\frac{2\pi}{3}\right) \right) \\ (x_3, y_3) &= \left(x \cdot \cos\left(\frac{2\pi}{3}\right) + y \cdot \sin\left(\frac{2\pi}{3}\right), -x \cdot \sin\left(\frac{2\pi}{3}\right) + y \cdot \cos\left(\frac{2\pi}{3}\right) \right). \end{aligned}$$

The quantity α_{overhang} is defined as

$$\alpha_{\text{overhang}} = \frac{5\pi}{6} + \frac{\alpha_{\text{out}}}{2} - \pi \text{ if } \frac{5\pi}{6} + \frac{\alpha_{\text{out}}}{2} > \pi, \text{ otherwise } 0, \quad (4.32)$$

and is introduced to account for the discontinuity of the arctan2-function at the values $-\pi$ and π . The overhang-region is marked in yellow (Fig. 4.5) where the T-branch intersects the x -axis at $\phi = \pi$.

4.3.5. ANISOTROPIC CONTRACTILE STRESS

As introduced before, the active stress is divided into two contributions σ_{bck} and σ_{PA} . For cells plated on the disc pattern, actin images (Fig. 4.1) show a polarized actin network with stress fibers having a dominant direction of alignment. This observation was further quantified (Tomas Andersen, 2018; Probst, 2018) by analyzing the distribution of traction forces and determining the dipole moment according to

$$M_{ij} = \int x_i T_j(\mathbf{x}) \, d\mathbf{x}, \quad (4.33)$$

in which T_j denotes the j -th component of the traction force vector (Butler *et al.*, 2002). Since the net torque exerted by the cell should be zero, M is expected to be symmetrical and the major and minor dipole axis can be determined from the largest and lowest eigenvalue of M , respectively. For cells plated on the hazard pattern with

their three families of aligned stress fibers (Fig. 4.1), Eq. (4.33) yields a much lower value for the ratio of major and minor dipole moment consistent with the image based observation that cells on hazard patterns are less polarized (*Probst, 2018*). Based on those experimental observations the active stress tensor σ_a is assumed to be anisotropic and directed along the axis of stress fiber orientation. We further assume that this is still valid upon photoactivation since it has been shown that focal adhesion distribution and morphology is not affected by light stimulation and further, it does not induce formation of new stress fibers (*Oakes et al., 2017; Valon et al., 2017*). This is consistent with our experiments as we do not observe changes to the cytoskeletal organization during and after photoactivation.

Mathematically, we define the direction of the anisotropic active stress tensor by means of the angle φ with respect to the x -axis of the coordinate system

$$\begin{aligned}\sigma_a(\varphi) &= \begin{pmatrix} \cos \varphi & -\sin \varphi \\ \sin \varphi & \cos \varphi \end{pmatrix} \begin{pmatrix} \sigma_{\text{bck}} + \sigma_{\text{PA}}(t) & 0 \\ 0 & 0 \end{pmatrix} \begin{pmatrix} \cos \varphi & \sin \varphi \\ -\sin \varphi & \cos \varphi \end{pmatrix} \\ &= (\sigma_{\text{bck}} + \sigma_{\text{PA}}(t)) \cdot \begin{pmatrix} \cos^2 \varphi & \frac{1}{2} \sin(2\varphi) \\ \frac{1}{2} \sin(2\varphi) & \sin^2 \varphi \end{pmatrix}.\end{aligned}\quad (4.34)$$

In the case of the disc pattern we set $\varphi^{\text{DP}} = \pi/2$ such that the stress tensor is given by

$$\sigma_a^{\text{DP}}(\varphi) = \begin{pmatrix} 0 & 0 \\ 0 & \sigma_{\text{bck}} + \sigma_{\text{PA}}(t) \end{pmatrix}.\quad (4.35)$$

For the hazard pattern we define three regions Ω_1, Ω_2 and Ω_3 (Figs. 4.5 and 4.10) with stress fiber orientations defined by the angles $\varphi_1^{\text{HP}} = -\pi/3$, $\varphi_2^{\text{HP}} = \pi/3$ and $\varphi_3^{\text{HP}} = 0$, respectively. This yields for the stress tensors

$$\sigma_{a,\Omega_1}^{\text{HP}} = (\sigma_{\text{bck}} + \sigma_{\text{PA}}(t)) \begin{pmatrix} \cos^2(\frac{\pi}{3}) & -\frac{1}{2} \sin(\frac{2\pi}{3}) \\ -\frac{1}{2} \sin(\frac{2\pi}{3}) & \sin^2(\frac{\pi}{3}) \end{pmatrix},\quad (4.36)$$

$$\sigma_{a,\Omega_2}^{\text{HP}} = (\sigma_{\text{bck}} + \sigma_{\text{PA}}(t)) \begin{pmatrix} \cos^2(\frac{\pi}{3}) & \frac{1}{2} \sin(\frac{2\pi}{3}) \\ \frac{1}{2} \sin(\frac{2\pi}{3}) & \sin^2(\frac{\pi}{3}) \end{pmatrix},\quad (4.37)$$

$$\sigma_{a,\Omega_3}^{\text{HP}} = (\sigma_{\text{bck}} + \sigma_{\text{PA}}(t)) \begin{pmatrix} 1 & 0 \\ 0 & 0 \end{pmatrix}.\quad (4.38)$$

4.3.6. PARAMETRIZATION AND SCALING CONSIDERATIONS FROM ANALYTICAL SOLUTION

As can be seen from the model introduction in the previous sections, the parameter space of our model is high dimensional. Hence, a direct optimization of all free parameters by fitting the model to the experimental readout (substrate strain energy as function of time) is not feasible. We therefore decide to fix those parameters that are well established in the literature and only optimize those, that are specific to our experimental setup. The known parameter include the substrate properties with Young's modulus $E_s = 4.47$ kPa, Poisson's ratio $\nu_s = 0.5$, and a substrate thickness of approx-

imately $h_s = 50 \mu\text{m}$. Considering a lateral cell size of about $L_c = 50 \mu\text{m}$, the spring stiffness density is $Y_s = 3 \times 10^8 \text{N m}^3$. For the adhesion bond we choose a standard value of $k_a = 2.5 \text{pN nm}^{-1}$ (Balaban *et al.*, 2001) which together with $d = 1 \mu\text{m}$ (Hu *et al.*, 2017) yields $Y_a \approx 2 \times 10^9 \text{N m}^{-3}$. We conclude that the adhesion layer is the stiffer contribution and the cell mainly perceives the stiffness of the elastic gel. The Young's modulus of the cell is set to $E_c = 10 \text{kPa}$ which corresponds to the typical value for strongly adherent cells and the Poisson's ratio to $\nu_c = 0.5$ according to typical values reported in the literature (Banerjee *et al.*, 2013; Edwards *et al.*, 2011; Oakes *et al.*, 2014; Solowiej-Wedderburn *et al.*, 2022). Fixing the cell viscosity at a value of 100kPa s yields a relaxation time constant of $\tau_c = 10 \text{s}$. Further we estimate an effective cell height of $h_c \approx 1 \mu\text{m}$.

The typical cell force is of the order of $F_{\text{tot}} = \mu\text{N}$ (Tomas Andersen, 2018). Given this value, we can estimate the expected order of magnitude of the remaining quantities, and will later see that they are in good agreement with our model fits. The total background traction stress can be approximated by Eq. (4.27), and yields

$$\sigma_{\text{bck}}^{\text{3D}} = \frac{\sigma_{\text{bck}}}{h_c} = \frac{F_{\text{tot}}}{2\pi r_0 h_c} \approx 10 \text{kPa} , \quad (4.39)$$

where we additionally divided by h_c to achieve units of kPa since σ_{bck} is the two-dimensional stress as discussed in the plane-stress and thin-layer approximation. For the localization length we find

$$l_p \approx 1 \mu\text{m} , \quad (4.40)$$

and exploiting the linear scaling for large disc radii we find for the substrate strain energy

$$E_s \approx 1 \text{pJ} . \quad (4.41)$$

4.3.7. FINITE ELEMENT IMPLEMENTATION AND TIME DISCRETIZATION

The weak form of the active Kelvin-Voigt model can be derived in exactly the same way as the one for the elastic solid. However, this time the stress-strain relationship is time-dependent since the stress is additionally proportional to the strain rate (Eq. (4.1)). Explicitly writing Eq. (4.1) in terms of the deformation field gives

$$\begin{aligned} \boldsymbol{\sigma} &= \left(1 + \tau_c \frac{\partial}{\partial t}\right) (\lambda \text{tr}(\boldsymbol{\varepsilon})\mathbf{I} + 2\mu\boldsymbol{\varepsilon}) + \boldsymbol{\sigma}_a \\ &= \lambda(\nabla \cdot \mathbf{u})\mathbf{I} + \mu(\nabla\mathbf{u} + \nabla\mathbf{u}^\top) + \tau_c\lambda(\nabla \cdot \dot{\mathbf{u}})\mathbf{I} + \tau_c\mu(\nabla\dot{\mathbf{u}} + \nabla\dot{\mathbf{u}}^\top) + \boldsymbol{\sigma}_a \\ &= \boldsymbol{\Sigma}_E(\mathbf{u}) + \boldsymbol{\Sigma}_\eta(\dot{\mathbf{u}}) + \boldsymbol{\sigma}_a , \end{aligned} \quad (4.42)$$

where we split the stress up in an elastic contribution $\boldsymbol{\Sigma}_E(\mathbf{u})$, which contains all terms involving \mathbf{u} , and a viscous contribution $\boldsymbol{\Sigma}_\eta(\dot{\mathbf{u}})$, which contains all terms involving the time derivative $\dot{\mathbf{u}}$. In order to use Eq. (4.42) in our weak form statement we discretize

the time derivatives of \mathbf{u} by means of a backward Euler¹ scheme of time step Δt , in which the time derivative at the $(n + 1)$ -th time step is approximated by

$$\dot{\mathbf{u}}^{(n+1)} = \frac{\mathbf{u}^{(n+1)} - \mathbf{u}^{(n)}}{\Delta t}. \quad (4.43)$$

Due to the linearity of the stress-strain relationship the time discretization directly translates to

$$\dot{\Sigma}_\eta^{(n+1)} = \frac{\Sigma_\eta^{(n+1)} - \Sigma_\eta^{(n)}}{\Delta t}, \quad (4.44)$$

and we find for the weak form

$$a(\mathbf{u}^{(n+1)}, \mathbf{v}) = \int_\Omega \Sigma_E^{(n+1)} : \mathbf{s}(\mathbf{v}) \Delta t \, d\Omega + \int_\Omega \Sigma_\eta^{(n+1)} : \mathbf{s}(\mathbf{v}) \, d\Omega + \int_\Omega Y \mathbf{u}^{(n+1)} \cdot \mathbf{v} \Delta t \, d\Omega \quad (4.45)$$

and

$$L^{(n+1)}(\mathbf{v}) = \int_\Omega \Sigma_\eta^{(n)} : \mathbf{s}(\mathbf{v}) \, d\Omega - \int_\Omega \sigma_a : \mathbf{s}(\mathbf{v}) \Delta t \, d\Omega, \quad (4.46)$$

such that we directly hand

$$a(\mathbf{u}^{(n+1)}, \mathbf{v}) = L^{(n+1)}(\mathbf{v}) \quad \forall \mathbf{v} \in \mathcal{V}(\Omega). \quad (4.47)$$

to the FEniCS solver (*Alnæs et al.*, 2015). The solver then automatically handles the implicit time discretization. For the hazard pattern, Eqs. (4.45) and (4.46) can be easily modified by using

$$\int_\Omega \sigma_a : \mathbf{s}(\mathbf{v}) \Delta t \, d\Omega = \sum_{i=1}^3 \int_{\Omega_i} \sigma_{a, \Omega_i}^{\text{HP}} : \mathbf{s}(\mathbf{v}) \Delta t \, d\Omega_i. \quad (4.48)$$

Meshing was performed with the open source software GMSH (*Geuzaine et al.*, 2009). All parameter optimizations are carried out with a downhill simplex method as developed by *Nelder et al.* (1965) and implemented within the scientific python library SciPy (*Virtanen et al.*, 2020).

4.4. RESULTS

Since our simulation results are only meaningful in the context of the experimental data, we present and discuss both together. The results section is divided into three parts. We first discuss the influence of pattern size on actin ordering and strain energy for the same pattern geometry and then the influence of actin architecture for the same projected area but different pattern geometry. Finally we investigate the influence of photoactivation duration on strain energy and strain energy gain.

¹In contrast to the very common and easy to implement explicit forward Euler scheme, the implicit backward scheme is numerically more expensive but by contrast much more stable with respect to the size of the time step

4.4.1. INFLUENCE OF PATTERN SIZE ON ACTIN ORDERING AND STRAIN ENERGY

If not stated otherwise we refer to the three pattern sizes $500\ \mu\text{m}^2$, $1000\ \mu\text{m}^2$ and $1500\ \mu\text{m}^2$ as small, medium and large pattern, respectively. In Fig. 4.6 we provide an overview of all important experimentally obtained quantities. Fig. 4.6A exemplarily depicts the three different fibronectin patterns together with actin and vinculin stained cells and the respective traction force maps as obtained by a TFM analysis. We further used a customized software from the Balland group which determines the actin orientation map by means of the so called structure tensor \mathbf{J} . The definition of \mathbf{J} is provided in Appendix A.4. In good agreement with similar experiments on well-adhered cells (*Mertz et al.*, 2012; *Oakes et al.*, 2014), the traction forces are located at the cell periphery and increase with increasing cell size. This is consistent with the quantification of the substrate displacement in Fig. 4.6B showing that increasing cell size leads to larger substrate displacements. Additionally, those examples emphasize the strong dipolar character of the cells in agreement with the study by *Mandal et al.* (2014). Measuring the decay of the substrate displacement towards the cell center, i.e. along the white lines in Fig. 4.6B allows us to quantify the force-localization length l_p as the distance from the edge at which the displacement field attains half of its maximal value. The statistical results of this measurement are shown in Fig. 4.6C1 and C2 and show a positive correlation between force-localization length and cell size. The results of the actin orientation analysis are further summarized in the so called actin order parameter S as depicted in Fig. 4.6D. A value of $S = 1$ corresponds to a perfectly ordered system in which the local actin orientation is parallel to the average orientation, whereas a value of $S = 0$ corresponds to orthogonality between local and average actin orientation i.e. an unordered cytoskeleton. We find that cell size and order parameter are positively correlated although saturation occurs towards the large pattern size around a value of $S = 0.5$ (Fig. 4.6D). As expected from other experimental studies (*Gupta et al.*, 2015) a higher degree of ordering results in higher substrate strain energies consistent with our strain energy measurement summarized in Fig. 4.6E which shows the baseline strain energy as a function of cell size. This correlation between cell size and strain energy was previously reported by (*Oakes et al.*, 2014; *Reinhart-King et al.*, 2005; *Tan et al.*, 2003; *Tseng et al.*, 2011). As an interim conclusion we find that force-localization length, actin ordering and substrate strain energy increase with cell size.

Fig. 4.7A shows the mean strain energy as a function of time for all three pattern sizes. At this point, we note that the analysis of the photoactivation experiments was performed on a reduced data set containing 8 cells for the small and large pattern sizes and 14 cells for the medium size. Photoactivation of all three pattern sizes with a 100 ms long light pulse leads to a strain energy increase which lasts for about 2 min and then relaxes for another 6 to 8 min back to its baseline level. The average baseline energy for the reduced data sets are 0.08 pJ, 0.26 pJ and 0.45 pJ on small, medium and large patterns, respectively, reflecting the trend of the full data set. Next, we quantify the strain energy gain by calculating the difference between the peak energy

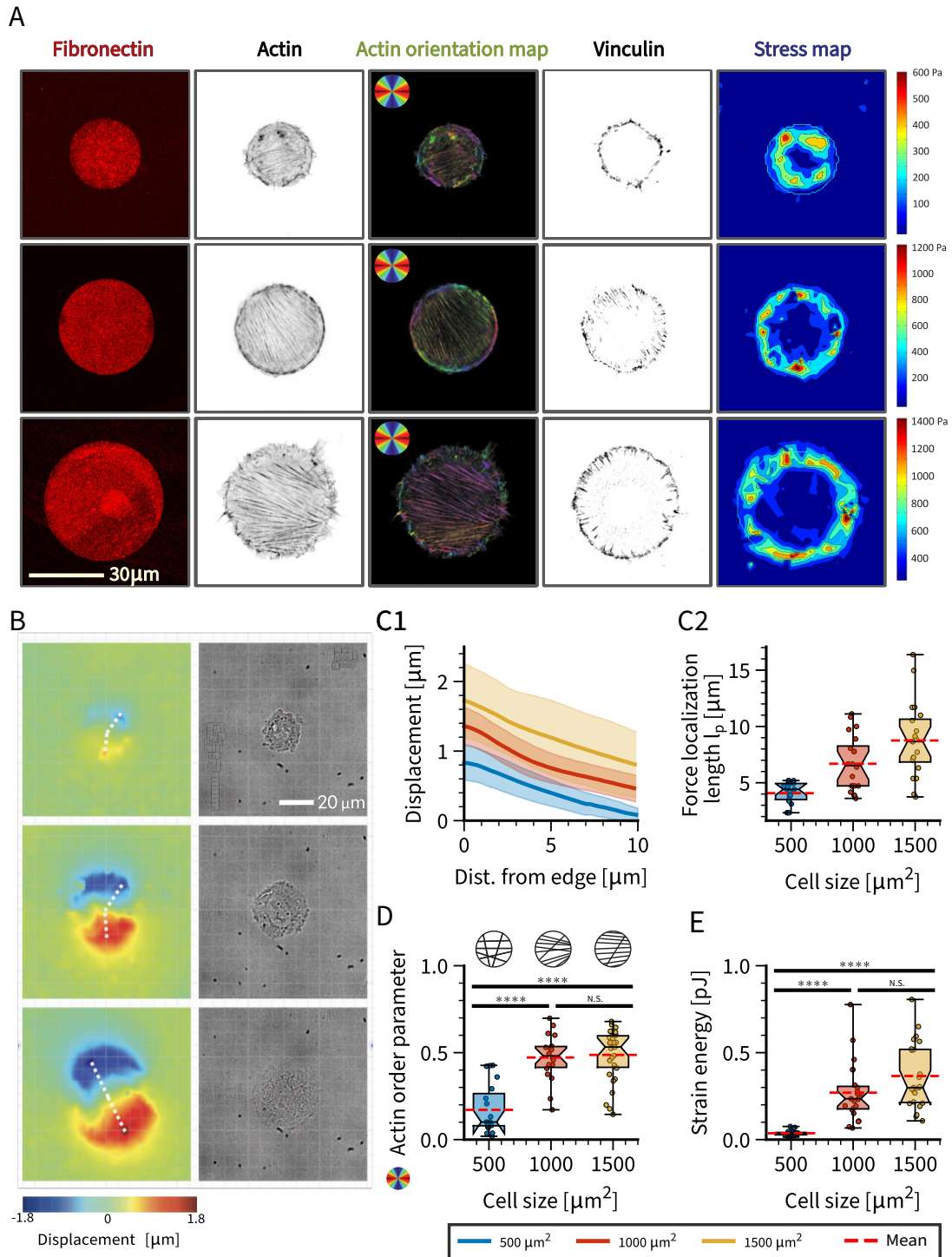


Figure 4.6: Panel **A** depicts the cells on disc-shaped fibronectin patterns on polyacrylamide hydrogels. Columns from left to right show: (i) Micro patterns of varying sizes (500 – 1000 – 1500 μm^2). (ii) Actin-stained cells. (iii) Actin-stained cells with actin orientation map. (iv) Visualization of adhesion pattern from vinculin-staining. (v) Traction force map resulting from traction force microscopy. Panel **B** exemplarily shows the substrate deformation map and bright-field images of the cells. Panel **C1** shows the quantification of the displacement decay with respect to the distance from the cell periphery (measured along the white lines as shown in **B**). Panel **C2** shows the measured force localization length for different pattern sizes taken as the distance from the periphery at which the displacement dropped to half of its maximal value. Panel **D** shows the actin order parameter as obtained from measurement of the global cellular actin alignment. Panel **E** depicts the baseline strain energy level of the cells plated on different pattern sizes before photoactivation. A 1-way ANOVA significance test yields a significant difference between the 500 μm^2 pattern size and the two larger patterns.

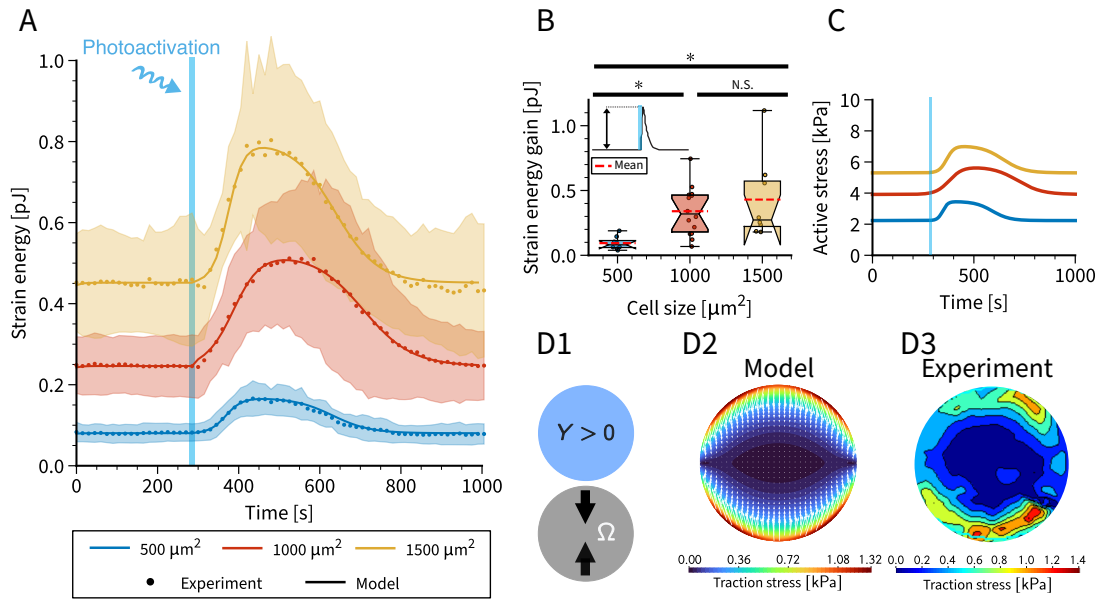


Figure 4.7: Cell size influences strain energy and strain energy gain after photoactivation. Panel **A** shows the dynamics of the strain energy during and after photoactivation with a 100 ms long light pulse (blue vertical line). Circles represent experimental mean data and shaded regions depict the standard deviation. The numerically computed strain energy is represented by the solid lines. The averages correspond to a reduced data set containing 8 ($500 \mu\text{m}^2$), 14 ($1000 \mu\text{m}^2$) and 8 ($1500 \mu\text{m}^2$) cells. Panel **B** denotes the statistical evaluation of the strain energy gain which is calculated as the difference between the peak energy value after photoactivation and the strain energy value right before photoactivation. Panel **C** shows the time course of the internal active stresses of the contractile cell layer, determined by fitting the FEM model to the strain energy curve. Panel **D** shows the FEM-setup of a dipolar contracting cell on a disc pattern as well as the numerically and experimentally obtained traction maps.

value after photoactivation and the strain energy value right before photoactivation (Fig. 4.7B). The strain energy gain after photoactivation, as illustrated in Fig. 4.7B, is 0.09 pJ for small, 0.30 pJ for medium and 0.42 pJ for large patterns thus optogenetic activation leads to a relative strain energy increase of approximately 100 % irrespective of cell size. The absolute strain energy gain, however, increases in proportion to the strain energy baseline. Moreover, attention needs to be drawn to the observation that the pre-photoactivation baseline level is almost perfectly recovered after perturbation which hints at a steady-state in the reaction-diffusion system of the membrane bound Rho-system and, further, that the cytoskeleton is not altered by the light-induced perturbation.

In order to gain additional insight into the strain energy dynamics as a function of cell size we fit our FEM-model as presented in the previous section to the experimental strain energy curve. The global results of the fits are depicted in Fig. 4.7A (solid lines) and are determined by the time course of the active stress as the main fit-result which is shown in Fig. 4.7C. The fact that the strain energy closely follows the active stress means that there is no significant delay between input (stress) and output (strain energy) and additionally reflects that the elastic modulus of the cell is dominant over its viscosity. Moreover it highlights that cells are well connected to the substrate. A comparison of the traction force maps as obtained by simulations (Fig. 4.7D1 and D2) and the experimentally measured TFM-map (Fig. 4.7D3) shows that our simulation

approach qualitatively captures a similar dipolar traction force field with peak-values in the same order of magnitude (~ 1.4 kPa) although the regions of larger tractions in the experimental map are smeared out compared to the simulations.

In detail, the fits are performed in two steps: First, the baseline energy is fitted by optimizing the force localization length l_p and the background stress σ_{bck} , and second, the model dynamics is fitted by optimizing the photoactivation stress σ_0 and the four time scales $t_{\text{act}}, t_{\text{rel}}, \tau_{\text{act}}$ and τ_{rel} according to the definition in Eq. (4.31). All fitting results can be found in Table A.2 and are visualized in Fig. 4.8A and B for baseline fit and photoactivation fit, respectively. Fig. 4.8A depicts that all numerically obtained counterparts to the experimental measurements show the same increase with cell size. Here, the most important quantity is the the background stress σ_{bck} as it cannot be directly measured and therefore only extracted by means of our model. The obtained order of magnitude ~ 4 kPa is in good agreement with other results from tissue stretching experiments (*Wyatt et al.*, 2020) and monolayer stress microscopy (*Trepat et al.*, 2009) as well as our scaling considerations in the previous section. An increase of baseline stress level with increasing cell size could be possibly traced back to the fact that the larger cells show a better developed actin cytoskeleton which may lead to larger local stresses.

As mentioned before, the dynamics of the force generation are described by the free parameters of the double sigmoid profile. The maximal photoactivation stress σ_{max} , as defined in Fig. 4.4C, is significantly lower for the small pattern size and approximately equal for the medium and large pattern (Fig. 4.8B). However, the total value of the stresses vary strongly as they are given by the sum $\sigma_a = \sigma_{\text{bck}} + \sigma_{\text{max}}$. We find that, irrespective of cell size, activation happens on a time scale of around $\tau_{\text{act}} \sim 20$ s and thus much faster than the relaxation process with a time scale of $\tau_{\text{rel}} \sim 50$ s. Those time scales must be directly linked to the time scales of the reaction-diffusion system of GEF and RhoA (*Valon et al.*, 2015). The onset, offset and duration of active force generation are defined by the centroids $t_{\text{act}}, t_{\text{rel}}$ and the difference $\Delta t = t_{\text{rel}} - t_{\text{act}}$. The onset of stress generation stays approximately constant at $t = 60$ s after PA-perturbation but the force generation duration Δt varies with cell size and shows that the medium pattern size remains activated for a longer time than the other two pattern sizes (Fig. 4.8B). The surprising result that all four time scales show a peak value at the medium pattern size might be linked to the observation that the cell size of $1000 \mu\text{m}^2$ is a typical spreading area for unconstrained cells on soft elastic substrates (*Nisenholz et al.*, 2014).

4.4.2. INFLUENCE OF ACTIN ARCHITECTURE ON STRAIN ENERGY AND FORCE GENERATION DYNAMICS

We follow exactly the same strategy as before but this time we study the role of varying actin architecture on the strain energy and the force generation dynamics. As already mentioned several times, the hazard pattern induces an actin architecture which is significantly different compared to the one for cells plated on the disc pattern as can be seen by comparing the actin and vinculin images in Fig. 4.9A. Further, we observe

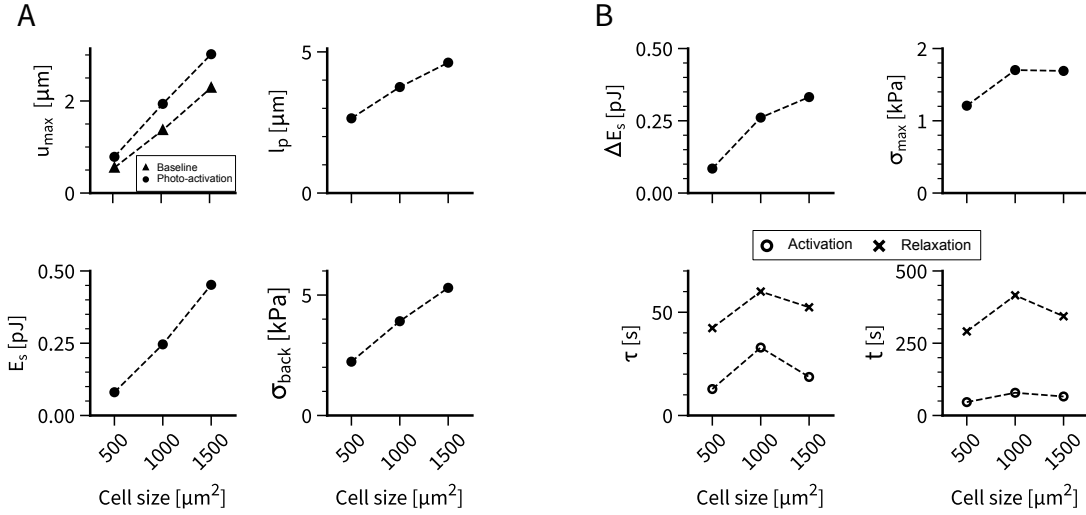


Figure 4.8: Result of the strain energy fit. Panel **A** illustrates the results of the baseline energy fits as a function of cell size. Panel **B** shows the optimized parameter set for the double sigmoid activation profile obtained from fits of the strain energy response upon photoactivation.

that the different actin organization and focal adhesion distribution drastically influence the exerted traction force pattern. Although they are still located at the cell periphery, they show clear peaks at the transitions of the three domains of distinct stress fiber orientation. Interestingly, although the actin order parameter is much lower for cells plated on the hazard pattern, the substrate strain energy of both conditions is approximately the same (Fig. 4.9B). The activation protocol for this experiment is identical to the one discussed before. We measure the strain energy response after illumination of the cells with a 100 ms long light pulse. The result of this experiment, again carried out on a reduced data set, is depicted in Fig. 4.10. The time course of the strain energy of the hazard pattern is similar to the disc pattern (Fig. 4.10A). Cells on hazard pattern reach their peak strain energy value at 2.71 ± 1.02 min after photoactivation while cells on the disc pattern have a time to peak of 3.43 ± 0.83 min. The strain energy gain was significantly higher for the dipolar cells on the disc pattern with a median value of 0.35 ± 0.05 pJ compared to the strain energy gain on the hazard pattern which only yields 0.18 ± 0.02 pJ (Fig. 4.10B). Fitting our mathematical model to the measured strain energy of the hazard pattern yields almost perfect fit results as shown by the solid lines in Fig. 4.10A and again allows to extract the internal active stress as a function of time (Fig. 4.10C). The FEM-model and a direct comparison of the simulated traction maps and an experimental example map are shown in Fig. 4.10D. As for the disc pattern, the FEM model captures the basic features of the experimental measurement. The order of magnitude (~ 1.6 kPa) as well as the topology of the experimental TFM field is reproduced by our simulations. All important quantities obtained by our model are gathered in Fig. 4.10E which shows that both, σ_{back} and σ_{max} are smaller for the hazard pattern which demonstrates that the force production in the less ordered hazard pattern is smaller. Further, we observe that the asymmetry ($\tau_{\text{rel}} - \tau_{\text{act}}$) between activation and relaxation time scale is larger for the hazard pattern which suggests that the actin organization influences the reaction-diffusion system of the underlying RhoA signaling cascade. Additionally,

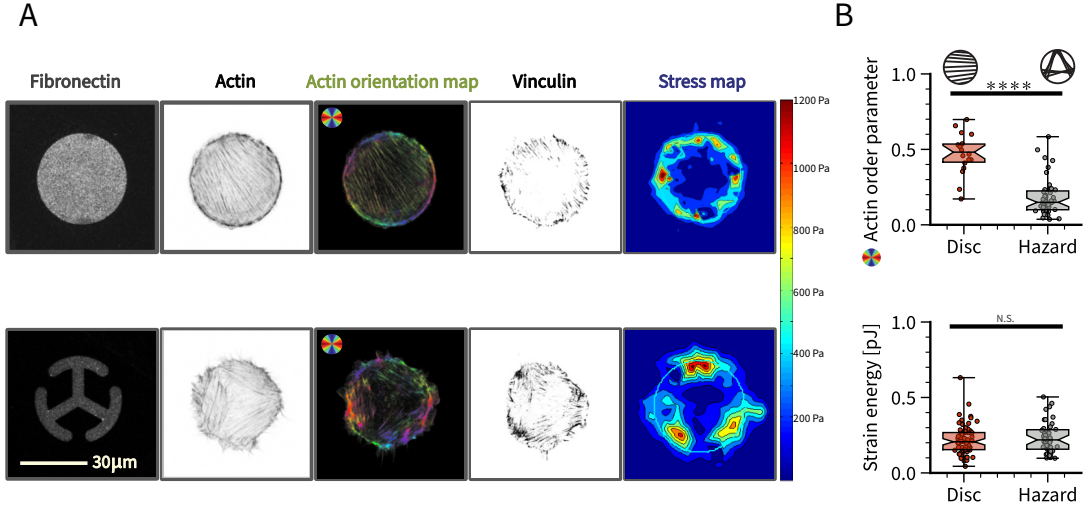


Figure 4.9: Panel **A** depicts the cells on disc- and hazard-shaped fibronectin patterns on polyacrylamide hydrogels. Columns from left to right show: (i) $1000\ \mu\text{m}^2$ disc- and hazard-shaped micro patterns. (ii) Actin-stained cells. (iii) Actin-stained cells with actin orientation map. (iv) Visualization of adhesion pattern from vinculin-staining. (v) Traction force map resulting from traction force microscopy. Panel **B** shows the actin order parameter and baseline energy level for the two conditions. A 1-way ANOVA test yields a significant difference for the order parameter and no significant differences for the baseline strain energy levels.

stress relaxation seems to set in earlier for the hazard pattern. At this point we want to draw the attention to two interesting observations: First, although the background stress σ_{bck} is slightly lower for the hazard pattern (compare Fig. 4.10C and E) it leads to a higher strain energy baseline than in the disc pattern with a higher background stress (Fig. 4.10A). Second, upon photoactivation the hazard pattern needs much less active stress increase to generate the corresponding strain energy response. We therefore conclude that the differently distributed and organized focal adhesions provide an increased force transmission to the substrate. In fact, the force localization length as obtained from simulations is smaller for the hazard pattern (Table A.2).

From a purely geometric perspective, cells plated on a hazard pattern would be expected to have less efficient force generation because the stress fibers enclose an angle and therefore may be working against each other. In the following, we consider two identical stress fibers which exert the same traction f on the substrate. Hence, in this minimalist framework, cells on the disc pattern are represented by two parallel stress fibers while cells on the hazard pattern are represented by two stress fibers which enclose an angle of $\gamma = 60^\circ$. A simple geometric consideration as depicted in Fig. 4.11A (inset) yields the total traction force as a function of γ

$$F_{\text{tot}} = f\sqrt{2(1 + \cos(\gamma))}, \quad (4.49)$$

which in turn leads to $F_{\text{tot}}^{\text{DP}} = 2f$ for the disc pattern and $F_{\text{tot}}^{\text{HP}} = \sqrt{3}f$ for the hazard pattern and therefore $F_{\text{tot}}^{\text{HP}} < F_{\text{tot}}^{\text{DP}}$. This shows that in case of the hazard pattern stress fibers have to pull stronger in order to generate the same net traction force which could be a possible explanation for their reduced force production capacity upon photoactivation.

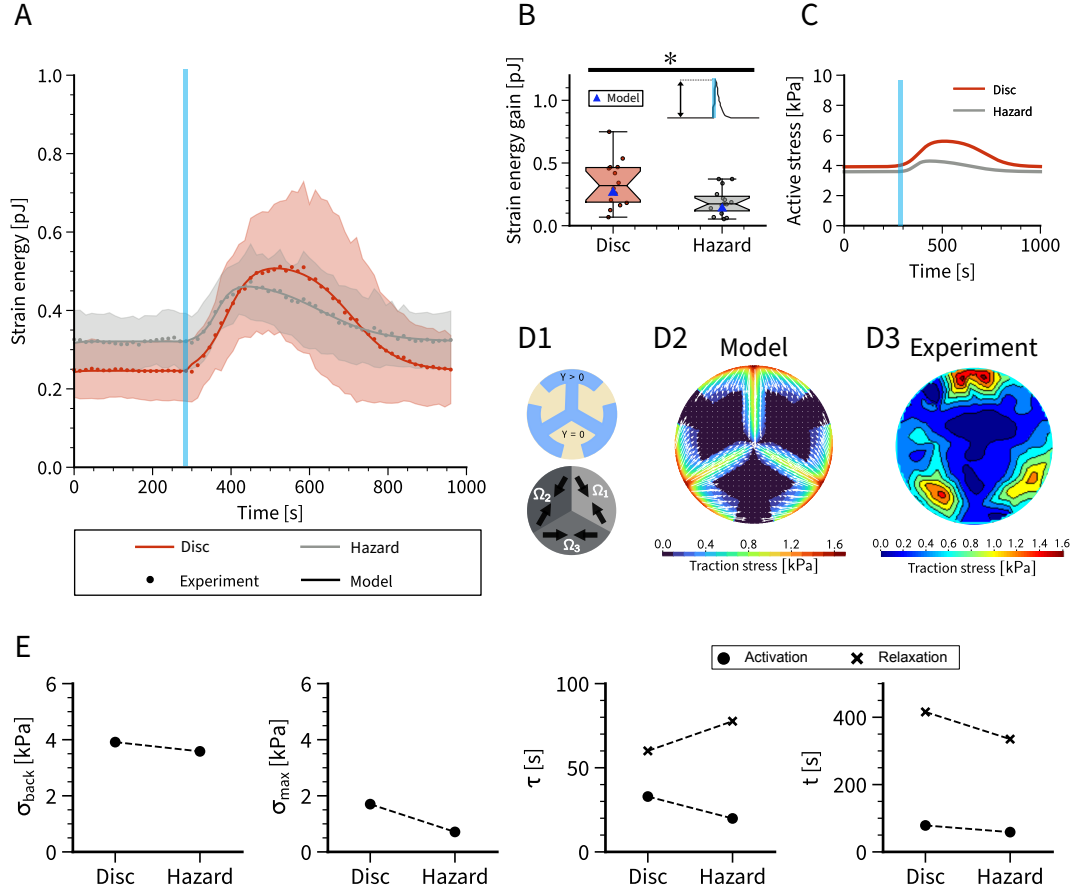


Figure 4.10: Actin organization influences strain energy and strain energy gain after photoactivation. Panel **A** shows the dynamics of the strain energy during and after photoactivation with a 100 ms long light pulse (blue vertical line). Dots represent experimental mean data and shaded regions depict the standard deviation. The numerically computed strain energy is represented by the solid lines. The averages correspond to a reduced data set containing 14 cells for disc and hazard pattern, respectively. Panel **B** denotes the statistical evaluation of the strain energy gain which is calculated as the difference between the peak energy value after photoactivation and the strain energy value right before photoactivation. The blue marker indicates the strain energy gain as predicted by the model fits in **A**. Panel **C** shows the time course of the internal active stresses of the contractile cell layer, determined by fitting the FEM model to the strain energy curve. Panel **D** shows the FEM-setup for cells on hazard pattern with three domains for the active stress as well as the numerically and experimentally obtained traction maps. Panel **E** shows the obtained background stress together with the optimized parameter set for the double sigmoid activation profile obtained from fits of the strain energy response upon photoactivation.

To better understand how actin polarization influences the baseline strain energy we simulated three different actin organizations on four different pattern geometries of varying adhesive area. Thereby all conditions have the same value for l_p and σ_{bck} . The result of the simulations is summarized in Fig. 4.11B where the symbol indicates the actin organization and the color refers to the adhesion pattern. We additionally compare the simulations to the analytical solution for the strain energy of an isotropic contracting disc on a ring pattern as a function of the adhesion area. This analytical solution is represented by the black solid line and was calculated according to Eq. (A.37) in Appendix A.5. The dashed line corresponds to the strain energy in the limiting case of a disc shaped adhesion pattern. From the analytical solution it is clear that the adhesion area has a non-trivial influence on the strain energy such that it increases for decreasing adhesion area. This is consistent with the results presented in (Solowiej-Wedderburn *et al.*, 2022) where the authors obtain the same dependency in case of larger substrate stiffnesses. On all pattern geometries the isotropic contraction results in the largest strain energy while the dipolar actin architecture yields the lowest values. Since all cell parameters are identical, we conclude that the strain energy is strongly influenced by the internal stress fiber organization. From a mathematical point of view one may conclude that $E_s \sim |\mathbf{T}|^2 dA \sim |\nabla \cdot \boldsymbol{\sigma}|^2 dA$ and thus the area over which stress gradients act determines the strain energy. In practice, high tractions are located near the cell periphery, however when considering the substrate displacement field of the hazard pattern (Fig. 4.11C) we additionally observe larger displacements along the T-shaped branches towards the cell center. This can be regarded as an effective increase of the cell periphery. In total, we conclude that the combination of adhesion geometry and actin architecture for the hazard pattern effectively provides a larger area of higher stress gradients than the combination of dipolar actin architecture on the disc pattern (Fig. 4.11C) such that for the same background stress one may expect higher strain energy values.

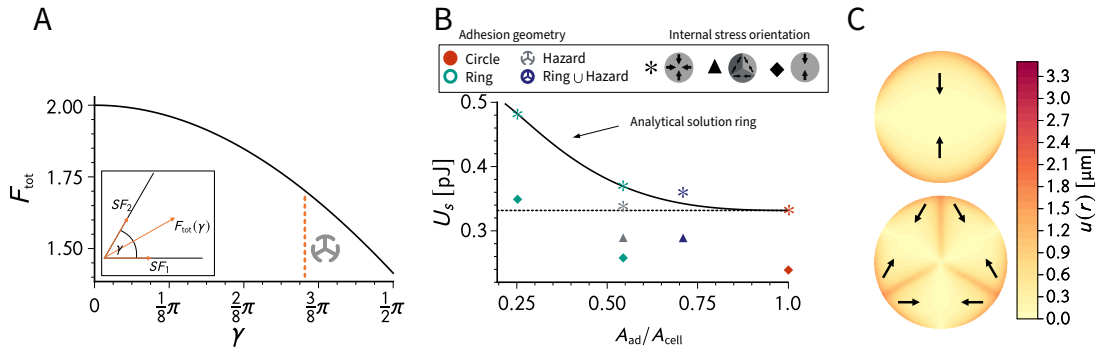


Figure 4.11: Influence of stress fiber arrangement and adhesive area on traction forces and substrate strain energy in FEM simulations. Panel **A** depicts the exerted traction force of two identical stress fibers which pull under an angle γ at a common adhesion site. Panel **B** depicts the substrate strain energy as a function of the adhesive area. In all cases values for active stress and substrate stiffness are identical. Symbols depict the internal stress anisotropy (cytoskeletal organization) while colors highlight the underlying adhesion geometry. The solid line corresponds to the substrate strain energy of an isotropically contracting disc on a ring pattern. A fully adhesive disc is represented by the dashed line. Panel **C** illustrates the substrate displacement field for the directional contraction on a disc pattern and the “triangular” contraction on a hazard pattern.

4.4.3. INFLUENCE OF VARYING PULSE DURATION ON FORCE GENERATION

In the final series of experiments cells on disc and hazard pattern were photoactivated by a series of light pulses of increasing duration. In between those pulses cells were given enough time to go back to their homeostatic energy level. We followed the same fitting procedure as before and once fitted to the strain energy baseline level and subsequently all six photoactivation peaks separately. The basic observations of the single pulse activation from the previous analysis still hold true. The strain energy is higher for cells plated on the hazard pattern and their force generation upon photoactivation is lower than for the disc pattern (Fig. 4.12A). The time course of the active stress is again very similar to the time course of the strain energy (Fig. A.1). By means of our mathematical model we extract the peak photoactivation stress as a function of the pulse duration. We find that active stress generation and pulse duration are positively correlated up to a pulse duration of 50 ms beyond which the active stress saturates as depicted in Fig. 4.12B. Exponential fits yield a maximal active stress of 1.81 kPa for the disc pattern and 0.84 kPa for the hazard pattern. The larger stress value for the disc pattern is not surprising as their actin cortex has a higher order parameter. Despite the clearly distinct saturation levels, both conditions saturate around a pulse duration of 25 ms. The time scales of the double sigmoid profile are shown in Fig. 4.12C and reveal a very surprising and complex internal dynamics. The onset t_{act} of stress generation is little influenced by pulse duration and stays approximately constant around values of 80 s for disc and 50 s for hazard pattern similar to the values obtained in the single pulse experiment (Fig. 4.10E). However, the relaxation centroids t_{rel} at first slightly increase with increasing pulse duration but then saturate around a value of 460 s for disc and 270 s for the hazard pattern. This highlights that cells on disc pattern stay longer activated as they have a larger stress plateau. In contrast, we observe strongly pronounced asymmetry between activation and relaxation time for the hazard pattern which decreases with increasing pulse duration. Hereby, the activation time scale stays approximately constant around a value of 15 s. In contrast, both activation and relaxation time scale slightly increase with increasing pulse duration for the disc pattern. Together our results suggest that the internal actin organization especially influences the way stress decreases back to its homeostatic setpoint. Further we conclude that the local dynamics of the actomyosin system are highly non-trivial and strongly depend on the local actin organization.

4.5. CONCLUSION

In this chapter, we combined traction force microscopy, non-neuronal optogenetics and a two-dimensional finite element model to study the influence of adhesion geometry on the force generation in cells. The standard continuum modeling approach, in the spirit of *Edwards et al.* (2011) and *Banerjee et al.* (2013), was extended in two ways: First, we introduced an anisotropic stress tensor to account for the architecture of the actin CSK. Second, we introduced viscoelasticity, similar to (*Prost et al.*, 2015), but with a viscoelastic solid (Kelvin-Voigt model). A Kelvin-Voigt model was chosen because of

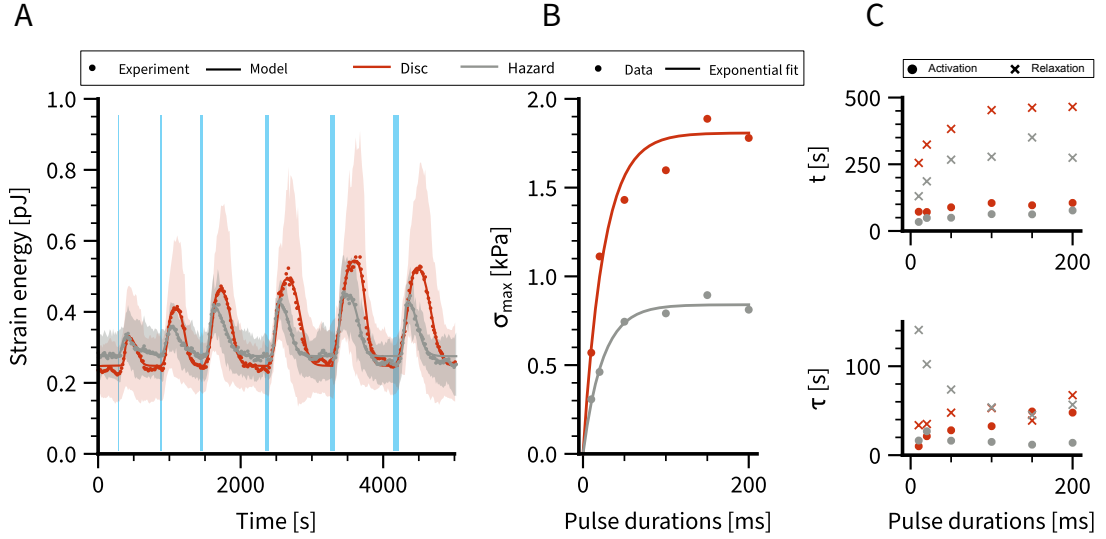


Figure 4.12: Panel **A** shows the dynamics of the strain energy during a series of light pulses of increased duration. The duration is highlighted by the width of the blue vertical lines. Dotted curves represent experimental mean data and shaded regions depict the standard deviation. The numerically computed strain energy is represented by the solid lines. The averages correspond to a reduced data set containing 7 cells. Panel **B** shows the maximal photoactivation stress as extracted by the model fits (circles). Lines correspond to exponential fits. Panel **C** shows the time constants of the double-sigmoid activation profile.

the homeostatic response of cells upon photoactivation with a clear setpoint.

In this sense our model was able to explain the influence of actin architecture and cell size on traction forces. We found that the homeostatic internal cell stresses and force transmission to the substrate are positively correlated with cell size. In contrast, changes in actin geometry had little influence on homeostatic stress and strain energy levels. Nevertheless, purely theoretical considerations could identify geometrical aspects which explain the tendency to higher strain energies for the disorganized in comparison to the polarized actin architecture. Therefore, this result highlights that it is indispensable to consider the internal actin organization of cells when it comes to designing a predictive mathematical model.

Optogenetic activation was introduced by phenomenological activation functions which could possibly describe the time course of the stress induced by the light perturbation. In this way we could partly decouple the optogenetic activation (input) and the resulting strain energy response as a function of time (output). Empirically, we found that the double-sigmoid best fits our experimental data as it respects the smooth shape of the experimental curve. Furthermore, its time course is very similar to the time course of myosin light chain activity during local RhoA perturbations (*Kamps et al.*, 2020; *Staddon et al.*, 2022). The amplitude and time constants of the double-sigmoid allowed us to quantify the differences between the two pattern geometries in the context of the distinct actin organization they induce. We found that the dynamics of internal force generation are remarkably distinct. Cells on hazard pattern are less responsive to photoactivation compared to cells on disc pattern. However, the strain energy response is not as distinct as the stress response which suggest that the reduced force generation in the hazard pattern is compensated by stronger focal ad-

hesions which better couple to the fibronectin pattern. By means of a minimal model we identified a possible reason for the reduced stress generation for cells plated on the hazard pattern. The triangular arrangement of stress fibers suggests that they partly work against each other. Therefore, stress fibers have to be stronger in order to exert the same net traction forces as stress fibers that pull in the same direction. Hence, this simple consideration may explain the lower force generation capabilities for cells on the hazard pattern but we note that this consideration completely disregards the influence of the reaction diffusion system. In the future, the latter could be investigated by modeling the interplay between actomyosin system and photoactivation on a microscopic level for example by means of agent based methods (*Belmonte et al.*, 2017; *Stam et al.*, 2017).

From the resulting time scales we deduce that for cells on hazard pattern stress builds up earlier and increases on a faster time scale. This is different for cells on the disc pattern for which stress builds up much later but remains elevated for a longer time span. Furthermore, we found that stress relaxation in cells on the hazard pattern was strongly influenced by the duration of photoactivation as stress relaxation becomes faster with increasing pulse duration. This could not be observed for the more polarized cells on the disk pattern. In addition, on both pattern, stresses saturate for a pulse duration of approximately 25 ms. However, the stress saturation level for the disc pattern is more than twice that of the hazard pattern and in addition remains high for a longer time.

Since our results indicate highly versatile dynamics associated with actin architecture, we expect even greater dynamic variability when cells are optogenetically activated during their spreading process. This could possibly even make it possible to control the spreading process by directing the formation of the actin CSK in a specific direction.

In suammary, we found that actin architecture of adherent cells plays a major role in terms of force generation and regulation of the underlying biochemistry of the RhoA signaling pathway. Moreover, our results suggest that the spreading process, particularly evident in actin architecture, influences the way the cell later perceives its environment.

Chapter 5

Optogenetic control of cell pairs

Motivated by the results of Chapter 4, where we successfully combined theoretical modeling and experimental techniques to gain insight into the dynamics of force generation from optogenetically activated single cells, we now turn to a similar study of cell pairs. While the focus in the previous chapter was on the dynamics of force generation, in this study we apply similar computational and experimental techniques but in the context of a multicellular system. In particular, we focus on the force transmission across cells. The results presented in this chapter are based on the manuscript with the working title “*Force propagation between epithelial cells depends on active coupling and mechano-structural polarization*” (not yet published) and were obtained in close collaboration with Artur Ruppel, Vladimir Misiak and Martial Balland from the Université Grenoble Alpes, who conducted the optogenetic experiments and TFM.

5.1. INTRODUCTION

Force generation of adherent cells is an essential mechanism by which cells probe their environment. Processing these external mechanical and geometric influences affects the future behavior of the cell which in turn may have drastic effects on survival, proliferation, differentiation, migration and fate (C. S. *Chen et al.*, 1997; *Geiger et al.*, 2009; *Janmey et al.*, 2009). Transferring this to the multicellular level, the interplay of these processes is essential for tissue growth and morphogenesis as it controls position, shape, size and cell number. Therefore, investigating mechanisms by which force generation is regulated and further how these forces are propagated across tissues is key to understanding the large-scale behavior of cells particularly during development or other physiological and pathological processes (*Heisenberg et al.*, 2013). Recent studies addressed some of these important questions and could show that mechanical signals can propagate on length scales much larger than the typical cell size (*Peyret et al.*, 2019; *Serra-Picamal et al.*, 2012). For confined epithelial cell sheets, *Peyret et al.* (2019) could even provide evidence for oscillatory states suggesting an underlying active mechanism of cell contractility in combination with F-actin polymerization. In addition, *Ng et al.* (2014) demonstrated that passive cells may act as attenuators for wave propagation in epithelial tissues. In summary, these studies suggest that cells actively sustain the strength of mechanical signals and thereby propagating it across tissues. However, many questions still remain unanswered and little is known about certain aspects such as the distance that force signals may travel and how tissue polarization influences signal propagation.

Therefore, we introduce a minimal tissue which aids in deepening the understanding of how mechanical signals are transmitted across intercellular junctions and thereby addressing some of the above mentioned questions. This system is comprised of two interacting epithelial cells on an H-shaped micropattern (doublet). The minimalist design allows spatio-temporal control of active force generation while monitoring force propagation across the cell-cell junction. The active force generation is controlled by non-neuronal optogenetics based on the CRY2/CIBN system (*Valon et al.*, 2015; *Valon et al.*, 2017) while force propagation within the substrate and within the cell is quantified by means of TFM and MSM, respectively.

To give a general overview, we explain some of the experimental detail in Section 5.2.

Further, in Section 5.3 we introduce the anisotropic contour model as an analysis tool to link cell shape and traction forces. The model-based analysis allows us to characterize the homeostatic state of the cell doublet which is further compared to a single cell on the same pattern. We find that the presence of a cell-cell junction induces changes in the mechanostructural polarization of the system and a redistribution of traction forces.

In Section 5.4 we use a similar finite element model as introduced in Chapter 4, however, this time for the adhesion geometry of the H-pattern. Further, we use a finite element formulation of the contour model as presented in Section 3.3. By photoactivation of the full doublet and full singlet we are able to parametrize both of our models in order to naturally extend them to local photoactivation. Next, we use both, the two track modeling approach and a combination of TFM and MSM to demonstrate that cells in a cell doublet are actively coupled. We then show that the propagation of the active force depends on system parameters such as the length of the intercellular junction and the mechanical polarization, and that the force propagation is most efficient perpendicular to the direction of mechano-structural polarization.

Finally, in Section 5.5 we verify that our findings translate to larger systems. By following the same procedure as for the minimal system, we show that in small cell clusters stress propagation is amplified perpendicular to the axis of mechano-structural polarization.

5.2. EXPERIMENTAL SETUP

All experiments were carried out on opto-MDCK and opto-MDCK LifeAct cells which have been kindly provided by Manasi Kelkar and Guillaume Charras. The cells were then plated on micropatterned polyacrylamide hydrogels with a Young's modulus of 20 kPa which were fabricated by the method briefly outlined in Section 1.2.2. After seeding the cells onto the sample they were left untouched for 16 h to 28 h. This was enough time to allow formation of cell doublets as initial single cells (singlets) divided on the pattern. E-cadherin, vinculin and actin images exemplarily highlight the location of the cell-cell junction, focal adhesions as well as internal stress and peripheral stress fibers. The vertical stress fibers at the left and right cell rim are in very good approximation straight. However, the horizontal peripheral stress fibers,

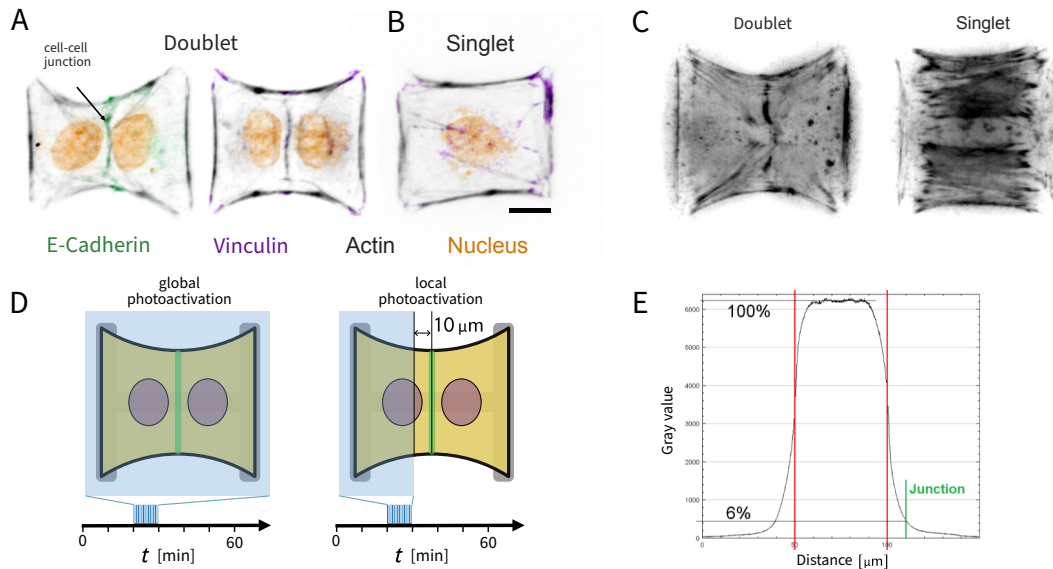


Figure 5.1: Panel **A** and **B** show immunostaining of the opto-MDCK cells with E-Cadherin Vinculin and Actin labeled in green, violet and black, respectively. Nucleus is shown in orange. Panel **C** exemplarily shows life act images of cell doublets and single cell highlighting their internal actin organization and stress fiber orientation. Panel **D** schematically illustrates the two main activation setups stimulation on the whole pattern (left) and on the left half of the pattern (right). Panel **E** shows the intensity profile of the light pulse and its distance from the cell cell junction when activating only the left cell in a cell doublet.

which span between the vertical bars of the H-pattern, exhibit the typical invaginated shape known from cells on pillar arrays (Fig. 5.1A,B).

Cell doublets and single cells can be distinguished on the basis of the cell-cell junction and the number of nuclei (Fig. 5.1A,B). Another striking difference between doublets and singlets is the internal actin architecture most visible in the stress fiber orientation. As can be seen in Fig. 5.1C the singlet exhibits strong internal stress fibers in vertical alignment while the stress fibers in the doublet are less pronounced and rather pointing from the corner towards the cell center. More examples can be found in Fig. A.2A and B.

RhoA activation is controlled analogously to the experiments in Chapter 4 by the CRY2/CIBN system (for details we refer to Section 1.2.3 and Chapter 4). However, the activation protocol differs in two points: First, additionally to global photoactivation, singlets and doublets were also locally activated by illumination of only the left half of the pattern as depicted in the cartoon in Fig. 5.1D. And secondly, this time we activated the cells not with a single light pulse, but with one pulse per minute for 10 min where each pulse had a duration of 200 ms. The intensity profile of the light pulse of 470 nm wavelength is depicted in Fig. 5.1E and we note that the center of the intensity profile was adjusted such that activation of the right half was prevented. For further experimental details as well as information concerning the TFM and the MSM we refer the reader to Artur Ruppel's PhD thesis (*Ruppel, 2022*).

5.3. CHARACTERIZATION OF THE HOMEOSTATIC STATE OF DOUBLETS AND SINGLETS

In this section we provide a detailed description of how we combine cell shape image analysis i.e. automated tracking of peripheral actin fibers, TFM and contour models of cellular adhesion to quantify basic cell properties. First we briefly introduce the ATM and explain how we connect it to traction force measurements. Then we discuss the application to our data.

5.3.1. CONTOUR MODEL BASED CELL SHAPE ANALYSIS

The main concept of contour models have been intensively discussed in Section 1.3.2 and Section 2.2 and are in the following applied to infer basic cell properties based on measurements of the shape of the free spanning actin fiber (Fig. 5.1). The polarized nature of the actin CSK is incorporated through an anisotropic surface tension tensor. The whole contour shape analysis is a composite of several different steps. At first one has to define the mathematical frame work, which in our case is defined by the analytical expression of the contour shape. Next, one has to connect the contour shape to experimentally measured traction force patterns. Once these two steps are accomplished, several numerical steps have to be carried out. These include an image based tracking procedure (fiber tracking) to segment the shape of the fiber and an automated fitting procedure to obtain the cell parameters that define the contour shape. The central quantities of this analysis are surface and line tension of the cell.

ANISOTROPIC TENSION MODEL

Like the TEM, the ATM is based on the force balance equation

$$\frac{d}{ds} (\lambda \mathbf{T}) + (\boldsymbol{\Sigma}_{\text{in}} - \boldsymbol{\Sigma}_{\text{out}}) \mathbf{N} = 0, \quad (5.1)$$

where λ denotes the line tension of the fiber, $\boldsymbol{\Sigma}_{\text{in}} - \boldsymbol{\Sigma}_{\text{out}}$ the surface tension difference across the fiber and \mathbf{T} and \mathbf{N} the two-dimensional Frenet-Serret frame (Section 2.2). The main difference between the STM/TEM and the ATM is that the assumption of a homogeneous isotropic cortex fails in the presence of strongly embedded internal stress fibers. In this scenario, the isotropic surface tension is modified by a directional component aligned with the direction of the internal stress fibers as demonstrated by (Giomini, 2019; Pomp *et al.*, 2018). Since the H-shaped micropattern in all our experiments has two axes of symmetry, we assume an anisotropic surface tension tensor of the form

$$\boldsymbol{\Sigma}_{\text{out}} - \boldsymbol{\Sigma}_{\text{in}} = \begin{pmatrix} \sigma_x & 0 \\ 0 & \sigma_y \end{pmatrix}. \quad (5.2)$$

An essential consequence of this assumption is that, in contrast to the STM and TEM, the line tension varies along the fiber as the second term in Eq. (5.1) has a non-vanishing tangential component for $\sigma_x \neq \sigma_y$. Exploiting the relation between the

tangent vector and the turning angle $\mathbf{T} = (\cos \theta, \sin \theta)$ (Eq. (2.71)) and writing the normal vector as $\mathbf{N} = (-\partial_s y(s), \partial_s x(s))$ allows us to integrate Eq. (5.1) with respect to the arc length parameter s to obtain

$$\lambda \cos \theta - \sigma_x y = C_1^x \quad (5.3)$$

$$\lambda \sin \theta + \sigma_y x = C_1^y, \quad (5.4)$$

where C_1^x and C_1^y denote arbitrary integration constants. Dividing Eq. (5.4) by Eq. (5.3), using $\tan \theta = dy/dx$ and subsequently integrating with respect to x yields

$$\frac{2yC_1^x}{\sigma_x \sigma_y} - \frac{2yC_1^y}{\sigma_x \sigma_y} + \frac{y^2}{\sigma_y} + \frac{x^2}{\sigma_x} = C, \quad (5.5)$$

with C being an additional integration constant. Eq. (5.5) describes an ellipse which, without loss of generality, can be centered around the origin of the coordinate system by setting $C_1^x = C_1^y = 0$ such that

$$\frac{x^2}{a} + \frac{y^2}{b} = 1. \quad (5.6)$$

The semi-axes are given by $a = \sqrt{C\sigma_x}$ and $b = \sqrt{C\sigma_y}$. In the case of $\sigma_x = \sigma_y$ the ellipse attains a circular shape which is consistent with the results of the STM and TEM. Having identified the shape of the contour, we are now interested in finding an analytical expression for the line tension. From Eqs. (5.3) and (5.4) we have

$$\tan \theta = -\frac{x\sigma_y}{y\sigma_x}. \quad (5.7)$$

By solving once for x and once for y and inserting the result into Eq. (5.6) we obtain

$$x^2 = \frac{\sigma_x^2 C \tan^2 \theta}{\sigma_y + \sigma_x \tan^2 \theta}, \quad (5.8)$$

$$y^2 = \frac{C \sigma_y^2}{\sigma_y + \sigma_x \tan^2 \theta}. \quad (5.9)$$

The square of Eq. (5.1) additionally yields

$$\lambda^2 = \sigma_x^2 y^2 + \sigma_y^2 x^2, \quad (5.10)$$

and hence we obtain a closed analytical expression for the line tension as a function of the turning angle θ and the parameters σ_x, σ_y and C

$$\lambda(\theta) = \sigma_x \sqrt{\sigma_y C} \sqrt{\frac{1 + \tan^2 \theta}{1 + \frac{\sigma_x}{\sigma_y} \tan^2 \theta}}. \quad (5.11)$$

For completeness we note that by decomposing the anisotropic surface tension into an isotropic and a directional contribution it can be shown that the integration constant C is connected to a minimal value for the line tension. This minimal value is attained

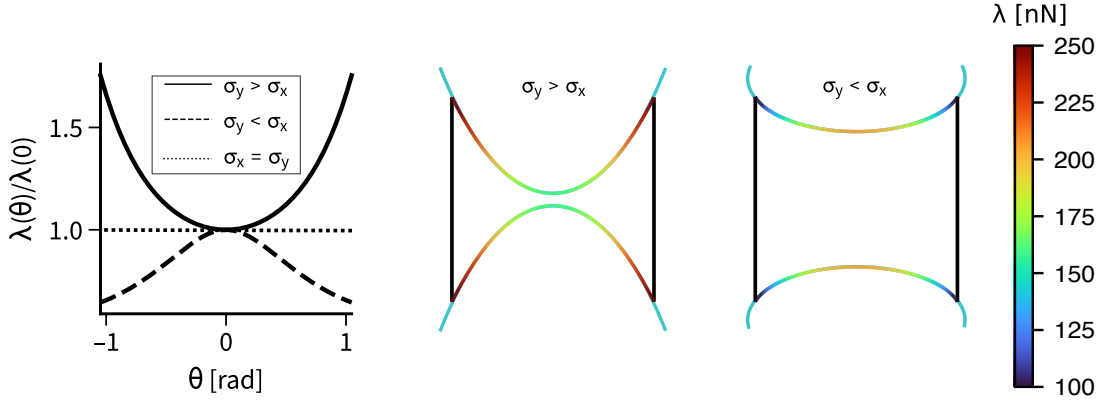


Figure 5.2: Graphical representation of the line tension λ as a function of the turning angle for different ratios of σ_x and σ_y . For our choice of reference frame $\theta = 0$ corresponds to the middle of the fiber. At this point the line tension is either maximal ($\sigma_x > \sigma_y$) or minimal ($\sigma_y > \sigma_x$). In the case of isotropy ($\sigma_x = \sigma_y$) the line tension λ remains constant.

where the tangent vector is orthogonal to the directional contribution, identifying it as a material parameter (Giomi, 2019; Pomp *et al.*, 2018). However, within our description cells are always oriented such that the distance vector \mathbf{d} between the adhesion points of the free spanning arc points along the x -direction of the coordinate system. As a consequence, the prefactor $\lim_{\theta \rightarrow 0} \lambda(\theta) \equiv \lambda_0 = \sigma_x \sqrt{\sigma_y C}$ only represents an extremal value of the line tension. Depending on the ratio of the surface tension components, this extremum is either a maximum for $\sigma_x/\sigma_y > 1$ or a minimum for $\sigma_x/\sigma_y < 1$. In case of $\sigma_x = \sigma_y$ we obtain a constant line tension independent of the turning angle. Plots of the line tension as a function of the turning angle and two exemplarily (exaggerated) cell shapes are shown in Fig. 5.2.

THE ADHESION FORCE

The equilibrium shape of the ATM is a result of the local force balance at every point along the fiber in between the two endpoints. However, for adherent cells, stress fibers (especially peripheral stress fibers) typically start and end at adhesion sites through which the cell establishes a connection to the underlying substrate. In case of point like adhesion, the additional force balance at the two ends is enforced by an additional adhesion force (Bischofs *et al.*, 2009)

$$\mathbf{f}_{\text{ad}} = - \sum_k \mathbf{F}_{\text{trac}}(\mathbf{x}) \delta(\mathbf{x} - \mathbf{x}_k) , \quad (5.12)$$

where the index k runs over all adhesion sites, δ is the Dirac delta distribution and \mathbf{F}_{trac} is the traction force exerted onto the substrate. For simplicity, we use the force balance equation for the isotropic case where $\sigma_x = \sigma_y$ and thus the arc exhibits a constant curvature κ . In this case the full force balance equation reads

$$(\lambda \kappa - \sigma) \mathbf{N} = -\mathbf{f}_{\text{ad}} = \sum_k \mathbf{F}_{\text{trac}}(\mathbf{x}) \delta(\mathbf{x} - \mathbf{x}_k) . \quad (5.13)$$

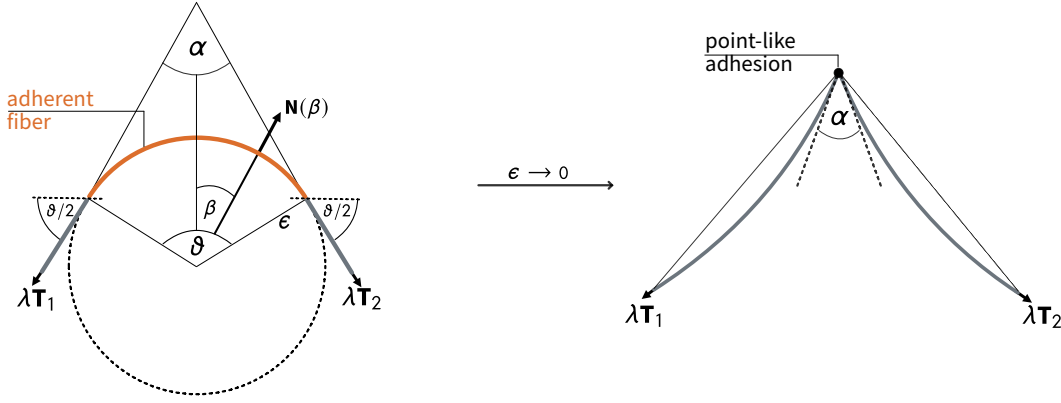


Figure 5.3: Geometrical description of a circular adhesion site (orange) of radius ϵ . The adherent fiber connects the two free spanning arcs which pull with the same line tension λ in tangential direction at the transition from adherent to non-adherent. \mathbf{N} is the outward directed normal on the circle segment going from $\beta = -\vartheta/2$ to $\beta = \vartheta/2$. The limit of an infinitesimal adhesion patch (point-like) leads to a kink at the connection point with opening angle α .

At the adhesion points \mathbf{x}_k , both sides of Eq. (5.13) diverge as $|\kappa| \rightarrow \infty$ in case of a kink. Nevertheless, it is possible to determine the adhesion/traction force as the limit of a continuous circular adhesion patch as depicted in Fig. 5.3. For the sake of simplicity, we assume the line tension of the adherent portion of the fiber to be equal to the line tension of the two free arcs which are smoothly attached on each side. Then, the force balance equation for the continuous adherent fiber reads

$$(\lambda\kappa - \sigma)\mathbf{N} = -\mathbf{f}_{\text{ad}}. \quad (5.14)$$

Using $\mathbf{N} = -\sin\theta\mathbf{e}_x + \cos\theta\mathbf{e}_y$ and $\theta = -\beta$, we obtain

$$\mathbf{F}_{\text{ad}} = \int_{-\vartheta/2}^{\vartheta/2} \mathbf{f}_{\text{ad}} \epsilon d\beta = - \int_{-\vartheta/2}^{\vartheta/2} (\lambda - \sigma\epsilon) \mathbf{N}(\beta) d\beta = -2(\lambda - \sigma\epsilon) \sin\left(\frac{\vartheta}{2}\right) \mathbf{N}(0). \quad (5.15)$$

Next, by taking the limit $\epsilon \rightarrow 0$, the traction force on a point like adhesion site reduces to

$$\mathbf{F}_{\text{trac}} = - \lim_{\epsilon \rightarrow 0} \mathbf{F}_{\text{ad}} = 2\lambda \sin\left(\frac{\vartheta}{2}\right) \mathbf{N}(0). \quad (5.16)$$

The opening angle of the kink is given by $\alpha = \pi - \vartheta$. In conclusion we find that the total traction force exerted at a point like adhesion site is given by the vector sum of the line tensions of the two attached free spanning arcs. We also see, that in this limit the surface tension does not contribute to the traction force directly but indirectly through the radius of curvature of the arc. We conclude that the above findings should also hold in case of arcs with distinct line tensions such that for a point like adhesion we generally propose

$$\mathbf{F}_{\text{trac}} = \lambda_i \mathbf{T}_i + \lambda_j \mathbf{T}_j. \quad (5.17)$$

Eq. (5.17) forms the basis of the cell shape analysis. The traction force measurement defines the left-hand side while the shape of the free spanning arc enters through the tangent vectors on the right-hand side.

FIBER TRACKING

For the quantification of the cell shape based on actin images like the ones shown in Fig. 5.1C, we used a semi-automatic algorithm developed in the research group of Martial Balland at Université Grenoble Alpes which was implemented in MATLAB (*MATLAB*, 2018). As the peripheral fiber moves during contraction we had to fit all 60 consecutive time frames for each cell in order to capture its motion, whereby our data sets include 10 to 40 cells per condition. In total we used this approach to track the contour in several thousand images¹. For each cell, tracking starts by defining the start and end point of the fiber at the first time frame. Next, equally spaced parallel lines perpendicular to the overall fiber direction are drawn, bounded by the endpoints of the fiber. Based on intensity variations the intersections of these lines and the fiber are detected. Intensity fluctuations that may lead to badly detected points are taken care of by a consistency check including a temporal median filter which removed points distant from the mean value by more than two times the standard deviation within a moving time window of ten frames. Additional spatial filtering included removal of outliers that exceeded the range of three times the standard deviation of the average spatial position. Further we imposed an additional constraint that the angles between connecting lines of two adjacent points should stay below 15°. The vertical fibers stay in good approximation straight and static and are therefore not tracked. Drawing of straight lines along the vertical fiber complement the fiber tracking and result in a complete contour of the cell.

FORCE DECOMPOSITION

Analysing the cell shape is equivalent to quantifying the minimal number of key parameters like line and surface tension based on the shape of the free spanning fiber and other quantities accessible through experiments. A basic sketch of the relevant parameters is given in Fig. 5.4A. By means of our analysis we assume that all traction contribution stems from the combined action of the free spanning arc and the vertical “adherent” fiber of length L such that it can be written as

$$\mathbf{F}_{\text{trac}} = F_{\text{ad}}\mathbf{e}_y + \lambda\mathbf{T}(\theta_{\text{fa}}) + \sigma_x\frac{L}{2}\mathbf{e}_x, \quad (5.18)$$

where \mathbf{F}_{trac} is the traction force measured in the substrate, θ_{fa} denotes the tangent angle at the focal adhesion and $\lambda\mathbf{T}(\theta_{\text{fa}})$ is the line tension at the focal adhesion. The last term in Eq. (5.18) is a correction term stemming from the surface tension which acts perpendicular to the vertical fiber. We note that a force decomposition like this assumes a point like adhesion at the intersection of the two fibers for which the force vectors add up (Eq. (5.17))

The right image of Fig. 5.4B schematically illustrates the procedure of determining

¹Alternatively we tried the ImageJ plugin JFilament (*Li et al.*, 2009; *Smith et al.*, 2010) which failed (only) because of too long computing time in view of the large amount of image data. Nevertheless, JFilament is a great tool to automatically track linear objects in an image sequence if the performance is not important.

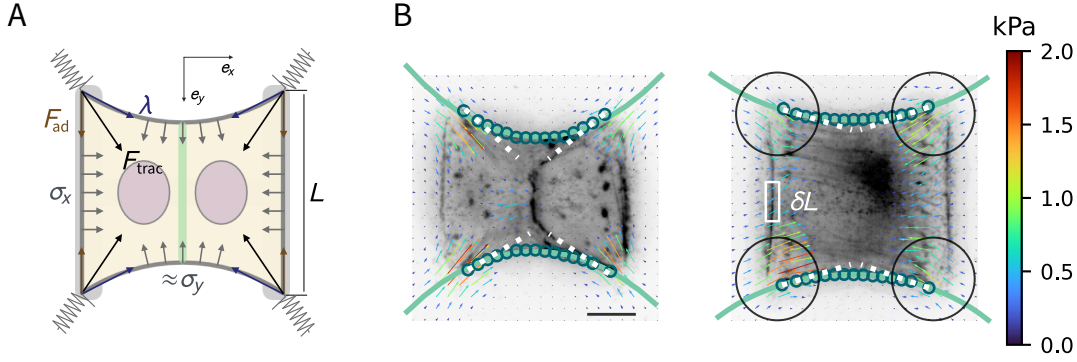


Figure 5.4: Parametrization and result of the shape analysis procedure. Panel **A** shows the parameters which are involved in the shape analysis of the cell according to the contour model. The traction force in the corner is decomposed into contributions stemming from the action of the line tension of the free fiber, the adherent fiber and the x -component of the surface tension tensor. Panel **B** exemplarily depicts the result of the cell shape analysis for doublets (left) and singlets (right) with the fiber tracking data (blue circles), the traction force maps (colored arrows), the tangent vectors at the adhesion points (white dashed lines) and the elliptical arc fitted to the free fiber (green line). Black circles denote the area over which traction forces were integrated and then projected onto the tangent of the free fiber to obtain its line tension and the y -axis to obtain the force of the adherent fiber. The white box schematically illustrates the procedure for estimating the x -component of the surface tension (additional information can be found in the main text). The scale bar corresponds to $10\ \mu\text{m}$.

F_{trac} and the correction term. The total traction force F_{trac} was computed by splitting the traction force map into four quadrants around the symmetry center of the cell. Then, we integrated the traction forces within a radius of $12\ \mu\text{m}$ around the maximal traction peak in each quadrant. This procedure overestimates the traction force in x -direction resulting in the necessity for the correction term. Therefore, the overall force contribution originating from the x -component of the surface tension was estimated by defining a small region (Fig. 5.4B white square) around the center of the adherent fiber. Since the vertical dimension δL was chosen to be very small and very distant from the corners we may assume that the traction stresses integrated over the box are the contribution from the surface tension. This allowed us to estimate the x -component of the surface tension $\sigma_x = \delta F / \delta L$ directly from the TFM maps, where δF corresponds to the integral of the traction stresses over the small window. Finally, by solving Eq. (5.18) for λ and F_{ad} we obtain

$$\lambda = \frac{1}{T_x} \left(F_{\text{trac},x} - \sigma_x \frac{L}{2} \right), \quad (5.19)$$

$$F_{\text{ad}} = F_{\text{trac},y} - \frac{T_y}{T_x} \left(F_{\text{trac},x} - \sigma_x \frac{L}{2} \right), \quad (5.20)$$

where the tangent of the free arc at the focal adhesions are the remaining unknowns and determined by the fit.

CIRCLE AND ELLIPSE FITTING PROCEDURE

It turned out, that fitting ellipses directly to “short” arcs is very unstable and highly depends on the initialization of the fit parameters. This is because one can find a

wide range of ellipses that fit equally well. Due to our large data sets it was not feasible to fit ellipses by hand. Therefore, we decided to use a very stable and fast circle fitting algorithm to obtain an estimate for the tangent vector at the adhesion point². For the circle fitting we exploited a *Hyper least squares* algorithm presented in (Kanatani *et al.*, 2011) based on algebraic distance minimization. Together with already determined parameters from TFM data and circle fitting which include σ_x , θ_{fa} , $\mathbf{T}(\theta_{\text{fa}})$ and $\lambda(\theta_{\text{fa}})$, the remaining unknowns are the y -component of the surface tension σ_y as well as the center of the ellipse \mathbf{x}_c . Using Eq. (5.11) evaluated at θ_{fa} yields

$$a = \frac{\lambda(\theta_{\text{fa}})}{\sqrt{\sigma_x \sigma_y}} \sqrt{\frac{1 + \frac{\sigma_x}{\sigma_y} \tan^2(\theta_{\text{fa}})}{1 + \tan^2(\theta_{\text{fa}})}} \quad (5.21)$$

$$b = \frac{\lambda(\theta_{\text{fa}})}{\sigma_x} \sqrt{\frac{1 + \frac{\sigma_x}{\sigma_y} \tan^2(\theta_{\text{fa}})}{1 + \tan^2(\theta_{\text{fa}})}}, \quad (5.22)$$

such that the shape of the ellipse purely depends on σ_y and its position is defined by its center \mathbf{x}_c

$$\frac{(x - x_c)^2}{a^2} + \frac{(y - y_c)^2}{b^2} = 1. \quad (5.23)$$

We then minimized the squared distance of all tracking points along the fiber to the ellipse (Eq. (5.23)) and optimized the values for σ_y and the center of the ellipse. Exemplarily, a graphical result of the whole shape analysis procedure is depicted in Fig. 5.4B which, additionally to actin and TFM data, shows the result of fiber tracking (circles) together with the resulting ellipse fit for a single time frame. Supplementary, we compare the standard deviations for circle fits and ellipse fits in Fig. A.3A. In all cases, the ellipse fit yields a smaller standard deviation, although the differences vary for the different aspect ratios of the pattern. Based on the visual impression together with the standard deviation of the contour fits, we conclude that the ATM is a suitable description for the shape of the free arc and in our case better suited than the standard TEM model.

5.3.2. RESULTS

We will now compare the result of the cell shape analysis to TFM and MSM measurements to gain insight into the fundamental differences between singlets and doublets. In particular, we focus on the influence of the intercellular junction on fundamental properties such as actin organization, strain energy, internal cell stresses, and cell shape-influencing parameters such as line tension and surface tension.

As a result of the traction force analysis (Fig. 5.5A) we found that the traction pattern of singlets and doublets on average look very alike. Although the traction force magnitude in both conditions is very similar, the quantification of the substrate

²Although it is also possible to obtain the tangent vector directly from the fiber tracking data, we found through trial and error that this method is prone to large fluctuations.

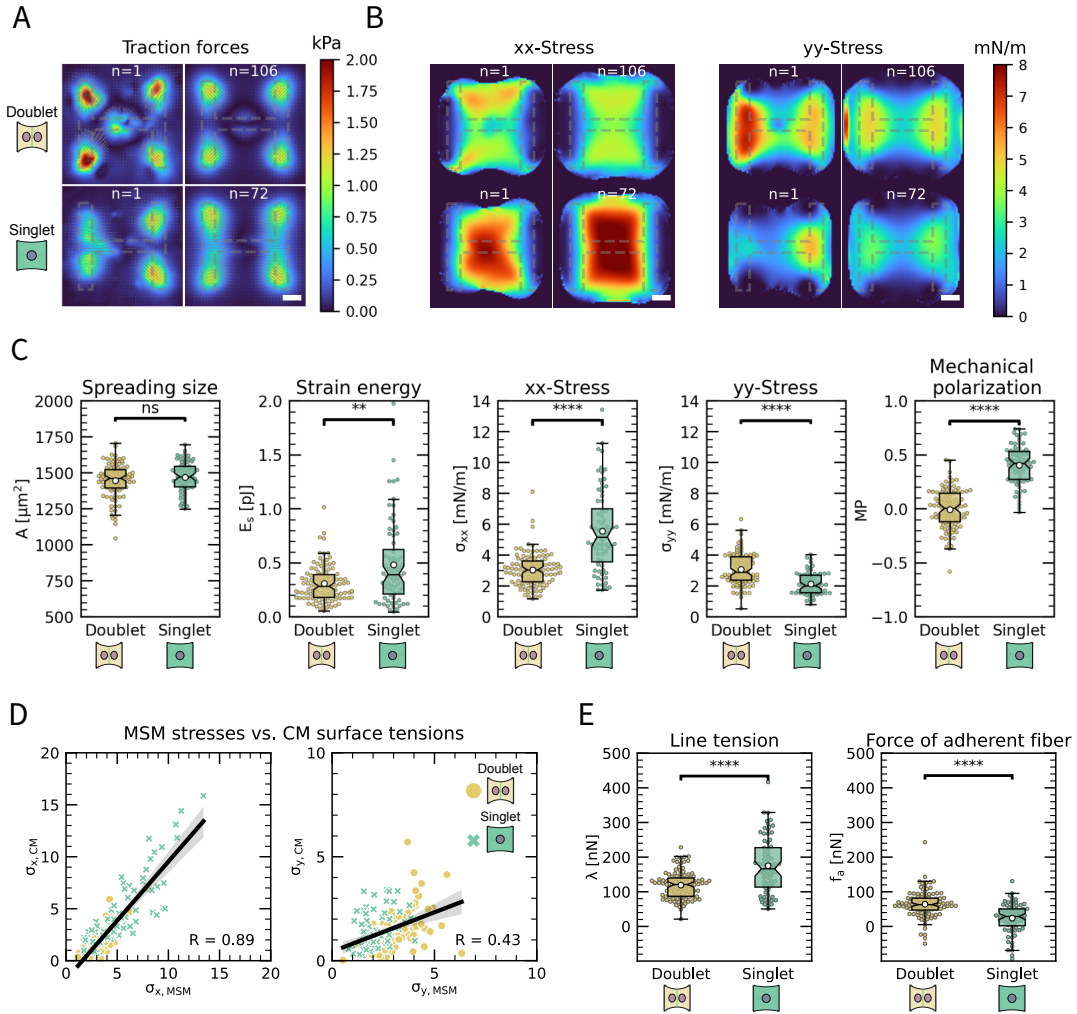


Figure 5.5: Results of the traction force analysis and monolayer stress microscopy in comparison to the contour shape analysis. Panel A shows the traction force maps of doublets and singlets. Individual samples are shown on the left side and averages are shown on the right side. Panel B depicts the result of the monolayer stress microscopy applied to the traction force maps in panel A. Individual samples are shown on the left side and averages are shown on the right side. Panel C shows boxplots of: Spreading size, representing the cell area within the cell periphery. Strain energy in the substrate, deduced from traction force map and bead displacements. Average xx- and yy-stress calculated from the stress maps shown in panel B. Mechanical polarization defined as the difference of xx- and yy-stress divided by their sum. Panel D shows correlation plots of the average xx- and yy-stresses from monolayer stress microscopy and the surface tensions from the cell shape analysis. Yellow dots correspond to doublets and green crosses correspond to singlets. The black line represents the linear regression of the data and the 95% confidence interval is shown as a grey shaded area. The R-value denotes the Pearson correlation coefficient. Panel E summarizes the result of the cell shape analysis represented by boxplots of the line tension of the free fiber and the force of the adherent vertical fiber. Doublets and singlets are shown in yellow and green, respectively. All plots show data from $n = 106$ doublets from $N = 10$ samples and $n = 72$ singlets from $N = 12$ samples. Scale bars correspond to $10\ \mu\text{m}$.

strain energy yielded a slightly lower value for doublets than for singlets (Fig. 5.5B), in spite of the equal spreading area (Fig. 5.5C). However, singlets have to spread a much smaller volume over the same area. As a consequence this may result in a higher tension. Further, singlets do not have to establish any cell-cell junction and thus could be better coupled to the substrate.

Next, we performed a MSM analysis by exploiting the python based software pyTFM (*Bauer et al., 2021*) providing our TFM data as input. The results of this analysis are shown in Fig. 5.5B and C. Since the thin-layer approximation is essential for the MSM, the obtained stresses have the physical unit of a surface tension given by $[\sigma_{ii}^{\text{MSM}}] = \text{mN m}^{-1}$. We found that the internal stresses in σ_{xx}^{MSM} (x -direction) and σ_{yy}^{MSM} (y -direction) are similar on average, indicating a more isotropic internal actin structure. In contrast, for singlets the stress in x -direction yielded a significantly larger value (Fig. 5.5B,C). Based on this observation we defined the mechanical polarization as

$$\text{MP} = \frac{\sigma_{xx}^{\text{MSM}} - \sigma_{yy}^{\text{MSM}}}{\sigma_{xx}^{\text{MSM}} + \sigma_{yy}^{\text{MSM}}}, \quad (5.24)$$

which allows to quantify and compare the internal cellular stress distribution of these systems. This quantity assigns a value of 1 to a horizontally polarized system ($\sigma_{yy}^{\text{MSM}} = 0$), a value of 0 to an isotropic system ($\sigma_{xx}^{\text{MSM}} = \sigma_{yy}^{\text{MSM}}$) and a value of -1 to a vertically polarized system ($\sigma_{xx}^{\text{MSM}} = 0$). Indeed, we found a mean value of $\text{MP} \approx 0$ for doublets and $\text{MP} \approx 0.4$ for singlets which means that σ_{xx}^{MSM} is approximately three times larger than σ_{yy}^{MSM} . Analogously to Chapter 4, we quantified the structural polarization i.e. the internal stress fiber orientation by computing the structure tensor \mathbf{J} for the actin images (Appendix A.4). We found a strong correlation between structural and mechanical polarization (Fig. A.2C). This confirms that singlets have predominantly horizontally oriented stress fibers, while doublets have mostly diagonal orientations (from corner to center). Our findings suggest that intercellular junctions may prevent horizontal stress fiber organization by acting as a barrier. Hence, the cell-cell junction may strongly alter the mechanical polarization of cell-cell systems.

Through the MSM analysis we could estimate the internal cell stresses purely based on the traction force measurement. However, this approach ignores the mechanical properties of the cell periphery and the action of the internal actin structure onto the peripheral stress fibers. Therefore, we applied the contour model which allows us to extract values for the surface tension of the actin cortex and the line tension of the free spanning fiber. As can be seen in Fig. 5.5D, the results of the contour analysis are in good agreement with the MSM. The surface tension components as predicted by the cell shape analysis are well-correlated with the cell stresses obtained by the MSM. In particular, we found that in doublets the y -component of the surface tension dominates over the x -component, while in singlets it is the reverse (Fig. 5.5D), which again agrees with the MSM measurement. Following the trend of the structural and mechanical polarization singlets exhibit strong peripheral stress fibers with a higher line tension ($\approx 180 \text{ nN}$) than in doublets ($\approx 120 \text{ nN}$) (Fig. 5.5E). Interestingly, the force of the adherent fiber is larger in doublets than in singlets, which again, is consistent with the trend of mechanical and structural polarization of doublets (Fig. 5.5E). Our values

for the line tension in the free fiber are, moreover, also consistent with previously reported values for the line tension. For example, for fibroblasts adhered to X-shaped pattern *Labouesse et al.* (2015) find a line tension of approximately 60 nN for traction force magnitudes in the order of 500 Pa. Taken together, we interpret our results as a cell-cell junction induced redistribution of forces from the free to the adherent fiber.

5.4. PHOTOACTIVATION- DOUBLETS VS. SINGLETSS

Following on from the previous section we decided to aim for a two-track simulation approach including two-dimensional FEM simulations (2D FEM) and contour model finite element simulations (contour FEM) for the optogenetic experiments. The former allow to directly control the internal active stresses on the activated and non-activated side which consequently are directly comparable to the MSM stresses upon photoactivation. The latter allow to quantify curvature changes of the free peripheral fiber as a result of global and local photoactivation and provide insight to the mechanics of the peripheral stress fiber. We make use of the global photoactivation experiments to parameterize both of our FEM approaches. After parametrization we simulate local photoactivation in order to quantify the effect of active coupling between the activated and non-activated side.

5.4.1. MODELING

TWO DIMENSIONAL FEM ON H-PATTERN

The approach for the two-dimensional simulation is very similar to Chapter 4. The cell is described as a thin viscoelastic contractile sheet adhered to the H-shaped micropattern. By exploiting the results of the static MSM quantification of the previous section, we may directly incorporate the mechanical polarization into our model

$$\boldsymbol{\sigma}_{\text{bck}} = \begin{pmatrix} \sigma_{xx}^{\text{bck}} & 0 \\ 0 & \sigma_{yy}^{\text{bck}} \end{pmatrix} = \sigma_{xx}^{\text{bck}} \begin{pmatrix} 1 & 0 \\ 0 & \frac{1-\text{MP}}{1+\text{MP}} \end{pmatrix}. \quad (5.25)$$

In contrast to Chapter 4 the time course of the measured substrate strain energy exhibits an overall concave shaped rising edge (Fig. 5.7). This is most likely a consequence of the altered activation protocol. Instead of a single light pulse we activated the cells ten times with a 200 ms long light pulse every minute. Data points were taken every 60 s. Therefore, instead of a double-sigmoidal activation profile we decided to use the combination of an increasing saturating exponential and a sigmoidal shaped decrease (Fig. 5.6A)

$$\sigma_{\text{PA}}(t) = \sigma_0 \left(1 - e^{-\frac{t-t_{\text{act}}}{\tau_{\text{act}}}} \right) \left(1 - \frac{1}{1 + e^{-\frac{t-t}{\tau_{\text{rel}}}}} \right), \quad (5.26)$$

as it leads to almost perfect fits (Fig. 5.7A). The parameter t_{act} was, according to the experimental activation time point, set to $t_{\text{act}} = 20$ min. The stress increase upon

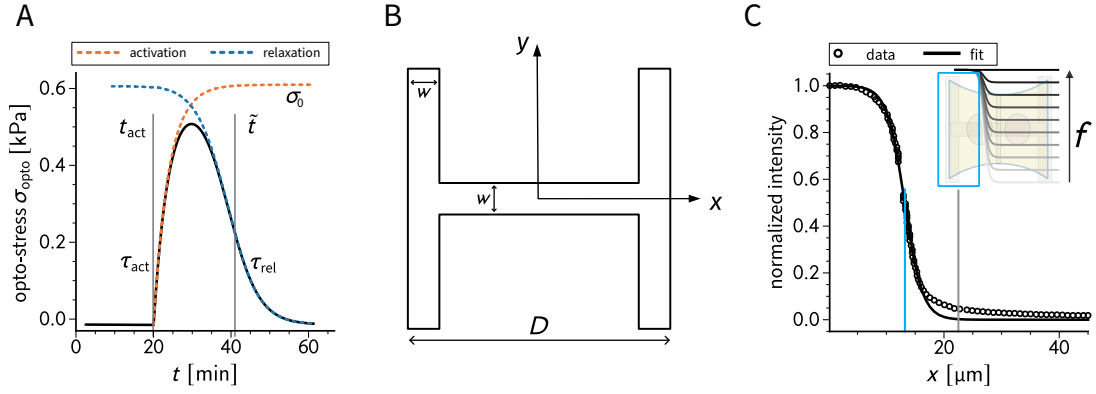


Figure 5.6: Active stress profile, parametrization of the H-pattern and spatial intensity profile of the light-pulse during photoactivation. Panel **A** shows the active stress profile used to model stress generation upon photoactivation. It is constructed by combination of an increasing saturating exponential and a sigmoidal shaped decrease. t_{act} denotes the time point of photoactivation (left vertical grey line), τ_{act} , τ_{rel} and \tilde{t} resemble the activation and relaxation time scale and the onset of stress relaxation (right vertical grey line), respectively. Panel **B** illustrates the parametrization of the H-pattern. Panel **C** shows the spatial intensity profile of the light pulse during illumination of the left half of the pattern. Circles denote experimental data and the black solid line depicts a sigmoidal fit. The vertical blue line shows the center of the sigmoid and the grey line depicts the center of the pattern. The inset shows the intensity profile for a varying degree of active coupling which was used to account for an active feedback on the non-activated portion of the pattern.

photoactivation is defined by the activation time scale τ_{act} . The stress relaxation is characterized by two time scales \tilde{t} and τ_{rel} describing the onset of stress relaxation and the time scale of relaxation, respectively. σ_0 is the common saturation level. The fibronectin-coated pattern is illustrated in Fig. 5.6B and mathematically implemented by

$$(x, y)_{Y \neq 0} = \left\{ x, y \mid x \leq w - \frac{D}{2} \vee x \geq \frac{D}{2} - w \vee -\frac{w}{2} \leq y \leq \frac{w}{2} \right\}, \quad (5.27)$$

where we, according to the experiments, set $w = 5 \mu\text{m}$ and $D = 45 \mu\text{m}$.

The effect of local photoactivation was introduced by the intensity profile of the light pulse. The intensity profile was approximated by a sigmoid

$$I(x) = 1 - \frac{1}{1 + e^{-a(x-b)}}, \quad (5.28)$$

and the free parameters $a = 0.65$ and $b = 13.19$ were obtained by fitting Eq. (5.28) to the measured curve (Fig. 5.6C). In order to account for an active response on the non-stimulated side of the pattern, we modify the intensity profile such that it reaches a constant level f as $x \rightarrow \infty$

$$\tilde{I}(x) = (1 - f) \left(1 - \frac{1}{1 + e^{-a(x-b)}} \right) + f. \quad (5.29)$$

The parameter $f \in [-1, 1]$ controls an active stress level on the non-activated side and is referred to as the *degree of active coupling*. Positive and negative values for f correspond to active contraction and active relaxation, respectively. A value of $f = 1$ is equivalent to the case of global photoactivation. The intensity profile as a function of f is shown in Fig. 5.6C (inset). The time-dependent opto-stress tensor is modified

by the spatial distribution of the intensity profile by multiplication³

$$\tilde{\sigma}_{\text{PA}}(x, t) = \sigma_{\text{PA}}(t)\tilde{I}(x) . \quad (5.30)$$

CONTOUR BASED FEM

The modeling procedure for the contour simulation is very similar to the two-dimensional version explained above. The aim was to quantify the active coupling between activated and non-activated side. The contour FEM is implemented analogously to Section 3.3 with a weak form as presented in Eq. (3.35). Yet, in order to use our contour FEM to complement the experimental measurements, we need to increase the level of detail for the mechanical properties of the free fiber.

In the spirit of the TEM we split the line tension into an active and elastic contribution where the first accounts for the elastic properties of the cross-linking proteins within the actin bundle and the latter is an active contribution stemming from myosin II motors. Therefore, we assume

$$\lambda = \lambda_{\text{el}} + \lambda_{\text{act}} . \quad (5.31)$$

This specific choice corresponds to the case of a parallel connection of active and elastic elements. In a serial connection the total line tension would be fully determined by the active motors. *Labouesse et al.* (2015), however, showed that a purely serial linkage of active and elastic elements cannot explain the observed shape changes of free spanning arcs during drug induced inhibition of myosin II activity, which motivates our choice for a parallel connection of active and passive elements.

We further assumed a linear constitutive relation between stress and strain for the elastic component

$$\lambda_{\text{el}} = EA\epsilon = EA(\nu(\hat{s}) - 1) , \quad (5.32)$$

which is directly connected to the stretch of the fiber $\nu(\hat{s})$ as defined in Eq. (2.58). The rest length of the fiber is set to the spanning distance $\hat{L} = d$ but in principle a value of $d < \hat{L}$ is possible. Here, EA denotes the one-dimensional modulus of the fiber as a product of Young's modulus E and the cross-sectional area A of the fiber. Consensus values for single actin filaments are for example $A_{\text{fil}} = 18.8 \text{ nm}^2$ and $E_{\text{fil}} = 2.8 \text{ GPa}$ (*Gittes et al.*, 1993). Hence, single actin filaments have a one-dimensional modulus of $E_{\text{fil}}A_{\text{fil}} = 52.6 \text{ nN}$. Interestingly, the one dimensional modulus for stress fibers is in the same order of magnitude $E_{\text{fib}}A_{\text{fib}} = 45.6 \text{ nN}$ with $E_{\text{fib}} = 1.45 \text{ MPa}$ and $A_{\text{fib}} = 31416 \text{ nm}^2$ (*Deguchi et al.*, 2006) despite having a three orders of magnitude smaller Young's modulus. From this one may conclude that not actin itself but rather the cross-linking proteins, such as α -actinin and myosin II, mainly dictate the elastic properties of stress fibers (*Guthardt Torres et al.*, 2012). The above calculation should

³To keep the activation profile static in the lab-frame (Eulerian frame) we incorporate the, although in many cases negligible, deformation by shifting the activation profile according to the displacement field of the previous time step such that $I(x) = \hat{I}(X + u_x)$. Here, the coordinate X is fixed in the material.

only be regarded as a rough estimate. Based on the reported value by (*Labouesse et al.*, 2015) we conclude that reasonable values are around $EA = 50 \text{ nN} - 350 \text{ nN}$ and set this value to $EA = 300 \text{ nN}$ throughout our contour simulations. All other fixed values for this simulation can be found in Table A.8.

In the context of the contour model we define global activation by an overall increase in surface tension

$$\sigma_i^{\text{PA,max}} = \sigma_i + \sigma_i \cdot \text{RSI}_i^{\text{max}}, \quad (5.33)$$

where $\sigma_i^{\text{PA,max}}$ denotes the respective surface tension component at maximum strain energy, $\text{RSI}_i^{\text{max}}$ is the maximal relative surface tension increase and $i = x, y$. Further, we assume the active line tension to remain unchanged during photoactivation. We motivate this by the observation, that the arc is pulled towards the cell interior upon photoactivation and hence the average radius of curvature of the arc decreases. This indicates that photoactivation has a stronger influence on the contractility of the cortex than on the peripheral arc as can be expected from the Laplace law with $R = \lambda/\sigma$. In this sense, we prevent the ambiguity by keeping λ_{act} fixed throughout, knowing that this might underestimate the surface tension.

Local photoactivation is obviously introduced in exactly the same way as for the 2D FEM simulations by multiplying the photoactivation contribution with the spatial profile (Fig. 5.6C)

$$\sigma_i^{\text{PA,max}}(\hat{s}) = \sigma_i + \sigma_i \cdot \text{RSI}_i^{\text{max}} \cdot \tilde{I}(\hat{s}), \quad (5.34)$$

this time as a function of the arc-length parameter of the unstretched fiber⁴.

PARAMETRIZATION OF THE 2D FEM THROUGH GLOBAL PHOTOACTIVATION

All model parameters were obtained by fitting the 2D FEM model to the experimental strain energy curve from the global photoactivation of singlets and doublets. We first determined the active background stress by fitting our model to the baseline of the strain energy curve from which we obtain σ_{xx}^{bck} . In a second step we then fitted the temporal evolution of the strain energy by optimizing the free parameters $\sigma_0, \tau_{\text{act}}$ and \tilde{t} in Eq. (5.26). The results of the strain energy fits along the Frobenius norm of the total internal stress of the cell layer and the simulated traction force maps are gathered in Fig. 5.7. The optimized parameters are summarized in Table A.6. For both conditions, our model perfectly captures the time course of the relative strain energy (Fig. 5.7A). Cells contract throughout the period of the repeated light pulses, but begin to relax almost immediately after photoactivation terminates. However, the overall strain energy response in doublets is almost twice as large as for singlets. This may be a consequence of the high level of background stress in singlets. Interestingly,

⁴Keeping the activation profile fixed in the laboratory (Eulerian) frame can be achieved by the mapping between the arc length parameters $s(\hat{s}) = \int_0^{\hat{s}} \left| \frac{\partial \mathbf{x}}{\partial q} \right| dq$. Then, the intensity profile has to be shifted to the position \hat{s} at which $x(s) = \hat{s}/2$. For this one has to implement the finite element simulations by an updated Lagrangian approach and shift the intensity profile in each iteration step.

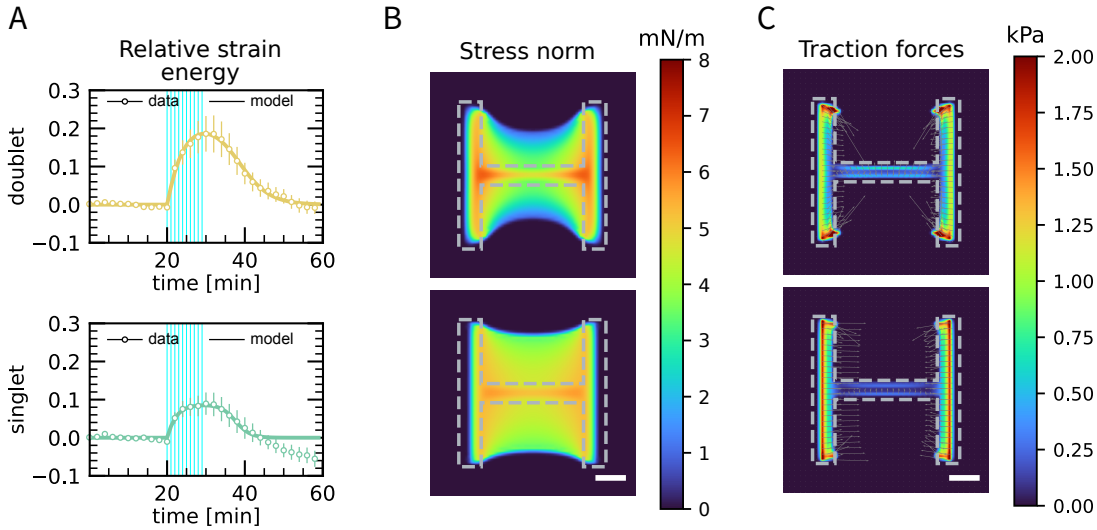


Figure 5.7: Parametrization of the two-dimensional finite element simulations based on the substrate strain energy obtained from global photoactivation of doublets (top row) and singlets (bottom row) on H-patterns. Panel **A** shows the relative substrate strain energy for doublets and singlets as a function of time. The first 20 time frames denote the baseline. The vertical blue lines indicate the time points of photoactivation with a 200 ms long light pulse every minute for 10 min. The strain energy curves were normalized by first subtracting the individual baseline energies (average of the first 20 time frames) and then dividing by the average baseline energy of cell doublets/singlets in the corresponding data set. The data is shown as circles and error bars denote the s.e.m. The fit of the simulated substrate strain energy is depicted by the solid line. Panel **B** shows the Frobenius norm of the total internal cell stress before photoactivation resulting from the finite element simulation. Panel **C** shows the simulated traction force maps. Scale bars correspond to 10 μm . Additional maps comparing singlets and doublets during global photoactivation are shown in Figs. A.4 and A.5.

after photoactivation singlets relax further below their initial level of contractility, whereas doublets recover their homeostatic baseline level (Fig. 5.7A). Moreover, in Fig. 5.7B we show the Frobenius norm of the total baseline stress tensor for doublets and singlets in the deformed configuration as obtained from simulations. As expected, the cell contour of the doublets is stronger invaginated than for singlets as σ_{yy}^{bck} is much larger in doublets (Table A.6). Further, the stresses in singlets are larger in the non-adhesive parts of the simulation domain. In addition, the resulting traction maps resemble the essential features of the experimentally obtained traction maps (Fig. 5.5A). For doublets, the traction maps in Fig. 5.7C show peaks in the corners of the pattern consistent with the experiments. However, here it has to be noted that the very localized large peaks are an artifact of the discrete nature of FEM in combination with the sharp corners of the pattern. For singlets, the large stresses in x -direction result in traction forces all along the vertical bars of the H-shaped pattern (Fig. 5.7C). Besides the absence of clear traction peaks in the corners we point out that the TFM maps show a non-negligible traction force along the vertical bars too (Fig. 5.5A).

PARAMETRIZATION OF THE CONTOUR FEM BY GLOBAL PHOTOACTIVATION

The starting point for the parametrization of the contour FEM simulations were the (experimental) results obtained from the cell shape analysis i.e. the motion of the free spanning stress fibers. In particular, we obtained average values for a , b , σ_x and σ_y as well as the relative stress increase ($\text{RSI}_i^{\text{exp}}$) during photoactivation. From the

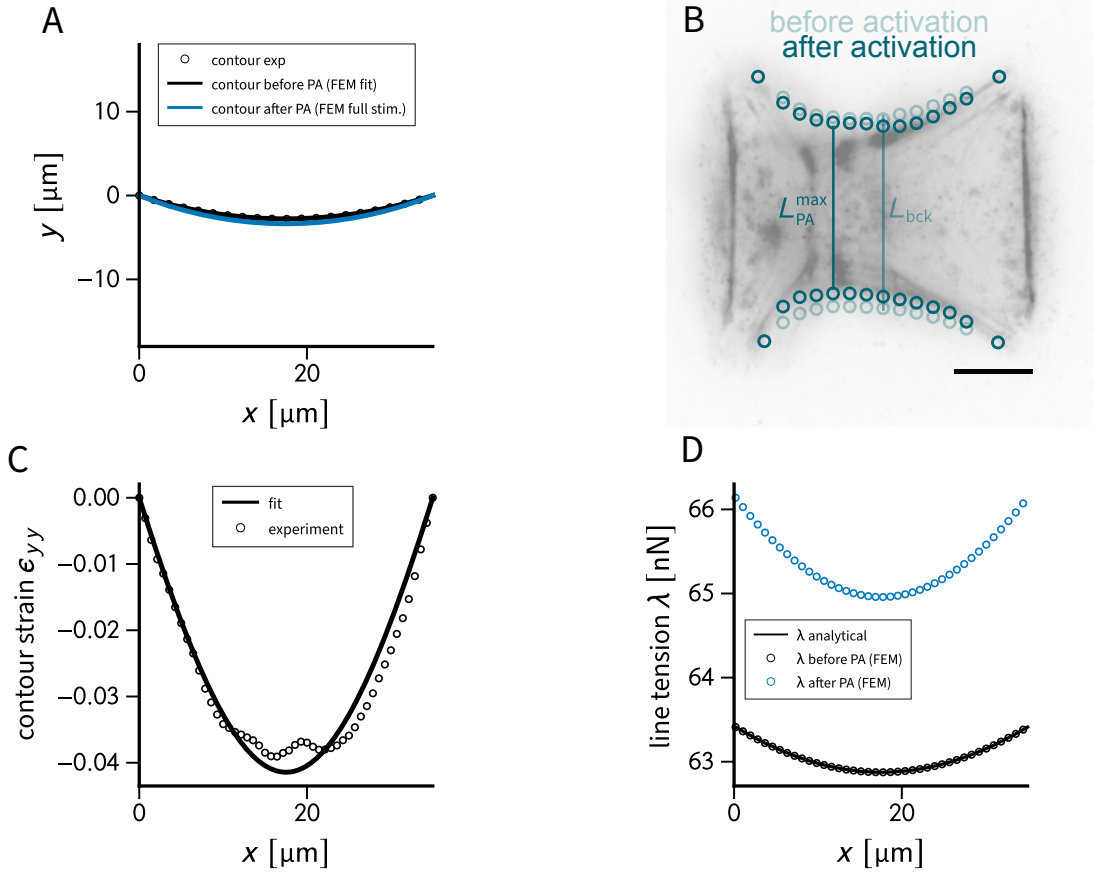


Figure 5.8: Parametrization of the contour FEM through global photoactivation. Panel **A** shows the average cell contour obtained as the average fitting ellipse for a spanning distance of $d = 35 \mu\text{m}$ (full circles). The black line shows the fit of the contour FEM to the average ellipse to obtain the active line tension λ_{act} in the peripheral fiber. The blue line depicts the cell contour at maximal surface tension for a globally stimulated cell. Panel **B** shows the contour strain measurement of the free stress fiber. The inter-stress fiber distance after ($L_{\text{PA}}^{\text{max}}$) and before (L_{bck}) photoactivation is measured along the x -axis for each tracking point (circles) which defines a contour strain. Panel **C** shows the fit of the contour FEM (solid line) to the experimentally measured contour strain (hollow circles). Panel **D** shows the line tension along the fiber, obtained by the contour FEM, before photoactivation (black circles) and at maximal surface tension (blue hollow circles). The shown line tensions correspond to the cases depicted in panel **A** and the parameters listed in Table A.8. The solid line shows the analytically predicted line tension according to Eq. (5.11).

values of the homeostatic state we defined an average contour by fixing the surface tension components σ_x and σ_y as well as the semi-axis a . Subsequently, we computed $b = a\sqrt{\sigma_y/\sigma_x}$. This was necessary since we averaged all those quantities independently of each other such that the averages of the single quantities not necessarily belong to the same elliptical arc as they are connected through the undetermined parameter C . Based on actin images the spanning distance of the fiber was estimated to an average value of $d = 35 \mu\text{m}$ (corresponding to the inner edge of the vertical bars of the H-pattern). The average cell periphery was then obtained by the portion of the average ellipse for which the endpoints have a spanning distance d (Fig. 5.8A). First, we fitted the simulated contour to the average contour by treating λ_{act} as a free parameter (Fig. 5.8A (black line)). For this we again used a simplex algorithm (Nelder *et al.*, 1965).

After that we optimized the values for the relative stress increase in x - and y -

direction (RSI_x^{\max} and RSI_y^{\max} in Eq. (5.34)) to fit the measured contour strain to the one computed with the contour FEM at maximum strain energy. Fig. 5.8B illustrates the contour strain measurement on image data, but is performed in the same way in the simulation. We measure the vertical inter-stress fiber distance after (L_{PA}^{\max}) and before (L_{bck}) photoactivation along the x -axis for each tracking point (circles). This procedure defines a contour strain

$$\varepsilon_{yy} = \frac{L_{\text{PA}}^{\max}}{L_{\text{bck}}} - 1. \quad (5.35)$$

The negative values for the contour strain (Fig. 5.8C) indicate that the free arcs are towards the cell interior during photoactivation. During minimization we made sure that the optimized RSI_i^{\max} lie within the standard deviation of the experimental (cell shape analysis) values $\text{RSI}_i^{\text{exp}}$. This was achieved by using a sequential least squares programming algorithm (SLSQP) (*Kraft et al.*, 1988) implemented in SciPy (*Virtanen et al.*, 2020) which, in contrast to the simplex algorithm, allows constrained minimization. The result of this optimization is depicted in (Fig. 5.8C). The optimized parameters are listed in Table A.8. The parameter estimation based on the global photoactivation data was then completed by a consistency check. We numerically calculated the line tension once by Eq. (5.31) and compared it to the analytical formula in Eq. (5.11) with the input parameters of the simulation. The two approaches perfectly agree (Fig. 5.8D (black line and circles)). Moreover, the additional contour strain upon photoactivation increases the overall line tension (Fig. 5.8D). However, relative to the endpoints of the fiber, the line tension in the center remains minimal as the anisotropy of the actin CSK is not changed during activation.

5.4.2. RESULTS

In order to quantify stress propagation in doublets and singlets we activated the left half of the pattern according to the protocol described in Section 5.2 and determined how this localized stress increase propagates to the non-activated side of the system.

QUALITATIVE STUDY OF LOCAL PHOTACTIVATION - FORCE PROPAGATION

In analogy to the global photoactivation, we quantified the substrate strain energy based on the TFM measurement. However, this time we separately computed the strain energy for the left and right half of the pattern. Based on this quantification we found a striking difference between doublets and singlets (Fig. 5.9A).

In doublets, the strain energy increased on both sides of the pattern, while for singlets only a very slight global increase was notable. In addition, the strain energy of singlets decreases below the initial baseline level without recovery while doublets show a homeostatic response to local RhoA perturbation. Fig. 5.9B additionally shows the corresponding traction force differences between the time point of peak strain energy and the baseline. Red color indicates a traction force increase and blue color depicts a traction force decrease. The FEM simulations showed that simple activation of the left half of the pattern cannot reproduce either case, since the increase in traction force on

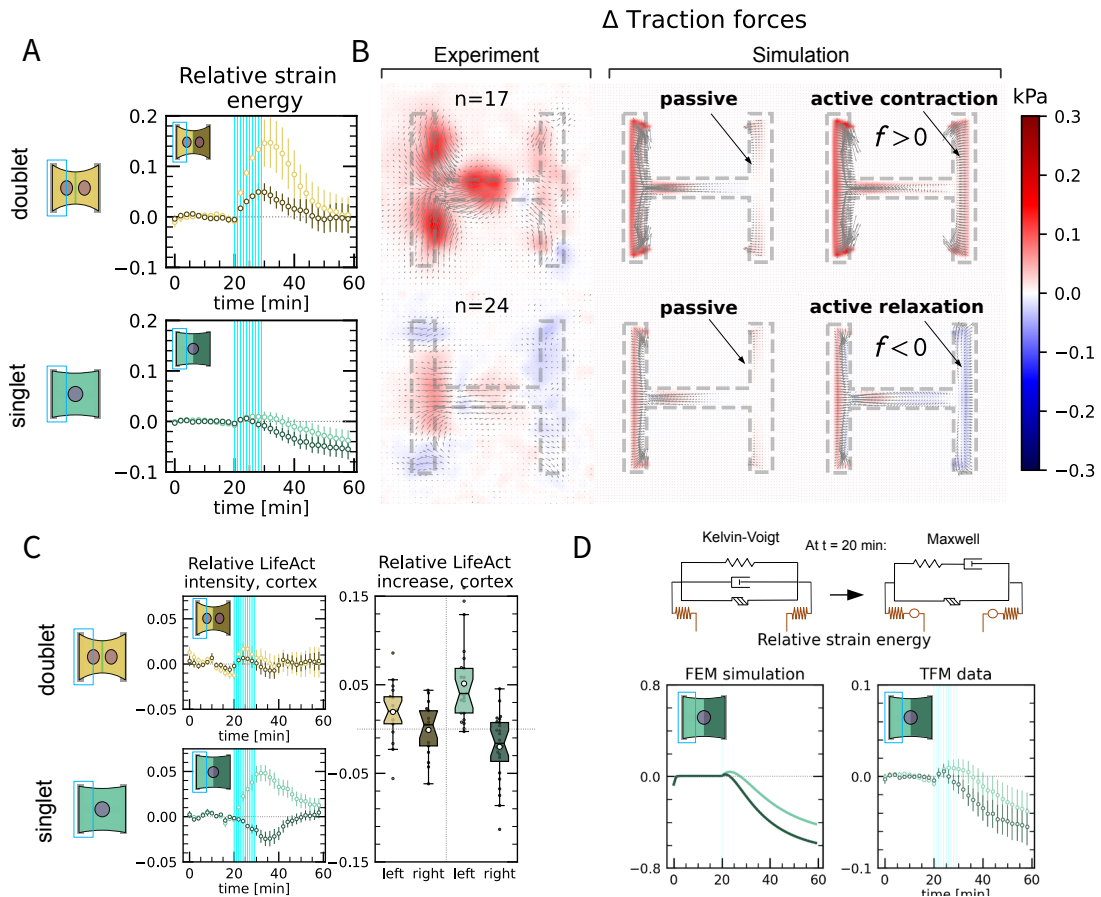


Figure 5.9: Comparison of local optogenetic activation in doublets and singlets. Panel **A** shows the relative strain energy response in doublets (top) and singlets (bottom) for local photoactivation of the left half of the pattern. Strain energy is shown separately for the left half (bright) and right half (dark) of the pattern. The first 20 time frames denote the baseline. The vertical blue lines indicate the time points of photoactivation with a 200 ms long light pulse every minute for 10 min. The strain energy curves were normalized by first subtracting the individual baseline energies (average of the first 20 time frames) and then dividing by the average baseline energy of cell doublets/singlets in the corresponding data set. The data is shown as circles and error bars denote the s.e.m. The left column of panel **B** shows the difference of the average traction force maps after and before photoactivation of doublets (top) and singlets (bottom). The middle column shows corresponding FEM simulations where the left cell was activated corresponding to a purely passive right cell (traction increase indicated by arrows). The right column shows FEM simulations with an active response of the right cell denoted by the degree of active coupling f . Panel **C** compares the lifeact intensity measurement of the activated (bright) and non-activated side (dark) in doublets and singlets. The left sub-panel shows a LifeAct intensity measurement over time. The sub-panel on the right depicts the relative actin intensity value two minutes after photoactivation for the activated and non-activated side. Panel **D** (top) shows the basic elements of the FEM simulation for a qualitative model for fluidization. The dynamics of the singlet can be reproduced by a switch from a Kelvin-Voigt model to a Maxwell model upon photoactivation. Panel **D** (bottom) shows the comparison of the simulated and measured strain energies in the left (bright) and right (dark) half of the pattern during local photoactivation of the left half of the singlet. The experimental relative strain energy curves were calculated in the same way as in **A**. Further details can be found in Appendix A.2. All experimental plots show data from $n = 17$ doublets from $N = 2$ samples and $n = 24$ singlets from $N = 6$ samples.

the non-activated part of the pattern is too low for doublets and too high for singlets. The strain energy curves of the FEM simulations corresponding to the middle column of Fig. 5.9B are shown in Fig. A.3B, emphasizing that a purely passive reaction cannot reproduce and explain the experimental data for both, doublets and singlets. To test whether the observations could be described by active coupling between the activated and non-activated side we made use of the degree of active coupling f as defined in Eq. (5.29). Treating f as a fit parameter allowed to qualitatively reproduce the TFM measurements as can be seen by comparing the first and last column of Fig. 5.9B. These qualitative simulations revealed a positive coupling $f > 0$ for doublets and a negative coupling $f < 0$ for singlets. This implies that in doublets, a contraction on the left side induces an active contraction on the right side i.e. a contraction of the non-activated cell. A negative value for singlets implies that the non-stimulated side actively relaxes as a consequence of contraction on the left side. To study this even further, we tracked the behavior of the actin cytoskeleton during light-stimulation by means of actin fluorescence imaging (F-actin reporter LifeAct). We found that in doublets, the relative actin intensity remains in good approximation constant as can be seen in Fig. 5.9C. Conversely, for the singlets, our data indicates that local RhoA activation on one side is compensated by a stress and F-actin decrease in the non-activated domain. Further, the transient RhoA activation destabilizes the homeostatic state of the singlet as the total traction stresses keep decreasing long after light perturbation. Motivated by other studies (*Andreu et al.*, 2021; *Krishnan et al.*, 2009) we hypothesize that our observations might be a result of acute fluidization of the cytoskeleton upon local stress increase. In contrast to doublets, there is no junctional barrier in singlets and hence F-actin may flow from the non-activated to the activated side during PA. This would also explain the observation that the actin increase and decrease approximately add up to zero (Fig. 5.9C). In Fig. 5.9D we show that a quasi one-dimensional model for fluidization qualitatively captures the time course of the strain energy. Here we introduce fluidization by a model switch from a solid like Kelvin-Voigt-model to a fluid-like Maxwell model. Due to this spontaneous model switch the viscous element provides a strain energy increase in response of the sudden switch. By introducing a viscoelastic coupling to the substrate, analogously to (*Oakes et al.*, 2017), we allow flow-like behavior leading to a strain energy decrease. The finite element implementation as well as the parameterization can be found in Appendix A.2. These results suggest active coupling between cells in cell doublets, with contraction of the left cell inducing contraction in the right cell, consistent with previous qualitative findings (*Hino et al.*, 2020; *Z. Liu et al.*, 2010).

In summary, our results suggests that the intercellular junction supports force propagation across the pattern presumably due to mechanotransductory mechanisms and by preventing fluidization.

QUANTIFICATION OF ACTIVE COUPLING IN CELL DOUBLETS

In order to quantify the magnitude of the active response of the non-activated cell we directly compared a series of FEM simulations to the stress distributions obtained

by MSM (Fig. 5.10A). For this, we varied the degree of active coupling f as a free parameter ranging from -1 to 1 in steps of $\Delta f = 0.1$, in other words, we increased the active response on the non-activated side in steps of 10%. For each value of f , the stress difference $\Delta\sigma_{xx}(x, y)$ and $\Delta\sigma_{yy}(x, y)$ between baseline and maximum strain energy were computed. Subsequently, we averaged the resulting stress difference maps over the y -axis. In this way, we obtain a stress profile as a function of x for each value of f . In Fig. 5.10B we show that the resulting stress profiles for MSM and FEM qualitatively agree but hint towards a distinct coupling strength for stresses in x and y -direction, respectively. In order to consistently compare the experimental to the simulated profiles, the stress increase was normalized by integrating the right half of the curves and dividing that by the integral of the whole curve. This procedure allowed us to translate the family of curves (Fig. 5.10B) into a relationship between the normalized stress response for σ_{xx} and σ_{yy} and the degree of active coupling f as depicted in Fig. 5.10C. Separately for σ_{xx} and σ_{yy} we determined the degree of active coupling which best matches the normalized response of the right half of the experimental profile. The respective results are shown as yellow squares in Fig. 5.10C. As could be expected from the shape of the stress profiles in Fig. 5.10B, our results yield different coupling strengths for σ_{xx} and σ_{yy} . For the y -direction we found a positive active coupling of $f = 0.2$ but a negative active coupling of $f = -0.05$ for the x -direction. This is most likely a due to the fact that forces in x -direction always have to be balanced between the cells. In contrast, y -directed forces are predominantly balanced between cell and substrate and not across the cell-cell junction. Therefore, the cells may contract independently of each other in y -direction.

Following the ideas of the contour model one might expect that partially activating a cell leads to a local increase in surface tension which in turn has to result in a non-symmetrical contour. On the right hand side of Fig. 5.10D we show the typical contour of a partially activated cell as predicted by the contour FEM (Fig. 5.10D). Within the assumptions of our model, local photoactivation leads to a skewed contour which is dragged into the activation region. The degree of skewness depends on the strength of the surface tension. Additionally, the line tension along the contour drastically changes. Obviously, Eq. (5.11) no longer holds as the line tension attains its maximal value at the focal adhesion in the activated half. This again demonstrates that the contour model may predict the traction force increase during local photoactivation as well as the directional change of those forces as the tangent angle changes. In marked contrast to the contour FEM without feedback (Fig. 5.10D (right sub-panel)), our experimental data show a very symmetric deformation of the contour in a large majority of all locally activated cell doublets. The conservation of symmetry supports the result previously demonstrated with the MSM that the non-activated cell actively contracts in the y -direction.

To estimate the degree of active coupling purely based on the shape of the cell, we followed the same procedure as for the 2D FEM and successively increased the degree of active coupling for the surface tension in steps of $\Delta f = 0.1$ from $f = 0$ to $f = 1$. For each value of f we then calculated the contour strain (Eq. (5.35)) in the same way as for the parameterization through global photoactivation. The resulting family

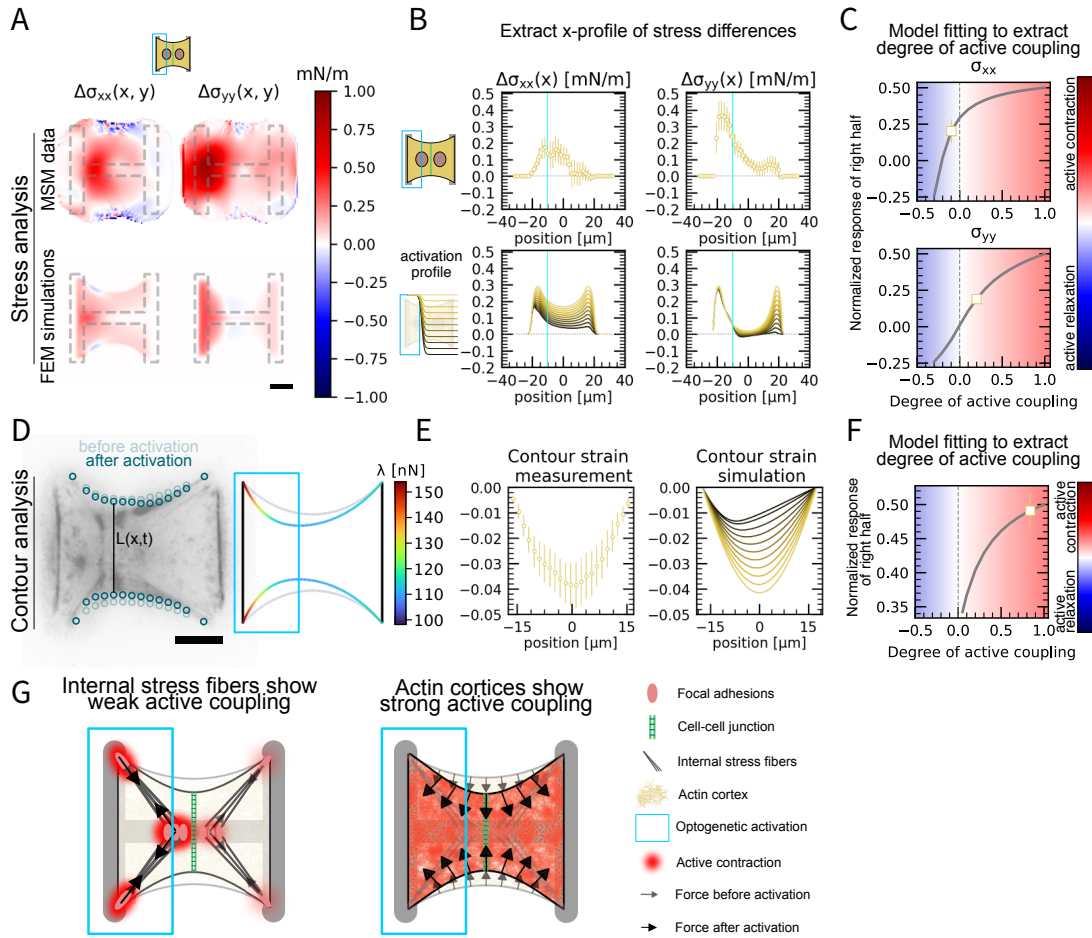


Figure 5.10: Active coupling in cell doublets. Panel **A** shows the difference of average cell stresses in x -direction (left) and y -direction (right) after and before photoactivation. The top row corresponds to the MSM quantification and the bottom row shows the FEM simulations. Panel **B** (top row) shows the MSM stress maps in **A** averaged over the y -axis. The data is shown as circles and error bars denote the s.e.m. The bottom row shows the FEM simulations for different active stresses (different values for the degree of active coupling) in the right half leading to a family of curves. Panel **C** (grey line) shows the normalized response of the right half obtained from the FEM simulations as a function of the degree of active coupling. The data point corresponds to the normalized response obtained from the experimental curves in **B** and was placed on top of the grey line to obtain the degree of active coupling. Panel **D** shows the contour strain measurement of the free stress fiber. On the experimental images (left sub-panel), the inter-stress fiber distance after and before photoactivation is measured along the x -axis which defines a contour strain. The right sub-panel exemplarily shows a contour simulation of a fiber where the left half of the cell has been activated. It is clearly skewed and exhibits an asymmetric distribution of the line tension along the fiber. Panel **E** shows the result of the contour strain measurement (left sub-panel). The right sub-panel shows the same contour strain quantification for simulated contours where the right half of the contour has been progressively activated similar to **B**. This leads to the depicted family of curves. Panel **F** (grey line) shows the normalized response of the right half obtained from the contour FEM simulations as a function of the degree of active coupling. The data point corresponds to the normalized response obtained from the experimental curves in **E** and was placed on top of the grey line to obtain the degree of active coupling. Panel **G** summarizes the results of the previous panels. The TFM and MSM analysis only measure the forces that are transmitted to the substrate. These forces are dominated by the activity of internal stress fibers. The contour shape of the free fiber is determined by the contractility of the cortex and the free fiber itself. The stronger active coupling in the contour suggests a better coupling of the cortices and a comparatively weaker active coupling of the stress fibers. All experimental plots show data from $n = 17$ doublets from $N = 2$ samples. Scale bars correspond to $10\ \mu\text{m}$.

of curves, together with the contour strain measurement, is depicted in Fig. 5.10E. Asymmetry in the contour strain is high for low values of f and low for high values of f with a limiting case of symmetrical response for $f = 1$. Further, we normalize the response by integrating the right half of the curve and normalizing that by the integral of the whole curve.

By this procedure we again translate the family of curves into a single curve which measures the normalized response of the right half as a function of the degree of active coupling. In agreement with the results from MSM and the 2D FEM simulations we found a positive degree of active coupling. However, the value of $f = 0.8$ (Fig. 5.10F (yellow box)) is much larger than the one from the previous quantification. Hence, the contour strain measurement indicates an almost global response of the cell doublet to local stimulation.

Taken together, the traction forces are mainly dominated by the strong internal stress fibers supplemented by a contribution from the peripheral stress fiber. This assumption is based on the observation that the traction peaks are mostly located in the corners of the pattern. The actin cortex itself must play subordinate role, since it has little direct influence on traction forces and can transmit forces to the substrate only along the vertically adherent fiber. As no significant constant horizontal force is present in the TFM, we assume that the TFM measurement mostly represents the action of the stress fibers. In contrast, the shape of the free spanning arc is strongly influenced by the cortex and the properties of the free stress fiber. Since the internal stress fibers are directly coupled to the substrate and therefore most likely transmit little force across the intercellular junction (Fig. 5.10G, left), this could explain the weaker level of active coupling revealed by the MSM measurements. Based on the quantification of the contour strain, the cortices therefore exhibit much stronger active coupling (Fig. 5.10G, right).

STRESS PROPAGATION AND STRUCTURAL POLARIZATION

Our results indicate that stress propagation in doublets is much more efficient in the y -direction than in the x -direction. In order to test if this observation is connected to the structural and mechanical polarizations, we manipulated the internal actin organization by changing the pattern geometry. The overall H-shape of the pattern remains but the aspect ratio was varied once to a $y : x = 1 : 2$ (1to2) and $y : x = 2 : 1$ (2to1). In this way the spreading area stays constant. The basic quantification pipeline as developed in the previous sections could be directly applied to the experiments for the different aspect ratios. Fig. 5.11 A,B and C show the results of the experimental quantification before photoactivation. The average traction force maps hint at distinct internal stress fiber organization as the angle of traction forces changes as a function of the aspect ratio. For the 1to2-pattern, forces have a larger x -component while for the 2to1-pattern, the y -component dominates. The MSM results in Fig. 5.11B show how the different TFM inputs affect the internal cell stresses. The stresses in the y -direction are largest for the 2to1 pattern and smallest for the 1to2 pattern, and the reverse is true for the x -direction. Cells on the 1to1-pattern show almost isotropic internal

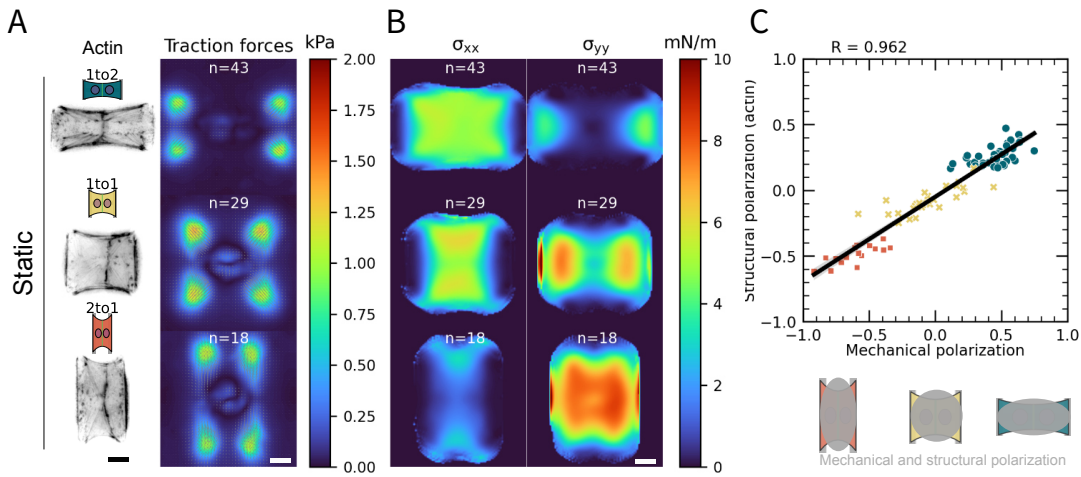


Figure 5.11: Influence of micropattern aspect ratio on the mechanical and structural polarization of doublets. Panel **A** depicts actin images (left) and average TFM maps (right) of cell doublets on H-pattern with aspect ratios 1to2 (top), 1to1 (middle) and 2to1 (bottom). Panel **B** shows the average internal cell stresses obtained by application of MSM to the TFM maps. Panel **C** shows the correlation of mechanical and structural polarization. The black line corresponds to a linear regression of the data and the shaded region denotes the 95% confidence interval for this regression. The R-value shown is the Pearson correlation coefficient. All experimental plots show data from $n = 43$ 1to2 doublets from $N = 6$ samples, $n = 29$ 1to1 doublets from $N = 2$ samples and $n = 18$ 2to1 doublets from $N = 3$ samples. Scale bars correspond to $10 \mu\text{m}$.

stresses. As before, mechanical and structural polarization are strongly correlated and both, the internal stresses and the actin organization vary drastically in between the different aspect ratios (Fig. 5.11C).

By repeating the local photoactivation experiment, the measurement and the FEM modeling procedure, we could investigate the influence of structural polarization on force propagation (Fig. 5.12A-C). Since we had no data for global photoactivation this time, our model was calibrated by the baseline fit and the results of the mechanical polarization alone. As we determined stresses in a normalized fashion in x - and y -direction separately, the absolute values had little influence on the relative stress profiles and the resulting normalized response of the right half (Fig. 5.12C). Parameters as used for the simulations are gathered in Table A.7. In the following we refer to the activated cell as the *sender cell* and the non-activated cell as the *receiver cell*. As before, we always activated the left cell.

A comparison of the three aspect ratios shows that the stress response of the receiver cell depends strongly on the aspect ratio. On 1to2-patterns cells are polarized mainly into the direction of possible stress propagation i.e. along the x -axis. Here, the receiver cell relaxes upon activation of the sender cell. Conversely, for doublets on 2to1-pattern, cells are mainly polarized perpendicular to the axis of stress propagation (x -axis) and the receiver cell actively contracts upon stimulation of the sender cell. A quantification of the degree of active coupling by means of our FEM procedure confirms the strong active coupling for cells on 2to1-pattern. In general we find that an increasing mechanical and structural polarization induces a stronger active coupling as can be seen in Fig. 5.12D.

Analogously to the previous section we then repeated the same quantification for

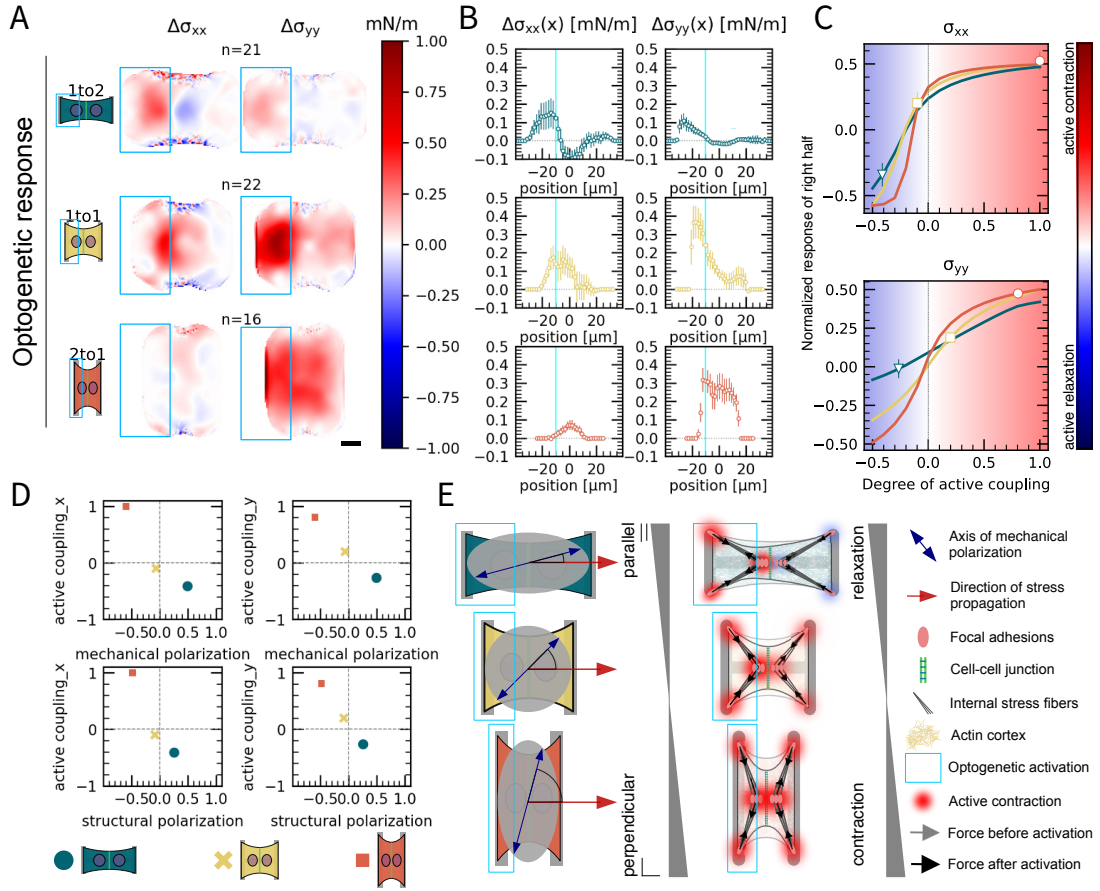


Figure 5.12: Efficiency of force transmission for differing mechanical and structural polarization in doublets. Panel **A** shows the difference of average cell stresses in x -direction (left) and y -direction (right) after and before photoactivation for aspect ratios 1to2 (top), 1to1 (middle) and 2to1 (bottom). The illuminated region is highlighted by the blue rectangle. Panel **B** shows the MSM stress maps in **A** averaged over the y -axis. The data is shown as circles and error bars denote the s.e.m. Panel **C** shows the normalized response of the right half for all aspect ratios, obtained by the FEM simulation, as a function of the degree of active coupling. The data point corresponds to the normalized response obtained from the experimental curves in **B** and was placed on top of the grey line to obtain the degree of active coupling. Panel **D** shows the degree of active coupling plotted against the average mechanical and structural polarization of the doublets. Panel **E** summarizes the findings of the previous panels. The relative response of the non-activated cell varies drastically in the different aspect ratios. In the 1to2 doublet, where the transmission direction and axis of polarization are aligned, the non-activated cell relaxes upon stimulation of the left cell. In contrast, for the doublets on 2to1 patterns, where the transmission direction is perpendicular to the average direction of polarization the non-activated cell contracts almost as strongly as the activated cell. All experimental plots show data from $n = 43$ 1to2 doublets from $N = 6$ samples, $n = 29$ 1to1 doublets from $N = 2$ samples and $n = 18$ 2to1 doublets from $N = 3$ samples. Doublets with unstable stress behavior before photoactivation were excluded before the analysis of the optogenetic data. Scale bars correspond to $10 \mu\text{m}$.

the coupling of the cortices. The results are shown in Fig. A.3E-G. Qualitatively, we found that the contour strain is symmetric for the 1to1 and 2to1 doublets, but shows a very strong asymmetry for the elongated 1to2 doublets. This agrees with the results of Fig. 5.12C, which shows the lowest degree of active coupling for 1to2 doublets. A quantitative analysis reveals stronger active coupling for 1to1 doublets than for 2to1 doublets. To put these results into perspective, one should note that the contour strain measurement for the 2to1 doublets was subject to large fluctuations as the contour strain is very small.

In summary, we found that the degree of active coupling increases with increasing mechanostuctural polarization and thus stresses transmit most efficiently perpendicular to the polarization axis (Fig. 5.12E).

5.5. STRESS PROPAGATION IN SMALL TISSUES

Finally, we concluded our study by investigating to what extent the results presented above translate to larger systems such as small cell clusters. The small cell monolayers were experimentally realized by plating 10–20 cells on a rectangular shaped micropattern with an area of $150\ \mu\text{m} \times 40\ \mu\text{m}$. The results of the TFM, MSM and the analysis of the internal actin structure for the small cell clusters are shown in Fig. 5.13A-C. As can be seen from Fig. 5.13C, the tissues exhibit a strong mechanostuctural polarization in direction of the long axis of the pattern. F-actin images further reveal strong peripheral actin cables along the borders of the pattern but a less dominant internal actin structure (Fig. A.6).

Subsequently, photoactivation of either the left or the top half of the pattern then allowed to study stress propagation along and perpendicular to the axis of mechanostuctural polarization. Purely qualitatively, Fig. 5.13D shows that in both cases local photoactivation is accompanied by a stress increase in the non-activated part of the tissue. By using our 2D-FEM approach and following the same quantification strategy as before, we find that the degree of active coupling attains a higher value if the axis of polarization and the direction of stress propagation are perpendicular to each other (Fig. 5.13E,F). In addition, we estimated the distance stress propagates by measuring the distance at which the stress decreases to 20% of its maximal value. This distance is on average three times larger if the direction of stress propagation is perpendicular to the axis of mechanostuctural polarization (Fig. 5.13E) The results of this analysis are placed in the context of the previous results in Fig. 5.13G. Here, the active coupling in x - and y -direction is plotted as a function of both, the mechanical polarization and the structural polarization. Consistent with the previous results for doublets on different H-patterns, mechanostuctural polarization and active coupling are correlated also in larger cell clusters. Overall, our results suggest that the correlation between mechanical polarization, structural polarization, and active coupling is typical for epithelia, regardless of system size.

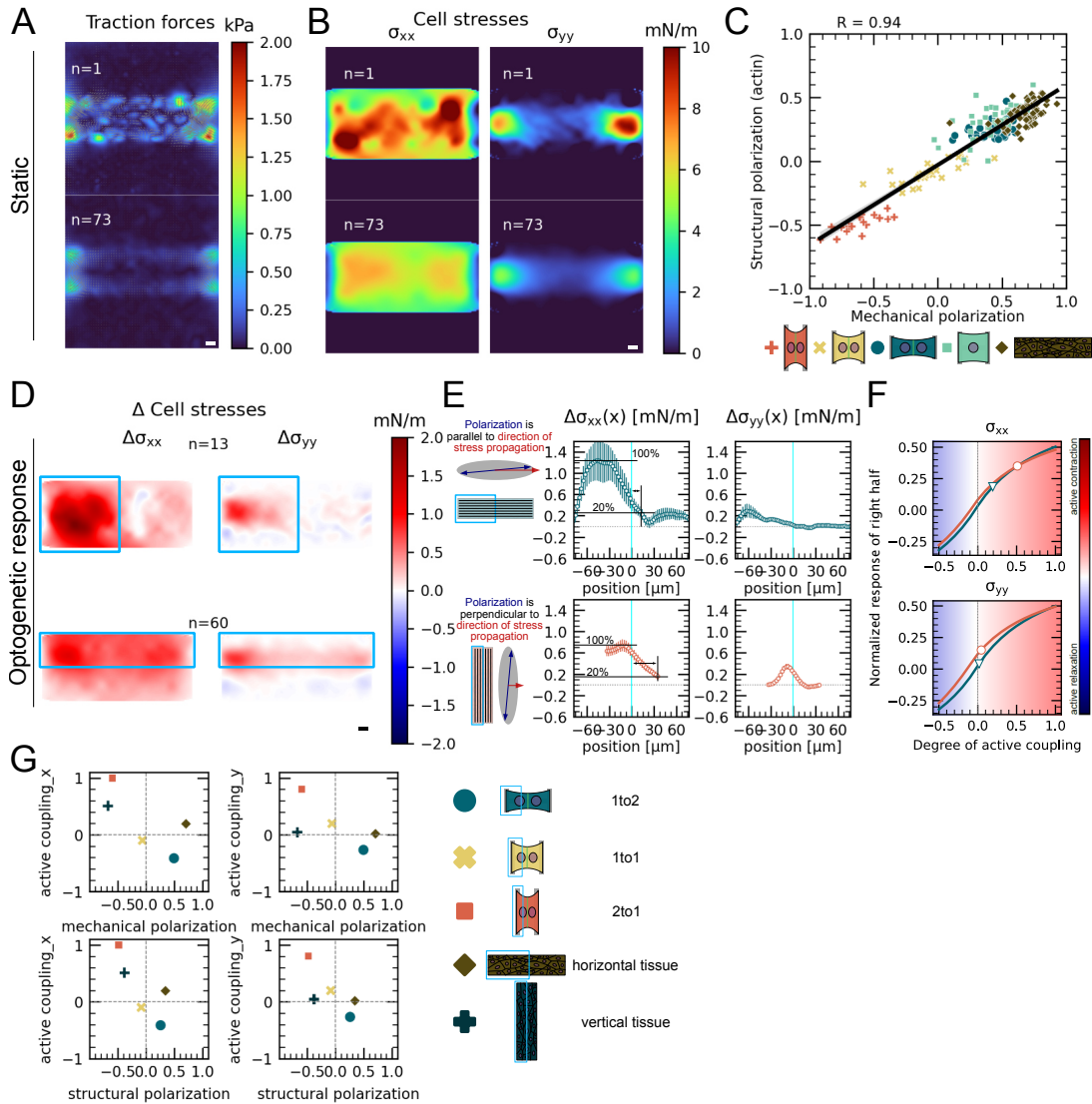


Figure 5.13: Stress propagation in small monolayers. Panel **A** shows a representative (top) and the average (bottom) TFM maps of a small monolayer on a rectangular micropattern. Panel **B** shows the corresponding cell stresses obtained by application of MSM to the TFM maps. Panel **C** shows the correlation of mechanical and structural polarization across all considered conditions. The black line corresponds to a linear regression of the data and the shaded region denotes the 95% confidence interval for this regression. The R-value shown is the Pearson correlation coefficient. Panel **D** shows the difference of average cell stresses in x -direction (left) and y -direction (right) after and before photoactivation. The illuminated region is highlighted by the blue rectangle. Panel **E** shows the MSM stress maps in **A** averaged over the y -axis. Here, the coordinate system corresponds to the tissue orientation as depicted in the small cartoon on the left side. The data is shown as circles and error bars denote the s.e.m. Panel **F** shows the normalized response of the right half (non-activated half), obtained by the FEM simulation, as a function of the degree of active coupling. The data point corresponds to the normalized response obtained from the experimental curves in **E** and was placed on top of the grey line to obtain the degree of active coupling. Panel **G** shows the degree of active coupling plotted against the average mechanical and structural polarization for all considered conditions. The experimental plots in **A**, **B**, **D**, **E** and **F** show data from $n = 13$ tissues from $N = 2$ samples. photoactivated on the left and from $n = 60$ tissues from $N = 3$ samples photoactivated on the top. Scale bars correspond to $10\ \mu\text{m}$.

5.6. SUMMARY AND DISCUSSION

In this chapter we studied how cell-generated forces propagate from one cell to another across the intercellular junction. Further, we investigated how this process is influenced by mechanical and structural polarization of the system. A combination of several experimental techniques such as micropatterning, TFM, MSM and optogenetics with finite element modeling of thin elastic sheets and contour models of cell adhesion allowed to quantify the observations in greater detail.

We started in Section 5.3 by exploiting anisotropic contour models in combination with image analysis to characterize the differences between singlets and doublets. This approach allowed us to obtain characteristics like line and surface tension of the two conditions. The analysis showed that an intercellular junction not only influences the mechanical polarization of the system but also alters the line tension of actin bundles in the cell periphery.

Next, in Section 5.4 we parametrized a two-dimensional FEM model similar to Chapter 4 with respect to global photoactivation of singlets and doublets. Moreover, we introduced an FEM description for contour models which treats the free peripheral stress fiber as an active linear elastic material. For both approaches we introduced local photoactivation by incorporating the spatial profile of the experimental light pulse. A comparison of the computational methods with the experimental measurements revealed that cells in a cell doublet are actively coupled. We verified this by local photoactivation of only one cell in the doublet which led to an active contractile response of the non-activated cell. Using the 2D FEM simulations, we were able to show that a purely passive, non-activated cell cannot explain the experimental traction force maps and the corresponding increase in substrate strain energy. In addition, the results of the cell shape analysis show an almost symmetrical shape deformation in response to asymmetrical stimulation. The cell shape deformation is mainly dictated by the activity of the actin cortex, and a comparison of the cell shape measurements and the contour FEM suggests that active coupling is stronger for the cortices than for the internal stress fibers. However, it is plausible that this is strongly influenced by the mechanical properties of the cells and tissue, as well as the geometric and mechanical characteristics of the substrate. According to our data, the mechanical signals are propagated up to two cell lengths due to the active coupling mechanism. Yet, we only considered transient activation signals and it would be interesting to study if the signals may travel farther by maintaining signal strength over a longer period of time. Additionally, the mechanical signals can travel very fast compared to biochemical signals. This is clearly demonstrated by the fact that we did not notice any delay between the force signals of sender and receiver cell with a temporal resolution of one frame per minute. In marked contrast to the cell doublets, the non-activated region in single cells showed acute fluidization of the actin structure. Hence, the absence of a cell-cell junction prevents local stress increase and instead leads to F-actin flow. This finding emphasizes the importance of cellularisation of tissue as it allows for compartmentalization and efficient transmission of stress.

Moreover, we demonstrated that the efficiency of the force propagation, i.e. the

strength of intercellular coupling, strongly depends on the anisotropy of the actin organization and force distribution. In detail, we were able to quantify that force signals propagate most efficiently perpendicular to the axis of mechanostructural polarization. Future work will be essential to determine the precise influence subcellular structures have on the mechanochemical feedback loops and further it will be necessary to better decipher which molecular mechanisms are involved in signal detection, transduction and amplification. At present, it remains puzzling which stimulus is detected by the receiver cell. Possible mechanisms could be either strain-induced, e.g., by changing the concentration and spatial localization of the involved signaling molecules during deformation, or stress-induced, e.g., by opening cryptic binding sites of certain molecules and/or increasing dissociation constants. From the modeling side, it would be necessary to create a computational framework which incorporates the biochemistry of the RhoA pathway and couple this directly to active stress generation. This would allow active force generation to be modeled in terms of intrinsic mechanochemical feedback, rather than introducing active mechanisms through a heuristic approach as presented in this chapter. From the experimental side it would be interesting to study the emergence and time evolution of RhoA/ROCK and MLC activity in the passive cell. This could help to identify whether the signal of the sender cell is predominantly processed in the vicinity of the intercellular junction or at focal adhesions.

Finally, we investigated how active coupling and force propagation translates to small tissues. In agreement with previous findings for cell doublets, we found that force transmission is more efficient perpendicular to the axis of mechanostructural polarization even in small monolayers. This suggests that the underlying mechanisms operate across scales. We therefore conclude that our results support the findings of other studies that have investigated the importance of intercellular forces and force transmission for collective cell behavior (*Sunyer et al.*, 2016; *D. T. Tambe et al.*, 2011; *Vedula et al.*, 2014).

Chapter 6

Coupling Biochemistry to Cell Mechanics

In the previous chapter we investigated force generation and subsequent force propagation in a cell pair, where one cell acts as the sender cell and the other as the receiver cell. Active force generation upon photoactivation of the sender cell was introduced by means of a predefined active stress profile. The active feedback was modeled phenomenologically by elevating the level of active stress in the receiver cell. This procedure could be successfully exploited to analyze experimental data and hence verify that the receiver cell actively responds to contraction of the sender cell. However, this heuristic approach reaches its limits when it comes to investigating the molecular mechanisms behind active force generation and the mechanotransduction in the receiver cell. In this chapter, we want to extend our finite element models by directly coupling active force generation to biochemical signaling pathways. We further demand that the model for the reaction kinetics allows optogenetic perturbation, preferably with a clear setpoint and reversibility.

6.1. INTRODUCTION

The combination of biochemistry and mechanics is a common approach in the field of mechanochemistry and is used to study the emergence of mechanical and chemical patterns associated with tissue formation and embryogenesis. Theoretical modeling of such systems involves the use of so-called "morphogens" whose concentration fields cause changes in cell and/or tissue shape which then feed back onto the dynamics of the morphogens. The details of these concepts are, for example, discussed in the work by *Allena et al.* (2013) where the authors provide a method that couples cell mechanics and morphogen transport to describe *Drosophila* embryogenesis. *Mercker et al.* (2016) extended this approach and further investigated the role of several possible mechanochemical feedback loops and their connection to distinct emerging equilibrium patterns.

The idea of relating the generation of active stresses in viscoelastic fluids to the concentrations of their molecular regulators, such as myosin II motors, is a central idea in active gel physics, used for example to model the active behavior of the actin CSK (*Juelicher et al.*, 2007; *Prost et al.*, 2015). More related to the discussions of the previous chapters, *Besser et al.* (2007) introduced a mathematical model which

combines a one-dimensional viscoelastic model of stress fibers and NMII-tractility through a reaction diffusion system of the Rho pathway. They additionally introduced a positive biochemical-mechanical feedback loop by accounting for signaling at focal adhesions. This positive feedback could explain spatial gradients in the periodic MLC- α -actinin pattern in stress fibers stimulated with calyculin A. Just recently, *Zmurchok et al.* (2018) demonstrated by means of a minimalist model for Rho GTPase activity that positive tension dependent feedbacks from coupling to a one-dimensional Kelvin-Voigt model lead to non-trivial cell behavior. By performing a bifurcation analysis they show that their proposed system gives rise to bistability where the two states represent permanently contracted or relaxed cells, respectively, but also that oscillatory states are possible. Additionally they consider a system of small cell clusters by including their model into CPM simulations.

In addition, local pulsatile contractions of the actin cortex play an important role in cell and tissue morphogenesis. For example *Bement et al.* (2015) identified an activator-inhibitor relationship between RhoA and F-actin which leads to the emergence of spiral contraction waves during cytokinesis in embryonic cells of *Xenopus*. Very similar surface contraction waves have been observed for starfish oocytes during maturation and could be modeled by coupled reaction kinetics of actin and NMII (*Bischof et al.*, 2017). *Kamps et al.* (2020) designed a very detailed model for the reaction kinetics of GEF, RhoA and MLC which exhibits three types of states: stable, excitable and oscillatory ones. Accompanied by experimental measurements which include optogenetic perturbations of GEF, they provide a fully parametrized model. Very recently, *Staddon et al.* (2022) coupled a basic activator-inhibitor reaction diffusion system comprised of RhoA, as the activator, and myosin II, as the inhibitor, to the mechanics of Kelvin-Voigt and Maxwell models. By introducing mechanochemical feedback the authors demonstrate the emergence of propagating pulsatile contractions as well as topological turbulence in RhoA flows.

Following along the lines of this recent progress made in the area, with this chapter we aim at designing a model that includes the stiffness and geometry of the adhesive environment (i), allows to introduce elastic interaction with neighboring cells (ii) and accounts for active stress generation and possible mechanotransduction in terms of a reaction-diffusion system (iii).

We start in Section 6.2 with the finite element formulation of a cell pair model. First, we discuss the mathematical treatment of diffusion in a deformable domain. Second, we exploit a discontinuous Galerkin method to introduce the non-permeable cell-cell junction which is a crucial feature of an interacting cell pair. Then we complete the cell pair model by discussing how we connect MLC concentration and active stress generation.

Subsequently, in Section 6.3 we start with a review of the model by *Kamps et al.* (2020) and based on this, extract the main features of a linear signaling cascade in order to qualitatively reproduce optogenetic activation.

Finally, in Section 6.4 we test the implementation of the cell pair model. For this we will combine it with the RD-system by *Kamps et al.* (2020) to demonstrate that traveling RhoA and myosin waves cannot pass the intercellular junction. Subsequently

we will use our linearized reaction-diffusion system to demonstrate that a strain dependent feedback can qualitatively reproduce the symmetric response of the cell doublet upon stimulation of the left cell (Section 5.4.2).

We close with an outlook where we will discuss how this model can be used in future studies and how one would generalize it to model propagation of mechanical waves for example in epithelial sheets.

6.2. BLUEPRINT FOR A CELL PAIR MODEL

Before we discuss the details of the underlying reaction diffusion system which we use to model cellular contractility, we first want to discuss the arising difficulties of the numerical treatment in a general way. Within this modeling approach the cell is represented by an elastic contractile sheet analogously to the previously introduced FEM models. However here, we aim at modeling active contractility not by a predefined time dependent active stress profile but by resolving the underlying reaction-diffusion system for GEF, RhoA and myosin. The involved reactants are assumed to diffuse within the contractile sheet and additionally obey certain reaction kinetics, typically described by a well-defined activator inhibitor scheme. The homeostatic contractile state of an adherent cell is given by the steady state solution of the reaction diffusion system. Without having specified an appropriate RD system yet, we note that active stresses are effectively generated by active MLC at the end of the signaling pathway. The spatio-temporal distribution of actively generated stresses is therefore determined by both, the reaction kinetics and diffusive properties of MLC. Further, active generated stresses may lead to global and local contractions which directly feed back to the RD-system.

Qualitatively, shrinkage of the contractile sheet is expected to result in advection terms and locally/globally elevated concentrations. Hence, a fundamental difficulty in the treatment such systems is that diffusion processes are naturally treated in the Eulerian frame while the mechanics of the elastic domain is better described in the Lagrangian frame. In this sense, we begin with a very general description of RD-equations on time dependent domains and subsequently use methods from continuum mechanics to transform it to the Lagrangian coordinate system. Once we derived the RD-equations in the Lagrangian reference frame we will generally discuss the numerical implementation by means of a discontinuous Galerkin (DG) approach. This will be a crucial step when it comes to an adequate, closed and computationally efficient description of an interacting pair of cells.

6.2.1. REACTION DIFFUSION ON DEFORMABLE DOMAIN

Let $c(\mathbf{x}, t)$ be the concentration of a signaling protein in the deformed configuration at time t . The time evolution of $c(\mathbf{x}, t)$ can be deduced by imposing mass conservation i.e.

$$\frac{d}{dt} \int_{\Omega(t)} c(\mathbf{x}, t) \, d\mathbf{x} = \int_{\Omega(t)} [-\nabla \cdot \mathbf{j} + R_c(t)] \, d\mathbf{x} , \quad (6.1)$$

where $\mathbf{j} = -\mathbf{D}\nabla c(\mathbf{x}, t)$ is, according to Fick's first law, the diffusion flux, \mathbf{D} the diffusion tensor and R_c a source or sink term accounting for the reaction kinetics. The left-hand side of Eq. (6.1) can be evaluated using Reynolds transport theorem which eventually yields

$$\frac{d}{dt} \int_{\Omega(t)} c(\mathbf{x}, t) d\mathbf{x} = \int_{\Omega(t)} \frac{\partial}{\partial t} c(\mathbf{x}, t) + \nabla \cdot (\mathbf{v}(\mathbf{x}, t)c(\mathbf{x}, t)) d\mathbf{x}. \quad (6.2)$$

Using Eq. (6.2) and the fact that both integrands in Eq. (6.1) have to be equal we obtain the diffusion equation on the time dependent domain

$$\frac{\partial}{\partial t} c(\mathbf{x}, t) + \nabla \cdot (\mathbf{v}(\mathbf{x}, t)c(\mathbf{x}, t)) = \nabla \cdot (\mathbf{D}\nabla c(\mathbf{x}, t)) + R_c(t), \quad (6.3)$$

where $\mathbf{v}(\mathbf{x}, t)$ corresponds to the velocity of the deforming material. Hence, the time dependency of the domain leads to two additional terms, an advection term $\mathbf{v} \cdot \nabla c(\mathbf{x}, t)$ due to growth and dilution induced flows and an enrichment/dilution term $c(\mathbf{x}, t)\nabla \cdot \mathbf{v}$ due to local volume changes. The pull back of Eq. (6.3) to the reference configuration is done by means of the deformation gradient tensor $\hat{\mathbf{F}}$, its determinant $\hat{J} = \det(\hat{\mathbf{F}})$ and the transformation $d\mathbf{x} = \hat{J} d\hat{\mathbf{x}}$ (Section 2.1.1). Expressing the left-hand side of Eq. (6.3) in terms of material coordinates gives

$$\frac{d}{dt} \int_{\Omega(t)} c(\mathbf{x}, t) d\mathbf{x} = \lim_{\Delta t \rightarrow 0} \frac{1}{\Delta t} \left(\int_{\Omega(t+\Delta t)} c(\mathbf{x}, t + \Delta t) d\mathbf{x} - \int_{\Omega(t)} c(\mathbf{x}, t) d\mathbf{x} \right) \quad (6.4)$$

$$= \lim_{\Delta t \rightarrow 0} \frac{1}{\Delta t} \left(\int_{\Omega(0)} \hat{c}(\hat{\mathbf{x}}, t + \Delta t) \hat{J}(\hat{\mathbf{x}}, t + \Delta t) d\hat{\mathbf{x}} - \int_{\Omega(0)} \hat{c}(\hat{\mathbf{x}}, t) \hat{J}(\hat{\mathbf{x}}, t) d\hat{\mathbf{x}} \right) \quad (6.5)$$

$$= \int_{\Omega(0)} \frac{\partial}{\partial t} (\hat{c}(\hat{\mathbf{x}}, t) \hat{J}) d\hat{\mathbf{x}}, \quad (6.6)$$

where we used that $c(\mathbf{x}, t) = \hat{c}(\hat{\mathbf{x}}, t)$. The same procedure applied to the right-hand side of Eq. (6.3) and recalling Piola's identity $\hat{J}\nabla \cdot \mathbf{a} = \hat{\nabla} \cdot (\hat{J}\mathbf{F}^{-1}\mathbf{a})$ for any given vector field \mathbf{a} , one finds

$$\begin{aligned} \int_{\Omega(t)} [\nabla \cdot (\mathbf{D}\nabla c(\mathbf{x}, t)) + R_c(t)] d\mathbf{x} &= \int_{\Omega(0)} [\nabla \cdot (\mathbf{D}\nabla c(\mathbf{x}, t)) + R_c(t)] \hat{J} d\hat{\mathbf{x}} \\ &= \int_{\Omega(0)} \left[\hat{\nabla} \cdot (\hat{J}\hat{\mathbf{F}}^{-1}\mathbf{D}\hat{\mathbf{F}}^{-T}\hat{\nabla}\hat{c}) + \hat{J}R_c(t) \right] d\hat{\mathbf{x}}, \end{aligned} \quad (6.7)$$

where $\hat{\nabla}$ denotes derivative with respect to material coordinates. Finally, the reaction diffusion equation on a time dependent domain expressed in coordinates of the reference configuration is given by

$$\frac{\partial}{\partial t} (\hat{J}\hat{c}) - \hat{\nabla} \cdot (\hat{J}\hat{\mathbf{D}}\hat{\mathbf{C}}^{-1}\hat{\nabla}\hat{c}) - \hat{J}R_c(t) = 0, \quad (6.8)$$

where $\hat{\mathbf{C}} = \hat{\mathbf{F}}^T\hat{\mathbf{F}}$ denotes the Cauchy-Green deformation tensor and we further assumed an isotropic diffusion tensor $\mathbf{D} = D\mathbf{I}$ with scalar diffusivity D . From the Lagrangian point of view there are now two terms arising due to the time dependence of the

domain. On the one hand, expansion of the time derivative in the first term Eq. (6.8) allows to rewrite it as

$$\hat{J} \frac{\partial}{\partial t} \hat{c} - \hat{\nabla} \cdot \left(\hat{J} \mathbf{D} \hat{\mathbf{C}}^{-1} \hat{\nabla} \hat{c} \right) - (\hat{J} R_c(t) - \hat{c} \partial_t \hat{J}) = 0, \quad (6.9)$$

which shows that compression ($\partial_t \hat{J} < 0$) and dilation ($\partial_t \hat{J} > 0$) of the elastic domain effectively alters the reaction kinetics. On the other hand, diffusivity transitions from isotropic to anisotropic $\hat{J} \mathbf{D} \hat{\mathbf{C}}^{-1}$ during deformation i.e. decreases along the principal axis of deformation. Additionally, we note that in case of a static domain we recover the standard reaction diffusion equation as $\hat{J} = 1$ and $\hat{\mathbf{C}} = \mathbf{I}$.

6.2.2. DIFFUSION WITH HINDRANCE - MEMBRANE

The presented methods can be generalized to a variety of different problems which aim at modeling diffusive transport also across interfaces. Hence, we start the discussion as before in a very general sense and later discuss the necessary restrictions which characterize the cell doublet. For the presentation of the method we follow the work by *Hansen et al.* (2018) who used a similar DG implementation to model fluorescence loss in photobleaching.

Let Ω_l and Ω_r be two domains separated by a semi-permeable membrane Γ_M as depicted in Fig. 6.1A. Further, let \hat{c}_l and \hat{c}_r be the concentrations of a species in the left and right subdomain right at the membrane, respectively. According to Fick's law, the flux is generally given by $\mathbf{j} = -\alpha \hat{\nabla} \hat{c}$ where we set $\alpha \equiv \hat{J} \mathbf{D} \hat{\mathbf{C}}^{-1}$ (Eq. (6.8)). Integration across the membrane Γ_M allows to rewrite the flux as

$$\mathbf{j} = p(\hat{c}_l - \hat{c}_r) \mathbf{N}_l, \quad (6.10)$$

where \mathbf{N}_l is the normal vector on the membrane pointing from Ω_l to Ω_r and p measures the permeability of Γ_M in units of $\mu\text{m s}^{-1}$ (Fig. 6.1A).

Approximating the permeability p by dividing the flux by the jump in concentration is common practice in experiments (*Friedman, 2008; Hansen et al., 2018*). If the concentration in the subdomain Ω_r is greater than in Ω_l solutes flow back into Ω_l in agreement with Fick's law. Therefore, the problem that needs to be solved is given by:

$$\frac{\partial}{\partial t} (\hat{J} \hat{c}) - \hat{\nabla} \cdot \left(\alpha \hat{\nabla} \hat{c} \right) - \hat{J} R_c(t) = 0, \quad \hat{\mathbf{x}} \in \Omega, \quad t \geq 0, \quad (6.11)$$

such that the interface condition at the membrane and the assumed zero-flux boundary conditions are fulfilled. The interface and boundary conditions read

$$\mathbf{j} \cdot \mathbf{N}_l = -\alpha \hat{\nabla} \hat{c}_l \cdot \mathbf{N}_l = p[[\hat{c}]] \cdot \mathbf{N}_l, \quad \mathbf{x} \in \Gamma_M, \quad (6.12)$$

$$\hat{\nabla} \hat{c} \cdot \mathbf{N} = 0, \quad \mathbf{x} \in \partial\Omega, \quad (6.13)$$

where \mathbf{N} denotes the outward pointing normal vector on $\partial\Omega$ and $[[\hat{c}]] \equiv \hat{c}_r \mathbf{N}_r + \hat{c}_l \mathbf{N}_l = (\hat{c}_r - \hat{c}_l) \mathbf{N}_l$ is the short-hand notation for a jump.

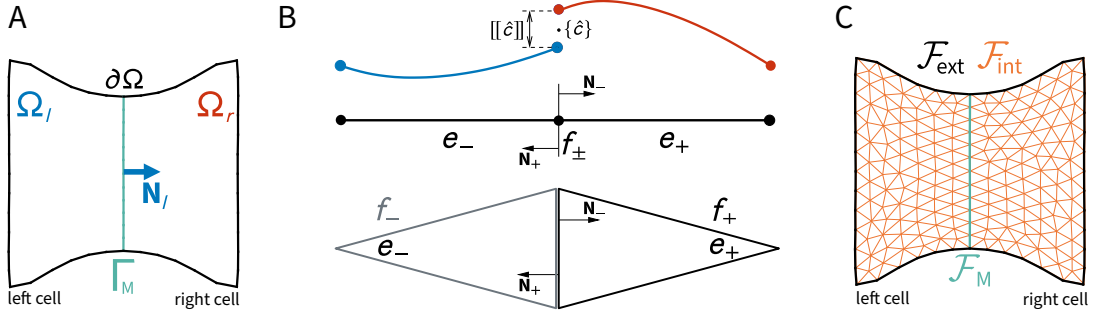


Figure 6.1: Illustration of the relevant quantities for the discontinuous Galerkin formulation of the cell pair model with intercellular junction (membrane). Panel **A** depicts the simulation domain which is split into left cell Ω_l and right cell Ω_r with overall boundary $\partial\Omega$. The two domains are separated by an internal interface Γ_M which models the intercellular junction. For Ω_l the outward pointing normal vector points into Ω_r , and vice versa for Ω_r . Panel **B** shows the fundamental feature of the DG implementation. Adjacent elements are labelled by \pm and function values (blue and red) may jump across element facets. Panel **C** is a schematic illustration of a meshed domain. For the construction of the DG weak form it is crucial to distinguish between external \mathcal{F}_{ext} (black), internal \mathcal{F}_{int} (orange) and membrane facets \mathcal{F}_M (green). A stabilizing term enforces continuity of the solution across the internal facets only. Jumps across the membrane facets are necessary to account for discontinuous transition of the solution from the left cell to the right cell.

6.2.3. WEAK FORM FOR DISCONTINUOUS GALERKIN APPROACH

The interface condition in Eq. (6.12) prevents a naive FEM-implementation as described in the previous chapters. In order to account for abrupt concentration changes from one subdomain to the other we need a method which allows discontinuous functions across the membrane. The standard choice for such a problem is the discontinuous Galerkin method. In contrast to the continuous Galerkin methods, continuity and smoothness of the involved DG-functions is only enforced element-wise such that the solution may be discontinuous across element boundaries (compare blue and red functions in Fig. 6.1B). However, continuity across elements can be enforced by introducing penalty terms. These methods are known as interior penalty discontinuous Galerkin methods (IPDG) (Arnold, 1982; Babuška, 1973; Wheeler, 1978).

At this point it is necessary to introduce some additional notation. Let $\mathcal{T}(\Omega)$ be the triangulation of the domain Ω into finite elements $e \in \mathcal{T}(\Omega)$. Further, let \mathcal{F} denote the union of the boundary facets of all elements e . We distinguish between external facets \mathcal{F}_{ext} , internal facets \mathcal{F}_{int} and membrane facets \mathcal{F}_M such that $\mathcal{F} = \mathcal{F}_{\text{ext}} \cup \mathcal{F}_{\text{int}} \cup \mathcal{F}_M$ with $\mathcal{F}_{\text{int}} = \mathcal{F} \setminus (\mathcal{F}_{\text{ext}} \cup \mathcal{F}_M)$ (Fig. 6.1C). Next, by \hat{c}_- and \hat{c}_+ we denote scalar valued functions on two neighboring elements e_- and e_+ . The normal vectors on a common facet of e_{\pm} are given by \mathbf{N}_{\pm} . For example, \mathbf{N}_- defines the outward directed normal on e_- pointing into e_+ . Following the standard DG notations we introduce the jump and the average of a quantity as $[[\hat{c}]] \equiv \hat{c}_+ \mathbf{N}_+ + \hat{c}_- \mathbf{N}_-$ and $\{\hat{c}\} \equiv (\hat{c}_+ + \hat{c}_-)/2$, respectively. Analogously, for piecewise vector valued functions $\hat{\mathbf{q}}$ one defines jump and average as $[[\hat{\mathbf{q}}]] \equiv \hat{\mathbf{q}}_+ \mathbf{N}_+ + \hat{\mathbf{q}}_- \mathbf{N}_-$ and $\{\hat{\mathbf{q}}\} \equiv (\hat{\mathbf{q}}_+ + \hat{\mathbf{q}}_-)/2$, respectively. Moreover, one may use these definitions to prove the identity

$$[[\hat{\mathbf{q}}\hat{c}]] = [[\hat{\mathbf{q}}]]\{\hat{c}\} + \{\hat{\mathbf{q}}\}[[\hat{c}]]. \quad (6.14)$$

In the first step of the derivation of the DG weak form we multiply Eq. (6.11)

with a suitable test function $w \in \mathcal{V}$ and integrate over the whole simulation domain Ω which gives

$$\int_{\Omega} \frac{\partial}{\partial t} (\hat{J}\hat{c})w \, d\hat{\mathbf{x}} - \int_{\Omega} \hat{\nabla} \cdot (\alpha \hat{\nabla} \hat{c}) w \, d\hat{\mathbf{x}} - \int_{\Omega} \hat{J}R_c(t)w \, d\hat{\mathbf{x}} = 0. \quad (6.15)$$

Instead of directly using partial integration on the middle term of Eq. (6.15) we first split it into a sum over element integrals and then apply Green's first theorem to obtain

$$\begin{aligned} \int_{\Omega} \hat{\nabla} \cdot (\alpha \hat{\nabla} \hat{c}) w \, d\hat{\mathbf{x}} &= \sum_{e \in \mathcal{T}(\Omega)} \int_e \hat{\nabla} \cdot (\alpha \hat{\nabla} \hat{c}) w \, d\hat{\mathbf{x}} \\ &= \sum_{f_e \in \mathcal{F}(\Omega)} \int_{f_e} \alpha \hat{\nabla} \hat{c} \cdot \tilde{\mathbf{N}}_e w \, ds - \sum_{e \in \mathcal{T}(\Omega)} \int_e \alpha \hat{\nabla} \hat{c} \cdot \hat{\nabla} w \, d\hat{\mathbf{x}}. \end{aligned} \quad (6.16)$$

Here, f_e denotes the facets of element e and $\tilde{\mathbf{N}}_e$ describes the outward directed normal vector on the facets of the element. The first term in Eq. (6.16) is split again into the exterior, interior and membrane facets

$$\begin{aligned} \sum_{f_e \in \mathcal{F}(\Omega)} \int_{f_e} \alpha \hat{\nabla} \hat{c} \cdot \tilde{\mathbf{N}}_e w \, ds &= \sum_{f_e \in \mathcal{F}_{\text{ext}}(\Omega)} \int_{f_e} \alpha \hat{\nabla} \hat{c} \cdot \tilde{\mathbf{N}}_e w \, ds \\ &\quad + \sum_{f_e \in \mathcal{F}_{\text{int}}(\Omega)} \int_{f_e} \alpha \hat{\nabla} \hat{c} \cdot \tilde{\mathbf{N}}_e w \, ds \\ &\quad + \sum_{f_e \in \mathcal{F}_{\text{M}}(\Omega)} \int_{f_e} \alpha \hat{\nabla} \hat{c} \cdot \tilde{\mathbf{N}}_e w \, ds. \end{aligned} \quad (6.17)$$

Note that each internal facet and each membrane facet is shared by two adjacent elements e_- and e_+ such that integrals along the common facets add up to a jump

$$\int_{f_{\pm}} \alpha \hat{\nabla} \hat{c} \cdot \tilde{\mathbf{N}}_{\pm} w \, ds = \int_f (\alpha_+ \hat{\nabla} \hat{c}_+ w_+ - \alpha_- \hat{\nabla} \hat{c}_- w_-) \cdot \tilde{\mathbf{N}}_+ \, ds = \int_f \llbracket \alpha \hat{\nabla} \hat{c} w \rrbracket \, ds. \quad (6.18)$$

Summing up over all elements e in Eq. (6.16) and Eq. (6.17) while respecting the interface and zero-flux boundary conditions yields

$$\int_{\Omega} \hat{\nabla} \cdot (\alpha \hat{\nabla} \hat{c}) w \, d\hat{\mathbf{x}} = - \int_{\Omega} \alpha \hat{\nabla} \hat{c} \cdot \hat{\nabla} w \, d\hat{\mathbf{x}} - \int_{\mathcal{F}_{\text{M}}} p[\hat{c}] \cdot \llbracket w \rrbracket \, ds + \int_{\mathcal{F}_{\text{int}}} \llbracket \alpha \hat{\nabla} \hat{c} w \rrbracket \, ds. \quad (6.19)$$

The middle term on the right hand side of Eq. (6.19) is the term which controls the boundary condition at the interface. It is obtained by inserting the interface condition Eq. (6.12) in the integral over the membrane facets in Eq. (6.17). The last term in Eq. (6.19) is further expanded using the identity in Eq. (6.14) which yields

$$\int_{\mathcal{F}_{\text{int}}} \llbracket \alpha \hat{\nabla} \hat{c} w \rrbracket \, ds = \int_{\mathcal{F}_{\text{int}}} \llbracket \alpha \hat{\nabla} \hat{c} \rrbracket \cdot \{w\} \, ds + \int_{\mathcal{F}_{\text{int}}} \{\alpha \hat{\nabla} \hat{c}\} \cdot \llbracket w \rrbracket \, ds. \quad (6.20)$$

Since the exact solution of the diffusion equation is expected to be smooth we enforce continuity of the fluxes by setting $\llbracket \alpha \hat{\nabla} \hat{c} \rrbracket = 0$. To further enforce continuity of the

solution we exploit $[[\hat{c}]] = 0$ and add a term to symmetrize the problem. Additionally, we ensure stability of the problem by adding a stabilizing term according to *Douglas et al.* (1976) which finally leads to

$$\int_{\mathcal{F}_{\text{int}}} [[\alpha \hat{\nabla} \hat{c} w]] \, ds = \int_{\mathcal{F}_{\text{int}}} \{\alpha \hat{\nabla} \hat{c}\} \cdot [[w]] \, ds + \underbrace{\int_{\mathcal{F}_{\text{int}}} \{\alpha \hat{\nabla} w\} \cdot [[\hat{c}]] \, ds}_{\text{symmetry}} - \underbrace{\int_{\mathcal{F}_{\text{int}}} \frac{s_N}{h} [[\hat{c}]] \cdot [[w]] \, ds}_{\text{stability}} . \quad (6.21)$$

In Eq. (6.21), s_N denotes the so-called Nitsche parameter, which must be chosen sufficiently large to ensure continuity across internal facets (*Nitsche*, 1971), and h the average element diameter. Next, we define

$$\begin{aligned} \mathcal{D}(\hat{c}, w, \alpha) := & \int_{\Omega} \alpha \hat{\nabla} \hat{c} \cdot \hat{\nabla} w \, d\mathbf{x} - \int_{\mathcal{F}_{\text{int}}} \{\alpha \hat{\nabla} \hat{c}\} \cdot [[w]] \, ds \\ & - \int_{\mathcal{F}_{\text{int}}} \{\alpha \hat{\nabla} w\} \cdot [[\hat{c}]] \, ds + \int_{\mathcal{F}_{\text{int}}} \frac{s_N}{h} [[\hat{c}]] \cdot [[w]] \, ds , \end{aligned} \quad (6.22)$$

and hence arrive at the final weak form statement of Eq. (6.11) which reads

$$\int_{\Omega} \frac{\partial}{\partial t} (\hat{J} \hat{c}) w \, d\mathbf{x} + \mathcal{D}(\hat{c}, w, \alpha) - \int_{\Omega} \hat{J} R_c(t) w \, d\mathbf{x} + \int_{\mathcal{F}_M} p [[\hat{c}]] \cdot [[w]] \, ds = 0 . \quad (6.23)$$

We note that an integral part of our model design is that continuity is only enforced on the internal edges thus jumps are possible only across the interface of the two subdomains i.e. across the membrane. The cell doublet is characterized by the choice of the permeability p . A non-zero value can be used to model various kinds of transport processes such as the transport of small molecules and ions in and out of the cell through its plasma membrane. Setting $p = 0$ corresponds to a non-permeable membrane. In our case this means that the reactants in each cell cannot pass the intercellular junction. This leads to a variety of possibilities in the description of a cell doublet. Cellular contractility in principle can be described by distinct reaction-diffusion systems in each cell. The RD-systems within the cells can then be coupled by appropriate mechano-chemical coupling terms to account for mechanosensing at the intercellular junction.

6.2.4. COUPLING TO MECHANICS

In order to couple the aforementioned reaction-diffusion system to mechanics we again chose a linear viscoelastic constitutive equation of the Kelvin-Voigt type. Therefore, the weak form for the mechanics of the adherent cell stays unchanged and is given by (Eq. (3.30) in Section 3.2)

$$\int_{\Omega} \boldsymbol{\sigma} : \frac{1}{2} (\nabla \mathbf{v} + \nabla \mathbf{v}^T) \, dx + \int_{\Omega} Y \mathbf{u} \cdot \mathbf{v} \, dx = 0 , \quad (6.24)$$

where Y denotes the substrate rigidity, $\mathbf{v} \in \mathbf{V}(\Omega)$ is a suitable vector valued test function, \mathbf{u} denotes the deformation field and $\boldsymbol{\sigma}$ describes the stress tensor given by

(Eq. (4.1))

$$\boldsymbol{\sigma} = \left(1 + \tau_c \frac{\partial}{\partial t}\right) (\lambda \operatorname{tr}(\boldsymbol{\varepsilon}) \mathbf{I} + 2\mu \boldsymbol{\varepsilon}) + \boldsymbol{\sigma}_a. \quad (6.25)$$

The mechanics naturally couples to the RD-system through the deformation gradient tensor $\hat{\mathbf{F}}$ and its determinant \hat{J} . The coupling of the RD system to mechanics is now introduced through the active stress tensor $\boldsymbol{\sigma}_a$. We assume that the active stress is proportional to the concentration of active MLC. In principle one could assume a linear relationship according to *Brand (2016)* but for reasons of numerical stability we chose a Hill-type function according to *Bois et al. (2011)* and *Nishikawa et al. (2017)* which limits the active stress. We generally propose

$$\sigma_a(c_m(t)) = \sigma_0 \frac{c_m(t)}{\tilde{c} + c_m(t)}, \quad (6.26)$$

where c_m denotes the concentration of MLC, σ_0 is a characteristic active stress and \tilde{c} controls the concentration above which σ_a becomes independent of c_m .

At this point we close the discussion on the numerical treatment. As before, the coupled system of PDEs is implemented in the automated finite element package FEniCs (*Alnæs et al., 2015*). Meshing of the cell pair domain was done with the open source software GMSH (*Geuzaine et al., 2009*) with an average element size of $h \approx 1 \mu\text{m}$ (much smaller than the mesh presented in Fig. 6.1C). The physical dimensions of the cell doublet are chosen according to the cell doublet in Chapter 5. The uncontracted cell doublet is thereby represented by a triangulated square domain with area $A = (45 \times 45) \mu\text{m}^2$. It should be noted that for the cell doublet, the mesh should be constructed such that it is completely represented by facets of the mesh. Otherwise, the interface condition cannot be interpreted correctly by the solver. At this point we will turn to the discussion of a suitable test system for the reaction-diffusion based description of cellular contractility.

6.3. RHOA-PATHWAY

Having reviewed the literature mentioned in the introduction of this chapter, we found that the model as presented by *Kamps et al. (2020)* contains all important components which are necessary for a profound description of the RhoA pathway. In contrast to the RhoA-actomyosin system as introduced by *Staddon et al. (2022)* it explicitly contains GEF as a downstream effector of RhoA, and thus provides an important interface for light-induced contraction as GEF activity can be controlled by optogenetic constructs like the CRY2/CIBN system. In combination with experimental measurements *Kamps et al. (2020)* designed a reaction scheme (Fig. 6.2A) for the active reactants GEF (G),

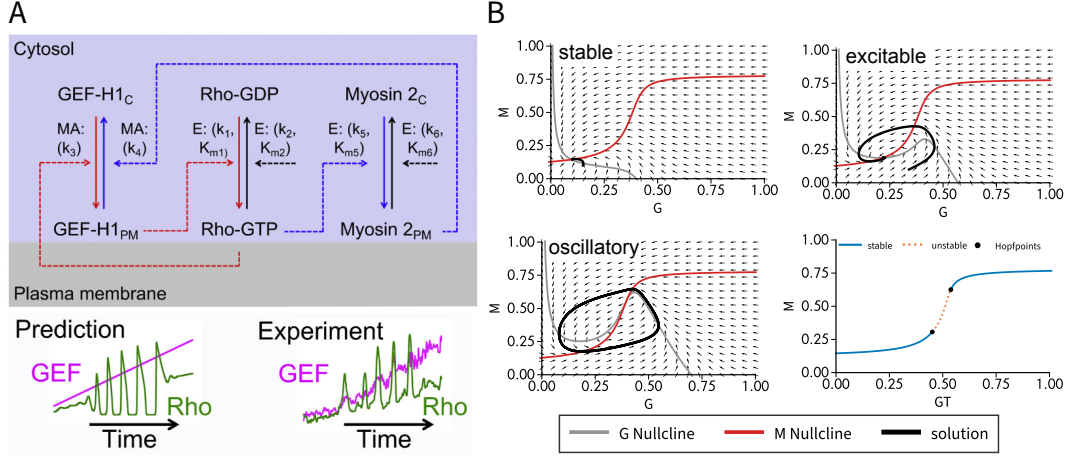


Figure 6.2: Overview of the RhoA-pathway as presented by *Kamps et al. (2020)*. Panel **A** (top) is an illustration of the reaction scheme. Cytosol associated signaling components denote the inactive forms while membrane associated components refer to the active forms. Transition between active and passive is modeled by mass action kinetics (MA) and Michaelis-Menten kinetics. Further, the model includes a positive and negative feedback loop which leads to a non-trivial dynamics. Panel **A** (bottom) shows that GEF concentration strongly influences the stability of the system and controls the cross-over from stable to oscillatory states. Panel **B** shows the mathematical analysis of the system presented in panel **A**. Parameters may be found in Table A.10 and the model equations in Appendix A.3.

RhoA (R) and myosin (M) which reads

$$\frac{dG}{dt} = k_3 R (G_T - G) - k_4 G M \quad (6.27)$$

$$\frac{dR}{dt} = \frac{k_1 G (R_T - R)}{K_{m1} + R_T - R} - k_2 \frac{R}{K_{m2} + R} \quad (6.28)$$

$$\frac{dM}{dt} = \frac{k_5 R (M_T - M)}{K_{m5} + M_T - M} - k_6 \frac{M}{K_{m6} + M} . \quad (6.29)$$

G_T , R_T and M_T denote the total concentrations of the species which the authors assume to be constant. The rate constants are denoted by k_i and the Michaelis-Menten constants are given by the K_{mi} .

The reaction scheme is visualized in Fig. 6.2A, where the membrane and cytosol associated species represent the active and passive states, respectively. This terminology stems from experimental studies which show that the active forms of RhoA and myosin are predominantly found in the vicinity of the plasma membrane and the submembraneous actin cortex. In contrast, the inactive forms are associated with the cytosol (*Citi et al., 1987; Garcia-Mata et al., 2011*). The RhoA protein for example exhibits a lipophilic end which enables it to bind to lipid membranes (*Seabra, 1998*). However, so-called guanosine dissociation inhibitors (GDIs) may bind to Rho-GDPs, not only keeping them in a permanently inactive state but also preventing its membrane localization by shielding the hydrophilic end and additionally making it soluble in the cytoplasm (*Somlyo et al., 2000*). The reaction scheme also highlights the two feedback loops which are important to describe the excitable and oscillatory dynamics that are observed in experiments. The positive feedback loop stems from the observation that RhoA activity at the membrane further induces GEF membrane recruitment.

Due to Rho activation by GEFs, this closes a positive feedback loop (*Kamps et al.*, 2020). The negative feedback loop can be traced back to the ability of myosin to inhibit the nucleotide exchange activity of GEFs by binding to their Dbl-homology domain (DH) (*C.-S. Lee et al.*, 2010). Essentially, the authors could identify the total concentration of active GEF as the main bifurcation parameter for the switch from stable to oscillatory states at intermediate GEF concentrations (Fig. 6.2A (bottom)). In experiments, they vary this bifurcation parameter by treating cells with nocodazole, which leads to depolymerization of microtubules from which GEFs are then released. The crossover from stable to oscillatory dynamics as a function of the total GEF concentration is illustrated in Fig. 6.2A (bottom).

The three regimes of their proposed activator-inhibitor scheme are presented in the phase-portraits in Fig. 6.2B. We reproduced these plots when attempting to find a suitable parameter space which could resemble our experimental findings of Chapter 4 and Chapter 5 but used a generalized parameter set taken from (*Tyson et al.*, 2003) where various different activator-inhibitor schemes are analyzed.

6.3.1. LINEAR RHOA - PATHWAY

In contrast to the work presented by *Kamps et al.* (2020) and *Staddon et al.* (2022) the focus in our work lies on the optogenetic perturbation of cells and not the pulsatile nature of the actin cortex. Based on the experimental findings of Chapter 4 and Chapter 5, we see optogenetic activation as a reversible process such that after activation cells eventually go back to their homeostatic contractility level. Further, in the experiments carried out by Tomas Andersen and Artur Ruppel at the Université Grenoble Alpes, we did not notice any oscillations or excitable behavior upon photoactivation, which suggests that we operate around a stable fixed point of the Rho system. There might be several reasons for this: On the one hand, the strain energy output in our experiments is dominated by stress fiber contractility and little influenced by the cortex itself. Since stress fibers are highly organized structures it is plausible to assume a differently organized reaction-diffusion system as for the rather unorganized actin cortex. The results of Chapter 4 support this assumption based on the different obtained activation and relaxation times for cells on disc and hazard patterns. On the other hand, the results of *Kamps et al.* (2020) show strong dependence on the total GEF concentration which suggests that the total GEF expression levels also influence the dynamics of the underlying Rho-response. Since cells transfected with the CRY2/CIBN system show a significantly higher baseline contractility we assume that this might correspond to the stable branch of high GEF concentrations (Fig. 6.2). Excitability is therefore completely controlled by the membrane recruitment of GEF and is according to *Valon et al.* (2015; 2017) scalable. Longer pulses lead to more GEF membrane recruitment until the system reaches saturation.

Strikingly, even very complex signaling cascades may effectively behave as linear transmitters which has been verified numerically and analytically for the Wnt-pathway, the ERK-pathway and the TGF β -pathway (*Nunns et al.*, 2018). Motivated by this, and to reduce the parameter space we assume a linear input-output rela-

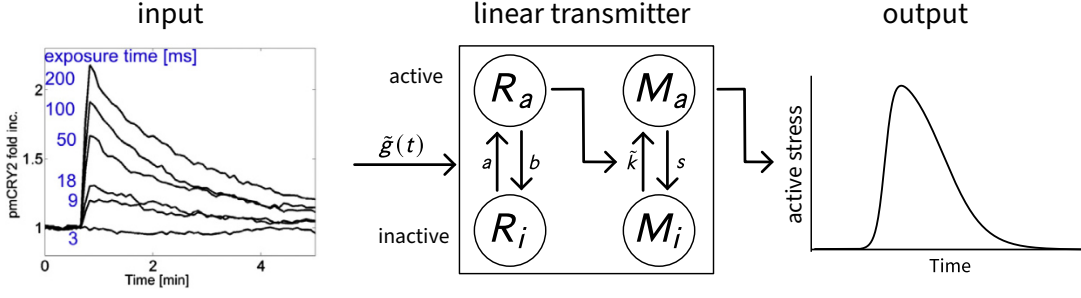


Figure 6.3: A simplified view on the RhoA-pathway. An exponentially decaying input signal with a steep initial increase is turned into a smooth output-signal. Based on the results of Chapter 4 and Chapter 5, optogenetic activation using the CRY2/CIBN construct seems to produce a homeostatic response of the activated cell. The simplest model which provides this specific input-output relationship is a weakly activated linear signaling cascade. Figures: Left plot adapted from (Valon *et al.*, 2015).

relationship between GEF plasma membrane recruitment and NMII induced contractility. This assumption not only reduces the number of unknown parameters it also allows an analytical solution. Our proposed RhoA-myosin reaction scheme is shown in Fig. 6.3. In our proposed model, GEF activity enters implicitly through a predefined input signal with a constant baseline and a time dependent contribution upon photoactivation. This input signal consequently triggers a reaction cascade by activating RhoA which in turn activates MLC. All reactions are modeled by a law of mass action with positive valued activation rate constants a and \tilde{k} . Further we assume that all active components deactivate spontaneously described by the positive valued rate constants b and s . Additionally, we postulate that the total amount of each signaling component is conserved such that the active components are given by the difference of the total concentration and the concentration of the inactive species R_i and M_i . Hence, we denote the active species by $R = R_T - R_i$ and $M = M_T - M_i$ which allows to write the reaction kinetics as

$$\frac{dR}{dt} = a\tilde{g}(t)(R_T - R) - bR \quad (6.30)$$

$$\frac{dM}{dt} = \tilde{k}R(M_T - M) - sM. \quad (6.31)$$

The function $\tilde{g}(t)$ accounts for a time dependent activation rate for RhoA mediated by light induced membrane recruitment of GEF. Another simplification is made by considering the limit of a weakly activated signaling cascade (Beguerisse-Díaz *et al.*, 2016) for which $R_T - R \approx R_T$ and $M_T - M \approx M_T$ such that the system can be written as

$$\frac{dr}{dt} = a\tilde{g}(t) - br, \quad \frac{dm}{dt} = kr - sm, \quad (6.32)$$

where we divided by the total concentration and hence set $r = R/R_T$, $m = M/M_T$ and $k = \tilde{k}R_T$. The function $\tilde{g}(t) := 1 + g(t)$ is split into a constant baseline and a time dependent activation function

$$g(t) = H(t - t_{\text{act}})\alpha e^{-\lambda(t - t_{\text{act}})}, \quad (6.33)$$

where $H(t)$ is the Heaviside function and α denotes the relative GEF increase at the membrane upon a single light pulse of a few hundred milliseconds which then decays according to a typical time constant λ around $\tau = 1/\lambda = 80\text{ s} - 200\text{ s}$ (*Valon et al.*, 2015). In case of no perturbation $g(t) = 0$ the steady states of r and m are fully determined by the rate constants

$$r_{\text{ss}} = \frac{a}{b}, \quad m_{\text{ss}} = \frac{ak}{bs}. \quad (6.34)$$

W.l.o.g. we perturb the steady state of the system at $t_{\text{act}} = 0$ with a light-pulse ($g(t) \neq 0$) and express the time evolution of the relative concentrations as

$$r(t) = r_{\text{ss}} + \delta r(t), \quad m(t) = m_{\text{ss}} + \delta m(t), \quad (6.35)$$

where $\delta r(t)$ and $\delta m(t)$ denote the time-dependent perturbations of the steady state. Together with Eq. (6.36) we end up with the time evolution of the perturbation which is given by

$$\frac{d\delta r}{dt} = aI(t) - b\delta r, \quad \frac{d\delta m}{dt} = k\delta r - s\delta m. \quad (6.36)$$

With our choice for $g(t)$ this system can be solved analytically which yields

$$\delta r(t) = \frac{a\alpha}{b - \lambda} \left(e^{-\lambda t} - e^{-bt} \right), \quad (6.37)$$

$$\delta m(t) = \frac{ak\alpha}{b - \lambda} \left(\frac{e^{-bt}}{b - s} - \frac{e^{-st}}{b - s} + \frac{e^{-\lambda t}}{s - \lambda} - \frac{e^{-st}}{s - \lambda} \right). \quad (6.38)$$

In experiments one usually quantifies the relative activity increase with respect to the activity baseline. We therefore normalize the perturbation with respect to the steady states as given in Eq. (6.34)

$$\delta \tilde{r}(t) = \frac{\delta r}{r_{\text{ss}}} = \frac{b\alpha}{b - \lambda} \left(e^{-\lambda t} - e^{-bt} \right), \quad (6.39)$$

$$\delta \tilde{m}(t) = \frac{\delta m}{m_{\text{ss}}} = \frac{b\alpha s}{b - \lambda} \left(\frac{e^{-bt}}{b - s} - \frac{e^{-st}}{b - s} + \frac{e^{-\lambda t}}{s - \lambda} - \frac{e^{-st}}{s - \lambda} \right). \quad (6.40)$$

The strength and time course of the relative RhoA and myosin perturbations is controlled by the two deactivation rates b and s as well as the strength of the input signal α and its decay rate λ . For the later performed two dimensional simulations we further add diffusion to the model.

6.3.2. PARAMETRIZATION

For the parametrization of the proposed linear signaling cascade we rely on the order of magnitudes found in the respective literature. Within the limits of our simplified model the total concentrations of RhoA and myosin are irrelevant since they do not explicitly enter the reaction kinetics in the weakly activated regime. The parameters are chosen such that the steady state concentrations of RhoA and myosin are roughly 10% of the total concentration (*Besser et al.*, 2007; *Staddon et al.*, 2022). Further, time scales are

Abbreviation	Used value	Ref. value	Reference
λ	0.01 s^{-1}	$0.008 \text{ s}^{-1} - 0.018 \text{ s}^{-1}$	(Valon <i>et al.</i> , 2015)
α	200 %	130 % – 220 %	(Valon <i>et al.</i> , 2015)
b	0.0165 s^{-1}	2 s^{-1}	(Kamps <i>et al.</i> , 2020)
k	0.1 s^{-1}	0.1408 s^{-1}	(Staddon <i>et al.</i> , 2022)
		0.147 s^{-1}	(Kamps <i>et al.</i> , 2020)
s	0.083 s^{-1}	0.0051 s^{-1}	(Kamps <i>et al.</i> , 2020)
		0.082 s^{-1}	(Staddon <i>et al.</i> , 2022)
m_{ss}	0.1	0.1 – 0.3	(Staddon <i>et al.</i> , 2022)
			(Besser <i>et al.</i> , 2007)
D_R, D_G	$0.28 \mu\text{m}^2 \text{ s}^{-1}$	$0.28 \mu\text{m}^2 \text{ s}^{-1}$	(Kamps <i>et al.</i> , 2020)
		$0.1 \mu\text{m}^2 \text{ s}^{-1}$	(Nishikawa <i>et al.</i> , 2017)
D_M	$0.03 \mu\text{m}^2 \text{ s}^{-1}$	$0.03 \mu\text{m}^2 \text{ s}^{-1}$	(Kamps <i>et al.</i> , 2020)
		$0.01 \mu\text{m}^2 \text{ s}^{-1}$	(Nishikawa <i>et al.</i> , 2017)
Deduced			
r_{ss}	0.083		
a	0.0014 s^{-1}	$< 0.002 \text{ s}^{-1}$	(Staddon <i>et al.</i> , 2022)

Table 6.1: Parameter values for the linearized RhoA signaling cascade. We set most of the parameters in accordance with the reported ranges. The parameters taken from (Kamps *et al.*, 2020) were obtained by taking the corresponding activation and deactivation rates in a weakly activated regime for which the Michaelis Menten terms can be linearly approximated. However, their model does not provide a basal activation rate. The reported rate constants as stated in the work of Staddon *et al.* (2022) were deduced from Michaux *et al.* (2018). The parameters r_{ss} and a were not independent and consequently deduced from the fixed parameters.

chosen such that the time course of the myosin concentration approximates the time course of the active stress in Chapter 4 and/or other reported measurements (Kamps *et al.*, 2020; Kowalczyk *et al.*, 2022; Staddon *et al.*, 2022; Valon *et al.*, 2017). The time course of the input signal was adapted to the measured CRY2 membrane recruitment and is described by a relaxation time of $\lambda \approx 10^{-2} \text{ s}$ (Valon *et al.*, 2015). All other relevant parameters are summarized in Table 6.1.

Fig. 6.4 shows the time evolution of the linear signaling cascade for the provided parameter estimates. In particular, Fig. 6.4A shows the relaxation into the steady state which is reached at $m_{\text{ss}} = 0.1$ and $r_{\text{ss}} = 0.083$, while in Fig. 6.4B one can see the time evolution of the RhoA perturbation and the myosin perturbation upon an input signal which resembles a two-fold increase of GEF concentration at the membrane. The time delay between input signal and the peak value of RhoA activity is given by

$$t_{\text{delay}} = \frac{\ln(\lambda/b)}{\lambda - b}, \quad (6.41)$$

and fully determined by the decay rate of RhoA and the input signal. Given this parametrization, myosin activity closely follows the RhoA activity similar to the excitable regime discussed by Staddon *et al.* (2022). The whole system as later used to qualitatively simulate the cell doublet is summarized in the phase portrait in Fig. 6.4C. However, the here presented graphs purely represent the reaction kinetics which be-

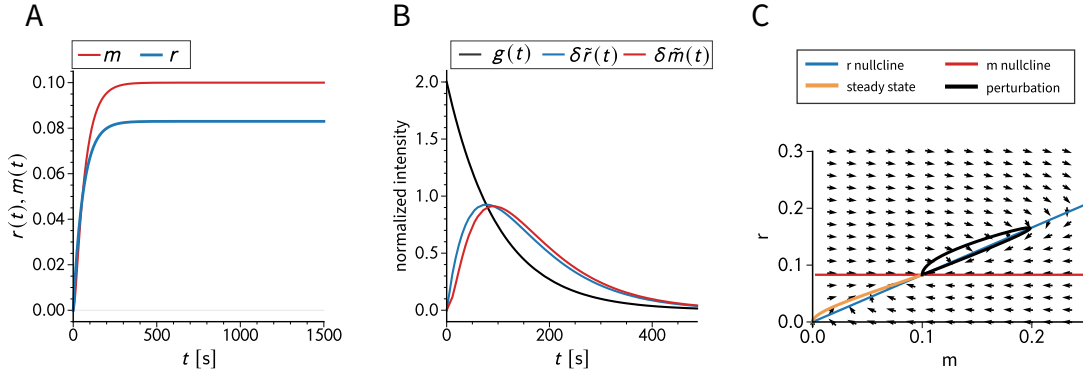


Figure 6.4: Reaction kinetics of the linearized RhoA-pathway. Panel **A** shows the evolution into the normalized steady state concentrations. Panel **B** depicts the time course of the RhoA and myosin perturbations normalized to the steady state. The time evolution is triggered by an exponentially decaying input signal $g(t)$. Panel **C** summarizes the full dynamics of the system in one phase portrait. In addition to the RhoA and myosin nullclines, it shows the relaxation into the steady state (yellow line) as well as the time evolution of the perturbation (black line). Parameters are chosen according to Table 6.1.

come affected (albeit slightly) by the coupling to mechanics due to changes in domain size. Further we performed a sanity check, shown in Fig. A.9, which demonstrates that rapid changes in domain size speed up reactions but do not change the overall steady state of the system. Additional information is given in Appendix A.3. Moreover, in Fig. A.9B we exploited the system by *Kamps et al.* (2020) to test the interface condition by verifying that traveling wave peaks cannot pass the intercellular junction. More details on this simulation are provided in Appendix A.3.

6.4. PHOTOACTIVATION WITH FEEDBACK

In this section we combine the methods introduced above to simulate local photoactivation in the cell pair model and introduce a strain dependent feedback in the non-activated cell upon photoactivation. We therefore solve the coupled equations Eqs. (6.23) and (6.24) together with Eqs. (6.25) and (6.26) and use the reaction kinetics of the linearized RhoA-pathway stated in Eq. (6.36).

6.4.1. BASELINE CONTRACTILITY

The baseline contractility is given by the steady state concentration of myosin. The active stress generated in the steady state is chosen to be in the same order of magnitude as the stresses in Chapter 5 and set to $\sigma_a(m_{ss}) = \sigma_0 m_{ss} / (\tilde{c} + m_{ss}) = 5$ kPa. Moreover, for simplicity we use an isotropic contractile stress. All parameters for the cell substrate coupling are summarized in Table A.5. The results of the equilibrium state before photoactivation are shown in Fig. 6.5. The constant myosin concentration (Fig. 6.5A) leads to a constant isotropic background stress which results in a total stress which is largest over the adhesive regions (Fig. 6.5).

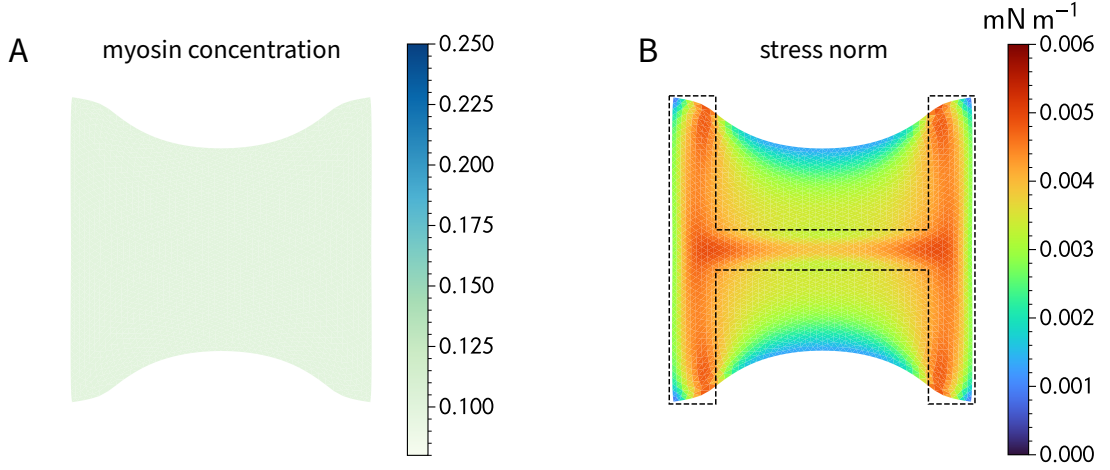


Figure 6.5: Baseline contractility in the cell pair model. Panel **A** shows the steady state myosin concentration in both cells. Panel **B** depicts the resulting internal cell stress for a cell pair adhered to a H-pattern. The constant myosin concentration leads per design to an isotropic constant contractile background stress.

6.4.2. PHOTOACTIVATION

This equilibrium state (Fig. 6.5) is the starting point for the photoactivation simulations. Upon photoactivation at $t = 300$ s we increase the GEF concentration by 200 % in the left cell. This leads to an increase in myosin concentration and consequently to contraction of the left cell. The contraction of the left cell then leads to a purely passive deformation in the right cell as the signaling components cannot pass the intercellular junction (see Fig. 6.6A).

At this point one has to specify how to couple the reaction diffusion system in the non-activated cell to the mechanical perturbation it experiences during contraction of the activated cell. The two obvious choices are either a force/stress-dependent or strain-dependent trigger. Motivated by experimental studies that cells directly react to stretching (*Hippler et al., 2020*) we decide to introduce a strain dependent feedback. For this we measure the strain difference in the passive cell with respect to the equilibrium configuration before photoactivation $\delta\varepsilon_{ij} = \varepsilon_{ij}(t > t_{\text{act}}) - \varepsilon_{ij}(t = t_{\text{act}})$. Further, we only consider positive strain differences $\delta\varepsilon_{+,ij} := \max(0, \delta\varepsilon_{ij})$ such that the RD-system in the right cell is only triggered in regions where the cell is stretched. Our measure of choice is

$$|\delta\varepsilon_+(t, x, y)| := \sqrt{\delta\varepsilon_{+,xx}^2 + \delta\varepsilon_{+,yy}^2}, \quad (6.42)$$

where ε_{xx} and ε_{yy} correspond to the diagonal components of the stress tensor. The RD-system in the right cell is then triggered by altering the basal activation rate of RhoA according to the measured passive strain difference

$$\frac{d\delta r}{dt} = a\xi|\delta\varepsilon_+| - b\delta r, \quad (6.43)$$

where ξ controls the strength of active coupling and has to be adjusted according to the typical strain differences. We heuristically found that a value of $\xi \approx 100$ leads to a

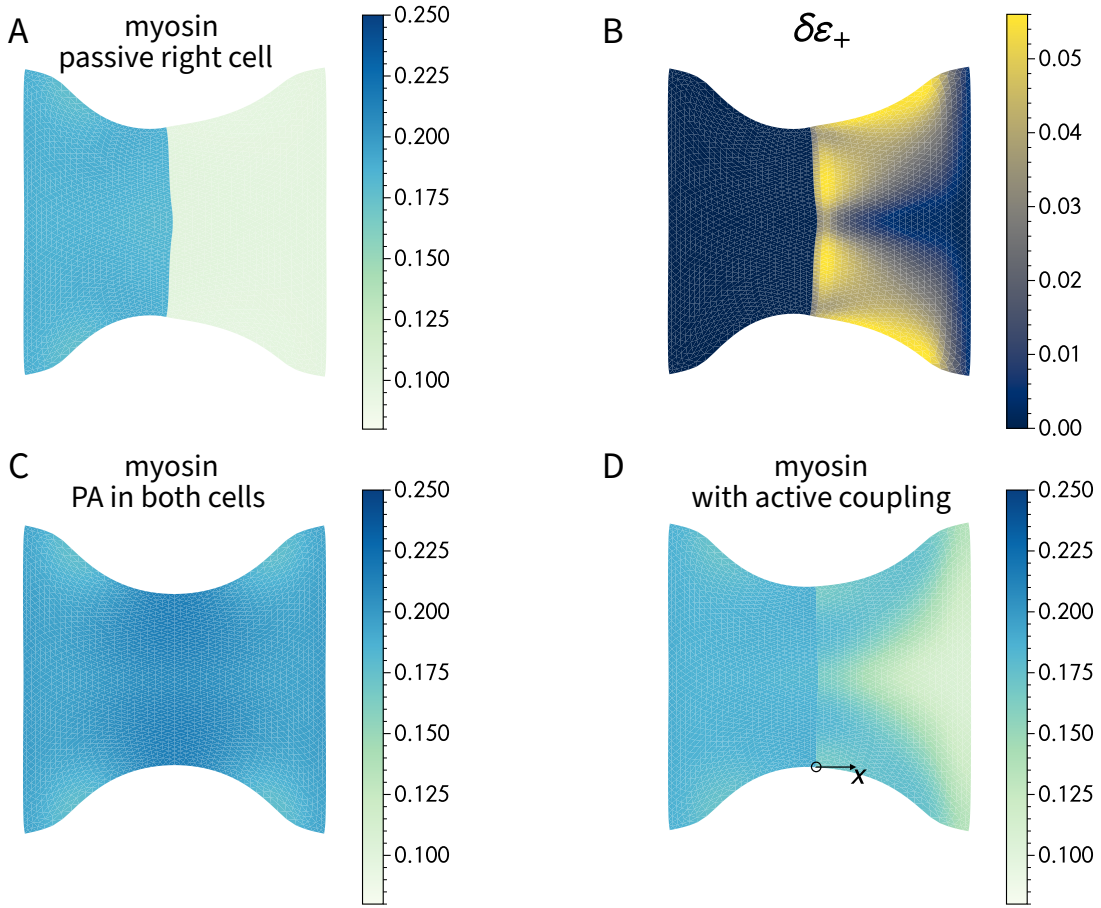


Figure 6.6: Influence of strain dependent active coupling on cell periphery. Panel **A** depicts the myosin concentration in the left cell. The right cell is passive and not activated. Hence the myosin concentration remains at its baseline level. Panel **B** shows the positive strain arising in the passive cell upon contraction of the left cell in the doublet. Regions of positive strain trigger RhoA activation within our model. Panel **C** depicts the case of global photoactivation. Myosin concentrations are equally elevated in both cells which leads to a symmetric cell shape. Panel **D** shows the cell shape if left and right cell are actively coupled. A strain dependent active coupling may explain an approximately symmetric response of the whole cell doublet even when only the left cell is activated. The symmetry of the symmetry between left and right is quantified by tracking the position of the symmetry center of the invaginated arc (black circle).

similar contraction in the right cell compared to the left cell. However, the magnitude of the value depends on several properties and is different for other cell and substrate parameters. In addition, other measures for the deformation of the passive cell may lead to different values of ξ . We then simulated photoactivation for 5 different values of ξ between $\xi = 0$ and $\xi = 100$. A graphical representation of the simulation is shown in Fig. 6.6. All images correspond to the same time step $t = 410$ s which is the time point of maximal strain energy. In case of $\xi = 0$ we obtain the purely passive response of the right cell and its concentration of active myosin remains at the baseline level throughout the contraction of the left cell. The regions where the right cell is stretched are shown in Fig. 6.6B. Clearly visible, high positive strains occur in the non-adherent parts of the right cell and are largest in the vicinity of the intercellular junction. In the purely passive case, the periphery is skewed and shows a clear asymmetry between left and right. As a cross-check, the contour of a symmetrically activated cell doublet

remains symmetric (Fig. 6.6C). For a value $\xi = 100$, i.e. strong active coupling, an initially asymmetric contour as in Fig. 6.6A turns into an almost symmetrical contour as the increase of active myosin along the cell periphery counteracts the deformation that is caused by the left cell.

To quantify the time course of the deformation, we track the strain energy and the x position of the symmetry center of the invaginated arc as a function of time for varying active coupling strengths (Fig. 6.6D). Fig. 6.7 displays the results of this simulation. In particular, Fig. 6.7A shows that, upon photoactivation, the strain energy increases with increasing coupling strength as one would expect. Further, Fig. 6.7B shows the influence of the coupling strength on the symmetry center of the invaginated arc. Thereby a negative value corresponds to the symmetry center being shifted towards the activated cell. For small values of ξ the asymmetry remains until the myosin concentration in the activated cell is back to its baseline level. This effect becomes weaker with increasing coupling strength. For a value of $\xi = 100$ the symmetry is recovered approximately 200s after PA. Additionally, the motion of the symmetry center is non-trivial as it moves back and forth during the interaction of the two cells like in a “tug-of-war”.

Next, for Fig. 6.7C and D we investigate the time course of the relative strain energy on the left and right half of the pattern separately. Comparing the strain energies for no active coupling and strong active coupling highlights that the active response of the right cell also increases the substrate strain energy on the left side (compare blue curves in Fig. 6.7C and D). In case of a purely passive right cell the strain energy on the right half shows a very weak instantaneous increase. In case of active coupling the maximal strain energy in the right cell is delayed.

Taken together, a strain dependent feed back onto the RD-system may produce a symmetric response of the cell doublet upon photoactivation of the left cell only. However, the right cell responds with a delay which is defined by the activation rates of the cascade.

6.5. CONCLUSION

In this chapter we introduced a discontinuous Galerkin model to describe an interacting pair of cells. The discontinuous nature of the approach allowed us to introduce an internal zero-flux boundary condition which accounts for the non-permeable character of the intercellular junction. To adequately couple a biochemical reaction-diffusion system and cell mechanics, we derived the diffusion equation on a deformable domain and introduced a concentration dependent active contractility. As a model system we proposed a linearized version of the RhoA-pathway and connected active force generation to the concentration of active myosin which is given by the output of the signaling cascade. The optogenetic control was introduced by an input signal which perturbs the signaling cascade.

We then exploited the linearized RhoA-pathway to simulate the local photoactivation experiments as discussed in Chapter 5. We could successfully demonstrate that photoactivation, and thus contraction of one cell, leads to an active response in

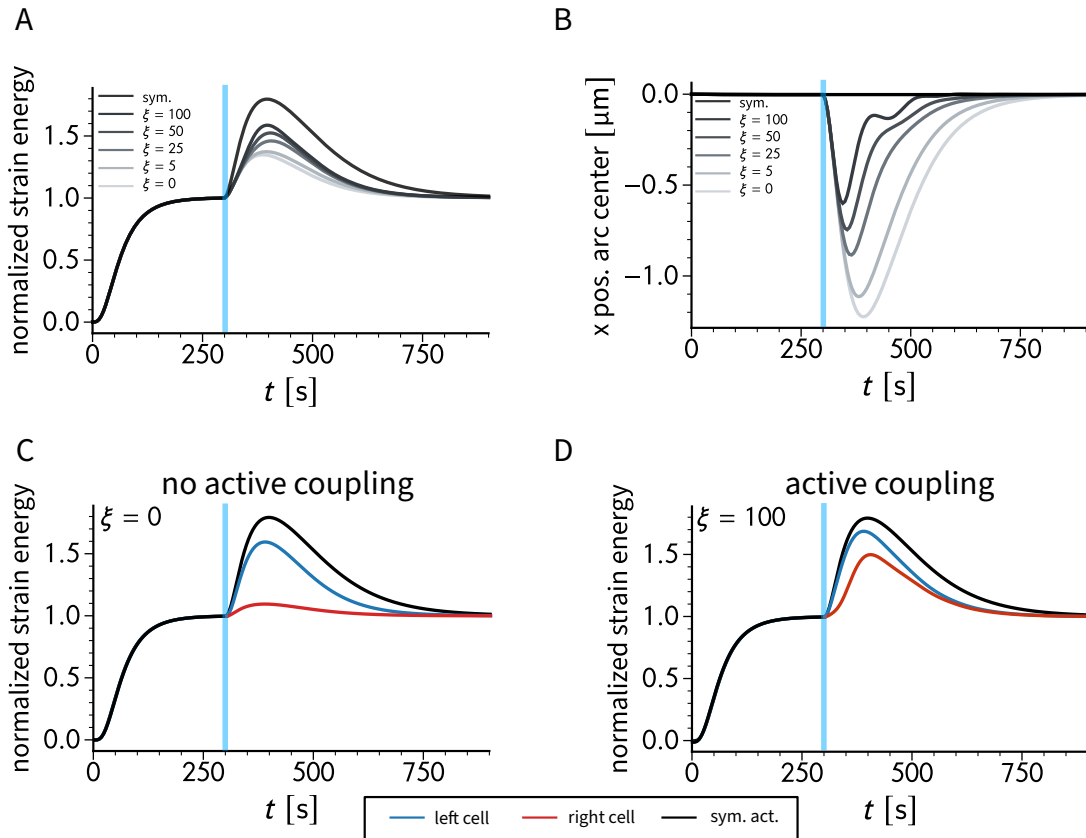


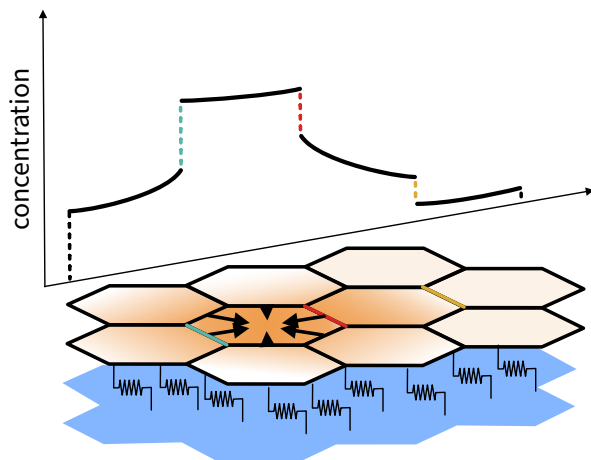
Figure 6.7: Quantification of the substrate strain energy and cell shape as a function of the active coupling strength. Panel **A** shows the time course of the substrate strain energy for varying parameters of the coupling strength ξ . Stronger coupling leads to larger strain energies. Panel **B** shows the x -position of the symmetry center of the invaginated arc as a function of time. Negative values indicate that this point is shifted towards the left cell. Active coupling weakens the symmetry break upon photoactivation and leads to a more symmetric response with increasing coupling strength. Panel **C** and **D** show the time course of the strain energy calculated over the left and right half of the pattern, respectively.

the non-activated cell by introducing a coupling parameter which triggers the RhoA cascade in the non-activated cell.

However, the results presented in this chapter only serve as a qualitative study and focused on the numerical implementation of the cell doublet. We are aware that the RhoA-pathway can, at all, only be linearized under very specific conditions and further studies should aim at testing the limits of this linear input-output relation which the results of Chapter 4 and Chapter 5 suggest. We would also like to point out that the approach discussed here can be combined with any type of reaction diffusion system and is not limited to the proposed reaction kinetics. Although *Staddon et al.* (2022) discussed an RD-system in combination with viscoelastic solids and fluids, they do not incorporate possible influences stemming from the geometry and rigidity of the ECM. If mechanical deformations trigger pulsatile contractions, non-trivial spatial patterns and pulsatory flows of RhoA and active myosin, it would be interesting to connect their emergence to properties of the ECM and interaction with other cells.

In future studies our proposed model could be exploited to study force transmission in larger cell clusters by means of FEM simulations. A model sketch is shown in Fig. 6.8. Similar to vertex models, one could represent an epithelial sheet of cells by compartmentalization of the simulation domain. However, each of the compartments represents a full cell, obeying a viscoelastic material law with connection to an elastic foundation. The intercellular junctions are then introduced as zero-flux boundary conditions, which is computationally much cheaper than defining a distinct biochemical RD-system in each cell. Within our approach the biochemical model can be represented by a single set of equations representing concentrations of signaling components which jump across the interfaces as illustrated in Fig. 6.8. Hence, for a system of N cells and a RD-system with k signaling components one would only have to solve k equations instead of $N \times k$ equations. Further, the active coupling between the cells is then again introduced by biochemical-mechanical coupling terms. In this way one can treat the cell layer as a whole elastic medium, keep the full complexity of the mechanical model and study local force production and subsequent force propagation in terms of the reaction kinetics, the mechanics of the cell, and the ECM. Additionally, mechanical polarization can be introduced analogously to Chapter 4 and Chapter 5.

Figure 6.8: Full discontinuous Galerkin FEM model of an adherent epithelial layer, where cellular contractility is modeled by a reaction-diffusion system (orange). The concentration of a signaling component is described by a single concentration field across the entire domain and is allowed to jump across cellular interfaces (colored lines). By coupling biochemistry and mechanics using appropriate coupling terms, cells can interact and contraction of a single cell can trigger contraction of other cells (black arrows). The cell layer is further treated as a whole elastic continuum connected to an elastic foundation (springs).



Chapter 7

Summary and outlook

Biological cells probe the physical properties of their environment by actively generating forces. This ability is provided by the highly dynamic actin cytoskeleton. For this work, I developed, parameterized, and applied finite element models of active viscoelastic thin films in combination with a numerical treatment of contour models to describe the mechanical properties of the actin cytoskeleton in strongly adherent single cells, cell pairs, and small cell clusters. These models have been applied in two collaborations with experimentalists to quantitatively study force generation and force propagation. Below, we provide a brief summary of our results and discuss suggestions for future theoretical and experimental studies.

In **Chapter 2** we laid down the mathematical foundation of both of the above mentioned models and recapitulated central analytical examples for each model class. This was an important step because the numerical implementation of the models could be validated by direct comparison with their analytical counterparts in **Chapter 3**.

Chapter 4 discusses the results of a first collaboration with experimentalists, where we studied fibroblasts, transfected with the optogenetic CRY2/CIBN system, on flat elastic substrates. In this context, we extended the basic simulation setup introduced in Chapter 3, in order to account for anisotropic internal cell stresses, viscoelastic properties of the cytoskeleton and position-dependent cell-substrate coupling. Based on experimental data of the optogenetically stimulated cells, we were able to parametrize our model and further use it to gain insight into the force generation dynamics provided by the light-induced perturbations of the RhoA pathway. Our computational results reveal a positive correlation between internal cell stresses and spread area, whereby the active generated stresses are in the order of \sim kPa. Beyond that, we were able to quantify the dynamics of tensional homeostasis after transient RhoA activation. In doing so, we identified the organization of the actin cytoskeleton as a crucial factor influencing the cellular response. Our results further showed a saturation behavior of the RhoA system for pulse durations larger than 25 ms that is independent of actin organization, in marked contrast to the dynamics of force generation.

In the future it would be interesting from an experimental point of view not only to study cells in a state of mature adhesion, but also to use optogenetic perturbations to directly interfere with the cells' spreading process. During spreading, the actin cytoskeleton is much more dynamic, and controlled light stimulation could possibly allow to guide it into a certain direction. On the theoretical side, one could extend

the model by introducing the precise distribution of focal adhesions as, in the current simulation approach, the cell fully adheres to all fibronectin coated regions equally strongly. This approach, however, would rely on precise image processing routines to properly segment the focal adhesions and most likely involve meshing algorithms to properly construct an FEM mesh which includes the segmented position of focal adhesions similar to the work by *Soiné et al.* (2015). Another improvement could be to describe the substrate as an elastic half-space and use traction force reconstruction methods known from TFM instead of estimating the effective spring stiffness density Y . Moreover, a three-dimensional treatment, similar to the model proposed by *Kim et al.* (2021) could be used to model three-dimensional cells in contact with planar substrates. Further, approaches like these would allow to incorporate the mechanical properties of the nucleus and, for example, enable the study of its influence on focal adhesion distribution and the associated traction force patterns.

Chapter 5 presented the results of a second collaboration with an experimental group where we investigated active coupling and force transmission between epithelial cells. A combination of traction force measurements, monolayer stress microscopy, image processing and contour models allowed us to characterize the influence of intercellular junctions on the mechanical and structural properties of cell pairs. By comparing single cells and interacting cell pairs under the same external conditions, we found that the cell-cell junction reduces the mechanostructural polarization of the system and additionally leads to a redistribution of forces in the peripheral stress fibers of a cell. In addition, we extended the continuum model by including local photoactivation, and developed a finite element description for the mechanics of the free spanning stress fiber to account for spatially varying loading conditions during optogenetic activation. The two-dimensional continuum approach allowed us to show that transient local photoactivation leads to a destabilization of tensional homeostasis in single cells most likely connected to cytoskeletal fluidization. In marked contrast, cell pairs showed a homeostatic response independent of the internal actin organization. Together with the experimental data, we quantified stress propagation across the intercellular junction by only activating one of the cells in the cell pair. In particular, a comparison of cell shape dynamics and force generation within this setup revealed a stronger active coupling of the cellular cortices than internal stress fibers. Furthermore, we identified the mechanostructural polarization of the cells as a major factor determining the efficiency of stress propagation which turned out to be most effective perpendicular to the polarization axis. This observation could even be verified for small epithelial cell collectives.

In the future it would be interesting from an experimental point of view to look at ways to realize a “passive” cell pair, for example, by suppressing the signaling abilities at the cell-cell interface while maintaining a stable mechanical connection between the cells. Further, it could be interesting to additionally test the effects that the duration of photoactivation has on the distance that mechanical signals can propagate. On the theoretical side, a natural starting point for future work would be a unified framework that combines finite element modeling of two dimensional elastic sheets and contour

models. This could be achieved by a combination of bulk and surface elasticity, in form of a line tension, similar to the approach presented by *Mailand et al.* (2019) in two dimensions. This is, however, not straight forward to implement, as the line tension is not independent of the curvature of the cell periphery. One way to solve this could be a finite element treatment of mixed dimensional coupled partial differential equations. Besides that, our numerical treatment of active coupling remained purely heuristic and does not incorporate cell signaling and mechanochemical feedbacks such that future work could focus on the computational design of such mechanisms in a finite element framework.

Chapter 6 addressed the emerging question of how to model a cell pair in terms of its key features, such as the presence of an intercellular connection. We presented a discontinuous Galerkin method to combine the biochemistry of the RhoA pathway, photoactivation, active force generation and the topological features of a cell pair. In particular, we coupled reaction-diffusion equations on deformable domains to the equations of mechanical equilibrium and modeled the intercellular junction as a non-permeable membrane which separates the two cells. This allowed us to introduce a strain-dependent coupling term which, depending on the degree of active coupling, could explain the (to a good approximation) global response of the cell doublet upon local photoactivation.

In the future it would be interesting to numerically investigate several different mechanochemical feedbacks. Both cell-cell junctions and focal adhesions are crucial signaling hubs of cells. The stress applied to these structures feeds back to the force-generating signaling pathways. Hence, due to their different localization within the cell this could affect the dynamics of the feedback in different ways depending on parameters such as substrate stiffness, substrate geometry, and internal actin organization. The simulated “feedback” patterns could then be compared to experimental measurements in which, for example, the spatiotemporal evolution of RhoA or MLC is tracked. Another application of the discontinuous Galerkin method would be the application of the above described scenario in the context of larger multicellular systems. One could think of quantifying force propagation in a tissue by photoactivation of a whole cell in an epithelial sheet as a function of distinct mechanochemical feedback terms.

In summary, this work contributes to a better understanding of force generation and force propagation in adherent cells and identifies the organization of the actin cytoskeleton as an essential component of these processes.

Chapter A

Appendix

A.1. SUPPLEMENTARY INFORMATION FOR CHAPTER 4

STATISTICAL ANALYSIS

To test the significance in between data, we performed both two-tailed Student's T-tests in the case of 2 data sets and non parametric Kruskal-Wallis test in the case of 3 data sets. For this we used the software GraphPad Prism (*Swift, 1997*). Error bars on graphs and boxplots correspond to the standard deviation. (*Andersen et al., 2022*)

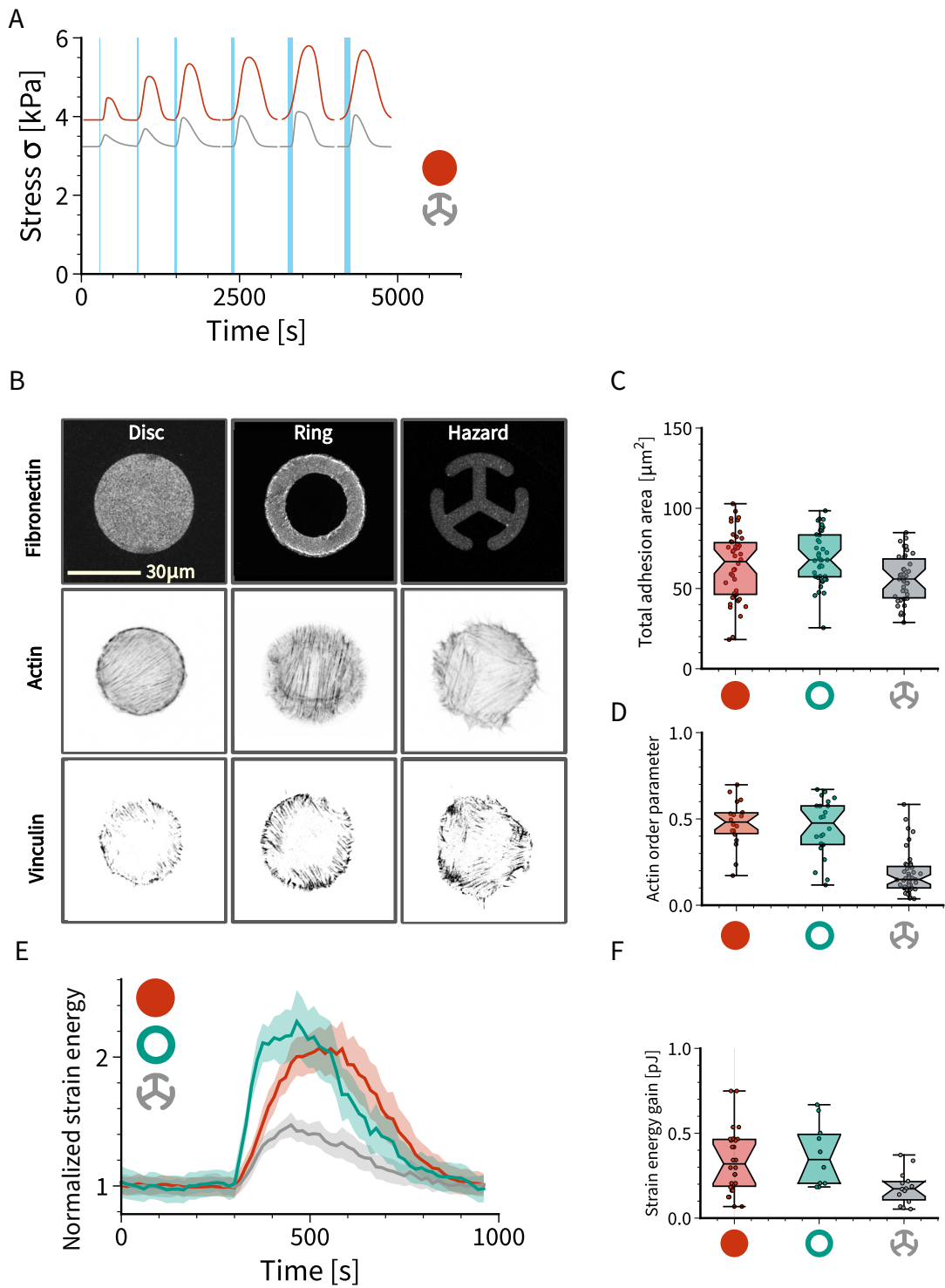


Figure A.1: Panel **A** depicts the time course of the active stress corresponding to the time course of the strain energy as shown in Fig. 4.12A. Panel **B** shows: from left to right: disc, hazard and ring fibronectin pattern on PAA hydrogels (i). Actin-labelled cells (ii). Vinculin staining (iii). Panel **C** compares the total adhesion area for all three patterns measured as the integrated vinculin signal. Panel **D** shows the actin order parameter. Panel **E** shows the time course of the average substrate strain energy normalized with respect to the baseline level. Panel **F** compares the mean strain energy gain during PA.

TABLES CHAPTER 4

Fixed parameter	Value
Young's modulus of the substrate E_s	4.47 kPa
Poisson's ratio of the substrate ν_s	0.5
Substrate thickness h_s	50 μm
Lateral cell size L_c	50 μm
Young's modulus of the cell E_c	10 kPa
Viscosity of the cell η_c	100 kPa s
Poisson's ratio of the cell ν_c	0.5
Cell layer thickness h_c	1 μm

Table A.1: Globally fixed cell and substrate parameters. Fixed across all simulations in Chapter 4.

Fit parameter	Disc 500 μm	Disc 1000 μm	Disc 1500 μm	Hazard
Force localization length l_p	2.65 μm	3.75 μm	4.62 μm	2.97 μm
Contractile background stress σ_{back}	2.23 kPa	3.91 kPa	5.30 kPa	3.58 kPa

Table A.2: Fit results as obtained from optimization of the strain energy baseline levels for all disc sizes and the hazard pattern.

Fit parameter	Disc 500 μm	Disc 1000 μm	Disc 1500 μm	Hazard
σ_0	1.2 kPa	1.8 kPa	1.8 kPa	0.8 kPa
σ_{\max}	1.2 kPa	1.7 kPa	1.7 kPa	0.7 kPa
t_{act}	46 s	79 s	66 s	59 s
t_{rel}	291 s	416 s	343 s	335 s
τ_{act}	13 s	33 s	19 s	20 s
τ_{rel}	42 s	60 s	52 s	78 s

Table A.3: Fit parameters of the strain energy gain for all disc sizes and the hazard pattern for 100 ms PA-duration. Amplitude and time scales correspond to the free parameters of the double sigmoid activation profile.

PA duration	10 ms	20 ms	50 ms	100 ms	150 ms	200 ms
Fit parameter	Values					
	Disc					
σ_0	0.6 kPa	1.1 kPa	1.5 kPa	1.7 kPa	1.9 kPa	1.9 kPa
σ_{\max}	0.6 kPa	1.1 kPa	1.4 kPa	1.6 kPa	1.9 kPa	1.8 kPa
t_{act}	72 s	71 s	89 s	105 s	96 s	105 s
t_{rel}	255 s	324 s	382 s	453 s	462 s	465 s
τ_{act}	10 s	21 s	30 s	33 s	49 s	48 s
τ_{rel}	34 s	35 s	48 s	53 s	39 s	67 s
	Hazard					
σ_0	0.9 kPa	1.0 kPa	0.9 kPa	0.9 kPa	0.9 kPa	0.9 kPa
σ_{\max}	0.3 kPa	0.5 kPa	0.7 kPa	0.8 kPa	0.9 kPa	0.8 kPa
t_{act}	34 s	49 s	50 s	63 s	62 s	77 s
t_{rel}	130 s	186 s	267 s	278 s	350 s	275 s
τ_{act}	16 s	27 s	16 s	15 s	12 s	14 s
τ_{rel}	141 s	102 s	74 s	54 s	45 s	57 s

Table A.4: Fit parameters for the activation with repeated pulses of increasing pulse duration for disc and hazard pattern. All pulses were fitted separately by using a double sigmoid activation profile. Stresses rounded to one digit after comma.

A.2. SUPPLEMENTARY INFORMATION FOR CHAPTER 5

STATISTICAL ANALYSIS AND BOXPLOTS

All boxplots show the inner quartile range as boxes and the whiskers extend to 1.5 times the inner quartile range. The notches show the 95 % confidence interval for the median and the white dot shows the sample mean. The Mann-Whitney-Wilcoxon U test was used to test for differences between singlets and doublets, with ns: $p > 0.05$, *: $p < 0.05$, **: $p < 0.01$, ***: $p < 0.001$ and ****: $p < 0.0001$. **Note:** This paragraph has been taken from the unpublished manuscript with the working title “*Force propagation between epithelial cells depends on active coupling and mechano-structural polarization*”.

DATA EXCLUSION FOR OPTOGENETIC EXPERIMENTS

Many cells showed an unstable baseline energy level, which made it difficult to evaluate the impact of photoactivation. Thus, we quantified the baseline stability of each cell by applying a linear regression to the relative strain energy curve before photoactivation and excluded all cells with a slope larger in absolute value than a threshold value. For Fig. 5.9, this process excluded 16 globally activated doublets, 7 globally activated singlets, 12 locally activated doublets and 17 locally activated singlets. For Fig. 5.12 A to C, this process excluded 22 1to2 doublets, 7 1to1 doublets and 2 2to1 doublets. **Note:** This paragraph has been taken from the unpublished manuscript with the working title “*Force propagation between epithelial cells depends on active coupling and mechano-structural polarization*”.

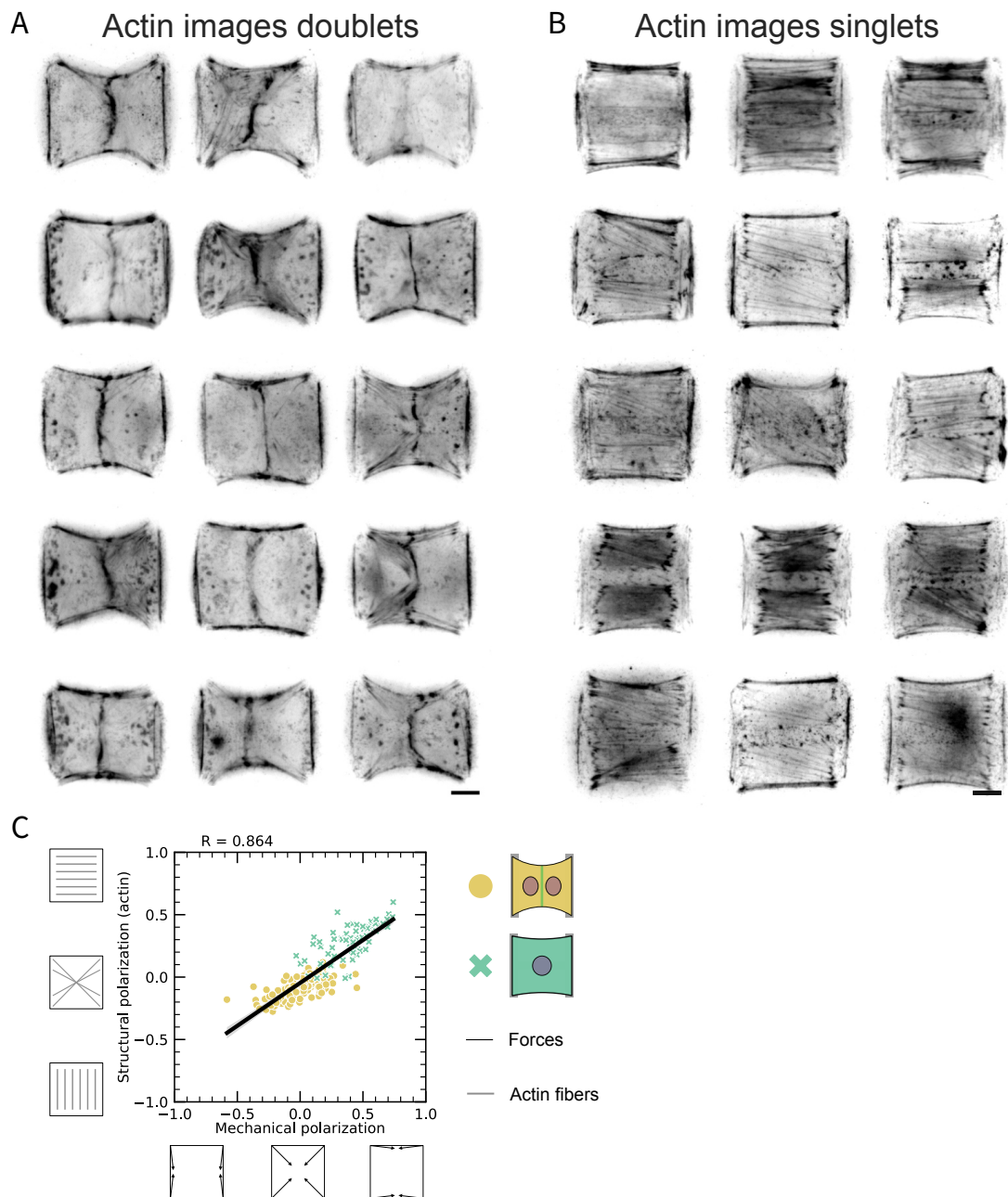


Figure A.2: Panel **A** and **B** show LifeAct images of opto-MDCK cell doublets (left) and singlets (right) spread on the H-pattern. Panel **B** shows the correlation of mechanical and structural polarization. The black line corresponds to a linear regression of the data and the shaded region denotes the 95 % confidence interval for this regression. The R-value shown is the Pearson correlation coefficient. Scale bars correspond to 10 μm .

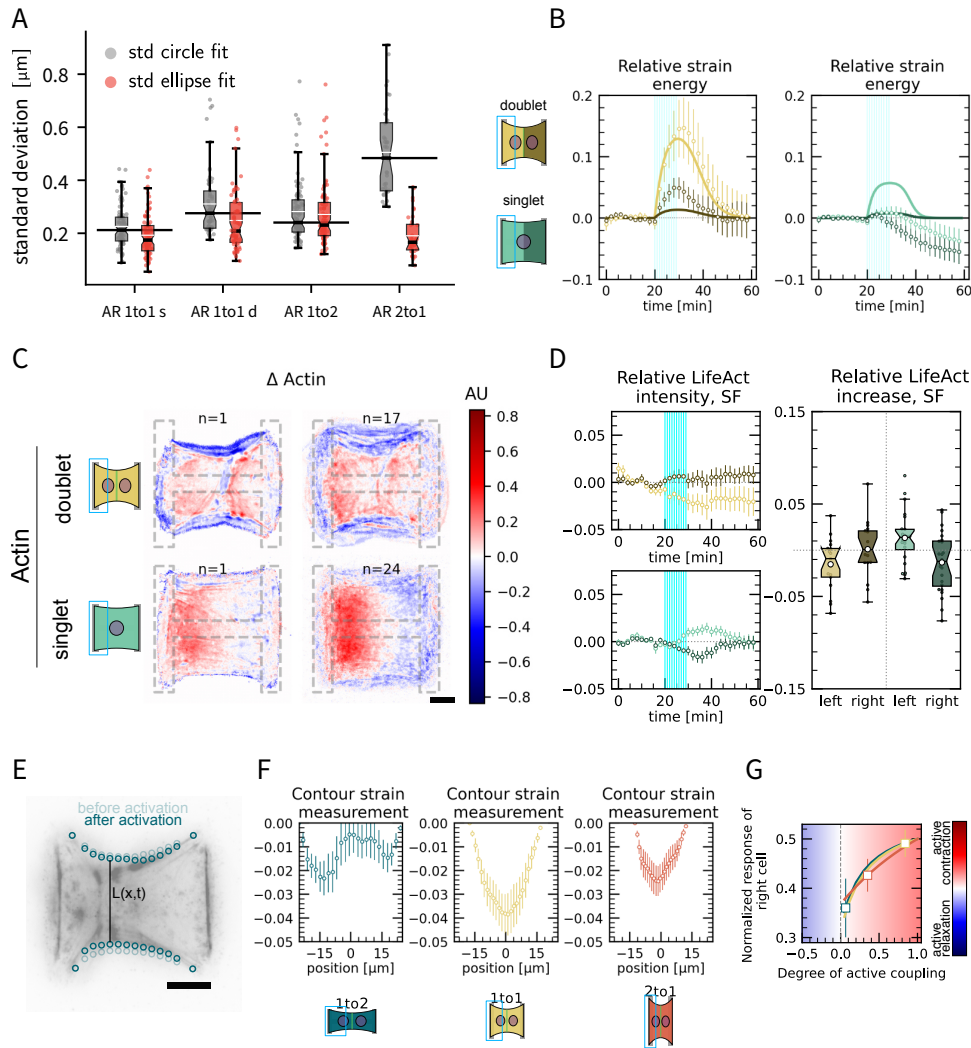


Figure A.3: Panel **A** shows the comparison of circle and ellipse fit of the shape of the free contour for singlets and doublets. For doublets all three pattern aspect ratios are shown. The black horizontal line corresponds to the median value of the circle fit. Panel **B** shows the relative strain energy response in doublets (left) and singlets (right) for local photoactivation of the left half of the pattern. Strain energy is shown separately for the left half (bright) and right half (dark) of the pattern. The first 20 time frames denote the baseline. The vertical blue lines indicate the time points of photo-activation with a 200 ms long light pulse every minute for 10 min. The strain energy curves were normalized by first subtracting the individual baseline energies (average of the first 20 time frames) and then dividing by the average baseline energy of cell doublets/singlets in the corresponding data set. The data is shown as circles and error bars denote the s.e.m. The solid lines represent FEM simulations were the non-activated half of the pattern remains completely passive. Panel **C** shows the difference of actin intensity after and before photactivation for doublets (top) and singlets (bottom) Panel **D** shows the LifeAct intensity measurement for the peripheral stress fiber as a function of time of the left half (bright) and right half (dark) fo doublets (top) and singlets (bottom) after local photoactivation. Boxplots on the right depict the relative actin intensity value two minutes after photoactivation for the activated and non-activated side. Panel **E** shows the contour strain measurement of the free stress fiber. On the experimental images, the inter-stress fiber distance after and before photoactivation is measured along the x -axis which defines a contour strain. Panel **F** shows the result of the contour strain measurement based on the method depicted in F. Panel **G** (grey line) shows the normalized response of the right half obtained from the contour FEM simulations as a function of the degree of active coupling. The data points corresponds to the normalized response obtained from the experimental curves in F and was placed on top of the grey line to obtain the degree of active coupling for each pattern aspect ratio. Scale bars correspond to 10 μm .

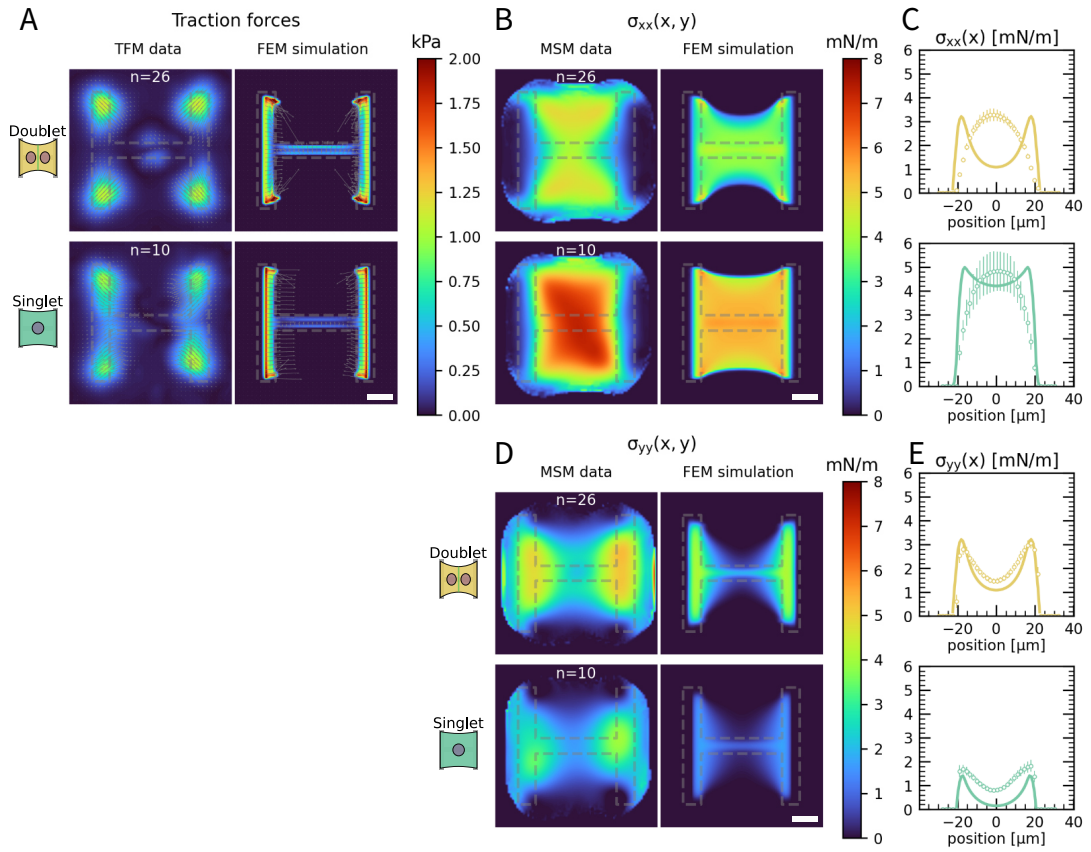


Figure A.4: Panel **A** compares the average TFM maps obtained by experiments (left) to the FEM simulations (right) for doublets (top) and singlets (bottom). Panels **B** and **D** compare the average internal cell stresses in x - and y -direction obtained by experiments (left) and FEM simulations (right) for doublets (top) and singlets (bottom). Panels **C** and **E** show the internal cell stresses from **B** and **D** averaged over the y -axis. The data is shown as circles and error bars denote the s.e.m. and the solid line corresponds to the FEM simulations. Scale bars correspond to 10 μm .

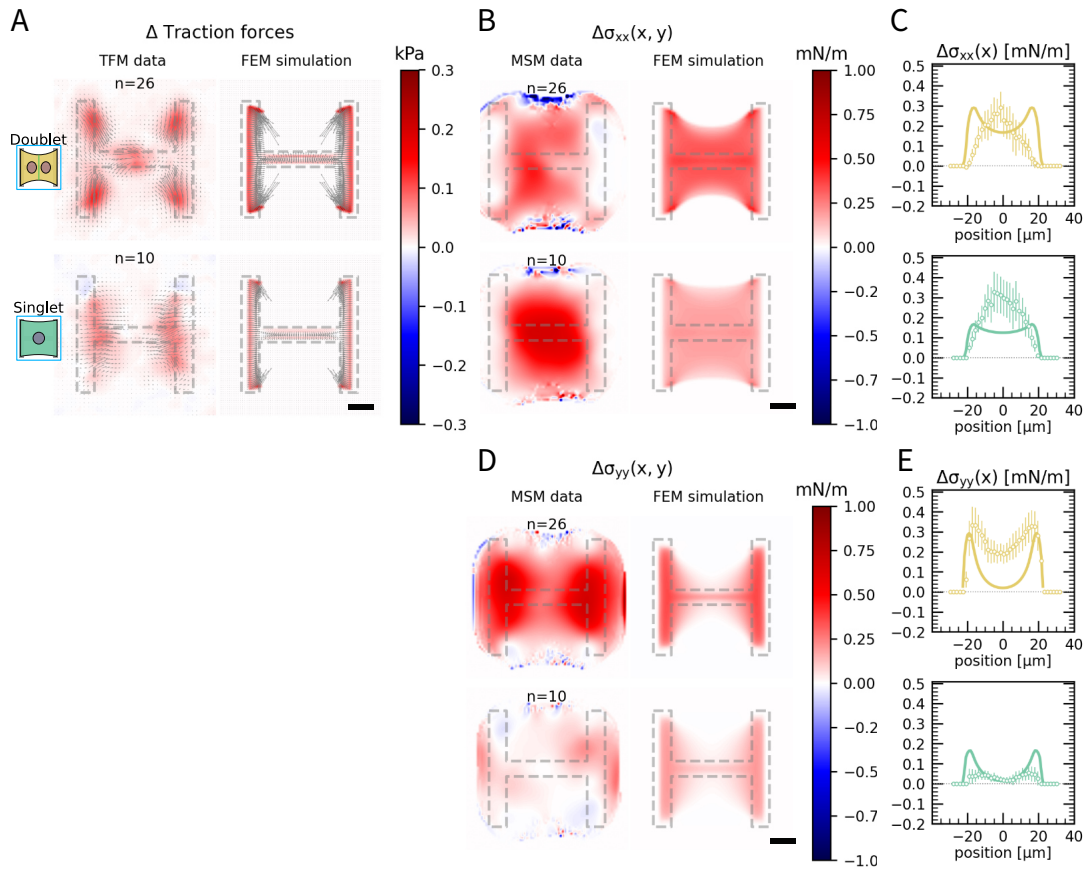


Figure A.5: Panel A compares the difference of the average TFM maps after and before photoactivation obtained by experiments (left) to the FEM simulations (right) for doublets (top) and singlets (bottom). Panels B and D compare the difference of the average internal cell stresses in x - and y -direction obtained by experiments (left) and FEM simulations (right) for doublets (top) and singlets (bottom). Panels C and E show the difference of the internal cell stresses from B and D averaged over the y -axis. The data is shown as circles and error bars denote the s.e.m. and the solid line corresponds to the FEM simulations. Scale bars correspond to 10 μm .

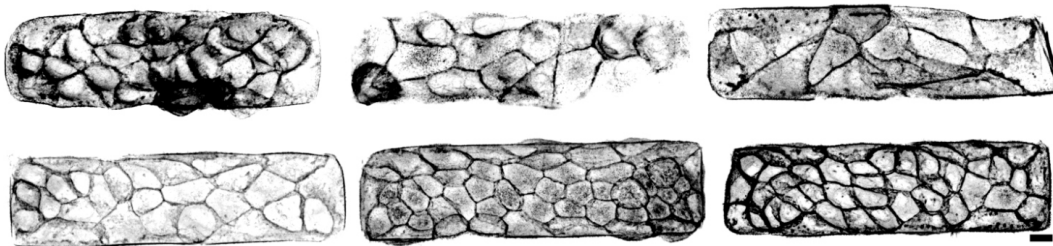


Figure A.6: Phalloidin stainings of actin structures of small tissues. Scale bar corresponds to 10 μm .

MINIMAL MODEL FOR FLUIDIZATION

The minimal model for fluidization which we used to characterize the local photoactivation of the singlet is depicted in Fig. A.7. Within this approach we model the response of the singlet by simply switching from the contractile equilibrium state (KV-model) to a Maxwell fluid with viscoelastic coupling to the substrate (coupling Stokes' elements γ and coupling springs Y in series). For simplicity we chose to use a quasi one-dimensional such that flow and contraction is assumed to happen only along the x-direction of a cell layer of length L . This type of Maxwell model (Fig. A.7A (right)) has been used before to study the flow dynamics of stress fibers (*Oakes et al.*, 2017). Further, we allow the viscous coupling γ to be different in the activation region. This is assumed to artificially introduce a symmetry break between activated and non-activated region (dotted line in Fig. A.7B)) as could be observed in experiments (Fig. 5.9D (right)). At this point it should be noted that, although we use the terms "activated" and "non-activated" we do not introduce active stresses but simply switch the model. We note that qualitatively similar results can be obtained by variation of the elastic modulus E_c between activated and non-activated region. Physically, this rather heuristic approach allows material flow towards the activation region. With regards to the actin intensity measurements in Fig. 5.9C, we identify this as the net flow of actin.

In the following we will only derive the weak form of the quasi one-dimensional Maxwell model. The corresponding weak form for the Kelvin-Voigt model can be derived analogously. For simplicity we further introduce the short-hand notation for the time derivative of a quantity u as $\dot{u} \equiv \partial_t u$. The constitutive relation of the active Maxwell model is given by Eq. (2.31)

$$\sigma - \sigma_{\text{bck}} + \tau_c(\dot{\sigma} - \dot{\sigma}_{\text{bck}}) = E_c \tau_c \dot{\epsilon}, \quad (\text{A.1})$$

where $\tau_c = E_c/\eta_c^{\text{MW}}$ is the relaxation constant for the Maxwell fluid, $\epsilon = \partial_x u(x, t)$ is the one-dimensional strain expressed in terms of the displacement field u and σ_{bck} is the active background stress which is assumed to be constant ($\dot{\sigma}_{\text{bck}} = 0$). Additionally, we assume stress free boundaries $\sigma(x = (0, L), t) = 0$ which corresponds to the assumption that flow of material is sustained by creation of new actin at the ends of the cell layer. According to Fig. A.7B, Stokes' friction and elastic foundation are in serial connection. Hence, the forces acting on these elements are equal which yields two dependent force balance equations coupled through the relation $u = u_Y + u_\gamma$.

$$h_c \frac{\partial \sigma}{\partial x}(x, t) = Y u_Y(x, t), \quad (\text{A.2})$$

$$h_c \frac{\partial \sigma}{\partial x}(x, t) = \gamma \dot{u}_\gamma(x, t), \quad (\text{A.3})$$

where we again use the thin-layer approximation by multiplication with the effective height of the cell layer h_c and further, by u_Y and u_γ denote the displacement of the Stokes' and spring element, respectively.

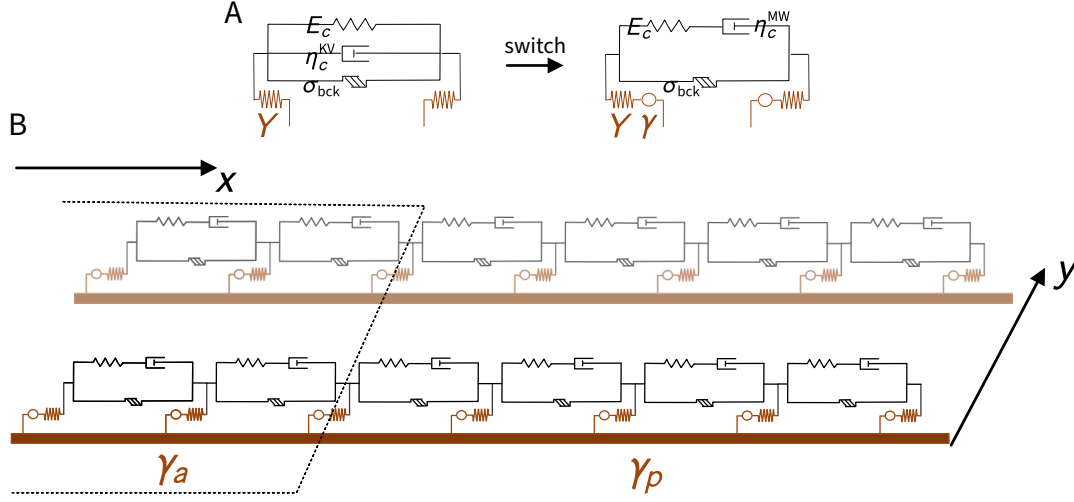


Figure A.7: Minimal model for fluidization. Panel **A** depicts the sudden model switch from a contracted KV-type model with elastic substrate coupling and stable energy baseline to a MW-type model with viscoelastic substrate coupling and a flow-like behavior. Panel **B** shows the quasi one-dimensional setup with a contraction and flow only along the x -direction but an additional spatial extent in y -direction. To account for the asymmetry between activated and non-activated side, we alter the viscous coupling γ in the activation region. However, other parameters such as the Young's modulus of the cell can also account for the symmetry break. We do not make any claims on what causes the symmetry break in the experimental observations.

Next, we take the derivative of Eq. (A.1) with respect to x which yields

$$\partial_x \sigma + \tau_c \partial_x \dot{\sigma} = \eta_c \partial_x^2 \dot{u}. \quad (\text{A.4})$$

Using the time derivative of Eq. (A.2) and Eq. (A.3) gives the final system of equations

$$Y u_Y + \tau_c Y \dot{u}_Y = \eta_c \partial_x^2 \dot{u} \quad (\text{A.5})$$

$$\gamma \dot{u}_\gamma + \tau_c \gamma \ddot{u}_\gamma = \gamma (\dot{u} - \dot{u}_Y) + \tau_c \gamma (\ddot{u} - \ddot{u}_Y) = \eta_c \partial_x^2 \dot{u}. \quad (\text{A.6})$$

In addition, the stress free boundaries yield

$$-\sigma_{bck} = \eta_c \partial_x \dot{u}. \quad (\text{A.7})$$

Following the recipe in Chapter 3 we multiply Eq. (A.5) and Eq. (A.6) with test functions $w_1 \in \mathcal{V}([0, L])$ and $w_2 \in \mathcal{V}([0, L])$, respectively, and obtain

$$\begin{aligned} \int_0^L Y u_Y w_1 dx + \int_0^L \tau_c Y \frac{u_Y - u_{n,Y}}{\Delta t} w_1 dx \\ + \int_0^L \eta_c \partial_x \frac{u - u_n}{\Delta t} \partial_x w_1 dx + \sigma_{bck} w_1 \Big|_0^L = 0, \end{aligned} \quad (\text{A.8})$$

and

$$\int_0^L \gamma \frac{u_\gamma - u_{n,\gamma}}{\Delta t} w_2 \, dx + \int_0^L \tau_c \gamma \frac{u_\gamma + u_{n-1,\gamma} - 2u_{n,Y}}{\Delta t^2} w_2 \, dx + \int_0^L \eta_c \partial_x \frac{u - u_n}{\Delta t} \partial_x w_2 \, dx + \sigma_{\text{bck}} w_2 \Big|_0^L = 0, \quad (\text{A.9})$$

where we did not replace u_γ by $u - u_Y$ for notational simplicity. For the time discretization we use a backward Euler scheme and second derivatives with respect to time are approximated by

$$\partial_t^2 u = \frac{u + u_{n-1} - 2u_n}{\Delta t^2}, \quad (\text{A.10})$$

where the indices n and $n - 1$ denote the two previous time steps.

The qualitative results of the implementation are shown in Fig. A.8. We first equilibrated the cell layer using a KV model and then subsequently at $t = t_{\text{act}}$ (grey vertical line) switched to an active Maxwell model. In the left panel of Fig. A.8A we show the time evolution of the substrate strain energy for different viscous substrate coupling strength (Stokes' elements) γ . For the quasi one-dimensional model, the substrate strain energy was calculated according to

$$E_s = \frac{1}{2} \int_0^{L_x} Y L_y u_Y^2 \, dx, \quad (\text{A.11})$$

where L_y is the extent of the cell layer in y -direction. A large value of γ leads to a steep increase in strain energy, since in this case the cell mainly feels and deforms the springs. Conversely, a very small for γ leads to almost frictionless coupling and the springs get barely deformed. Hence, the substrate strain energy decreases. For intermediate values of γ , with an order of magnitude as reported in the work by *Oakes et al.* (2014), the model switch leads to a transient behavior of the strain energy. Before the model switch, all elastic energy is stored in the spring of the substrate. Right after the model switch, the system starts to deform. At first, a high rate of deformation leads to a „stiff“ Stokes' element which in turn leads to larger deformations of the substrate spring which is followed by an increase in the substrate strain energy. Over time, the deformation rate slows down and the system starts to „flow“ such that the strain energy drops below the baseline level as the substrate deformation decreases. In Fig. A.8B we further show the flow velocity, i.e. the time derivative of the displacement field $v = \partial_t u$.

The same principle can be observed in the right panel of Fig. A.8A where the only difference to the left panel is a position dependent Stokes' element. Here, we set $\gamma_p = 0.5\gamma_a$, where γ_p gives the value in the region marked as dark grey (Fig. A.8C) while γ_a denotes the friction in the region marked as light grey (activation region). Here we respected the shape of the activation profile used in the experiments in Chapter 5 such that the activation region ends approximately 10 μm before the symmetry center of the cell layer. The strain energy was calculated by separately integrating the left and right half of the cell layer (light and dark green). As can be seen in Fig. A.8C, the distinct values of γ lead to an asymmetric flow profile with a larger flow towards the

“activation” region. The order of magnitude $\sim \mu\text{m h}^{-1}$ is consistent with the values found in (*Oakes et al.*, 2014). All other parameters used in this qualitative simulation are gathered in Table A.9

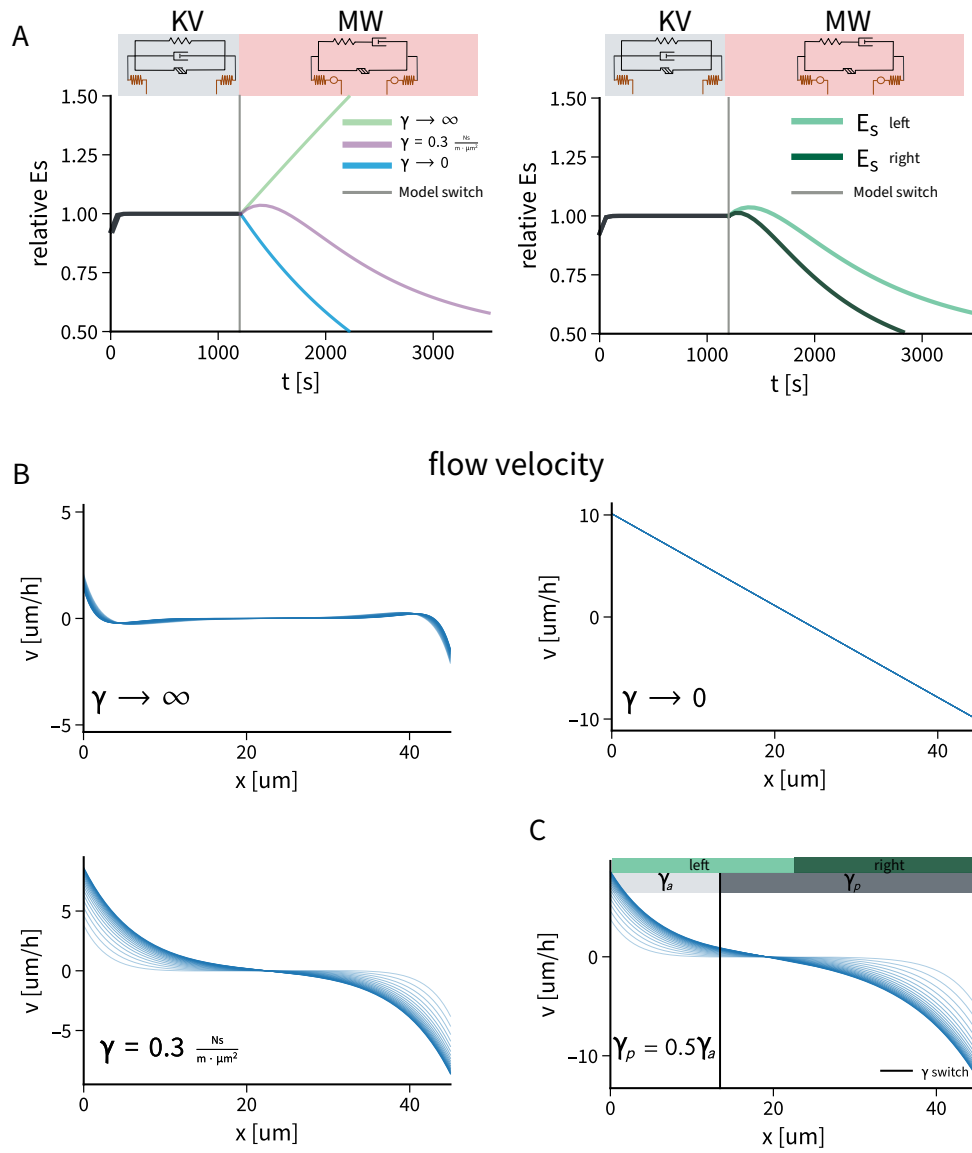


Figure A.8: Panel A (left) shows the time course of the relative substrate strain energy after a sudden switch from a KV to a MW model. For three different regimes. For very large values of γ , i.e. strong viscoelastic substrate coupling the strain energy increases. For very small values of γ the strain energy releases. For intermediate values of γ the strain energy exhibits a transient behavior with a small increase followed by a decrease below the baseline level. Panel A (right) shows the substrate strain energy on the left and the right half of the pattern for different values of γ spatially oriented as depicted by the grey bars in Panel C. Panel B shows the flow velocity of the cell material for different values of γ . Panel C shows the flow velocity corresponding to the transient strain energy behavior (right sub-panel in A). The parameters used for the simulation are gathered in Table A.9.

TABLES CHAPTER 5

Fixed parameter	Value
Substrate	
Young's modulus of the substrate E_s	20 kPa
Poisson's ratio of the substrate ν_s	0.5
Thickness of the substrate h_s	50 μm
Cell	
Young's modulus of cell E_c	10 kPa
Viscosity of the cell η_c	100 kPa s
Thickness of the cell h_c	1 μm
Poisson's ratio of the cell ν_c	0.5
Length of the cell L_c	50 μm

Table A.5: Fixed parameters for the two-dimensional finite element simulation.

Fit parameter	Singlet	Doublet
Baseline		
Background stress component σ_{xx}^{bck}	6.59 kPa	5.73 kPa
Background stress component σ_{yy}^{bck}	2.78 kPa	5.73 kPa
Full opto-stimulation		
Active stress σ_{act}	0.287 kPa	0.618 kPa
Activation time scale τ_{act}	133 s	227 s
Relaxation time scale τ_{rel}	113 s	236 s
Centroid \tilde{t}	1057 s	1117 s

Table A.6: Fit parameter as obtained by the two-dimensional finite element simulation.

Fit parameter	AR1to2	AR2to1
Baseline		
Background stress component σ_{xx}^{bck}	6.4 kPa	2.2 kPa
Background stress component σ_{yy}^{bck}	2.4 kPa	4.1 kPa
Opto-stimulation estimate		
Active stress σ_{act}	0.55 kPa	0.06 kPa

Table A.7: Fit parameter and parameter estimates for the AR1to2 and AR2to1 doublets. The background stress was obtained from a fit of the model to the strain energy baseline. Since no global photoactivation data was available, we estimated σ_{xx}^{bck} such that the maximal strain energy in the left half of the pattern matched the experimental value. σ_{yy}^{bck} was then obtained by means of the mechanical polarization.

Parameter	Value
Fixed	
Surface tension component σ_x	0.92 nN μm^{-1}
Surface tension component σ_y	1.12 nN μm^{-1}
Semi-axis a	61.94 μm
Semi-axis b	68.34 μm
One-dimensional elastic modulus EA	300 nN
Contour fit	
Active line tension λ_{act}	58.1 nN
Strain fit	
Relative surface tension increase $\text{RSI}_x^{\text{max}}$	0.11 nN μm^{-1}
Relative surface tension increase $\text{RSI}_y^{\text{max}}$	0.24 nN μm^{-1}

Table A.8: Fixed and optimized parameter for the contour shape analysis by means of the contour finite element simulation.

Fixed parameter	Value
Young's modulus of the substrate E_s	20 kPa
Poisson's ration of the substrate ν_s	0.5
Effective substrate thickness h_s	50 μm
Lateral cell size in x - and y -direct. L_c	45 μm
Young's modulus of the cell E_c	10 kPa
Viscosity of the cell η_c^{MW}	10 MPa s
Cell layer thickness h_c	1 μm
Background stress σ_{bck}	5 kPa
Spring stiffness density Y	1.26 mN $\text{m}^{-1} \mu\text{m}$

Table A.9: Fixed paramters used in the qualitative study of fluidization.

A.3. SUPPLEMENTARY INFORMATION FOR CHAPTER 6

REACTION SCHEME ALTERNATIVE (VICTOR JUMA)

The reaction scheme used for Fig. 6.2B is given by

$$\frac{dG_a}{dt} = k_3 R_a (G_T - G_a) - k_4 M_a G_a \quad (\text{A.12})$$

$$\frac{dR_a}{dt} = \frac{k_0 G_a (R_T - R_a)}{K_{r0} + (R_T - R_a)} + \frac{k_1 (R_T - R_a)}{K_{r1} + (R_T - R_a)} - \frac{k_2 R_a}{K_{r2} + R_a} \quad (\text{A.13})$$

$$\frac{dM_a}{dt} = \frac{k_5 R_a (M_T - M_a)}{K_{m5} + (M_T - M_a)} + \frac{k_7 (M_T - M_a)}{K_{m7} + (M_T - M_a)} - \frac{k_6 M_a}{K_{m6} + M_a}, \quad (\text{A.14})$$

and the parameters are chosen according to Table A.10.

CONTRACTION SPEEDS UP REACTIONS

In a homogeneous one-dimensional setup Eq. (6.9) can be simplified to

$$\partial_t \hat{c} = R_c(t) - \hat{c} \frac{\partial_t \hat{J}}{1 + \hat{J}}, \quad (\text{A.15})$$

as $\partial_x \hat{c} = 0$. Hence, the deformation of the domain, i.e. a fast compression speeds up the reaction process. This scenario is shown in Fig. A.9A for the case of an exponentially shrinking domain given by

$$\hat{J}(t) = A + B e^{-\alpha t}. \quad (\text{A.16})$$

SANITY TEST DISCONTINUOUS GALERKIN INTERNAL NO-FLUX BOUNDARY CONDITION

The internal no-flux boundary condition at the intercellular junction was, for illustrational purposes, tested with the model by *Juma (2019)* and *Kamps et al. (2020)*. In an oscillatory regime of the system, traveling RhoA and myosin waves form as a result of diffusion driven instabilities. We exploited this behavior to test whether an activity wave passes the intercellular junction or not. These simulations did not involve deformations of the simulation domain and we only simulated 6 coupled reaction-diffusion equations (three for active species and three for passive species). Thereby, the active species (membrane bound) are associated with a lower diffusivity compared to the inactive (cytosol associated) species. The total concentration of each species is assumed to be conserved. In general we have two equations for each species (GEF, RhoA, myosin)

$$\partial_t c_a = R_c(t) + D_{c,a} \nabla^2 c_a, \quad (\text{A.17})$$

$$\partial_t c_i = -R_c(t) + D_{c,i} \nabla^2 c_i, \quad (\text{A.18})$$

where the subscripts a and i denote the active and inactive states, respectively. To drive the instabilities, we initialized a homogenous concentration field with noise

$$c_{a,0}(x) = \tilde{c}_0 + \delta c (0.5 - \mathcal{U}_{[0,1]}(\mathbf{x})) , \quad (\text{A.19})$$

where $\mathcal{U}_{[0,1]}$ is the probability density function of the continuous uniform distribution, \tilde{c}_0 the homogenous concentration field and δc the noise. The reaction terms R_c are set according to Eqs. (6.27) to (6.29) and the parameters according to Table A.11.

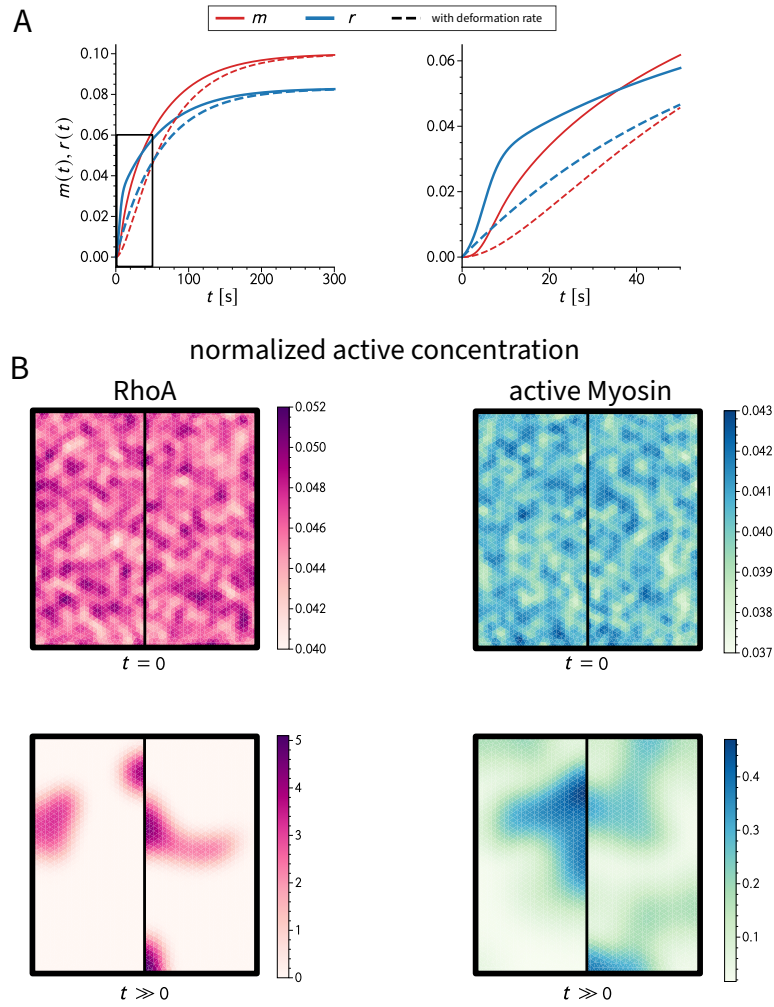


Figure A.9: Sanity check for the RD-system and the interface condition. Panel **A** shows that the a fast shrinking domain temporarily increases the reaction rates. Plot on the right corresponds to a zoomed in version of the left plot. The reaction kinetics correspond to the linear RhoA pathway and parameters are chosen according to Table 6.1. The shrinking domain was parametrized by $A = 0.1$, $B = 0.9$ and $\alpha = 0.5$. Panel **B** depicts traveling wave peaks of RhoA and myosin, simulated with the reaction diffusion model by *Kamps et al.* (2020). The intercellular junction prevents the wave peaks from passing and hence decouples the two domains. However, concentrations on the left and right hand side of the domain are mathematically described by a single scalar field.

TABLES CHAPTER 6

	Value	Unit	Source
G_T	NS	M	<i>Tyson et al. (2003)</i>
k_3	1	$M^{-1}s^{-1}$	”
k_4	0.65	$M^{-1}s^{-1}$	”
M_T	1	M	”
k_5	0.15	s^{-1}	”
k_6	0.1	$M s^{-1}$	”
k_7	0.025	s^{-1}	”
K_{m5}	0.5	M	”
K_{m6}	0.75	M	”
K_{m7}	0.75	M	”
R_T	1	M	”
k_0	1	s^{-1}	”
k_1	0.1	s^{-1}	”
k_2	0.5	$M s^{-1}$	”
K_{r0}	0.051	M	”
K_{r1}	0.051	M	”
K_{r2}	0.05	M	”

Table A.10: Parameters as used in Fig. 6.2B based on *Tyson et al. (2003)* and *Juma (2019)*.

	Value	Unit	Source
G_T	0.2	M	Kamps et al. (2020)
k_3	1.19	$M^{-1}s^{-1}$	"
k_4	3.98	$M^{-1}s^{-1}$	"
D_{G_a}	0.28	$\mu m^2 s^{-1}$	"
D_{G_i}	9.28	$\mu m^2 s^{-1}$	"
M_T	1.24	M	"
k_5	0.005838	s^{-1}	"
k_6	0.00039906	$M s^{-1}$	"
k_7	0.0	s^{-1}	"
K_{m5}	0.014	M	"
K_{m6}	0.0784	M	"
K_{m7}	0.0	M	"
D_{M_a}	0.03	$\mu m^2 s^{-1}$	"
D_{M_i}	0.9	$\mu m^2 s^{-1}$	"
R_T	0.443	M	"
k_0	9.3896	s^{-1}	"
k_1	0.0	s^{-1}	"
k_2	0.15198	$M s^{-1}$	"
K_{r0}	2.42	M	"
K_{r1}	0.0	M	"
K_{r2}	0.0745	M	"
D_{R_a}	0.28	$\mu m^2 s^{-1}$	"
D_{G_i}	9.28	$\mu m^2 s^{-1}$	"

Table A.11: Parameters as used in Fig. A.9B together with Eqs. (6.27) to (6.29).

A.4. ACTIN POLARIZATION ANALYSIS (STRUCTURE TENSOR)

This procedure has been used in Chapter 4 and Chapter 5 to quantify the polarization of the actin cytoskeleton. Here we note that in Chapter 4 the polarization of the actin cytoskeleton was called *actin order parameter* and in Chapter 5 referred to as *structural polarization*. Both expressions refer to the same quantity. The structure tensor of an image is given by the tensor components

$$\begin{aligned} J_{11} &= \iint w(x, y) \left(\frac{\partial I(x, y)}{\partial x} \right)^2 dx dy \\ J_{22} &= \iint w(x, y) \left(\frac{\partial I(x, y)}{\partial y} \right)^2 dx dy \\ J_{12} = J_{21} &= \iint w(x, y) \left(\frac{\partial I(x, y)}{\partial x} \right) \left(\frac{\partial I(x, y)}{\partial y} \right) dx dy, \end{aligned} \quad (\text{A.20})$$

where $I(x, y)$ is the intensity value of each pixel and $w(x, y)$ denotes a Gaussian local neighborhood with a waist of three pixels. On this local neighborhood one may define the orientation angle as

$$\tan(2\theta) = \frac{2J_{12}}{J_{22} - J_{11}}, \quad (\text{A.21})$$

which is only meaningful if the image contains oriented structures in this local neighborhood. One further defines coherency

$$\text{Coherency} = \frac{\sqrt{(J_{22} - J_{11})^2 + 4J_{12}^2}}{J_{11} + J_{22}}, \quad (\text{A.22})$$

which quantifies the degree of anisotropy. An average orientation angle can be obtained by averaging θ over all pixels for which the coherency is above a certain predefined threshold value C_{thresh}

$$\theta_m = \langle \theta \rangle_{>C_{\text{thresh}}} \quad (\text{A.23})$$

from which the structural polarization (order parameter) is obtained by

$$\text{Polarization} = S = \langle \cos(2(\theta - \theta_m)) \rangle. \quad (\text{A.24})$$

A value of $S = 0$ means that the local orientation is orthogonal to the average orientation and conversely, a value of $S = 1$ means that they are aligned.

FUNCTION DEFINITIONS

MODIFIED BESSEL FUNCTIONS OF THE FIRST AND SECOND KIND

Modified Bessel function of the first kind (*Abramowitz et al.*, 1988):

$$I_n(x) = \sum_{k=0}^{\infty} \frac{(x/2)^{n+2k}}{k!\Gamma(n+k+1)}, \quad I_{-n}(x) = \sum_{k=0}^{\infty} \frac{(x/2)^{2k-n}}{k!\Gamma(k+1-n)}, \quad (\text{A.25})$$

where $\Gamma(x)$ denotes the gamma function Recurrence formulas:

$$I_{n+1}(x) = I_{n-1}(x) - \frac{2n}{x}I_n(x) \quad (\text{A.26})$$

$$\frac{d}{dx}I_n(x) = I_{n-1}(x) - \frac{n}{x}I_n(x) \quad (\text{A.27})$$

Series expansion for $x \ll 1$:

$$I_n(x) = \frac{(x/2)^n}{\Gamma(n+1)} \left[1 + \frac{(x/2)^2}{1(1+n)} \left(1 + \frac{(x/2)^2}{2(2+n)} \left(1 + \frac{(x/2)^2}{3(3+n)} (1 + \dots) \right) \right) \right] \quad (\text{A.28})$$

Series expansion for $x \gg 1$:

$$I_n \approx \frac{\exp x}{\sqrt{2\pi x}} \left[1 - \frac{4n^2 - 1^2}{1(8x)} \left(1 - \frac{4n^2 - 3^2}{2(8x)} \left(1 - \frac{4n^2 - 5^2}{3(8x)} (1 - \dots) \right) \right) \right], \quad (\text{A.29})$$

Modified Bessel function of the second kind (*Abramowitz et al.*, 1988):

$$K_n(x) = \frac{\pi (I_{-n}(x) - I_n(x))}{2 \sin(n\pi)} \quad (\text{A.30})$$

MODIFIED STRUVE FUNCTION

Series expansion:

$$L_n(x) = \sum_{k=0}^{\infty} \frac{1}{\Gamma(k+3/2)\Gamma(k+n+3/2)} \left(\frac{x}{2}\right)^{2k+n+1} \quad (\text{A.31})$$

Further identities:

$$\int_0^x d\xi I_1(\xi)\xi = \frac{1}{2} (L_0(x)I_1(x) - L_1(x)I_0(x)) \quad (\text{A.32})$$

Limit $x \ll 1$:

$$\int_0^x d\xi I_1(\xi)\xi \approx \frac{x^3}{6} + \frac{x^5}{80} + \frac{x^7}{2688} + \mathcal{O}(x^9) \quad (\text{A.33})$$

Limit $x \gg 1$:

$$\int_0^x d\xi I_1(\xi)\xi \approx \frac{e^x}{\sqrt{2\pi x}} \left(x - \frac{7}{8}\right) \quad (\text{A.34})$$

A.5. ANALYTICAL CALCULATIONS

STRAIN ENERGY OF ISOTROPIC CONTRACTILE DISC ON RING PATTERN

According to Eq. (4.8) and for $Y = Y_s$ the substrate strain energy is given by

$$E_s = \frac{Y}{2} \int_0^{2\pi} d\phi \int_{r_i}^{r_o} r u_r^2(r) dr \quad (\text{A.35})$$

$$= \pi l_p^2 \frac{Y}{2} \int_{x_i}^{x_o} x u_r^2(x) dx \quad (\text{A.36})$$

were we used the substitution $r = x l_p$ and that in the rescaled version x_0 and x_i corresponds to the outer and inner ring radius, respectively (Fig. 2.4B). The relevant displacement field is given by Eq. (2.51) which describes the displacement field of the adherent portion of the cell layer. c_3 and c_4 are constants as defined in Section 2.1.2. It then follows

$$\begin{aligned} E_s &= \pi l_p^2 \frac{Y}{2} \int_{x_i}^{x_o} x (c_3 I_1(x) + c_4 K_1(x))^2 dx \\ &= \pi l_p^2 \frac{Y}{2} \int_{x_i}^{x_o} x (c_3^2 I_1^2(x) + c_4^2 K_1^2(x) + 2c_3 c_4 I_1(x) K_1(x)) dx \\ &= \pi l_p^2 \frac{Y}{2} \left(\underbrace{c_3^2 \int_{x_i}^{x_o} x I_1^2(x) dx}_{=\mathcal{I}_1} + \underbrace{c_4^2 \int_{x_i}^{x_o} x K_1^2(x) dx}_{=\mathcal{I}_2} + \underbrace{2c_3 c_4 \int_{x_i}^{x_o} x I_1(x) K_1(x) dx}_{=\mathcal{I}_3} \right). \end{aligned}$$

The integrals \mathcal{I}_1 to \mathcal{I}_3 the yield

$$\begin{aligned} \mathcal{I}_1 &= c_3^2 \frac{x^2}{2} \left(I_1^2(x) - I_0(x) I_2(x) \right) \Big|_{x_i}^{x_o} \\ \mathcal{I}_2 &= c_4^2 \frac{x^2}{2} \left(K_1^2(x) - K_0(x) K_2(x) \right) \Big|_{x_i}^{x_o} \\ \mathcal{I}_3 &= \frac{c_3 c_4}{2\sqrt{\pi}} G_{2,2}^{2,4} \left(x, \frac{1}{2} \middle| \begin{matrix} 1, \frac{3}{2} \\ 1, 2, 0, 0 \end{matrix} \right) \Big|_{x_i}^{x_o}. \end{aligned} \quad (\text{A.37})$$

here, G denotes the so-called Meijer G-function which in this specific notation is defined as

$$G_{m,n}^{p,q} \left(x, r \middle| \begin{matrix} a_1, \dots, a_p \\ b_1, \dots, b_q \end{matrix} \right) \equiv \frac{1}{2\pi i} \int_{\gamma_L} \frac{\prod_{j=1}^m \Gamma(p_j + s) \prod_{j=1}^n \Gamma(1 - a_j - s)}{\prod_{j=n+1}^p \Gamma(a_j + s) \prod_{j=m+1}^q \Gamma(1 - b_j - s)} x^{-s/r} ds. \quad (\text{A.38})$$

ELASTIC CATENARY

In analogy to the analytical derivation of the TEM in Section 2.2.2 we provide the analytical solution of the elastic catenary which exhibits a position-dependent line tension along the fiber. The basis of the calculation is the force balance equation as a

function of the unit reference length \hat{s}

$$\partial_{\hat{s}}\mathbf{F}(\hat{s}) + \mathbf{f}(\hat{s}) = 0, \quad (\text{A.39})$$

where \mathbf{F} denotes the contact force within the fiber and \mathbf{f} the externally applied load. Using that for the elastic catenary the load is normal to the reference configuration $\mathbf{f} = f_y \mathbf{e}_y = \text{const.}$ we obtain

$$\partial_{\hat{s}}(\lambda(\hat{s})\mathbf{T}\hat{s}) - f_y \mathbf{e}_y = 0. \quad (\text{A.40})$$

Here, we used that the contact force is always tangential to the fiber. This further leads to

$$\begin{aligned} \lambda T_x &= \text{const.} \equiv \lambda_c \\ \lambda T_y &= f_y \hat{s}, \end{aligned}$$

where we introduced λ_c as the constant x -component of the line tension. At this point we express the components of the tangent vector in terms of the turning angle $\theta(\hat{s})$ which leads to

$$\begin{aligned} \lambda \cos \theta &= \lambda_c \\ \lambda \sqrt{1 - \cos^2 \theta} &= f_y \hat{s}. \end{aligned}$$

From this we deduce the line tension as a function of the reference arc length as

$$\lambda = \sqrt{f_y^2 \hat{s}^2 + \lambda_c^2}. \quad (\text{A.41})$$

The shape can be calculated by exploiting that the stretch of a linear elastic fiber with one dimensional modulus is given by $\nu = (\lambda + EA)/EA$ and

$$\frac{dx}{d\hat{s}} = \frac{ds}{d\hat{s}} \frac{dx}{ds} = \nu \cos \theta = \nu \frac{\lambda_c}{\lambda} = \lambda_c \left(\frac{1}{EA} + \frac{1}{\lambda} \right) \quad (\text{A.42})$$

$$\frac{dy}{d\hat{s}} = \frac{ds}{d\hat{s}} \frac{dy}{ds} = \nu \sin \theta = \nu \frac{f_y \hat{s}}{\lambda} = f_y \hat{s} \left(\frac{1}{EA} + \frac{1}{\lambda} \right). \quad (\text{A.43})$$

Expressing λ in terms of the reference arc length parameter by means of Eq. (A.41) allows to integrate Eqs. (A.42) and (A.43) which gives

$$x(\hat{s}) = \frac{\lambda_c}{f_y} \text{arsinh}(\hat{s}/(\lambda_c/f_y)) + \frac{\lambda_c}{EA} \hat{s} + x_0 \quad (\text{A.44})$$

$$y(\hat{s}) = \sqrt{(\lambda_c/f_y)^2 + \hat{s}^2} + \frac{\lambda_c}{2(\lambda_c/f_y)EA} \hat{s}^2 + y_0. \quad (\text{A.45})$$

The integration constants x_0 and y_0 can be solved by using the boundary conditions

$$x(0) = 0, \quad y(0) = 0, \quad y(\hat{L}) = 0, \quad x(\hat{L}) = \hat{L}, \quad (\text{A.46})$$

where \hat{L} is the length of the unstretched fiber. This finally yields the contour of the elastic catenary which is given by

$$x(\hat{s}) = \frac{\lambda_c}{f_y} \operatorname{arsinh} \left(\frac{\lambda_c}{f_y} \left(\hat{s} - \frac{\hat{L}}{2} \right) \right) + \frac{\lambda_c}{EA} \left(\hat{s} - \frac{\hat{L}}{2} \right) + \frac{\lambda_c}{f_y} \operatorname{arsinh} \left(\frac{\lambda_c \hat{L}}{f_y 2} \right) + \frac{\lambda_c}{EA} \frac{\hat{L}}{2} \quad (\text{A.47})$$

$$y(\hat{s}) = \sqrt{\left(\frac{\lambda_c}{f_y} \right)^2 + \left(\hat{s} - \frac{\hat{L}}{2} \right)^2} + \frac{\lambda_c}{2(\lambda_c/f_y)EA} \left(\hat{s} - \frac{\hat{L}}{2} \right)^2 - \sqrt{\left(\frac{\lambda_c}{f_y} \right)^2 + \left(\frac{\hat{L}}{2} \right)^2} + \frac{\lambda_c}{2(\lambda_c/f_y)EA} \left(\frac{\hat{L}}{2} \right)^2. \quad (\text{A.48})$$

Finally, the last boundary condition in Eq. (A.46) gives an implicit equation which has to be solved to obtain λ_c

$$\frac{\hat{L}}{2} = \frac{\lambda_c}{f_y} \operatorname{arsinh} \left(\frac{f_y \hat{L}}{\lambda_c 2} \right) + \frac{\lambda_c}{EA} \frac{\hat{L}}{2}. \quad (\text{A.49})$$

The line tension then yields

$$\lambda = \sqrt{f_y^2 \left(\hat{s} - \frac{\hat{L}}{2} \right)^2 + \lambda_c^2}. \quad (\text{A.50})$$

The results of this analytical calculation are depicted in Fig. 3.4B-D and where used to validate the numerical implementation of the counter model.

List of Abbreviations

ABL1	Tyrosine-protein kinase ABL1
ADP	Adenosine diphosphate
ATP	Adenosine triphosphate
ATM	Anisotropic tension model
BC	Boundary condition
CSK	Cytoskeleton
CPM	Cellular Potts model
Dia	Diaphanous-related formin
DH	Dbl-homology
dTEM	Dynamic tension elasticity model
ECM	Extracellular matrix
ERK	Extracellular signal-regulated kinase
FTTC	Fourier transform traction cytometry
GAP	GTPase activating protein
GEF	Guanosine exchange factor
GDP	Guanosine diphosphate
GTP	Guanosine triphosphate
KV	Kelvin-Voigt
LOV	Light-oxygen-voltage-sensing
MBS	Myosin binding subunit
MDCK	Madin-Darby canine kidney
MLC	Myosin light chain
MLCP	Myosin light chain phosphatase
MSM	Monolayer stress microscopy
MTOC	Microtubule organizing center

MW	Maxwell
NM II	Non-muscle myosin II
PAA	Polyacrylamide
PDMS	Polydimethylsiloxane
PIV	Particle image velocimetry
PFM	Phase field model
PH	Pleckstrin homology
PTV	Particle tracking velocimetry
RLC	Regulatory light chain
ROCK	Rho-associated protein kinase
STM	Simple tension model
TEM	Tension elasticity model
TFM	Traction force microscopy

List of Figures

1.1	The three filament systems	3
1.2	The actin cytoskeleton	5
1.3	Structure and regulation of Non-muscle myosin II	7
1.4	Main signaling pathways for the regulation of the actin cytoskeleton	8
1.5	Cell-extracellular matrix and cell-cell adhesions	10
1.6	Mechanotransduction pathways	12
1.7	Force quantification based on micropillar arrays and traction force microscopy	13
1.8	Micropatterning and its applications in mechanobiology	16
1.9	Optogenetic control of RhoA with the CRY2/CIBN dimerization system	17
1.10	Cellular contractility modeled with discrete cable networks.	19
1.11	Continuum model for cellular contractility on elastic substrates. . .	21
1.12	Contour models of cellular adhesion.	23
1.13	Cellular Potts model, phase field model and vertex model	24
2.1	Continuum mechanics substructure.	28
2.2	Lagrangian and Eulerian description of continuum mechanics. . . .	29
2.3	Kelvin-Voigt and Maxwell model	34
2.4	Isotropically contracting disc on disc and ring pattern.	36
2.5	Radial displacement and stress field for contractile disc.	38
2.6	Basic notions for the mathematics of contour models	40
2.7	Tension elasticity model	41
3.1	FEM workflow	46
3.2	Linear Lagrange polynomials as FEM basis functions	49
3.3	Convergence of the two-dimensional FEM simulation	52
3.4	Sanity check for contour simulations with FEM	55
3.5	Full cell contour model	56
4.1	Actin organization on disc and hazard pattern	59
4.2	Description	60
4.3	Scaling of force and strain energy of isotropic disc	64
4.4	Time course of the substrate strain energy for different stress profiles	65
4.5	Description	67
4.6	Influence of pattern size on actin ordering and strain energy	72
4.7	Cell size influences strain energy and strain energy gain after pho- toactivation	73
4.8	Result of the strain energy fit for cells on disc pattern	75

4.9	Influence of actin organization on strain energy	76
4.10	Actin organization influences strain energy and strain energy gain after photoactivation	77
4.11	Influence of stress fiber arrangement and adhesive area on traction forces and substrate strain energy in FEM simulations	78
4.12	Influence of varying pulse duration on force generation	80
5.1	Experimental setup for single cells and cell pairs on H-pattern	85
5.2	Varying line tension in the anisotropic tension model	88
5.3	Continuous and point-like adhesion sites	89
5.4	Parametrization and result of the shape analysis procedure	91
5.5	Comparison of results of cell shape analysis and monolayer stress microscopy	93
5.6	Active stress profile, parametrization of the H-pattern and spatial intensity profile of the light-pulse	96
5.7	Parameterization of the two-dimensional FEM by global photoactivation	99
5.8	Parameterization of the contour FEM by global photoactivation.	100
5.9	Comparison of local optogenetic activation in doublets and singlets	102
5.10	Active coupling in cell doublets	105
5.11	Influence of micropattern aspect ratio on the mechanical and structural polarization of doublets	107
5.12	Efficiency of force transmission for differing mechanical and structural polarization in doublets	108
5.13	Stress propagation in small monolayers	110
6.1	Setup discontinuous Galerkin method	118
6.2	Model RhoA pathway with feedback	122
6.3	Linearized RhoA-pathway	124
6.4	Reaction kinetics of the linearized RhoA-pathway	127
6.5	Baseline contractility in the cell pair model	128
6.6	Influence of strain dependent active coupling on cell periphery	129
6.7	Substrate strain energy as a function of active coupling strength	131
6.8	Outlook epithelial sheet with discontinuous Galerkin method	132
A.2	Actin images of doublets and singlets and the correlation between mechanical and structural polarization	142
A.3	Supplementary information for local photactivation	143
A.4	Comparison TFM and FEM during global photoactivation I	144
A.5	Comparison TFM and FEM during global photoactivation II	145
A.6	Phalloidin stainings of actin structures of small tissues	145
A.8	Model switch for different viscous coupling	150
A.9	Sanity check for the RD-system and the interface condition	155

References

- Abedin, M., & King, N. (2010). Diverse evolutionary paths to cell adhesion. *Trends in cell biology*, 20(12), 734–742 (cit. on p. 9).
- Abeyaratne, R. *Continuum mechanics*. Lecture Notes. 1988. http://web.mit.edu/abeyaratne/lecture_notes.html (cit. on p. 27)
- Abramowitz, M., Stegun, I. A., & Romer, R. H. (1988). Handbook of mathematical functions with formulas, graphs, and mathematical tables. (Cit. on p. 159).
- Ahmed, A. M., & Barony, S. Y. (2020). Mixed finite element matrix for plate bending analysis using weighted-residual integral and weak formulation. *European Journal of Engineering and Technology Research*, 5(8), 990–999 (cit. on p. 48).
- Albert, P. J., & Schwarz, U. S. (2014). Dynamics of cell shape and forces on micropatterned substrates predicted by a cellular Potts model. *Biophysical Journal*, 106(11), 2340–2352. <https://doi.org/10.1016/j.bpj.2014.04.036> (cit. on p. 24)
- Albert, P. J., & Schwarz, U. S. (2016a). Dynamics of cell ensembles on adhesive micropatterns: Bridging the gap between single cell spreading and collective cell migration. *PLoS computational biology*, 12(4), e1004863 (cit. on p. 24).
- Albert, P. J., & Schwarz, U. S. (2016b). Modeling cell shape and dynamics on micropatterns. *Cell adhesion & migration*, 10(5), 516–528 (cit. on p. 24).
- Alberts, B., Johnson, A., Lewis, J., Raff, M., Roberts, K., Walter, P. et al. (2003). Molecular biology of the cell. *Scandinavian Journal of Rheumatology*, 32(2), 125–125 (cit. on pp. 4, 6, 8, 9).
- Allena, R., Muñoz, J. J., & Aubry, D. (2013). Diffusion-reaction model for drosophila embryo development. *Computer methods in biomechanics and biomedical engineering*, 16(3), 235–248 (cit. on p. 113).
- Alnæs, M., Blechta, J., Hake, J., Johansson, A., Kehlet, B., Logg, A., Richardson, C., Ring, J., Rognes, M. E., & Wells, G. N. (2015). The fenics project version 1.5. *Archive of Numerical Software*, 3(100) (cit. on pp. 49, 70, 121).
- Andersen, T., Wörthmüller, D., Probst, D., Wang, I., Moreau, P., Fitzpatrick, V., Boudou, T., Schwarz, U. S., & Balland, M. (2022). Cell size and actin architecture determine force generation in optogenetically activated adherent cells. *bioRxiv*. <https://doi.org/10.1101/2022.03.15.484408> (cit. on pp. 57, 58, 137)
- Andersen, T. [Tomas]. (2018). *Linking cellular tensional force dynamics with actin architecture* (Doctoral dissertation). Université Grenoble Alpes. (Cit. on pp. 58, 67, 69).

- Andreu, I., Falcones, B., Hurst, S., Chahare, N., Quiroga, X., Le Roux, A.-L., Kechagia, Z., Beedle, A. E., Elosegui-Artola, A., Trepac, X. *et al.* (2021). The force loading rate drives cell mechanosensing through both reinforcement and cytoskeletal softening. *Nature communications*, *12*(1), 1–12 (cit. on p. 103).
- Aranson, I., Kalatsky, V., & Vinokur, V. (2000). Continuum field description of crack propagation. *Physical review letters*, *85*(1), 118 (cit. on p. 25).
- Arnold, D. N. (1982). An interior penalty finite element method with discontinuous elements. *SIAM journal on numerical analysis*, *19*(4), 742–760 (cit. on p. 118).
- Babuška, I. (1973). The finite element method with penalty. *Mathematics of computation*, *27*(122), 221–228 (cit. on p. 118).
- Balaban, N. Q., Schwarz, U. S., Riveline, D., Goichberg, P., Tzur, G., Sabanay, I., Mahalu, D., Safran, S., Bershadsky, A., Addadi, L. *et al.* (2001). Force and focal adhesion assembly: A close relationship studied using elastic micropatterned substrates. *Nature cell biology*, *3*(5), 466–472 (cit. on pp. 9, 11, 57, 69).
- Banerjee, S., & Cristina Marchetti, M. (2013). Controlling cell-matrix traction forces by extracellular geometry. *New Journal of Physics*, *15*. <https://doi.org/10.1088/1367-2630/15/3/035015> (cit. on pp. 21, 58, 69, 79)
- Banerjee, S., & Marchetti, M. C. (2012). Contractile stresses in cohesive cell layers on finite-thickness substrates. *Physical Review Letters*, *109*(10), 1–5. <https://doi.org/10.1103/PhysRevLett.109.108101> (cit. on p. 60)
- Bar-Ziv, R., Tlusty, T., Moses, E., Safran, S. A., & Bershadsky, A. (1999). Pearling in cells: A clue to understanding cell shape. *Proceedings of the National Academy of Sciences of the United States of America*, *96*(18), 10140–10145. <https://doi.org/10.1073/pnas.96.18.10140> (cit. on p. 22)
- Bauer, A., Prechová, M., Fischer, L., Thievensen, I., Gregor, M., & Fabry, B. (2021). Pytfm: A tool for traction force and monolayer stress microscopy. *PLoS computational biology*, *17*(6), e1008364 (cit. on p. 94).
- Beguerisse-Díaz, M., Desikan, R., & Barahona, M. (2016). Linear models of activation cascades: Analytical solutions and coarse-graining of delayed signal transduction. *Journal of the Royal Society Interface*, *13*(121). <https://doi.org/10.1098/rsif.2016.0409> (cit. on pp. 66, 124)
- Belmonte, J. M., Leptin, M., & Nédélec, F. (2017). A theory that predicts behaviors of disordered cytoskeletal networks. *Molecular Systems Biology*, *13*(9), 941. <https://doi.org/10.15252/msb.20177796> (cit. on p. 81)
- Bement, W. M., Leda, M., Moe, A. M., Kita, A. M., Larson, M. E., Golding, A. E., Pfeuti, C., Su, K.-C., Miller, A. L., Goryachev, A. B. *et al.* (2015). Activator–inhibitor coupling between rho signalling and actin assembly makes the cell cortex an excitable medium. *Nature cell biology*, *17*(11), 1471–1483 (cit. on p. 114).

- Besser, A., & Schwarz, U. S. (2007). Coupling biochemistry and mechanics in cell adhesion: A model for inhomogeneous stress fiber contraction. *New Journal of Physics*, *9*(07), 1–27. <https://doi.org/10.1088/1367-2630/9/11/425> (cit. on pp. 64, 113, 125, 126)
- Biben, T., & Misbah, C. (2003). Tumbling of vesicles under shear flow within an advected-field approach. *Physical Review E*, *67*(3), 031908 (cit. on p. 25).
- Billington, N., Wang, A., Mao, J., Adelstein, R. S., & Sellers, J. R. (2013). Characterization of three full-length human nonmuscle myosin ii paralogs. *Journal of Biological Chemistry*, *288*(46), 33398–33410 (cit. on p. 7).
- Bischof, J., Brand, C. A., Somogyi, K., Májer, I., Thome, S., Mori, M., Schwarz, U. S., & Lénárt, P. (2017). A cdk1 gradient guides surface contraction waves in oocytes. *Nature communications*, *8*(1), 1–10 (cit. on p. 114).
- Bischofs, I. B., Klein, F., Lehnert, D., Bastmeyer, M., & Schwarz, U. S. (2008). Filamentous network mechanics and active contractility determine cell and tissue shape. *Biophysical Journal*, *95*(7), 3488–3496. <https://doi.org/10.1529/biophysj.108.134296> (cit. on pp. 19, 22, 23)
- Bischofs, I. B., Schmidt, S. S., & Schwarz, U. S. (2009). Effect of adhesion geometry and rigidity on cellular force distributions. *Physical Review Letters*, *103*(4), 1–4. <https://doi.org/10.1103/PhysRevLett.103.048101> (cit. on pp. 22, 23, 41, 43, 88)
- Blanchoin, L., Boujemaa-Paterski, R., Sykes, C., & Plastino, J. (2014). Actin dynamics, architecture, and mechanics in cell motility. *Physiological Reviews*, *94*(1), 235–263. <https://doi.org/10.1152/physrev.00018.2013> (cit. on pp. 4, 5)
- Block, J., Schroeder, V., Pawelzyk, P., Willenbacher, N., & Köster, S. (2015). Physical properties of cytoplasmic intermediate filaments. *Biochimica et Biophysica Acta (BBA)-Molecular Cell Research*, *1853*(11), 3053–3064 (cit. on p. 9).
- Boal, D. (2002). Mechanics of the cell cambridge university press. *New York, Cambridge, UK* (cit. on p. 18).
- Bois, J. S., Jülicher, F., & Grill, S. W. (2011). Pattern formation in active fluids. *Physical review letters*, *106*(2), 028103 (cit. on p. 121).
- Boudou, T., Andersen, T., & Balland, M. (2019). On the spatiotemporal regulation of cell tensional state. *Experimental cell research*, *378*(1), 113–117 (cit. on p. 57).
- Boyden, E. S., Zhang, F., Bamberg, E., Nagel, G., & Deisseroth, K. (2005). Millisecond-timescale, genetically targeted optical control of neural activity. *Nature neuroscience*, *8*(9), 1263–1268 (cit. on p. 15).
- Brand, C. A. (2016). *Forces and flow of contractile networks* (Doctoral dissertation). Universität Heidelberg. (Cit. on p. 121).

- Brand, C. A., Linke, M., Weißenbruch, K., Richter, B., Bastmeyer, M., & Schwarz, U. S. (2017). Tension and elasticity contribute to fibroblast cell shape in three dimensions. *Biophysical journal*, *113*(4), 770–774 (cit. on p. 19).
- Brenner, S. C., Scott, L. R., & Scott, L. R. (2008). *The mathematical theory of finite element methods* (Vol. 3). Springer. (Cit. on p. 52).
- Brock, A., Chang, E., Ho, C.-C., LeDuc, P., Jiang, X., Whitesides, G. M., & Ingber, D. E. (2003). Geometric determinants of directional cell motility revealed using microcontact printing. *Langmuir*, *19*(5), 1611–1617 (cit. on p. 15).
- Broedersz, C. P., & MacKintosh, F. C. (2014). Modeling semiflexible polymer networks. *Reviews of Modern Physics*, *86*(3), 995 (cit. on p. 19).
- Broussard, J. A., Jaiganesh, A., Zarkoob, H., Conway, D. E., Dunn, A. R., Espinosa, H. D., Janmey, P. A., & Green, K. J. (2020). Scaling up single-cell mechanics to multicellular tissues—the role of the intermediate filament–desmosome network. *Journal of cell science*, *133*(6), jcs228031 (cit. on p. 10).
- Brown, R., Prajapati, R., McGrouther, D., Yannas, I., & Eastwood, M. (1998). Tensional homeostasis in dermal fibroblasts: Mechanical responses to mechanical loading in three-dimensional substrates. *Journal of cellular physiology*, *175*(3), 323–332 (cit. on p. 57).
- Burnette, D. T., Shao, L., Ott, C., Pasapera, A. M., Fischer, R. S., Baird, M. A., Der Loughian, C., Delanoe-Ayari, H., Paszek, M. J., Davidson, M. W., Betzig, E., & Lippincott-Schwartz, J. (2014). A contractile and counterbalancing adhesion system controls the 3D shape of crawling cells. *Journal of Cell Biology*, *205*(1), 83–96. <https://doi.org/10.1083/jcb.201311104> (cit. on p. 5)
- Burridge, K., & Wittchen, E. S. (2013). The tension mounts: Stress fibers as force-generating mechanotransducers. *Journal of Cell Biology*, *200*(1), 9–19 (cit. on p. 5).
- Butler, J. P., Tolic-Nørrelykke, I. M., Fabry, B., & Fredberg, J. J. (2002). Traction fields, moments, and strain energy that cells exert on their surroundings. *American Journal of Physiology-Cell Physiology*, *282*(3), C595–C605 (cit. on pp. 14, 57, 67).
- Caillerie, D., John, K., Misbah, C., Peyla, P., & Raoult, A. (2010). A constitutive law for cross-linked actin networks by homogenization techniques. *arXiv preprint arXiv:1011.3196* (cit. on p. 18).
- Cavanaugh, K. E., Staddon, M. F., Banerjee, S., & Gardel, M. L. (2020). Adaptive viscoelasticity of epithelial cell junctions: From models to methods. *Current opinion in genetics & development*, *63*, 86–94 (cit. on pp. 18, 25).
- Chen, C. S., Mrksich, M., Huang, S., Whitesides, G. M., & Ingber, D. E. (1997). Geometric control of cell life and death. *Science*, *276*(5317), 1425–1428 (cit. on pp. 11, 83).

- Chojowski, R., Schwarz, U. S., & Ziebert, F. (2020). Reversible elastic phase field approach and application to cell monolayers. *European Physical Journal E*, *43*(10). <https://doi.org/10.1140/epje/i2020-11988-1> (cit. on pp. 24, 25)
- Citi, S., & Kendrick-Jones, J. (1987). Regulation of non-muscle myosin structure and function. *Bioessays*, *7*(4), 155–159 (cit. on p. 122).
- Clément, R., Dehapiot, B., Collinet, C., Lecuit, T., & Lenne, P. F. (2017). Viscoelastic Dissipation Stabilizes Cell Shape Changes during Tissue Morphogenesis. *Current Biology*, *27*(20), 3132–3142.e4. <https://doi.org/10.1016/j.cub.2017.09.005> (cit. on p. 33)
- Deguchi, S., Ohashi, T., & Sato, M. (2006). Tensile properties of single stress fibers isolated from cultured vascular smooth muscle cells. *Journal of biomechanics*, *39*(14), 2603–2610 (cit. on p. 97).
- Del Rio, A., Perez-Jimenez, R., Liu, R., Roca-Cusachs, P., Fernandez, J. M., & Sheetz, M. P. (2009). Stretching single talin rod molecules activates vinculin binding. *Science*, *323*(5914), 638–641 (cit. on p. 11).
- Dembo, M., & Wang, Y.-L. (1999). Stresses at the cell-to-substrate interface during locomotion of fibroblasts. *Biophysical journal*, *76*(4), 2307–2316 (cit. on pp. 13, 14, 57).
- Discher, D. E., Smith, L., Cho, S., Colasurdo, M., García, A. J., & Safran, S. (2017). Matrix mechanosensing: From scaling concepts in 'omics data to mechanisms in the nucleus, regeneration, and cancer. *Annual review of biophysics*, *46*, 295–315 (cit. on p. 57).
- Donea, J., & Huerta, A. (2003). *Finite element methods for flow problems*. John Wiley & Sons. (Cit. on p. 47).
- Douglas, J., & Dupont, T. (1976). Interior penalty procedures for elliptic and parabolic galerkin methods. *Computing methods in applied sciences* (pp. 207–216). Springer. (Cit. on p. 120).
- Edwards, C. M., & Schwarz, U. S. (2011). Force localization in contracting cell layers. *Physical Review Letters*, *107*(12), 1–5. <https://doi.org/10.1103/PhysRevLett.107.128101> (cit. on pp. 20, 21, 34, 58, 69, 79)
- Engler, A. J., Sen, S., Sweeney, H. L., & Discher, D. E. (2006). Matrix elasticity directs stem cell lineage specification. *Cell*, *126*(4), 677–689 (cit. on p. 11).
- Etienne-Manneville, S. (2011). Control of polarized cell morphology and motility by adherens junctions. *Seminars in cell & developmental biology*, *22*(8), 850–857 (cit. on p. 9).
- Farahani, P. E., Reed, E. H., Underhill, E. J., Aoki, K., & Toettcher, J. E. (2021). Signaling, deconstructed: Using optogenetics to dissect and direct information flow in biological systems. *Annual review of biomedical engineering*, *23*, 61–87 (cit. on p. 16).

- Farhadifar, R., Röper, J.-C., Aigouy, B., Eaton, S., & Jülicher, F. (2007). The influence of cell mechanics, cell-cell interactions, and proliferation on epithelial packing. *Current Biology*, *17*(24), 2095–2104 (cit. on pp. 24, 25).
- Finer, J. T., Simmons, R. M., & Spudich, J. A. (1994). Single myosin molecule mechanics: Piconewton forces and nanometre steps. *Nature*, *368*(6467), 113–119 (cit. on p. 6).
- Friedman, M. H. (2008). *Principles and models of biological transport*. Springer Science & Business Media. (Cit. on p. 117).
- Garcia-Mata, R., Boulter, E., & Burridge, K. (2011). The 'invisible hand': Regulation of rho gtpases by rhogdis. *Nature reviews Molecular cell biology*, *12*(8), 493–504 (cit. on p. 122).
- Geiger, B., Spatz, J. P., & Bershadsky, A. D. (2009). Environmental sensing through focal adhesions. *Nature reviews Molecular cell biology*, *10*(1), 21–33 (cit. on p. 83).
- Geuzaine, C., & Remacle, J.-F. (2009). Gmsh: A 3-d finite element mesh generator with built-in pre-and post-processing facilities. *International journal for numerical methods in engineering*, *79*(11), 1309–1331 (cit. on pp. 70, 121).
- Giomi, L. (2019). Contour Models of Cellular Adhesion. *Advances in Experimental Medicine and Biology*, *1146*, 13–29. https://doi.org/10.1007/978-3-030-17593-1_2 (cit. on pp. 23, 41, 86, 88)
- Gittes, F., Mickey, B., Nettleton, J., & Howard, J. (1993). Flexural rigidity of microtubules and actin filaments measured from thermal fluctuations in shape. *The Journal of cell biology*, *120*(4), 923–934 (cit. on pp. 19, 97).
- Gov, N. (2011). Moving under peer pressure. *Nature materials*, *10*(6), 412–414 (cit. on p. 21).
- Graner, F., & Glazier, J. A. (1992). Simulation of biological cell sorting using a two-dimensional extended potts model. *Physical review letters*, *69*(13), 2038 (cit. on p. 23).
- Gulhati, P., Bowen, K. A., Liu, J., Stevens, P. D., Rychahou, P. G., Chen, M., Lee, E. Y., Weiss, H. L., O'Connor, K. L., Gao, T. et al. (2011). Mtorc1 and mtorc2 regulate emt, motility, and metastasis of colorectal cancer via rhoa and rac1 signaling pathways. *Cancer research*, *71*(9), 3246–3256 (cit. on p. 57).
- Gupta, M., Sarangi, B. R., Deschamps, J., Nematbakhsh, Y., Callan-Jones, A., Margadant, F., Mège, R.-M., Lim, C. T., Voituriez, R., & Ladoux, B. (2015). Adaptive rheology and ordering of cell cytoskeleton govern matrix rigidity sensing. *Nature communications*, *6*(1), 1–9 (cit. on p. 71).
- Guthardt Torres, P., Bischofs, I. B., & Schwarz, U. S. (2012). Contractile network models for adherent cells. *Physical Review E - Statistical, Nonlinear, and Soft*

- Matter Physics*, 85(1), 1–13. <https://doi.org/10.1103/PhysRevE.85.011913> (cit. on pp. 19, 97)
- Gutierrez-Lemini, D. (2014). *Engineering viscoelasticity*. Springer. (Cit. on p. 34).
- Hanke, J., Probst, D., Zemel, A., Schwarz, U. S., & Köster, S. (2018). Dynamics of force generation by spreading platelets. *Soft Matter*, 14(31), 6571–6581. <https://doi.org/10.1039/c8sm00895g> (cit. on p. 21)
- Hansen, C. V., Schroll, H. J., & Wüstner, D. (2018). A discontinuous galerkin model for fluorescence loss in photobleaching. *Scientific reports*, 8(1), 1–13 (cit. on p. 117).
- Harris, A. K., Wild, P., & Stopak, D. (1980). Silicone rubber substrata: A new wrinkle in the study of cell locomotion. *Science*, 208(4440), 177–179 (cit. on p. 12).
- Harris, T. J., & Tepass, U. (2010). Adherens junctions: From molecules to morphogenesis. *Nature reviews Molecular cell biology*, 11(7), 502–514 (cit. on p. 10).
- Hartsock, A., & Nelson, W. J. (2008). Adherens and tight junctions: Structure, function and connections to the actin cytoskeleton. *Biochimica et Biophysica Acta (BBA)-Biomembranes*, 1778(3), 660–669 (cit. on p. 10).
- Heath, J. P. (1983). Behaviour and structure of the leading lamella in moving fibroblasts. i. occurrence and centripetal movement of arc-shaped microfilament bundles beneath the dorsal cell surface. *Journal of cell science*, 60(1), 331–354 (cit. on p. 4).
- Heisenberg, C.-P., & Bellaïche, Y. (2013). Forces in tissue morphogenesis and patterning. *Cell*, 153(5), 948–962 (cit. on p. 83).
- Hino, N., Rossetti, L., Marín-Llauradó, A., Aoki, K., Trepats, X., Matsuda, M., & Hirashima, T. (2020). Erk-mediated mechanochemical waves direct collective cell polarization. *Developmental cell*, 53(6), 646–660 (cit. on pp. 24, 103).
- Hippler, M., Weißenbruch, K., Richler, K., Lemma, E. D., Nakahata, M., Richter, B., Barner-Kowollik, C., Takashima, Y., Harada, A., Blasco, E. et al. (2020). Mechanical stimulation of single cells by reversible host-guest interactions in 3d microscavolds. *Science advances*, 6(39), eabc2648 (cit. on pp. 57, 128).
- Holst, M., & Stern, A. (2012). Geometric Variational Crimes: Hilbert Complexes, Finite Element Exterior Calculus, and Problems on Hypersurfaces. *Foundations of Computational Mathematics*, 12(3), 263–293. <https://doi.org/10.1007/s10208-012-9119-7> (cit. on p. 52)
- Holzappel, A. G. (2000). Nonlinear solid mechanics ii (cit. on p. 27).
- Hotulainen, P., & Lappalainen, P. (2006). Stress fibers are generated by two distinct actin assembly mechanisms in motile cells. *The Journal of cell biology*, 173(3), 383–394 (cit. on p. 5).

- Howard, J., & Clark, R. (2002). Mechanics of motor proteins and the cytoskeleton. *Appl. Mech. Rev.*, *55*(2), B39–B39 (cit. on pp. 2, 8).
- Howell, P., Kozyreff, G., & Ockendon, J. (2009). *Applied solid mechanics*. Cambridge University Press. (Cit. on pp. 28, 30).
- Hu, S., Dasbiswas, K., Guo, Z., Tee, Y.-H., Thiagarajan, V., Hersen, P., Chew, T.-L., Safran, S. A., Zaidel-Bar, R., & Bershadsky, A. D. (2017). Long-range self-organization of cytoskeletal myosin ii filament stacks. *Nature cell biology*, *19*(2), 133–141 (cit. on p. 69).
- Huber, F., Boire, A., López, M. P., & Koenderink, G. H. (2015). Cytoskeletal crosstalk: When three different personalities team up. *Current Opinion in Cell Biology*, *32*, 39–47. <https://doi.org/10.1016/j.ceb.2014.10.005> (cit. on pp. 3, 9)
- Hufnagel, L., Teleman, A. A., Rouault, H., Cohen, S. M., & Shraiman, B. I. (2007). On the mechanism of wing size determination in fly development. *Proceedings of the National Academy of Sciences*, *104*(10), 3835–3840 (cit. on p. 25).
- Huxley, A. F. (1957). Muscle structure and theories of contraction. *Prog. Biophys. Biophys. Chem*, *7*, 255–318 (cit. on p. 6).
- Iber, D., Tanaka, S., Fried, P., Germann, P., & Menshykau, D. (2015). Simulating tissue morphogenesis and signaling. *Tissue morphogenesis* (pp. 323–338). Springer. (Cit. on p. 24).
- Iskratsch, T., Wolfenson, H., & Sheetz, M. P. (2014). Appreciating force and shape—the rise of mechanotransduction in cell biology. *Nature reviews Molecular cell biology*, *15*(12), 825–833 (cit. on p. 11).
- Janmey, P. A., Winer, J. P., Murray, M. E., & Wen, Q. (2009). The hard life of soft cells. *Cell motility and the cytoskeleton*, *66*(8), 597–605 (cit. on p. 83).
- Jiang, H., & Grinnell, F. (2005). Cell–matrix entanglement and mechanical anchorage of fibroblasts in three-dimensional collagen matrices. *Molecular biology of the cell*, *16*(11), 5070–5076 (cit. on p. 10).
- Juelicher, F., Kruse, K., Prost, J., & Joanny, J.-F. (2007). Active behavior of the cytoskeleton. *Physics reports*, *449*(1-3), 3–28 (cit. on p. 113).
- Juma, V. (2019). *Data-driven mathematical modelling and simulation of rho-myosin dynamics* (Doctoral dissertation). University of Sussex. (Cit. on pp. 153, 156).
- Käfer, J., Hayashi, T., Marée, A. F., Carthew, R. W., & Graner, F. (2007). Cell adhesion and cortex contractility determine cell patterning in the drosophilaretina. *Proceedings of the National Academy of Sciences*, *104*(47), 18549–18554 (cit. on p. 24).
- Kamps, D., Koch, J., Juma, V. O., Campillo-Funollet, E., Graessl, M., Banerjee, S., Mazel, T., Chen, X., Wu, Y. W., Portet, S., Madzvamuse, A., Nalbant, P., & Dehmelt, L. (2020). Optogenetic Tuning Reveals Rho Amplification-Dependent

- Dynamics of a Cell Contraction Signal Network. *Cell Reports*, 33(9). <https://doi.org/10.1016/j.celrep.2020.108467> (cit. on pp. 64, 80, 114, 121–123, 126, 127, 153, 155)
- Kanatani, K., & Rangarajan, P. (2011). Hyper least squares fitting of circles and ellipses. *Computational Statistics & Data Analysis*, 55(6), 2197–2208 (cit. on p. 92).
- Kanchanawong, P., Shtengel, G., Pasapera, A. M., Ramko, E. B., Davidson, M. W., Hess, H. F., & Waterman, C. M. (2010). Nanoscale architecture of integrin-based cell adhesions. *Nature*, 468(7323), 580–584 (cit. on p. 10).
- Kassianidou, E., Brand, C. A., Schwarz, U. S., & Kumar, S. (2017). Geometry and network connectivity govern the mechanics of stress fibers. *Proceedings of the National Academy of Sciences*, 114(10), 2622–2627 (cit. on p. 19).
- Kennedy, M. J., Hughes, R. M., Peteya, L. A., Schwartz, J. W., Ehlers, M. D., & Tucker, C. L. (2010). Rapid blue-light-mediated induction of protein interactions in living cells. *Nature methods*, 7(12), 973–975 (cit. on p. 17).
- Khatau, S. B., Hale, C. M., Stewart-Hutchinson, P., Patel, M. S., Stewart, C. L., Searson, P. C., Hodzic, D., & Wirtz, D. (2009). A perinuclear actin cap regulates nuclear shape. *Proceedings of the National Academy of Sciences*, 106(45), 19017–19022 (cit. on p. 4).
- Kilian, K. A., Bugarija, B., Lahn, B. T., & Mrksich, M. (2010). Geometric cues for directing the differentiation of mesenchymal stem cells. *Proceedings of the National Academy of Sciences*, 107(11), 4872–4877 (cit. on p. 11).
- Kim, J., Mailand, E., Ang, I., Sakar, M. S., & Bouklas, N. (2021). A model for 3D deformation and reconstruction of contractile microtissues. *Soft Matter*. <https://doi.org/10.1039/d0sm01182g> (cit. on pp. 21, 134)
- Kojima, H., Ishijima, A., & Yanagida, T. (1994). Direct measurement of stiffness of single actin filaments with and without tropomyosin by in vitro nanomanipulation. *Proceedings of the National Academy of Sciences*, 91(26), 12962–12966 (cit. on p. 19).
- Konermann, S., Brigham, M. D., Trevino, A. E., Hsu, P. D., Heidenreich, M., Cong, L., Platt, R. J., Scott, D. A., Church, G. M., & Zhang, F. (2013). Optical control of mammalian endogenous transcription and epigenetic states. *Nature*, 500(7463), 472–476 (cit. on p. 15).
- Kong, F., García, A. J., Mould, A. P., Humphries, M. J., & Zhu, C. (2009). Demonstration of catch bonds between an integrin and its ligand. *Journal of Cell Biology*, 185(7), 1275–1284 (cit. on p. 11).
- Kowalczyk, M., Kamps, D., Wu, Y., Dehmelt, L., & Nalbant, P. (2022). Monitoring the response of multiple signal network components to acute chemo-optogenetic perturbations in living cells. *ChemBioChem*, 23(4), e202100582 (cit. on p. 126).

- Kraft, D. *et al.* (1988). A software package for sequential quadratic programming (cit. on p. 101).
- Krishnan, R., Park, C. Y., Lin, Y.-C., Mead, J., Jaspers, R. T., Trepats, X., Lenormand, G., Tambe, D., Smolensky, A. V., Knoll, A. H. *et al.* (2009). Reinforcement versus fluidization in cytoskeletal mechanoresponsiveness. *PloS one*, *4*(5), e5486 (cit. on p. 103).
- Kruse, K., Joanny, J.-F., Jülicher, F., Prost, J., & Sekimoto, K. (2005). Generic theory of active polar gels: A paradigm for cytoskeletal dynamics. *The European Physical Journal E*, *16*(1), 5–16 (cit. on p. 20).
- Labouesse, C., Verkhovskiy, A. B., Meister, J. J., Gabella, C., & Vianay, B. (2015). Cell shape dynamics reveal balance of elasticity and contractility in peripheral arcs. *Biophysical Journal*, *108*(10), 2437–2447. <https://doi.org/10.1016/j.bpj.2015.04.005> (cit. on pp. 95, 97, 98)
- Lacarbonara, W. (2013). *Nonlinear structural mechanics: Theory, dynamical phenomena and modeling*. Springer Science & Business Media. (Cit. on p. 38).
- Landau, L. D., Lifšic, E. M., Lifshitz, E. M., Kosevich, A. M., & Pitaevskii, L. P. (1986). *Theory of elasticity: Volume 7* (Vol. 7). Elsevier. (Cit. on p. 14).
- Langer, J., & Sekerka, R. (1975). Theory of departure from local equilibrium at the interface of a two-phase diffusion couple. *Acta Metallurgica*, *23*(10), 1225–1237 (cit. on p. 25).
- Langtangen, H. P., & Logg, A. (2017). *Solving pdes in python: The fenics tutorial i*. Springer Nature. (Cit. on pp. 46, 51).
- Latorre, E., Kale, S., Casares, L., Gómez-González, M., Uroz, M., Valon, L., Nair, R. V., Garreta, E., Montserrat, N., del Campo, A., Ladoux, B., Arroyo, M., & Trepats, X. (2018). Active superelasticity in three-dimensional epithelia of controlled shape. *Nature*, *563*(7730), 203–208. <https://doi.org/10.1038/s41586-018-0671-4> (cit. on pp. 3, 9)
- Lee, C.-S., Choi, C.-K., Shin, E.-Y., Schwartz, M. A., & Kim, E.-G. (2010). Myosin ii directly binds and inhibits dbl family guanine nucleotide exchange factors: A possible link to rho family gtpases. *Journal of Cell Biology*, *190*(4), 663–674 (cit. on p. 123).
- Lepidi, M., Gattulli, V., & Vestroni, F. (2007). Static and dynamic response of elastic suspended cables with damage. *International Journal of Solids and Structures*, *44*(25-26), 8194–8212 (cit. on p. 56).
- Letort, G., Ennomani, H., Gressin, L., Théry, M., & Blanchoin, L. (2015). Dynamic reorganization of the actin cytoskeleton [version 1; referees: 2 approved]. *F1000Research*, *4*(940), 1–11. <https://doi.org/10.12688/f1000research.6374.1> (cit. on p. 5)
- Levayer, R., & Lecuit, T. (2012). Biomechanical regulation of contractility: Spatial control and dynamics. *Trends in cell biology*, *22*(2), 61–81 (cit. on p. 6).

- Li, H., Shen, T., Smith, M. B., Fujiwara, I., Vavylonis, D., & Huang, X. (2009). Automated actin filament segmentation, tracking and tip elongation measurements based on open active contour models. *2009 IEEE International Symposium on Biomedical Imaging: From Nano to Macro*, 1302–1305 (cit. on p. 90).
- Liu, Z., Tan, J. L., Cohen, D. M., Yang, M. T., Sniadecki, N. J., Ruiz, S. A., Nelson, C. M., & Chen, C. S. (2010). Mechanical tugging force regulates the size of cell–cell junctions. *Proceedings of the National Academy of Sciences*, *107*(22), 9944–9949 (cit. on pp. 11, 103).
- Livne, A., & Geiger, B. (2016). The inner workings of stress fibers- from contractile machinery to focal adhesions and back. *Journal of Cell Science*, *129*(7), 1293–1304 (cit. on p. 5).
- Lodish, H., Berk, A., Kaiser, C. A., Kaiser, C., Krieger, M., Scott, M. P., Bretscher, A., Ploegh, H., Matsudaira, P. et al. (2008). *Molecular cell biology*. Macmillan. (Cit. on pp. 6, 7).
- Luciano, M., Xue, S.-L., De Vos, W. H., Redondo-Morata, L., Surin, M., Lafont, F., Hannezo, E., & Gabriele, S. (2021). Cell monolayers sense curvature by exploiting active mechanics and nuclear mechanoadaptation. *Nature Physics*, *17*(12), 1382–1390 (cit. on p. 11).
- Lundquist, E. A. (2006). Small gtpases. *WormBook*, 1 (cit. on p. 6).
- Mailand, E., Li, B., Eyckmans, J., Bouklas, N., & Sakar, M. S. (2019). Surface and bulk stresses drive morphological changes in fibrous microtissues. *Biophysical journal*, *117*(5), 975–986 (cit. on p. 135).
- Mandal, K., Wang, I., Vitiello, E., Orellana, L. A. C., & Balland, M. (2014). Cell dipole behaviour revealed by ecm sub-cellular geometry. *Nature communications*, *5*(1), 1–10 (cit. on p. 71).
- Marée, A. F., Jilkine, A., Dawes, A., Grieneisen, V. A., & Edelstein-Keshet, L. (2006). Polarization and movement of keratocytes: A multiscale modelling approach. *Bulletin of mathematical biology*, *68*(5), 1169–1211 (cit. on p. 24).
- MATLAB. (2018). *9.7.0.1190202 (r2019b)*. The MathWorks Inc. (Cit. on p. 90).
- Mattila, P. (2008). Lappalainen p. *Filopodia: molecular architecture and cellular functions*. *Nat Rev Mol Cell Biol*, *9*, 446–454 (cit. on p. 4).
- McBeath, R., Pirone, D. M., Nelson, C. M., Bhadriraju, K., & Chen, C. S. (2004). Cell shape, cytoskeletal tension, and rhoa regulate stem cell lineage commitment. *Developmental cell*, *6*(4), 483–495 (cit. on p. 11).
- Mercker, M., Brinkmann, F., Marciniak-Czochra, A., & Richter, T. (2016). Beyond Turing: Mechanochemical pattern formation in biological tissues. *Biology Direct*, *11*(1), 1–15. <https://doi.org/10.1186/s13062-016-0124-7> (cit. on p. 113)

- Mertz, A. F., Banerjee, S., Che, Y., German, G. K., Xu, Y., Hyland, C., Marchetti, M. C., Horsley, V., & Dufresne, E. R. (2012). Scaling of traction forces with the size of cohesive cell colonies. *Physical Review Letters*, *108*(19), 1–5. <https://doi.org/10.1103/PhysRevLett.108.198101> (cit. on pp. 21, 71)
- Michaelis, L., Menten, M. L. *et al.* (1913). Die kinetik der invertinwirkung. *Biochem. z*, *49*(333-369), 352 (cit. on p. 64).
- Michaux, J. B., Robin, F. B., McFadden, W. M., & Munro, E. M. (2018). Excitable rhoa dynamics drive pulsed contractions in the early c. elegans embryo. *Journal of Cell Biology*, *217*(12), 4230–4252 (cit. on p. 126).
- Muthinja, J. M., Ripp, J., Krüger, T., Imle, A., Haraszti, T., Fackler, O. T., Spatz, J. P., Engstler, M., & Frischknecht, F. (2018). Tailored environments to study motile cells and pathogens. *Cellular microbiology*, *20*(3), e12820 (cit. on p. 13).
- Nelder, J. A., & Mead, R. (1965). A simplex method for function minimization. *The computer journal*, *7*(4), 308–313 (cit. on pp. 70, 100).
- Ng, M. R., Besser, A., Brugge, J. S., & Danuser, G. (2014). Mapping the dynamics of force transduction at cell–cell junctions of epithelial clusters. *Elife*, *3*, e03282 (cit. on p. 83).
- Nisenholz, N., Rajendran, K., Dang, Q., Chen, H., Kemkemer, R., Krishnan, R., & Zemel, A. (2014). Active mechanics and dynamics of cell spreading on elastic substrates. *Soft matter*, *10*(37), 7234–7246 (cit. on p. 74).
- Nishikawa, M., Naganathan, S. R., Jülicher, F., & Grill, S. W. (2017). Controlling contractile instabilities in the actomyosin cortex. *Elife*, *6*, e19595 (cit. on pp. 121, 126).
- Nitsche, J. (1971). Über ein variationsprinzip zur lösung von dirichlet-problemen bei verwendung von teilräumen, die keinen randbedingungen unterworfen sind. *Abhandlungen aus dem mathematischen Seminar der Universität Hamburg*, *36*(1), 9–15 (cit. on p. 120).
- Nunns, H., & Goentoro, L. (2018). Signaling pathways as linear transmitters. *Elife*, *7*, e33617 (cit. on p. 123).
- Oakes, P. W., Banerjee, S., Marchetti, M. C., & Gardel, M. L. (2014). Geometry regulates traction stresses in adherent cells. *Biophysical Journal*, *107*(4), 825–833. <https://doi.org/10.1016/j.bpj.2014.06.045> (cit. on pp. 69, 71, 148, 149)
- Oakes, P. W., Wagner, E., Brand, C. A., Probst, D., Linke, M., Schwarz, U. S., Glotzer, M., & Gardel, M. L. (2017). Optogenetic control of rhoa reveals zyxin-mediated elasticity of stress fibres. *Nature communications*, *8*(1), 1–12 (cit. on pp. 18, 20, 68, 103, 146).
- Paszek, M. J., Zahir, N., Johnson, K. R., Lakins, J. N., Rozenberg, G. I., Gefen, A., Reinhart-King, C. A., Margulies, S. S., Dembo, M., Boettiger, D. *et al.* (2005).

- Tensional homeostasis and the malignant phenotype. *Cancer cell*, 8(3), 241–254 (cit. on p. 57).
- Pathak, A., & Kumar, S. (2012). Independent regulation of tumor cell migration by matrix stiffness and confinement. *Proceedings of the National Academy of Sciences*, 109(26), 10334–10339 (cit. on p. 11).
- Peglion, F., Llense, F., & Etienne-Manneville, S. (2014). Adherens junction treadmill during collective migration. *Nature cell biology*, 16(7), 639–651 (cit. on p. 9).
- Pellegrin, S., & Mellor, H. (2007). Actin stress fibres. *Journal of cell science*, 120(20), 3491–3499 (cit. on p. 4).
- Peyret, G., Mueller, R., d’Alessandro, J., Begnaud, S., Marcq, P., Mège, R.-M., Yeomans, J. M., Doostmohammadi, A., & Ladoux, B. (2019). Sustained oscillations of epithelial cell sheets. *Biophysical journal*, 117(3), 464–478 (cit. on p. 83).
- Phillips, R., Kondev, J., Theriot, J., Garcia, H. G., & Orme, N. (2012). *Physical biology of the cell*. Garland Science. (Cit. on pp. 2, 8, 9).
- Pixley, F. J. (2012). Macrophage migration and its regulation by csf-1. *International journal of cell biology*, 2012 (cit. on p. 8).
- Plotnikov, S. V., Sabass, B., Schwarz, U. S., & Waterman, C. M. (2014). High-resolution traction force microscopy. *Methods in cell biology* (pp. 367–394). Elsevier. (Cit. on pp. 13, 14).
- Pollard, T. D. (1986). Rate constants for the reactions of atp-and adp-actin with the ends of actin filaments. *The Journal of cell biology*, 103(6), 2747–2754 (cit. on p. 4).
- Pomp, W., Schakenraad, K., Balçloğlu, H. E., Van Hoorn, H., Danen, E. H., Merks, R. M., Schmidt, T., & Giomi, L. (2018). Cytoskeletal Anisotropy Controls Geometry and Forces of Adherent Cells. *Physical Review Letters*, 121(17), 1–5. <https://doi.org/10.1103/PhysRevLett.121.178101> (cit. on pp. 23, 86, 88)
- Probst, D. (2018). *Continuum modeling of cell contractility* (Doctoral dissertation). Universität Heidelberg. (Cit. on pp. 22, 66–68).
- Prost, J., Jülicher, F., & Joanny, J.-F. (2015). Active gel physics. *Nature physics*, 11(2), 111–117 (cit. on pp. 59, 79, 113).
- Purves, W. K., Sadava, D., Orians, G. H., & Heller, H. C. (2003). *Life: The science of biology: Volume iii: Plants and animals*. Macmillan. (Cit. on p. 3).
- Quarteroni, A., & Valli, A. (2008). *Numerical approximation of partial differential equations* (Vol. 23). Springer Science & Business Media. (Cit. on p. 50).
- Rajagopal, V., Holmes, W. R., & Lee, P. V. S. (2018). Computational modeling of single-cell mechanics and cytoskeletal mechanobiology. *Wiley Interdisciplinary*

- Reviews: Systems Biology and Medicine*, 10(2), 5–7. <https://doi.org/10.1002/wsbm.1407> (cit. on p. 4)
- Reddy, J. (1993). An introduction to the finite element method mcgraw-hill. *Inc., New York* (cit. on p. 46).
- Reinhart-King, C. A., Dembo, M., & Hammer, D. A. (2005). The dynamics and mechanics of endothelial cell spreading. *Biophysical journal*, 89(1), 676–689 (cit. on p. 71).
- Richter, T. (2017). *Fluid-structure interactions: Models, analysis and finite elements* (Vol. 118). Springer. (Cit. on p. 28).
- Riveline, D., Zamir, E., Balaban, N. Q., Schwarz, U. S., Ishizaki, T., Narumiya, S., Kam, Z., Geiger, B., & Bershadsky, A. D. (2001). Focal contacts as mechanosensors: Externally applied local mechanical force induces growth of focal contacts by an mdia1-dependent and rock-independent mechanism. *The Journal of cell biology*, 153(6), 1175–1186 (cit. on p. 10).
- Roca-Cusachs, P., Conte, V., & Trepast, X. (2017). Quantifying forces in cell biology. *Nature cell biology*, 19(7), 742–751 (cit. on p. 13).
- Ruppel, A. (2022). *Optogenetic interrogation of intercellular propagation of force signals* (Doctoral dissertation). Université Grenoble Alpes. (Cit. on pp. 15, 85).
- Sabass, B., Gardel, M. L., Waterman, C. M., & Schwarz, U. S. (2008). High resolution traction force microscopy based on experimental and computational advances. *Biophysical journal*, 94(1), 207–220 (cit. on p. 14).
- Saha, A., Nishikawa, M., Behrndt, M., Heisenberg, C.-P., Jülicher, F., & Grill, S. W. (2016). Determining physical properties of the cell cortex. *Biophysical journal*, 110(6), 1421–1429 (cit. on p. 33).
- Salvi, A. M., & DeMali, K. A. (2018). Mechanisms linking mechanotransduction and cell metabolism. *Current opinion in cell biology*, 54, 114–120 (cit. on pp. 11, 12).
- Schakenraad, K., Ernst, J., Pomp, W., Danen, E. H., Merks, R. M., Schmidt, T., & Giomi, L. (2020). Mechanical interplay between cell shape and actin cytoskeleton organization. *Soft Matter*, 16(27), 6328–6343 (cit. on p. 56).
- Schwarz, U. S. *Continuum mechanics*. Lecture Notes. 2018 (cit. on p. 28).
- Schwarz, U. S., & Safran, S. A. (2013). Physics of adherent cells. *Reviews of Modern Physics*, 85(3), 1327–1381. <https://doi.org/10.1103/RevModPhys.85.1327> (cit. on pp. 38, 57)
- Seabra, M. C. (1998). Membrane association and targeting of prenylated ras-like gtpases. *Cellular signalling*, 10(3), 167–172 (cit. on p. 122).

- Serra-Picamal, X., Conte, V., Vincent, R., Anon, E., Tambe, D. T., Bazellieres, E., Butler, J. P., Fredberg, J. J., & Trepap, X. (2012). Mechanical waves during tissue expansion. *Nature Physics*, *8*(8), 628–634 (cit. on p. 83).
- Seshu, P. (2003). *Textbook of finite element analysis*. PHI Learning Pvt. Ltd. (Cit. on p. 46).
- Shellard, A., & Mayor, R. (2021). Collective durotaxis along a self-generated stiffness gradient in vivo. *Nature*, *600*(7890), 690–694 (cit. on p. 11).
- Slaughter, W. S. (2012). *The linearized theory of elasticity*. Springer Science & Business Media. (Cit. on p. 35).
- Smith, M. B., Li, H., Shen, T., Huang, X., Yusuf, E., & Vavylonis, D. (2010). Segmentation and tracking of cytoskeletal filaments using open active contours. *Cytoskeleton*, *67*(11), 693–705 (cit. on p. 90).
- Sniadecki, N. J., & Chen, C. S. (2007). Microfabricated silicone elastomeric post arrays for measuring traction forces of adherent cells. *Methods in cell biology*, *83*, 313–328 (cit. on p. 13).
- Soiné, J. R., Brand, C. A., Stricker, J., Oakes, P. W., Gardel, M. L., & Schwarz, U. S. (2015). Model-based traction force microscopy reveals differential tension in cellular actin bundles. *PLoS computational biology*, *11*(3), e1004076 (cit. on p. 134).
- Solowiej-Wedderburn, J., & Dunlop, C. M. (2022). Sticking around: Cell adhesion patterning for energy minimization and substrate mechanosensing. *Biophysical journal* (cit. on pp. 34, 69, 78).
- Somlyo, A. P., & Somlyo, A. V. (2000). Signal transduction by g-proteins, rho-kinase and protein phosphatase to smooth muscle and non-muscle myosin ii. *The Journal of physiology*, *522*(2), 177–185 (cit. on p. 122).
- Staddon, M. F., Munro, E. M., & Banerjee, S. (2022). Pulsatile contractions and pattern formation in excitable actomyosin cortex. *PLoS computational biology*, *18*(3), e1009981 (cit. on pp. 64, 80, 114, 121, 123, 125, 126, 132).
- Stam, S., Freedman, S. L., Banerjee, S., Weirich, K. L., Dinner, A. R., & Gardel, M. L. (2017). Filament rigidity and connectivity tune the deformation modes of active biopolymer networks. *Proceedings of the National Academy of Sciences*, *114*(47), E10037–E10045 (cit. on p. 81).
- Strang, G. (1973). Piecewise polynomials and the finite element method. *Bulletin of the American Mathematical Society*, *79*(6), 1128–1137. <https://doi.org/10.1090/S0002-9904-1973-13351-8> (cit. on p. 52)
- Sunyer, R., Conte, V., Escribano, J., Elosequi-Artola, A., Labernadie, A., Valon, L., Navajas, D., García-Aznar, J. M., Muñoz, J. J., Roca-Cusachs, P. et al. (2016). Collective cell durotaxis emerges from long-range intercellular force transmission. *Science*, *353*(6304), 1157–1161 (cit. on p. 112).

- Sunyer, R., & Trepap, X. (2020). Durotaxis. Current Biology, 30(9), R383–R387 (cit. on p. 11).*
- Svitkina, T. (2018). The actin cytoskeleton and actin-based motility. Cold Spring Harbor Perspectives in Biology, 10(1), 1–21. <https://doi.org/10.1101/cshperspect.a018267> (cit. on p. 18)*
- Swift, M. L. (1997). Graphpad prism, data analysis, and scientific graphing. Journal of chemical information and computer sciences, 37(2), 411–412 (cit. on p. 137).*
- Tambe, D. T., Corey Hardin, C., Angelini, T. E., Rajendran, K., Park, C. Y., Serra-Picamal, X., Zhou, E. H., Zaman, M. H., Butler, J. P., Weitz, D. A. et al. (2011). Collective cell guidance by cooperative intercellular forces. Nature materials, 10(6), 469–475 (cit. on pp. 21, 112).*
- Tambe, D. T., Croutelle, U., Trepap, X., Park, C. Y., Kim, J. H., Millet, E., Butler, J. P., & Fredberg, J. J. (2013). Monolayer stress microscopy: Limitations, artifacts, and accuracy of recovered intercellular stresses. PloS one, 8(2), e55172 (cit. on p. 21).*
- Tan, J. L., Tien, J., Pirone, D. M., Gray, D. S., Bhadriraju, K., & Chen, C. S. (2003). Cells lying on a bed of microneedles: An approach to isolate mechanical force. Proceedings of the National Academy of Sciences, 100(4), 1484–1489 (cit. on pp. 12, 71).*
- Theisen, L. (2019). Simulation of non-equilibrium gas flows using the fenics computing platform. (Cit. on p. 49).*
- Théry, M. (2010). Micropatterning as a tool to decipher cell morphogenesis and functions. Journal of cell science, 123(24), 4201–4213 (cit. on pp. 15, 16).*
- Théry, M., Pépin, A., Dressaire, E., Chen, Y., & Bornens, M. (2006). Cell distribution of stress fibres in response to the geometry of the adhesive environment. Cell motility and the cytoskeleton, 63(6), 341–355 (cit. on p. 15).*
- Tischer, D., & Weiner, O. D. (2014). Illuminating cell signalling with optogenetic tools. Nature reviews Molecular cell biology, 15(8), 551–558 (cit. on p. 16).*
- Tojkander, S., Gateva, G., & Lappalainen, P. (2012). Actin stress fibers—assembly, dynamics and biological roles. Journal of cell science, 125(8), 1855–1864 (cit. on p. 4).*
- Tojkander, S., Gateva, G., Schevzov, G., Hotulainen, P., Naumanen, P., Martin, C., Gunning, P. W., & Lappalainen, P. (2011). A molecular pathway for myosin ii recruitment to stress fibers. Current Biology, 21(7), 539–550 (cit. on pp. 4, 5).*
- Tolić-Nørrelykke, I. M. (2008). Push-me-pull-you: How microtubules organize the cell interior. European biophysics journal, 37(7), 1271–1278 (cit. on p. 8).*

- Trepat, X., Wasserman, M. R., Angelini, T. E., Millet, E., Weitz, D. A., Butler, J. P., & Fredberg, J. J. (2009). Physical forces during collective cell migration. *Nature physics*, 5(6), 426–430 (cit. on p. 74).
- Trichet, L., Le Digabel, J., Hawkins, R. J., Vedula, S. R. K., Gupta, M., Ribault, C., Hersen, P., Voituriez, R., & Ladoux, B. (2012). Evidence of a large-scale mechanosensing mechanism for cellular adaptation to substrate stiffness. *Proceedings of the National Academy of Sciences*, 109(18), 6933–6938 (cit. on pp. 9, 13).
- Tseng, Q., Duchemin-Pelletier, E., Deshiere, A., Balland, M., Guillou, H., Filhol, O., & Théry, M. (2012). Spatial organization of the extracellular matrix regulates cell–cell junction positioning. *Proceedings of the National Academy of Sciences*, 109(5), 1506–1511 (cit. on p. 15).
- Tseng, Q., Wang, I., Duchemin-Pelletier, E., Azioune, A., Carpi, N., Gao, J., Filhol, O., Piel, M., Théry, M., & Balland, M. (2011). A new micropatterning method of soft substrates reveals that different tumorigenic signals can promote or reduce cell contraction levels. *Lab on a chip*, 11(13), 2231–2240 (cit. on p. 71).
- Tyson, J. J., Chen, K. C., & Novak, B. (2003). Sniffers, buzzers, toggles and blinkers: Dynamics of regulatory and signaling pathways in the cell. *Current opinion in cell biology*, 15(2), 221–231 (cit. on pp. 123, 156).
- Valon, L., Etoc, F., Remorino, A., Di Pietro, F., Morin, X., Dahan, M., & Coppey, M. (2015). Predictive Spatiotemporal Manipulation of Signaling Perturbations Using Optogenetics. *Biophysical Journal*, 109(9), 1785–1797. <https://doi.org/10.1016/j.bpj.2015.08.042> (cit. on pp. 7, 17, 18, 64, 66, 74, 84, 123–126)
- Valon, L., Marín-Llauradó, A., Wyatt, T., Charras, G., & Trepat, X. (2017). Optogenetic control of cellular forces and mechanotransduction. *Nature Communications*, 8. <https://doi.org/10.1038/ncomms14396> (cit. on pp. 17, 64, 68, 84, 123, 126)
- Van Rossum, G., & Drake, F. L. (2009). *Python 3 reference manual*. CreateSpace. (Cit. on p. 49).
- Van Rossum, G., & Drake Jr, F. L. (1995). *Python reference manual*. Centrum voor Wiskunde en Informatica Amsterdam. (Cit. on p. 49).
- Vedula, S. R. K., Hirata, H., Nai, M. H., Brugués, A., Toyama, Y., Trepat, X., Lim, C. T., & Ladoux, B. (2014). Epithelial bridges maintain tissue integrity during collective cell migration. *Nature materials*, 13(1), 87–96 (cit. on p. 112).
- Vicente-Manzanares, M., Ma, X., Adelstein, R. S., & Horwitz, A. R. (2009). Non-muscle myosin II takes centre stage in cell adhesion and migration. *Nature Reviews Molecular Cell Biology*, 10(11), 778–790. <https://doi.org/10.1038/nrm2786> (cit. on p. 7)

- Vignaud, T., Copos, C., Leterrier, C., Toro-Nahuelpan, M., Tseng, Q., Mahamid, J., Blanchoin, L., Mogilner, A., Théry, M., & Kurzawa, L. (2021). Stress fibres are embedded in a contractile cortical network. *Nature materials*, *20*(3), 410–420 (cit. on p. 20).
- Vignaud, T., Ennomani, H., & Théry, M. (2014). Polyacrylamide hydrogel micropatterning. *Methods in cell biology* (pp. 93–116). Elsevier. (Cit. on p. 15).
- Virtanen, P., Gommers, R., Oliphant, T. E., Haberland, M., Reddy, T., Cournapeau, D., Burrowski, E., Peterson, P., Weckesser, W., Bright, J. et al. (2020). Scipy 1.0: Fundamental algorithms for scientific computing in python. *Nature methods*, *17*(3), 261–272 (cit. on pp. 70, 101).
- Vishwakarma, M., Di Russo, J., Probst, D., Schwarz, U. S., Das, T., & Spatz, J. P. (2018). Mechanical interactions among followers determine the emergence of leaders in migrating epithelial cell collectives. *Nature Communications*, *9*(1). <https://doi.org/10.1038/s41467-018-05927-6> (cit. on p. 21)
- Vukušić, K., Buda, R., Bosilj, A., Milas, A., Pavin, N., & Tolić, I. M. (2017). Microtubule Sliding within the Bridging Fiber Pushes Kinetochore Fibers Apart to Segregate Chromosomes. *Developmental Cell*, *43*(1), 11–23.e6. <https://doi.org/10.1016/j.devcel.2017.09.010> (cit. on p. 3)
- Wagner, E., & Glotzer, M. (2016). Local rhoa activation induces cytokinetic furrows independent of spindle position and cell cycle stage. *Journal of Cell Biology*, *213*(6), 641–649 (cit. on p. 7).
- Wang, X., Chen, X., & Yang, Y. (2012). Spatiotemporal control of gene expression by a light-switchable transgene system. *Nature methods*, *9*(3), 266–269 (cit. on p. 15).
- Webster, K. D., Ng, W. P., & Fletcher, D. A. (2014). Tensional homeostasis in single fibroblasts. *Biophysical journal*, *107*(1), 146–155 (cit. on p. 57).
- Weißbruch, K., Grewe, J., Hippler, M., Fladung, M., Tremmel, M., Stricker, K., Schwarz, U. S., & Bastmeyer, M. (2021). Distinct roles of nonmuscle myosin ii isoforms for establishing tension and elasticity during cell morphodynamics. *eLife*, *10*, 1–35. <https://doi.org/10.7554/ELIFE.71888> (cit. on p. 22)
- Welte, M. A. (2004). Bidirectional transport along microtubules. *Current Biology*, *14*(13), R525–R537 (cit. on p. 8).
- Wen, J. H., Vincent, L. G., Fuhrmann, A., Choi, Y. S., Hribar, K. C., Taylor-Weiner, H., Chen, S., & Engler, A. J. (2014). Interplay of matrix stiffness and protein tethering in stem cell differentiation. *Nature materials*, *13*(10), 979–987 (cit. on p. 11).
- Weng, S., Shao, Y., Chen, W., & Fu, J. (2016). Mechanosensitive subcellular rheostasis drives emergent single-cell mechanical homeostasis. *Nature materials*, *15*(9), 961–967 (cit. on p. 57).

- Wheeler, M. F. (1978). An elliptic collocation-finite element method with interior penalties. *SIAM Journal on Numerical Analysis*, *15*(1), 152–161 (cit. on p. 118).
- Wyatt, T. P., Fouchard, J., Lisica, A., Khalilgharibi, N., Baum, B., Recho, P., Kabla, A. J., & Charras, G. T. (2020). Actomyosin controls planarity and folding of epithelia in response to compression. *Nature materials*, *19*(1), 109–117 (cit. on p. 74).
- Xu, K., Babcock, H. P., & Zhuang, X. (2012). Dual-objective STORM reveals three-dimensional filament organization in the actin cytoskeleton. *Nature Methods*, *9*(2), 185–188. <https://doi.org/10.1038/nmeth.1841> (cit. on p. 3)
- Yang, S., Lee, K. H., Woodhead, J. L., Sato, O., Ikebe, M., & Craig, R. (2019). The central role of the tail in switching off 10s myosin ii activity. *Journal of General Physiology*, *151*(9), 1081–1093 (cit. on p. 6).
- Yao, M., Qiu, W., Liu, R., Efremov, A. K., Cong, P., Seddiki, R., Payre, M., Lim, C. T., Ladoux, B., Mege, R.-M. *et al.* (2014). Force-dependent conformational switch of α -catenin controls vinculin binding. *Nature communications*, *5*(1), 1–12 (cit. on p. 11).
- Zand, M. S., & Albrecht-Buehler, G. (1989). What structures, besides adhesions, prevent spread cells from rounding up? *Cell Motility and the Cytoskeleton*, *13*(3), 195–211. <https://doi.org/10.1002/cm.970130307> (cit. on pp. 22, 23)
- Zhao, E. M., Zhang, Y., Mehl, J., Park, H., Lalwani, M. A., Toettcher, J. E., & Avalos, J. L. (2018). Optogenetic regulation of engineered cellular metabolism for microbial chemical production. *Nature*, *555*(7698), 683–687 (cit. on p. 15).
- Ziebert, F., Swaminathan, S., & Aranson, I. S. (2012). Model for self-polarization and motility of keratocyte fragments. *Journal of The Royal Society Interface*, *9*(70), 1084–1092 (cit. on p. 25).
- Zienkiewicz, O. C., Taylor, R. L., & Zhu, J. Z. (2005). *The finite element method: Its basis and fundamentals*. Elsevier. (Cit. on pp. 46, 49).
- Zmurchok, C., Bhaskar, D., & Edelstein-Keshet, L. (2018). Coupling mechanical tension and gtpase signaling to generate cell and tissue dynamics. *Physical biology*, *15*(4), 046004 (cit. on p. 114).

Danksagung

An dieser Stelle möchte ich mich ganz herzlich bei allen Personen bedanken, die auf unterschiedliche Art und Weise zum Gelingen dieser Arbeit beigetragen haben.

Ganz besonderer Dank gilt meinem Betreuer Ulrich Schwarz für die hervorragende Betreuung meiner Arbeit. Ohne seine wissenschaftliche Unterstützung und die damit verbundenen interessanten Diskussionen wäre diese nicht möglich gewesen. Neben der Unterstützung meiner Arbeit gab er mir die Möglichkeit, an internationalen Kollaborationen mitzuwirken, auf Tagungen meine Forschungsarbeit zu präsentieren und dabei viel über Biophysik und wissenschaftliche Kommunikation zu lernen. Als Doktorand Teil seiner Arbeitsgruppe sein zu dürfen, war für mich auf wissenschaftlicher und persönlicher Ebene eine tolle Erfahrung.

Ich möchte auch Prof. Heinz Horner für sein Interesse an meiner Arbeit und seine Bereitschaft, sie als Zweitgutachter zu bewerten, herzlichst danken.

Further, I warmly thank my collaboration partners Dimitri Probst, Artur Ruppel, Tomas Andersen, Vladimir Misiak, Thomas Boudou and Martial Balland for the good cooperation and many interesting discussions. I really hope that there will be another opportunity to meet you all in person.

Besonderer Dank gilt dabei Dir, Artur, für die viele Zeit und Leidenschaft, die du in unser Projekt investiert hast. Die Zusammenarbeit mit Dir hat mir sehr viel Freude bereitet und ich habe viel bei unseren zahlreichen Diskussionen lernen dürfen. Wir waren einfach ein super Team und ich hoffe sehr, dass sich unsere Wege früher oder später wieder kreuzen und wir unsere Kollaboration fortsetzen können.

Vielen Dank an alle Mitglieder der AG Schwarz, einschließlich aller ehemaligen Mitglieder, mit denen ich im Laufe der Jahre zusammenarbeiten und eine wirklich schöne Zeit verbringen durfte. Bei Falko Ziebert bedanke ich mich für die Zweitbetreuung meiner Arbeit und die vielen hilfreichen Anregungen in Bezug auf meine Projekte. Bei meinen Bürokollegen Felix Frey, Justin Grewe, Robert Chojowski und Santiago Gomez Melo bedanke ich mich für die erstklassige Atmosphäre im coolsten Büro am Philosophenweg 19 und die unterhaltsamen Kaffeepausen auf der Terrasse.

Many thanks also to former master student Santiago Gomez Melo for the successful collaboration and the time you invested in our project.

Des Weiteren möchte ich Justin Grewe, Gonen Golani, Falko Ziebert, Santiago Gomez Melo, Robert Chojowski, Rafael Gonzalez Albaladejo, Jaime Agudo-Canalejo und David Fischer für das sorgfältige Korrekturlesen meiner Arbeit und viele hilfreiche Verbesserungsvorschläge danken. Pintu Patra danke ich für viele nützliche Hinweise zu meiner Karriereplanung und dass er immer ein offenes Ohr für meine Sorgen und Probleme hatte.

Meinen beiden Freunden Kristian Kolthoff und Florian Laesecke danke ich für viele gute Spiele am Billardtisch, die wesentlich zu einer gesunden Work-Life-Balance beigetragen haben. Ein großes Dankeschön geht auch an meinen besten Freund Marcel Johannvorderbrüggen für die jahrelange Unterstützung und dafür, dass er immer an mich glaubt. Bei meinem Bruder Marvin und meiner Schwester Louisa bedanke ich mich für die moralische Unterstützung und dass sie immer für mich da sind. Ein ganz außerordentlicher Dank geht an meine Mama Tanja und meinen Opa Gernot. Ihr habt mir nicht nur ermöglicht, studieren zu gehen, sondern mich auch immer bedingungslos in all meinen Plänen und Zielen unterstützt. Dafür bin ich euch unendlich dankbar.